

Ministry of Science and Higher Education of the Russian Federation  
ITMO University

ISSN 2220-8054

***NANOSYSTEMS:***  
***PHYSICS, CHEMISTRY, MATHEMATICS***

**2022, volume 13(5)**

**Наносистемы: физика, химия, математика**

**2022, том 13, № 5**



# NANOSYSTEMS:

PHYSICS, CHEMISTRY, MATHEMATICS

## ADVISORY BOARD MEMBERS

**Chairman:** V.N. Vasiliev (*St. Petersburg, Russia*),  
V.M. Buznik (*Moscow, Russia*); V.M. Ievlev (*Voronezh, Russia*), P.S. Kop'ev (*St. Petersburg, Russia*), N.F. Morozov (*St. Petersburg, Russia*), V.N. Parmon (*Novosibirsk, Russia*),  
A.I. Rusanov (*St. Petersburg, Russia*),

## EDITORIAL BOARD

**Editor-in-Chief:** I.Yu. Popov (*St. Petersburg, Russia*)

### Section Co-Editors:

Physics – V.M. Uzdin (*St. Petersburg, Russia*),

Material science – V.V. Gusarov (*St. Petersburg, Russia*); O.V. Al'myasheva (*St. Petersburg, Russia*);

Chemistry – V.K. Ivanov (*Moscow, Russia*),

Mathematics – I.Yu. Popov (*St. Petersburg, Russia*).

### Editorial Board Members:

V.M. Adamyan (*Odessa, Ukraine*); A.P. Alodjants (*Vladimir, Russia*); S. Bechta (*Stockholm, Sweden*); J. Behrndt (*Graz, Austria*); M.B. Belonenko (*Volgograd, Russia*); A. Chatterjee (*Hyderabad, India*); A.V. Chizhov (*Dubna, Russia*); A.N. Enyashin (*Ekaterinburg, Russia*), P.P. Fedorov (*Moscow, Russia*); E.A. Gudilin (*Moscow, Russia*); H. Jónsson (*Reykjavik, Iceland*); A.A. Kiselev (*Durham, USA*); Yu.S. Kivshar (*Canberra, Australia*); S.A. Kozlov (*St. Petersburg, Russia*); P.A. Kurasov (*Stockholm, Sweden*); A.V. Lukashin (*Moscow, Russia*); I.V. Melikhov (*Moscow, Russia*); G.P. Miroshnichenko (*St. Petersburg, Russia*); I.Ya. Mittova (*Voronezh, Russia*); Nguyen Anh Tien (*Ho Chi Minh, Vietnam*); V.V. Pankov (*Minsk, Belarus*); K. Pankrashkin (*Orsay, France*); A.V. Ragulya (*Kiev, Ukraine*); V. Rajendran (*Tamil Nadu, India*); A.A. Rempel (*Ekaterinburg, Russia*); V.Ya. Rudyak (*Novosibirsk, Russia*); H.M. Sedighi (*Ahvaz, Iran*); D Shoikhet (*Karmiel, Israel*); P Stovicek (*Prague, Czech Republic*); V.M. Talanov (*Novocherkassk, Russia*); A.Ya. Vul' (*St. Petersburg, Russia*); A.V. Yakimansky (*St. Petersburg, Russia*), V.A. Zagrebnev (*Marseille, France*).

### Editors:

I.V. Blinova; A.I. Popov; A.I. Trifanov; E.S. Trifanova (*St. Petersburg, Russia*),  
R. Simoneaux (*Philadelphia, Pennsylvania, USA*).

**Address:** ITMO University, Kronverkskiy pr., 49, St. Petersburg 197101, Russia.

**Phone:** +7(812)607-02-54, **Journal site:** <http://nanojournal.ifmo.ru/>,

**E-mail:** [nanojournal.ifmo@gmail.com](mailto:nanojournal.ifmo@gmail.com)

## AIM AND SCOPE

The scope of the journal includes all areas of nano-sciences. Papers devoted to basic problems of physics, chemistry, material science and mathematics inspired by nanosystems investigations are welcomed. Both theoretical and experimental works concerning the properties and behavior of nanosystems, problems of its creation and application, mathematical methods of nanosystem studies are considered.

The journal publishes scientific reviews (up to 30 journal pages), research papers (up to 15 pages) and letters (up to 5 pages). All manuscripts are peer-reviewed. Authors are informed about the referee opinion and the Editorial decision.

# CONTENT

## MATHEMATICS

- T.K. Yuldashev, S.K. Zarifzoda  
**Inverse problem for Fredholm integro-differential equation with final redefinition conditions at the end of the interval** 483
- M.I. Muminov, T.A. Radjabov  
**On existence conditions of periodic solutions to a differential equation with constant argument** 491

## PHYSICS

- N.N. Ganikhodjaev, M.M. Rahmatullaev, M.R. Abdusalomova  
**Phase transitions for the "uncle-nephew" model** 498
- I.V. Pleshakov, O.V. Proskurina, V.I. Gerasimov, Yu.I. Kuz'min  
**Optical anisotropy in fullerene-containing polymer composites induced by magnetic field** 503

## CHEMISTRY AND MATERIAL SCIENCE

- M.V. Kaneva, E.V. Borisov, V.P. Tolstoy  
**Pt(0) microscrolls obtained on nickel surface by galvanic replacement reaction in  $H_2PtCl_6$  solution as the basis for creating new SERS substrates** 509
- M.E. Kotova, T.P. Maslennikova, V.L. Ugolkov, V.V. Gusarov  
**Formation, structure, composition in the dispersed state, and behavior of nanoparticles heated in the  $Mg(OH)_2$  -  $Ni(OH)_2$  system** 514
- A.A. Lobinsky, M.I. Tenevich  
**Synthesis 2D nanocrystals of Co-doped manganese oxide as cathode materials of zinc-ion hybrid supercapacitor** 525
- Ujwala M. Pagar, Uglal. P. Shinde  
**Preparation and investigation of the screen-printed cobalt oxide ( $Co_3O_4$ ) nanostructured thick film with annealing temperature** 530
- P.P. Fedorov, I.A. Novikov, V.V. Voronov,  
L.V. Badyanova, S.V. Kuznetsov, E.V. Chernova  
**Transformation of siderite in the zone of hypergenesis** 539

Runjun Sarma, Munmi Sarma, Manash Jyoti Kashyap <b>Synthesis and optical properties of MnSe nanostructures: a review</b>	<b>546</b>
N.K. Thach, I.S. Krechetov, V.V. Berestov, T.L. Lepkova, S.V. Stakhanova <b>Optimizing the carbonization temperature in the fabrication of waste cotton based activated carbon used as electrode material for supercapacitor</b>	<b>565</b>
Vilas Khairnar <b>Growth of carbon nanotubes on a finely dispersed nickel metal and study its electrochemical application</b>	<b>574</b>
M.A. Lobaev, A.L. Vikharev, A.M. Gorbachev, D.B. Radishev, E.A. Arkhipova, M.N. Drozdov, V.A. Isaev, S.A. Bogdanov, V.A. Kukushkin <b>Investigation of boron-doped delta layers in CVD diamond grown on single-sector HPHT substrates</b>	<b>578</b>
<b>Information for authors</b>	<b>585</b>

## Inverse problem for Fredholm integro-differential equation with final redefinition conditions at the end of the interval

Tursun K. Yuldashev<sup>1,a</sup>, Sarvar K. Zarifzoda<sup>2,b</sup>

<sup>1</sup>Tashkent State University of Economics, Tashkent, Uzbekistan

<sup>2</sup>Tajik National University, Dushanbe, Tajikistan

<sup>a</sup>tursun.k.yuldashev@gmail.com, <sup>b</sup>sarvar8383@list.ru

Corresponding author: Tursun K. Yuldashev, tursun.k.yuldashev@gmail.com

**ABSTRACT** The questions of solvability and construction of solutions of an inverse problem for second-order Fredholm integro-differential equation with degenerate kernel, final conditions at the end of the interval, two parameters, and two redefinition data are considered. The sets of regular parameter values are determined and the corresponding solutions are constructed. The specific features of the inverse problem are studied. Criteria for the unique solvability of the posed inverse problem are established.

**KEYWORDS** integro-differential equation, degenerate kernel, final conditions at the end of a segment, parameters, redefinition data, solvability.

**FOR CITATION** Yuldashev T.K., Zarifzoda S.K. Inverse problem for Fredholm integro-differential equation with final redefinition conditions at the end of the interval. *Nanosystems: Phys. Chem. Math.*, 2022, **13** (5), 483–490.

### 1. Problem statement

The differential and integro-differential equations have applications in biological, chemical and physical sciences, ecology, biotechnology, industrial robotics, pharmacokinetics, biophysics at micro- and nano-scales [1–13]. Today, for ordinary integro-differential equations, new problems are posed and a large number of papers, devoting to study of integro-differential equations, are published. Problems with nonlocal conditions for differential and integro-differential equations were considered in [14–35]. Integro-differential equations with degenerate kernel were considered in [36–40].

In this paper, we study the solvability of the inverse problem for second-order ordinary Fredholm integro-differential equation with degenerate kernel, two parameters, and final conditions at the end of the interval. This paper differs from papers mentioned above in requirement of finding two unknown redefinition data. This inverse problem has features related with the corresponding direct problem. Let us describe the latter one. We consider on the segment  $[0; T]$  integro-differential equation of the form

$$u''(t) + (\lambda^2 - \alpha(t)) u(t) = \nu \int_0^T K(t, s) u(s) ds, \quad (1)$$

where  $T, T > 0$ , is given real number,  $\lambda, \lambda > 0$ , is real parameter,  $\nu$  is real nonzero parameter,  $\alpha(t) \in C[0; T]$  is positive function,  $K(t, s) = \sum_{i=1}^k a_i(t) b_i(s)$ ,  $a_i(t), b_i(s) \in C[0; T]$ . It is assumed that the systems of functions  $\{a_i(t)\}$  and  $\{b_i(s)\}$ ,  $i = \overline{1, k}$  are linear independent.

We consider equation (1) with the following conditions

$$u(T) = \varphi_1, \quad u'(T) = \varphi_2, \quad (2)$$

$$u(t_1) = \psi_1, \quad u'(t_1) = \psi_2, \quad (3)$$

where  $0 < t_1 < T < \infty$ ,  $\varphi_j = \text{const}$ ,  $\varphi_j$  are constant quantities of redefinition,  $\psi_j = \text{const}$ ,  $j = 1, 2$ . The choice of conditions (2) with the final data is related to the fact that in many practical applications, it is not possible to determine the initial conditions. For example, when studying the technological process of aluminum production, before the start of the production cycle, the raw material passes through firing and the state of the raw material at the beginning of the production cycle is not known. However, the final expected state of the output will be known or we can find it from known intermediate state.

**Formulation of the problem.** It is required to find a triple of unknowns

$$\{u(t) \in C^2[0; T], \varphi_i \in \mathbb{R}, i = 1, 2\},$$

where the first one is a function satisfying equation (1), the second and the third are values from conditions (2) and (3).

Note that the problem is formulated in such a way that the direct problem (1), (2) has a unique solution for all values of the parameter  $\lambda$ , and the inverse problem (1)–(3) has a unique solution only for certain values of this parameter  $\lambda$ . In addition, the second parameter  $\nu$  also plays an important role in the issue of solvability.

**2. Solution of the direct problem (1), (2)**

Taking into account the degeneracy of the kernel, we rewrite equation (1) in the following form

$$u''(t) + \lambda^2 u(t) = \nu \sum_{i=1}^k a_i(t) \tau_i + \alpha(t) u(t), \tag{4}$$

where

$$\tau_i = \int_0^T b_i(s) u(s) ds. \tag{5}$$

Solving the inhomogeneous differential equation (4) by the method of variation of arbitrary constants, we obtain the representation

$$u(t) = A_1 \cos \lambda t + A_2 \sin \lambda t + \frac{\nu}{\lambda} \sum_{i=1}^k \tau_i \int_0^t \sin \lambda(t-s) a_i(s) ds + \frac{1}{\lambda} \int_0^t \sin \lambda(t-s) \alpha(s) u(s) ds, \tag{6}$$

where  $A_1, A_2$  are yet arbitrary constants. By differentiating (6) one time, we obtain

$$u'(t) = -\lambda A_1 \sin \lambda t + \lambda A_2 \cos \lambda t + \frac{\nu}{\lambda} \sum_{i=1}^k \tau_i \int_0^t \lambda \cos \lambda(t-s) a_i(s) ds + \frac{1}{\lambda} \int_0^t \lambda \cos \lambda(t-s) \alpha(s) u(s) ds. \tag{7}$$

To find the unknown coefficients, we use the final conditions (2). Then, from representations (6) and (7) we arrive at a system of algebraic equations (SAE)

$$\begin{cases} A_1 \cos \lambda T + A_2 \sin \lambda T = \gamma_1, \\ -A_1 \sin \lambda T + A_2 \cos \lambda T = \gamma_2, \end{cases} \tag{8}$$

where

$$\gamma_1 = \varphi_1 - \frac{\nu}{\lambda} \sum_{i=1}^k \tau_i \beta_{1i} - \frac{1}{\lambda} \int_0^T \sin \lambda(T-s) \alpha(s) u(s) ds, \tag{9}$$

$$\gamma_2 = \varphi_2 - \frac{\nu}{\lambda} \sum_{i=1}^k \tau_i \beta_{2i} - \frac{1}{\lambda} \int_0^T \cos \lambda(T-s) \alpha(s) u(s) ds, \tag{10}$$

$$\beta_{1i} = \int_0^T \sin \lambda(T-s) a_i(s) ds, \quad \beta_{2i} = \int_0^T \cos \lambda(T-s) a_i(s) ds.$$

For the unique solvability of SAE (8), the condition

$$\delta_0 = \begin{vmatrix} \cos \lambda T & \sin \lambda T \\ -\sin \lambda T & \cos \lambda T \end{vmatrix} \neq 0$$

should be fulfilled. Since  $\delta_0 = 1$ , this condition is fulfilled for all values of the parameter  $\lambda$ . Consequently, SAE (8) has the unique solution

$$A_1 = \delta_1 = \begin{vmatrix} \gamma_1 & \sin \lambda T \\ \gamma_2 & \cos \lambda T \end{vmatrix} = \varphi_1 \cos \lambda T - \varphi_2 \sin \lambda T + \frac{\nu}{\lambda} \sum_{i=1}^k \tau_i \int_0^T \sin \lambda s a_i(s) ds + \frac{1}{\lambda} \int_0^T \sin \lambda s \alpha(s) u(s) ds, \tag{11}$$

$$A_2 = \delta_2 = \begin{vmatrix} \cos \lambda T & \gamma_1 \\ -\sin \lambda T & \gamma_2 \end{vmatrix} = \varphi_1 \sin \lambda T + \varphi_2 \cos \lambda T + \frac{\nu}{\lambda} \sum_{i=1}^k \tau_i \int_0^T \cos \lambda s a_i(s) ds + \frac{1}{\lambda} \int_0^T \cos \lambda s \alpha(s) u(s) ds. \quad (12)$$

Substituting (11) and (12) into representation (6), we obtain

$$u(t) = \varphi_1 \chi_1(t) + \varphi_2 \chi_2(t) + \frac{\nu}{\lambda} \sum_{i=1}^k \tau_i \chi_{3i}(t) + \frac{1}{\lambda} \int_0^t H(t, s, \lambda) \alpha(s) u(s) ds, \quad (13)$$

where

$$\chi_1(t) = \cos \lambda(T - t) - \sin \lambda(T - t), \quad \chi_2(t) = \cos \lambda(T + t) - \sin \lambda(T - t),$$

$$\chi_{3i}(t) = \int_0^T H(t, s, \lambda) a_i(s) ds,$$

$$H(t, s, \lambda) = \begin{cases} \sin \lambda(t + s), & t < s \leq T, \\ \sin \lambda(t - s) + \cos \lambda t \sin \lambda s + \lambda \sin \lambda t \sin \lambda s, & 0 \leq s < t. \end{cases}$$

Although function (13) is a solution to the direct problem (1), (2), it contains quantities that are still unknown. To find these quantities  $\tau_i$ , we substitute representation (13) into (5) and arrive at a new SAE:

$$\tau_i - \frac{\nu}{\lambda} \sum_{j=1}^k \tau_j \sigma_{3ij}(t) = \varphi_1 \sigma_{1i} + \varphi_2 \sigma_{2i} + \sigma_{4i}, \quad (14)$$

where

$$\sigma_{1i} = \int_0^T b_i(s) \cos \lambda(T - s) ds, \quad \sigma_{2i} = -\int_0^T b_i(s) \sin \lambda(T - s) ds,$$

$$\sigma_{3ij} = \int_0^T b_i(s) \int_0^T H(s, \theta, \lambda) a_j(\theta) d\theta ds, \quad \sigma_{4i} = \frac{1}{\lambda} \int_0^T b_i(s) \int_0^T H(s, \theta, \lambda) \alpha(\theta) u(\theta) d\theta ds.$$

To establish the unique solvability of SAE (14), we introduce the following matrix

$$\Theta_0(\nu, \lambda) = \begin{pmatrix} 1 - \frac{\nu}{\lambda} \sigma_{311} & \frac{\nu}{\lambda} \sigma_{312} & \dots & \frac{\nu}{\lambda} \sigma_{31k} \\ \frac{\nu}{\lambda} \sigma_{321} & 1 - \frac{\nu}{\lambda} \sigma_{322} & \dots & \frac{\nu}{\lambda} \sigma_{32k} \\ \dots & \dots & \dots & \dots \\ \frac{\nu}{\lambda} \sigma_{3k1} & \frac{\nu}{\lambda} \sigma_{3k2} & \dots & 1 - \frac{\nu}{\lambda} \sigma_{3kk} \end{pmatrix}$$

and consider the values of the parameter  $\nu$ , for which the Fredholm determinant differs from zero:

$$\Delta_0(\nu, \lambda) = \det \Theta_0(\nu, \lambda) \neq 0. \quad (15)$$

Determinant  $\Delta_0(\nu, \lambda)$  in (15) is a polynomial with respect to  $\frac{\nu}{\lambda}$  of the degree not higher than  $k$ . The algebraic equation  $\Delta_0(\nu, \lambda) = 0$  has no more than  $k$  different real roots. We denote them by  $\mu_l$  ( $l = \overline{1, p}$ ,  $1 \leq p \leq k$ ). Then  $\nu = \nu_l = \lambda \mu_l$  are called the characteristic (irregular) values of the kernel of the integro-differential equation (1). So, we introduce the following two designations

$$\Omega_1 = \{(\nu, \lambda) : \nu = \lambda \mu_l, \lambda \in (0, \infty)\}, \quad \Omega_2 = \{(\nu, \lambda) : \nu \neq \lambda \mu_l, \lambda \in (0, \infty)\}.$$

The set  $\Omega_1$  is the set of irregular values of the kernel of the integro-differential equation (1). While the set  $\Omega_2$  is the set of regular values of the kernel.

On the number set  $\Omega_2$  we consider a matrix

$$\Theta_{im}(\nu, \lambda) = \begin{pmatrix} 1 - \frac{\nu}{\lambda} \sigma_{311} & \dots & \frac{\nu}{\lambda} \sigma_{31(i-1)} & \sigma_{m1} & \frac{\nu}{\lambda} \sigma_{31(i+1)} & \dots & \frac{\nu}{\lambda} \sigma_{31k} \\ \frac{\nu}{\lambda} \sigma_{321} & \dots & \frac{\nu}{\lambda} \sigma_{32(i-1)} & \sigma_{m2} & \frac{\nu}{\lambda} \sigma_{32(i+1)} & \dots & \frac{\nu}{\lambda} \sigma_{32k} \\ \dots & \dots & \dots & \dots & \dots & \dots & \dots \\ \frac{\nu}{\lambda} \sigma_{3k1} & \dots & \frac{\nu}{\lambda} \sigma_{3k(i-1)} & \sigma_{mk} & \frac{\nu}{\lambda} \sigma_{3k(i+1)} & \dots & 1 - \frac{\nu}{\lambda} \sigma_{3kk} \end{pmatrix},$$

$m = 1, 2, 4$ . Taking into account the known properties of the matrix  $\Theta_{im}(\nu, \lambda)$ , we apply the Cramer method on the spectral set  $\Omega_2$  and obtain solutions of SAE (14) in the form

$$\tau_i = \varphi_1 \frac{\Delta_{1i}(\nu, \lambda)}{\Delta_0(\nu, \lambda)} + \varphi_2 \frac{\Delta_{2i}(\nu, \lambda)}{\Delta_0(\nu, \lambda)} + \frac{\Delta_{4i}(\nu, \lambda, u)}{\Delta_0(\nu, \lambda)}, \quad i = \overline{1, k}, \quad (\nu, \lambda) \in \Omega_2, \tag{16}$$

where  $\Delta_{im}(\nu, \lambda) = \det \Theta_{im}(\nu, \lambda)$ ,  $m = 1, 2, 4$ . Substituting solutions (16) into function (13), we obtain

$$u(t, \nu, \lambda) = \varphi_1 h_1(t, \nu, \lambda) + \varphi_2 h_2(t, \nu, \lambda) + \frac{\nu}{\lambda} \sum_{i=1}^k \frac{\Delta_{4i}(\nu, \lambda, u)}{\Delta_0(\nu, \lambda)} \chi_{3i}(t) + \int_0^T \bar{H}(t, s, \lambda) u(s, \nu, \lambda) ds, \quad (\nu, \lambda) \in \Omega_2, \tag{17}$$

where

$$h_j(t, \nu, \lambda) = \chi_j(t) + \frac{\nu}{\lambda} \sum_{i=1}^k \frac{\Delta_j(\nu, \lambda)}{\Delta_0(\nu, \lambda)} \chi_{3i}(t), \quad j = 1, 2,$$

$$\chi_{3i}(t) = \int_0^T H(t, s, \lambda) a_i(s) ds, \quad \bar{H}(t, s, \lambda) = \frac{1}{\lambda} H(t, s, \lambda) \alpha(s).$$

Note that representation (17) is equivalent to the direct problem (1), (2) for regular values of the parameter  $\nu$ . However,  $\varphi_1$  and  $\varphi_2$  have not been determined yet.

### 3. Solution of the inverse problem (1)–(3)

For convenience, representation (17) can be written in the following form

$$u(t, \nu, \lambda) = \varphi_1 \left[ \cos \lambda(T-t) - \sin \lambda(T-t) + \frac{\nu}{\lambda} \sum_{i=1}^k \frac{\Delta_1(\nu, \lambda)}{\Delta_0(\nu, \lambda)} \chi_{3i}(t) \right] +$$

$$+ \varphi_2 \left[ \cos \lambda(T+t) - \sin \lambda(T-t) + \frac{\nu}{\lambda} \sum_{i=1}^k \frac{\Delta_2(\nu, \lambda)}{\Delta_0(\nu, \lambda)} \chi_{3i}(t) \right] +$$

$$+ \frac{\nu}{\lambda} \sum_{i=1}^k \frac{\Delta_{4i}(\nu, \lambda, u)}{\Delta_0(\nu, \lambda)} \chi_{3i}(t) + \int_0^T \bar{H}(t, s, \lambda) u(s, \nu, \lambda) ds, \quad (\nu, \lambda) \in \Omega_2. \tag{18}$$

We differentiate (18) one time:

$$u'(t, \nu, \lambda) = \varphi_1 \left[ \lambda \sin \lambda(T-t) + \lambda \cos \lambda(T-t) + \frac{\nu}{\lambda} \sum_{i=1}^k \frac{\Delta_1(\nu, \lambda)}{\Delta_0(\nu, \lambda)} \chi'_{3i}(t) \right] +$$

$$+ \varphi_2 \left[ -\lambda \sin \lambda(T+t) + \lambda \cos \lambda(T-t) + \frac{\nu}{\lambda} \sum_{i=1}^k \frac{\Delta_2(\nu, \lambda)}{\Delta_0(\nu, \lambda)} \chi'_{3i}(t) \right] +$$

$$+ \frac{\nu}{\lambda} \sum_{i=1}^k \frac{\Delta_{4i}(\nu, \lambda, u)}{\Delta_0(\nu, \lambda)} \chi'_{3i}(t) + \int_0^T \bar{H}'(t, s, \lambda) u(s, \nu, \lambda) ds, \quad (\nu, \lambda) \in \Omega_2, \tag{19}$$

where

$$\chi'_{3i}(t) = \int_0^T H'(t, s, \lambda) a_i(s) ds,$$

$$H'(t, s, \omega) = \begin{cases} \lambda \cos \lambda(t+s), & t < s \leq T, \\ \lambda \cos \lambda(t-s) - \lambda \sin \lambda t \sin \lambda s + \lambda^2 \cos \lambda t \sin \lambda s, & 0 \leq s < t. \end{cases}$$

$$\bar{H}'(t, s, \lambda) = \frac{1}{\lambda} H'(t, s, \lambda) \alpha(s).$$

Then, applying intermediate conditions (3) to functions (18) and (19), we arrive at the solution of the following SAE:

$$\begin{cases} \varphi_1 [\chi_1(t_1, \lambda) + \varepsilon_{11}] + \varphi_2 [\chi_2(t_1, \lambda) + \varepsilon_{12}] = \bar{\psi}_1, \\ \varphi_1 [\chi'_1(t_1, \lambda) + \varepsilon_{21}] + \varphi_2 [\chi'_{2n}(t_1, \lambda) + \varepsilon_{22}] = \bar{\psi}_2, \end{cases} \tag{20}$$

where

$$\begin{aligned} \varepsilon_{1j} &= \frac{\nu}{\lambda} \sum_{i=1}^k \frac{\Delta_j(\nu, \lambda)}{\Delta_0(\nu, \lambda)} \chi_{3i}(t_1), \quad \varepsilon_{2j} = \frac{\nu}{\lambda} \sum_{i=1}^k \frac{\Delta_j(\nu, \lambda)}{\Delta_0(\nu, \lambda)} \chi'_{3i}(t_1), \quad j = 1, 2, \\ \bar{\psi}_1 &= \psi_1 - \frac{\nu}{\lambda} \sum_{i=1}^k \frac{\Delta_{4i}(\nu, \lambda, u)}{\Delta_0(\nu, \lambda)} \chi_{3i}(t_1) + \int_0^T \bar{H}(t_1, s, \lambda) u(s, \nu, \lambda) ds, \end{aligned} \tag{21}$$

$$\bar{\psi}_2 = \psi_2 - \frac{\nu}{\lambda} \sum_{i=1}^k \frac{\Delta_{4i}(\nu, \lambda, u)}{\Delta_0(\nu, \lambda)} \chi'_{3i}(t_1) + \int_0^T \bar{H}'(t_1, s, \lambda) u(s, \nu, \lambda) ds. \tag{22}$$

The fulfillment of the following condition ensures the unique solvability of SAE (20):

$$\begin{aligned} V_0(\lambda) &= \begin{vmatrix} \chi_1(t_1, \lambda) + \varepsilon_{11} & \chi_2(t_1, \lambda) + \varepsilon_{12} \\ \chi'_1(t_1, \lambda) + \varepsilon_{21} & \chi'_2(t_1, \lambda) + \varepsilon_{22} \end{vmatrix} = \\ &= -\lambda \sin 2\lambda T - \lambda \cos 2\lambda T + 2\lambda \sin \lambda(T - t_1) \cos \lambda(T - t_1) - \lambda \cos 2\lambda(T - t_1) - \\ &\quad - \lambda \varepsilon_{11} [\sin \lambda(T + t_1) + \cos \lambda(T - t_1)] - \lambda \varepsilon_{12} [\sin \lambda(T - t_1) + \cos \lambda(T - t_1)] - \\ &\quad - \varepsilon_{21} [\cos \lambda(T + t_1) - \lambda \sin \lambda(T - t_1)] - \varepsilon_{22} [\sin \lambda(T - t_1) - \lambda \cos \lambda(T - t_1)] + \\ &\quad + \varepsilon_{11} \varepsilon_{22} - \varepsilon_{21} \varepsilon_{12} \neq 0. \end{aligned} \tag{23} \end{aligned}$$

Before proceeding to the solution of SAE (20), we consider condition (23) for the general case. To do this, suppose the opposite:

$$\begin{aligned} & -\lambda \sin 2\lambda T - \lambda \cos 2\lambda T + 2\lambda \sin \lambda(T - t_1) \cos \lambda(T - t_1) - \lambda \cos 2\lambda(T - t_1) - \\ &\quad - \lambda \varepsilon_{11} [\sin \lambda(T + t_1) + \cos \lambda(T - t_1)] - \lambda \varepsilon_{12} [\sin \lambda(T - t_1) + \cos \lambda(T - t_1)] - \\ &\quad - \varepsilon_{21} [\cos \lambda(T + t_1) - \lambda \sin \lambda(T - t_1)] - \varepsilon_{22} [\sin \lambda(T - t_1) - \lambda \cos \lambda(T - t_1)] + \\ &\quad + \varepsilon_{11} \varepsilon_{22} - \varepsilon_{21} \varepsilon_{12} = 0. \end{aligned} \tag{24}$$

Condition (24) is a transcendental equation and the set of its solutions with respect to  $\lambda$  denote by  $\mathfrak{S}$ . So, on the set

$$\Omega_3 = \{(\nu_n, \lambda) : |\Delta_0(\nu, \lambda)| > 0, \nu_n \neq \lambda \mu_l, \lambda \in \mathfrak{S}\}$$

SAE (20) is not one valued solvable. But, on the other set

$$\Omega_4 = \{(\nu_n, \lambda) : |\Delta_0(\nu, \lambda)| > 0, |V_0(\lambda)| > 0, \nu_n \neq \lambda \mu_l, \lambda \in (0; \infty) \setminus \mathfrak{S}\}$$

SAE (20) is one valued solvable. Taking into account notations (21) and (22), we obtain

$$\varphi_j = \psi_1 w_{j1} + \psi_2 w_{j2} + \frac{\nu}{\lambda} \sum_{i=1}^k \frac{\Delta_{4i}(\nu, \lambda, u)}{\Delta_0(\nu, \lambda)} w_{j3i} + \int_0^T W_j(s, \lambda) u(s, \nu, \lambda) ds, \quad j = 1, 2, \tag{25}$$

where

$$\begin{aligned} w_{11} &= V_0^{-1}(\chi'_2(t_1) + \varepsilon_{22}), \quad w_{12} = V_0^{-1}(-\chi_2(t_1) + \varepsilon_{12}), \\ w_{21} &= V_0^{-1}(\chi'_1(t_1) + \varepsilon_{21}), \quad w_{22} = V_0^{-1}(\chi_1(t_1) + \varepsilon_{11}), \\ w_{13}(\lambda) &= -[\chi_{3i}(t_1, \lambda) w_{11}(\lambda) + \chi'_{3i}(t_1, \lambda) w_{12}(\lambda)], \\ w_{23}(\lambda) &= -[\chi_{3i}(t_1, \lambda) w_{21}(\lambda) + \chi'_{3i}(t_1, \lambda) w_{22}(\lambda)], \\ W_1(s, \lambda) &= H(t_1, s) w_{11}(\lambda) + H'(t_1, s) w_{12}(\lambda), \\ W_2(s, \lambda) &= H(t_1, s) w_{21}(\lambda) + H'(t_1, s) w_{22}(\lambda). \end{aligned}$$

Representations in (25) are expressions of unknown quantities  $\varphi_1$  and  $\varphi_2$  in terms of an unknown function  $u(t, \nu, \lambda)$ . Therefore, we need to uniquely define the function  $u(t, \nu, \lambda)$ . Substituting representations (25) into equation (17), we obtain in the final form the following functional-integral equation

$$\begin{aligned} u(t, \nu, \lambda) &= W(t, \nu, \lambda, u) \equiv \psi_1 g_1(t, \nu, \lambda) + \psi_2 g_2(t, \nu, \lambda) + \\ &\quad + \frac{\nu}{\lambda} \sum_{i=1}^k \frac{\Delta_{4i}(\nu, \lambda, u)}{\Delta_0(\nu, \lambda)} g_{3i}(t) + \int_0^T G(t, s, \nu, \lambda) u(s, \nu, \lambda) ds, \quad (\nu, \lambda) \in \Omega_5, \end{aligned} \tag{26}$$

where

$$\begin{aligned} g_1(t, \nu, \lambda) &= w_{11}(\lambda) h_1(t, \nu, \lambda) + w_{21}(\lambda) h_2(t, \nu, \lambda), \\ g_2(t, \nu, \lambda) &= w_{12}(\lambda) h_1(t, \nu, \lambda) + w_{22}(\lambda) h_2(t, \nu, \lambda), \\ g_{3i}(t) &= g_1(t, \nu, \lambda) \chi_{3i}(t_1) + g_2(t, \nu, \lambda) \chi'_{3i}(t_1) + \chi_{3i}(t), \end{aligned}$$

$$G(t, s, \nu, \lambda) = g_1(t, \nu, \lambda) \bar{H}(t_1, s) + g_2(t, \nu, \lambda) \bar{H}'(t_1, s) + \bar{H}(t, s).$$

Note that this functional-integral equation makes sense only for values of parameters  $\nu, \lambda$  from the set  $\Omega_4$ . In addition, in the functional-integral equation (26), the unknown function  $u(t, \nu, \lambda)$  is under the sign of the determinant and under the sign of the integral. Let us investigate this equation in the question of unique solvability. To this end, consider the space of functions continuous on the interval  $[0; T]$ . In this space, we introduce the norm as follows:  $\|u(t)\| = \max_{0 \leq t \leq T} |u(t)|$ .

**Theorem.** Let be fulfilled the following condition

$$\rho = \frac{|\nu|}{\lambda} \sum_{i=1}^k \left| \frac{\bar{\Delta}_{4i}(\nu, \lambda)}{\Delta_0(\nu, \lambda)} \right| \|g_{3i}(t)\| + \int_0^T \|G(t, s, \nu, \lambda)\| ds < 1,$$

where  $|\bar{\Delta}_{4i}(\nu, \lambda)|$  is defined from (30). Then the functional-integral equation (26) has the unique solution for values of parameters  $\nu, \lambda$  from the set  $\Omega_4$  and for all  $t \in [0; T]$ . This solution can be found from the following iterative Picard process

$$\begin{cases} u_0(t, \nu, \lambda) = \psi_1 g_1(t, \nu, \lambda) + \psi_2 g_2(t, \nu, \lambda), \\ u_k(t, \nu, \lambda) = W(t, \nu, \lambda, u_{k-1}), \quad k = 1, 2, 3, \dots \end{cases}$$

**Proof.** Since  $\psi_j$  and  $g_j(t, \nu, \lambda)$ ,  $j = 1, 2$ , are bounded, then for zero approximation we obtain the estimate

$$|u_0(t, \nu, \lambda)| = |\psi_1| |g_1(t, \nu, \lambda)| + |\psi_2| |g_2(t, \nu, \lambda)| \leq M (|\psi_1| + |\psi_2|) < \infty, \tag{27}$$

where  $M = \max \{ \|g_1(t, \nu, \lambda)\|, \|g_2(t, \nu, \lambda)\| \}$ .

Similarly to (27), taking into account the property of the determinant, we obtain an estimate for the first difference of the approximation

$$|u_1(t, \nu, \lambda) - u_0(t, \nu, \lambda)| \leq \frac{|\nu|}{\lambda} \sum_{i=1}^k \left| \frac{\Delta_{4i}(\nu, \lambda, u_0)}{\Delta_0(\nu, \lambda)} \right| \|g_{3i}(t)\| + M (|\psi_1| + |\psi_2|) \int_0^T \|G(t, s, \nu, \lambda)\| ds. \tag{28}$$

where  $|\Delta_{i4}(\nu, \lambda, u_0)| = |\det \Theta_{i4}(\nu, \lambda, u_0)|$ ,

$$\Theta_{i4}(\nu, \lambda, u_0) = \begin{pmatrix} 1 - \frac{\nu}{\lambda} \sigma_{311} & \dots & \frac{\nu}{\lambda} \sigma_{31(i-1)} & \sigma_{41}(u_0) & \frac{\nu}{\lambda} \sigma_{31(i+1)} & \dots & \frac{\nu}{\lambda} \sigma_{31k} \\ \frac{\nu}{\lambda} \sigma_{321} & \dots & \frac{\nu}{\lambda} \sigma_{32(i-1)} & \sigma_{42}(u_0) & \frac{\nu}{\lambda} \sigma_{32(i+1)} & \dots & \frac{\nu}{\lambda} \sigma_{32k} \\ \dots & \dots & \dots & \dots & \dots & \dots & \dots \\ \frac{\nu}{\lambda} \sigma_{3k1} & \dots & \frac{\nu}{\lambda} \sigma_{3k(i-1)} & \sigma_{4k}(u_0) & \frac{\nu}{\lambda} \sigma_{3k(i+1)} & \dots & 1 - \frac{\nu}{\lambda} \sigma_{3kk} \end{pmatrix},$$

$$\sigma_{4i}(u_0) = M (|\psi_1| + |\psi_2|) \int_0^T |b_i(s)| \int_0^T |\bar{H}(s, \theta, \lambda)| d\theta ds.$$

Continuing this process, we obtain by induction that

$$\begin{aligned} |u_k(t, \nu, \lambda) - u_{k-1}(t, \nu, \lambda)| \leq & \\ & + \frac{|\nu|}{\lambda} \sum_{i=1}^k \left| \frac{\Delta_{4i}(\nu, \lambda, u_{k-1}) - \Delta_{4i}(\nu, \lambda, u_{k-2})}{\Delta_0(\nu, \lambda)} \right| \|g_{3i}(t)\| + \\ & + \int_0^T \|G(t, s, \nu, \lambda)\| |u_{k-1}(s, \nu, \lambda) - u_{k-2}(s, \nu, \lambda)| ds. \end{aligned}$$

This implies the estimate

$$\|u_k(t, \nu, \lambda) - u_{k-1}(t, \nu, \lambda)\| \leq \rho \|u_{k-1}(t, \nu, \lambda) - u_{k-2}(t, \nu, \lambda)\|, \tag{29}$$

where

$$\begin{aligned} \rho = \frac{|\nu|}{\lambda} \sum_{i=1}^k \left| \frac{\bar{\Delta}_{4i}(\nu, \lambda)}{\Delta_0(\nu, \lambda)} \right| \|g_{3i}(t)\| + \int_0^T \|G(t, s, \nu, \lambda)\| ds, \\ |\bar{\Delta}_{4i}(\nu, \lambda)| = |\det \bar{\Theta}_{4i}(\nu, \lambda)|, \end{aligned} \tag{30}$$

$$\bar{\Theta}_{4i}(\nu, \lambda) = \begin{pmatrix} 1 - \frac{\nu}{\lambda} \sigma_{311} & \cdots & \frac{\nu}{\lambda} \sigma_{31(i-1)} & \bar{\sigma}_{41} & \frac{\nu}{\lambda} \sigma_{31(i+1)} & \cdots & \frac{\nu}{\lambda} \sigma_{31k} \\ \frac{\nu}{\lambda} \sigma_{321} & \cdots & \frac{\nu}{\lambda} \sigma_{32(i-1)} & \bar{\sigma}_{42} & \frac{\nu}{\lambda} \sigma_{32(i+1)} & \cdots & \frac{\nu}{\lambda} \sigma_{32k} \\ \cdots & \cdots & \cdots & \cdots & \cdots & \cdots & \cdots \\ \frac{\nu}{\lambda} \sigma_{3k1} & \cdots & \frac{\nu}{\lambda} \sigma_{3k(i-1)} & \bar{\sigma}_{4k} & \frac{\nu}{\lambda} \sigma_{3k(i+1)} & \cdots & 1 - \frac{\nu}{\lambda} \sigma_{3kk} \end{pmatrix},$$

$$\bar{\sigma}_{4i} = \int_0^T |b_i(s)| \int_0^T |\bar{H}(s, \theta, \lambda)| d\theta ds.$$

According to the theorem,  $\rho < 1$ . Estimates (27), (28) and (29) imply that the operator on the right side of (26) is contractive. This implies the existence of a single fixed point. Consequently, the functional-integral equation (26) has the unique solution on the set  $\Omega_4$  of values of parameters  $\nu, \lambda$  for all  $t \in [0; T]$ . The theorem is proved.

Now, the function  $u(t, \nu, \lambda) \in C^2[0; T]$  is already known. In order to determine the unknown quantities  $\varphi_1$  and  $\varphi_2$ , we will substitute the solution  $u(t, \nu, \lambda) \in C^2[0; T]$  of equation (26) into representations (25). Then, the quantities  $\varphi_1$  and  $\varphi_2$ , are uniquely determined.

#### 4. Conclusion

We have considered questions of the unique solvability of the inverse problem for the second-order Fredholm integro-differential equation (1) with a degenerate kernel, final conditions (2) at the end of the interval, two parameters, and two redefinition data. Sets of regular parameter values are defined. The features that arise when solving the inverse problem (1)–(3) are studied. Criteria for the unique solvability of the posed inverse problem are established.

**Remark 1.** For values of parameters  $(\nu, \lambda)$  from the set  $\Omega_3$ , the uniqueness of the set of solutions to the inverse problem (1)–(3) is violated. Because in this case condition (23) is not satisfied.

**Remark 2.** For values of parameters  $(\nu, \lambda)$  from the set  $\Omega_1$ , the inverse problem (1)–(3) does not make sense. Because in this case condition (15) is not satisfied. But, the direct problem (1), (2) has an infinite set of solutions, if  $\varphi_1 = \varphi_2 = 0$  and  $\alpha(t) \equiv 0$  for all  $t \in [0; T]$ .

#### References

- [1] Cavalcanti M. M., Domingos Cavalcanti V. N., Ferreira J. Existence and uniform decay for a nonlinear viscoelastic equation with strong damping. *Math. Methods in the Appl. Sciences*, 2001, **24**, P. 1043–1053.
- [2] Bykov Ya. V. *On some problems in the theory of integro-differential equations*. Izdatelstvo Kirg. Gos. Univ-ta, Frunze, 1957, 327 p. (in Russian).
- [3] Dzhumabaev D. S., Bakirova E. A. Criteria for the well-posedness of a linear two-point boundary value problem for systems of integro-differential equations. *Differential Equations*, 2010, **46**(4), P. 553–567.
- [4] Dzhumabaev D. S., Mynbayeva S. T. New general solution to a nonlinear Fredholm integro-differential equation. *Eurasian Math. Journal*, 2019, **10**(4), P. 24–33.
- [5] Gianni R. Equation with nonlocal boundary condition. *Mathematical Models and Methods in Applied Sciences*, 1993, **3**(6), P. 789–804.
- [6] Giacomini G., Lebowitz J. L. Phase segregation dynamics in particle systems with long range interactions. *I. Macroscopic limits. J. of Statist. Phys.*, 1997, **87**, P. 37–61.
- [7] Falaleev M. V. Integro-differential equations with a Fredholm operator at the highest derivative in Banach spaces and their applications. *Izv. Irkutsk. Gos. Universiteta. Matematika*, 2012, **5**(2), P. 90–102 (in Russian).
- [8] Fedorov E. G., Popov I. Yu. Analysis of the limiting behavior of a biological neurons system with delay. *J. Phys.: Conf. Ser.*, 2021, **2086**, P. 012109.
- [9] Fedorov E. G., Popov I. Yu. Hopf bifurcations in a network of FitzHugh-Nagumo biological neurons. *International Journal of Nonlinear Sciences and Numerical Simulation*, 2021.
- [10] Fedorov E. G. Properties of an oriented ring of neurons with the FitzHugh-Nagumo model. *Nanosystems: Phys. Chem. Math.*, 2021, **12**(5), P. 553–562.
- [11] Sidorov N. A. Solution of the Cauchy problem for a class of integro-differential equations with analytic nonlinearities. *Differ. Uravneniya*, 1968, **4**(7), P. 1309–1316 (in Russian).
- [12] Ushakov E. I. *Static stability of electrical circuits*. Nauka, Novosibirsk, 1988. 273 p. (in Russian)
- [13] Vainberg M. M. Integro-differential equations. *Itogi Nauki*, 1962, VINITI, Moscow, 1964, P. 5–37 (in Russian).
- [14] Yuldashev T. K., Odinaev R. N., Zarifzoda S. K. On exact solutions of a class of singular partial integro-differential equations. *Lobachevskii Journal of Mathematics*, 2021, **42**(3), P. 676–684.
- [15] Yuldashev T. K., Zarifzoda S. K. On a new class of singular integro-differential equations. *Bulletin of the Karaganda University. Mathematics series*, 2021, **101**(1), P. 138–148.
- [16] Abildayeva A. T., Kaparova R. M., Assanova A. T. To a unique solvability of a problem with integral condition for integro-differential equation. *Lobachevskii Journal of Mathematics*, 2021, **42**(12), P. 2697–2706.
- [17] Assanova A. T., Dzhumabaev D. S. Correct solvability of a nonlocal boundary value problem for systems of hyperbolic equations. *Doklady Mathematics*, 2003, **68**(1), P. 46–49.
- [18] Assanova A. T., On the solvability of nonlocal problem for the system of Sobolev-type differential equations with integral condition. *Georgian Mathematical Journal*, 2021, **28**(1), P. 49–57.
- [19] Assanova A. T., Dzhumabaev D. S. Well-posedness of nonlocal boundary value problems with integral condition for the system of hyperbolic equations. *Journal of Mathematical Analysis and Applications*, 2013, **402**(1), P. 167–178.
- [20] Assanova A. T., Imanchiyev A. E., Kadirbayeva Zh. M. A nonlocal problem for loaded partial differential equations of fourth order. *Bulletin of the Karaganda university-Mathematics*, 2020, **97**(1), P. 6–16.

- [21] Assanova A. T., Tokmurzin Z. S. A nonlocal multipoint problem for a system of fourth-order partial differential equations. *Eurasian Math. Journal*, 2020, **11**(3), P. 8–20.
- [22] Gordeziani D. G., Avalishvili G. A. Gordeziani solutions of nonlocal problems for one-dimensional vibrations of a medium. *Matematicheskoye Modelirovaniye*, 2000, **12**(1), P. 94–103 (in Russian).
- [23] Dzhumabaev D. S. Well-posedness of nonlocal boundary value problem for a system of loaded hyperbolic equations and an algorithm for finding its solution. *Journal of Mathematical Analysis and Applications*, 2018, **461**(1), P. 1439–1462.
- [24] Ivanchov N. I. Boundary value problems for a parabolic equation with integral conditions. *Differential Equations*, 2004, **40**(4), P. 591–609.
- [25] Pao C. V. Numerical solutions of reaction-diffusion equations with nonlocal boundary conditions. *J. of Computational and Applied Mathematics*, 2001, **136**(1-2), P. 227–243.
- [26] Ochilova N. K., Yuldashev T. K. On a nonlocal boundary value problem for a degenerate parabolic-hyperbolic equation with fractional derivative. *Lobachevskii Journal of Mathematics*, 2022, **43**(1), P. 229–236.
- [27] Tikhonov I. V. Theorems on uniqueness in linear nonlocal problems for abstract differential equations. *Izvestiya: Mathematics*, 2003, **67**(2), P. 333–363.
- [28] Yurko V. A. Inverse problems for first-order integro-differential operators. *Math Notes*, 2016, **100**(6), P. 876–882.
- [29] Yuldashev T. K. Determination of the coefficient and boundary regime in boundary value problem for integro-differential equation with degenerate kernel. *Lobachevskii Journal of Mathematics*, 2017, **38**(3), P. 547–553.
- [30] Yuldashev T. K., Kadirkulov B. J. Inverse boundary value problem for a fractional differential equations of mixed type with integral redefinition conditions. *Lobachevskii Journal of Mathematics*, 2021, **42**(3), P. 649–662.
- [31] Yuldashev T. K., Saburov Kh. Kh., Abduvahobov T. A. Nonlocal problem for a nonlinear system of fractional order impulsive integro-differential equations with maxima. *Chelyabinskii Phys.-Mathem. Journal*, 2022, **7**(1), P. 113–122.
- [32] Yuldashev T. K., Rakhmonov F. D. Nonlocal problem for a nonlinear fractional mixed type integro-differential equation with spectral parameters. *AIP Conference Proceedings*, 2021, **2365**(060003), P. 1–20.
- [33] Zaripov S. K. Construction of an analog of the Fredholm theorem for a class of model first order integro-differential equations with a singular point in the kernel. *Vestnik Tomsk. gos. universiteta. Matematika i mekhanika*, **46**, 2017, P. 24–35.
- [34] Zaripov S. K. A construction of analog of Fredholm theorems for one class of first order model integro-differential equation with logarithmic singularity in the kernel. *Vestnik Samar. gos. tekhn. univ. Fiz.-mat. nauki*, **21**(2), 2017, P. 236–248.
- [35] Zaripov S. K. On a new method of solving of one class of model first-order integro-differential equations with singularity in the kernel. *Matematicheskaya fizika i kompyuternoe modelirovanie*, 2017, **20**(4), P. 68–75.
- [36] Yuldashev T. K. On Fredholm partial integro-differential equation of the third order. *Russian Mathematics*, 2015, **59**(9), P. 62–66.
- [37] Yuldashev T. K. On a boundary-value problem for a fourth-order partial integro-differential equation with degenerate kernel. *Journal of Mathematical Sciences*, 2020, **245**(4), P. 508–523.
- [38] Yuldashev T. K. Determining of coefficients and the classical solvability of a nonlocal boundary-value problem for the Benney–Luke integro-differential equation with degenerate kernel. *Journal of Mathematical Sciences*, **254**(6), 2021, P. 793–807.
- [39] Yuldashev T. K. Inverse boundary-value problem for an integro-differential Boussinesq-type equation with degenerate kernel. *Journal of Mathematical Sciences*, 2020, **250**(5), P. 847–858.
- [40] Yuldashev T. K., Apakov Yu. P., Zhuraev A. Kh. Boundary value problem for third order partial integro-differential equation with a degenerate kernel. *Lobachevskii Journal of Mathematics*, 2021, **42**(6), P. 1317–1327.

---

*Submitted 27 August 2022; revised 17 September 2022; accepted 18 September 2022*

*Information about the authors:*

*Tursun K. Yuldashev* – Tashkent State University of Economics, Karimov street, 49, TSUE, Tashkent, 100066, Uzbekistan; tursun.k.yuldashev@gmail.com

*Sarvar K. Zarifzoda* – Tajik National University, st. Khovaron, apt. 381, Shohmansur district, Dushanbe, Tajikistan; sarvar8383@list.ru

*Conflict of interest:* the authors declare no conflict of interest.

## On existence conditions for periodic solutions to a differential equation with constant argument

Mukhiddin I. Muminov<sup>1,2,a</sup>, Tirkash A. Radjabov<sup>1,b</sup>

<sup>1</sup>Samarkand State University, Samarkand, Uzbekistan

<sup>2</sup>V. I. Romanovskiy Institute of Mathematics, Uzbekistan Academy of sciences, 100174, Tashkent, Uzbekistan

<sup>a</sup>mmuminov@mail.ru, <sup>b</sup>radjabovtirkash@yandex.com

Corresponding author: M. I. Muminov, mmuminov@mail.ru

**ABSTRACT** We deal with a linear differential equation with piecewise constant argument. The considered equation with the initial condition has the unique solution. We obtain the sufficient conditions for existence of  $n$ -periodic solution for the considered problem and describe the positivity conditions for the solution.

**KEYWORDS** partial differential equation, piecewise constant arguments, periodic solution, asymptotically stable

**ACKNOWLEDGEMENTS** Authors were partially supported by [grant number FZ-20200929224] of Fundamental Science Foundation of Uzbekistan. Authors thank the referee for valuable comments and gratefully acknowledge.

**FOR CITATION** Muminov M.I., Radjabov T.A. On existence conditions for periodic solutions to a differential equation with constant argument. *Nanosystems: Phys. Chem. Math.*, 2022, **13** (5), 491–497.

### 1. Introduction

Differential equations with piecewise constant arguments (briefly DEPCA) occur when trying to extend the theory of functional differential equations with continuous arguments to differential equations with discontinuous arguments. In [1] Cooke and Wiener studied a new differential equation alternately of retarded and advanced type. They have shown that all equations with piecewise constant delays have characteristics similar to the equations studied in [2]. These equations are closely related to impulse and loaded equations and, especially, to difference equations of a discrete argument. The equations are similar in structure to those found in certain “sequential-continuous” models of disease dynamics [5]. Differential equations with piecewise constant arguments are usually referred to as a hybrid system. It can model certain harmonic oscillators with almost periodic forcing [3], [4]. For a survey of work on ordinary and partial differential equations with piecewise constant arguments (DEPCA) we refer the reader to [6], [7]. Functional differential equations with deviated argument provide a mathematical model for systems where the changes of state depend upon its past history or its future. DEPCA also arises in the process of replacing some terms of differential equation by their piecewise constant approximations. This point of view has applications in impulsive or loaded differential equations of control theory, and stabilization of systems with discrete (sample) control [7], [8]. Recently published papers [13] and [14] studied DEPCA special form. Authors reduced  $n$ -periodic solvable problem to the study of a system of  $n$  linear equations. Furthermore, by applying the well-known properties of linear system in algebra, all existence conditions are described for  $n$ -periodic solutions that yields explicit formula for the solutions of the equations.

Paper [17] dealt with a non-autonomous piecewise linear difference equation

$$x'(t) = -g(x([t])),$$

where  $g$  is a linear signal function that describes a discrete version of a single neuron model. The authors investigated the periodic behavior of solutions relative to the periodic sequence with the period of three internal decay rate. More precisely, they showed that only periodic cycles with period  $3k$ ,  $k = 1, 2, 3, \dots$  can exist. Further, the considered model is investigated in [18]. The authors proved that the model contains a large quantity of initial conditions that generate eventually periodic solutions.

In inertial neural networks, inertial terms are described by the first-order derivative terms which have important meaning in engineering technology, biology, physics and information systems. For more details, see, e.g., [19–21]. The problems of periodic solutions for neutral-type inertial neural networks with single and multiple variables delays are investigated in [22–24].

In this paper, we consider a linear differential equations with piecewise constant argument of the form

$$T'(t) + a(t)T(t) + b(t)T([t]) = 0, \quad t > 0, \quad (1)$$

with

$$T(0) = T_0, \quad (2)$$

where nonzero functions  $a(t), b(t)$  are  $n$ -periodic and continuous on  $\mathbb{R}_+ = [0, \infty)$ , where  $n$  is a positive integer number. Note that the general case of the problem (1, 2) was studied in [15], where authors obtain the existence conditions for solutions and proved Gronwall type integral inequality as an application. In this note, we obtain the existence conditions for periodic solution to this initial value problem. We obtain the explicit formula and the positivity conditions for the solutions. As an application of the obtained result, we derive a condition for non-asymptotically stable solution of a certain class of partial differential equations with piecewise constant argument, which claims the correctness of the conditions of asymptotic stability conditions for the solution given in [7].

**2. On a solution of equation**

Let us define a definition of solution for (1, 2).

**Definition 2.1.** A function  $T(t)$  is called a solution of (1, 2) if the following conditions are satisfied:

- (i)  $T(t)$  is continuous on  $\mathbb{R}_+$ ;
- (ii)  $T'(t)$  exists and is continuous in  $\mathbb{R}_+$ , with possible exception at points  $[t] \in \mathbb{R}_+$ , where one-sided derivatives exist;
- (iii)  $T(t)$  satisfies Eq. (1, 2) in  $\mathbb{R}_+$ , with the possible exception at the points  $[t] \in \mathbb{R}_+$ .

**Example 2.1.** Let  $a(t) = 1$  and  $b(t) = \beta \sin 2\pi t$ , where  $\beta$  is a real number satisfying the equation

$$\left(1 - \frac{\beta}{1 + 4\pi^2}(1 - e)\right) - e = 0.$$

For this case the function  $T(t)$  on  $\mathbb{R}_+$  defined as

$$T(t) = T_0 e^{-t} \left(1 - \frac{\beta}{1 + 4\pi^2} (1 + e^t (\sin 2\pi t - \cos 2\pi t))\right), \quad t \in [0, 1).$$

is one periodic solution of (1, 2).

Denote

$$M(i, t) = e^{-\int_i^t a(m)dm} \left(1 - \int_i^t b(s)e^{\int_i^s a(r)dr} ds\right), \quad t > i, \quad i = 0, 1, 2, \dots$$

**Theorem 2.1.** The solution of (1, 2) is well defined for all  $t \geq 0$  and is given by

$$T(t) = T_0 \prod_{i=0}^{n-1} (M(i, i+1)) M(n, t) \quad \text{for } t \in [n, n+1), \quad n = 0, 1, 2, \dots \tag{3}$$

*Proof.* The solution of (1, 2) in  $t \in [0, 1)$  is

$$T(t) = T_0 e^{-\int_0^t a(s)ds} \left(1 - \int_0^t b(s)e^{\int_0^s a(r)dr} ds\right) = T_0 M(0, t) \quad \text{for } t \in [0, 1).$$

Then

$$T(1) = \lim_{t \rightarrow 1-0} T(t) = T_0 M(0, 1).$$

The solution of (1, 2) in  $t \in [1, 2)$  has the form

$$T(t) = T(1) e^{-\int_1^t a(s)ds} \left(1 - \int_1^t b(s)e^{\int_1^s a(r)dr} ds\right)$$

or

$$T(t) = T_0 M(0, 1) M(1, t) \quad \text{for } t \in [1, 2).$$

Let the function

$$T(t) = T_0 \prod_{i=0}^{k-2} (M(i, i+1)) M(k-1, t) \quad \text{for } t \in [k-1, k), \quad k = 3, 4, \dots$$

be a solution of (1, 2) in  $[k-1, k)$ , then the function

$$T(t) = T_0 \prod_{i=0}^{k-1} (M(i, i+1)) M(k, t) \quad \text{for } t \in [k, k+1), \quad k = 3, 4, \dots \tag{4}$$

is a solution of (1, 2) in  $t \in [k, k+1)$ . □

### 3. On periodic solutions

**Theorem 3.1.** Let  $a(t)$  and  $b(t)$  be  $n$ -periodic continuous functions. Then the solution for (1, 2) is  $n$ -periodic iff

$$\prod_{i=0}^{n-1} M(i, i + 1) = 1.$$

*Proof.* Let  $T(t)$  be a  $n$ -periodic solution for (1, 2). Then  $T(n) = T_0$ . As  $t = n$ , by (3), one obtains  $1 = \prod_{i=0}^{n-1} (M(i, i + 1))$ .

Conversely, let  $\prod_{i=0}^{n-1} M(i, i + 1) = 1$ . We show that  $T(n + t) = T(t)$  for all  $t \in \mathbb{R}_+$ . Let  $t + n \in [n + k, n + k + 1)$ , where  $k$  is an integer number. Then

$$T(t + n) = T_0 \prod_{i=0}^{n+k-1} M(i, i + 1) M(n + k, t + n) \quad \text{for } t + n \in [n + k, n + k + 1).$$

Changing the variables  $r' = \rho + n, s = s' + n$  in the integral

$$M(n + k, t + n) = e^{-\int_{n+k}^{t+n} a(r') dr'} \left( 1 - \int_{n+k}^{t+n} b(s) e^{\int_{n+k}^s a(r) dr} ds \right)$$

we obtain

$$M(n + k, t + n) = e^{-\int_k^t a(\rho) d\rho} \left( 1 - \int_k^t b(s') e^{\int_{n+k}^{s'+n} a(r) dr} ds' \right).$$

Then, changing variable  $r = r' + n$  gives one

$$M(n + k, t + n) = e^{-\int_k^t a(\rho) d\rho} \left( 1 - \int_k^t b(s') e^{\int_k^{s'} a(r') dr'} ds' \right),$$

i.e.  $M(n + k, t + n) = M(k, t)$  for all  $t + n \in [n + k, n + k + 1)$ . Using this equation, we provide the following calculations

$$\begin{aligned} \prod_{i=0}^{n+k-1} M(i, i + 1) &= \prod_{i=0}^{n-1} M(i, i + 1) \prod_{i=n}^{n+k-1} M(i, i + 1) = \prod_{i=n}^{n+k-1} M(i, i + 1) \\ &= \prod_{j=0}^{k-1} M(j + n, j + n + 1) = \prod_{j=0}^{k-1} M(j, j + 1). \end{aligned}$$

Therefore

$$\begin{aligned} T(t + n) &= T_0 \prod_{i=0}^{n+k-1} M(i, i + 1) M(n + k, t + n) \\ &= T_0 \prod_{i=0}^{k-1} M(i, i + 1) M(k, t) = T(t) \quad \text{for } t \in [k, k + 1). \end{aligned}$$

□

**Example 3.1.** Let  $a(t) = \pi^2$  and  $b(t) = \beta \sin 2\pi t$ . For this case, the function  $M(i, t)$  is represented as

$$M(i, t) = e^{-\pi^2(t-i)} - \frac{\beta e^i}{\pi^2(1 + 4\pi^2)} \left( e^{-\pi^2(t-i)} + \sin 2\pi t - \cos 2\pi t \right) \quad \text{for } t > i.$$

(a) Let  $\beta$  be a root of

$$M(0, 1)M(1, 2) = 1.$$

Then, the solution for (1, 2) is unique 2-periodic solution defined as

$$T(t) = \begin{cases} T_0 M(0, t), & t \in [0, 1), \\ T_0 M(0, 1)M(1, t), & t \in [1, 2). \end{cases}$$

(b) Let  $\beta$  be a root of

$$M(0, 1)M(1, 2)M(2, 3) = 1.$$

Then, the solution for (1, 2) is unique 3-periodic solution defined as

$$T(t) = \begin{cases} T_0 M(0, t), & t \in [0, 1), \\ T_0 M(0, 1)M(1, t), & t \in [1, 2), \\ T_0 M(0, 1)M(1, 2)M(2, t), & t \in [2, 3). \end{cases}$$

**Theorem 3.2.** Let  $a(t)$  and  $b(t)$  be  $n$ -periodic continuous functions and

$$\prod_{i=0}^{n-1} M(i, i + 1) = 1.$$

Then, the problem (1, 2) has positive solution if any one of the following hypotheses holds true:

- (i)  $b(t) \leq 0$ ; or
- (ii)  $b(t) \geq 0$  and

$$\max_{0 \leq t \leq n} b(t)e^{\int_i^t a(r)dr} < 1.$$

*Proof.* Let  $T(t)$  be a solution of the problem. Then, by Theorem 3.1,  $T(t)$  is  $n$ -periodic and by Theorem 2.1, it has the form

$$T(t) = T_0 \prod_{i=0}^{k-1} M(i, i + 1) M(k, t) \quad \text{for } t \in [k, k + 1), k = 0, 1, \dots, n - 1.$$

(i) If  $b(t) \geq 0$  then  $1 - \int_i^t b(s)e^{\int_i^s a(r)dr} ds > 0, \quad t > i, i = 0, 1, \dots, n - 1.$  Hence,  $T(t) > 0, t \in [0, n].$

(ii) If  $b(t) \geq 0$  and

$$\max_{0 \leq t \leq n} b(t)e^{\int_i^t a(r)dr} < 1.$$

Then,

$$\int_i^t b(s)e^{\int_i^s a(r)dr} ds < \max_{0 \leq t \leq n} b(t)e^{\int_i^t a(r)dr}(t - i) < 1 \quad \text{for } t \in [i, i + 1), i = 0, 1, \dots, n - 1.$$

This leads to inequality  $M(i, t) > 0$  for  $t > i, i = 0, 1, \dots, n - 1.$  □

**The case  $a(t)$  and  $b(t)$  are constant**

We analyze periodic solutions of (1), (2) for the case when the functions  $a(t)$  and  $b(t)$  are constant functions, i.e.  $a(t) = a$  and  $b(t) = b.$  In this case the solution (3) has the form

$$T(t) = T_0 \left( e^{-a} - \frac{b}{a}(1 - e^{-a}) \right)^n \left( e^{-a(t-n)} - \frac{b}{a}(1 - e^{-a(t-n)}) \right), \quad t \in [n, n + 1). \tag{5}$$

Note that for this case if  $b = -a$  then the Cauchy problem (1), (2) has only constant solution  $T(t) = T_0.$

**Theorem 3.3.** Let  $b = \frac{(e^a + 1)a}{e^a - 1}.$  Then, the Cauchy problem (1), (2) has unique 2-periodic solution

$$T(t) = \begin{cases} T_0 \left( e^{-at} - \frac{b}{a}(1 - e^{-at}) \right), & t \in [0, 1), \\ -T_0 \left( e^{-a(t-1)} - \frac{b}{a}(1 - e^{-a(t-1)}) \right), & t \in [1, 2). \end{cases}$$

*Proof.* Let  $T(t)$  be a solution of (1), (2) defined as (5). We show that  $T(t) = T(t + 2)$  for  $t \in [0, \infty).$  Note that  $e^{-a} - \frac{b}{a}(1 - e^{-a}) = -1$  for  $b = \frac{(e^a + 1)a}{e^a - 1}.$  Hence, by (5), one has

$$T(t) = T_0 (-1)^n \left( e^{-a(t-n)} - \frac{b}{a}(1 - e^{-a(t-n)}) \right), \quad t \in [n, n + 1).$$

Hence,

$$T(t + 2) = T_0 (-1)^{n+2} \left( e^{-a(t-n)} - \frac{b}{a}(1 - e^{-a(t-n)}) \right), \quad t + 2 \in [n + 2, n + 3),$$

i.e.  $T(t) = T(t + 2).$  □

Remark that equation (1, 2) has no non-integer  $w$ -periodic solution. However, if the solution  $T(t)$  of this equation is periodic then  $T(t)$  is constant function or 2-periodic function.

#### 4. Application

In this section, we consider the partial differential equation (PDE) with piecewise constant arguments

$$u_t(x, t) = a^2(t)u_{xx}(x, t) - b(t)u(x, [t]), \tag{6}$$

$$u(0, t) = u(1, t) = 0, \tag{7}$$

$$u(x, 0) = v(x), \tag{8}$$

where  $v$  is a continuous function on  $[0, 1]$ ,  $a(t)$  and  $b(t)$  are  $n$ -periodic functions on  $[0, \infty)$ .

It has been shown in [12] that PDEs (6-8) with piecewise constant time naturally arise in the process of approximating PDEs using piecewise constant arguments. It is important to investigate boundary value problems (BVP) and initial-value problems for EPCA in partial derivatives and explore the influence of certain discontinuous delays on the behavior of solutions to some typical problems of mathematical physics. For example, the measuring of the lateral heat change at discrete moments of time leads to the equation with piecewise continuous delay [11].

**Definition 4.1.** A function  $u(x, t)$  is called a solution of (6-8) if the following conditions are satisfied:

- (i)  $u(x, t)$  is continuous on  $\Omega = [0, 1] \times \mathbb{R}_+, \mathbb{R}_+ = [0, \infty)$ ;
- (ii)  $u_t$  and  $u_{xx}$  exist and are continuous in  $\Omega$ , with possible exception at points  $(x, [t]) \in \Omega$ , where one-sided derivatives exist with respect to second argument;
- (iii)  $u(x, t)$  satisfies Eq. (6) in  $\Omega$ , with the possible exception at the points  $(x, [t]) \in \Omega$  and conditions (7) and (8).

**Definition 4.2.** (see [7]). If any solution  $u(x, t)$  of (6) satisfies

$$\lim_{t \rightarrow \infty} u(x, t) = 0, \quad x \in [0, 1],$$

then the zero solution of (6) is called asymptotically stable.

By using separation of variables, the formal solution  $u(x, t)$  in (6-8) can be represented as (see [9])

$$u(x, t) = \sum_{j=1}^{\infty} T_j(t) \sin(j\pi x), \tag{9}$$

where  $T_j(t)$  is the solution of the initial equation

$$\begin{aligned} T_j'(t) &= -a^2(t)\pi^2 j^2 T_j(t) - b(t)T_j([t]), \\ T_j(0) &= v_j. \end{aligned} \tag{10}$$

Here

$$\begin{aligned} v_j &= 2 \int_0^1 v(x) \sin(j\pi x) dx, \\ v(x) = u(x, 0) &= \sum_{j=1}^{\infty} v_j \sin(j\pi x). \end{aligned}$$

Note that by Theorem 3.1, if  $\prod_{i=0}^{n-1} M_j(i, i + 1) = 1$  for some  $j \in \mathbb{N}$ , where

$$M_j(i, t) = e^{-j^2 \pi^2 \int_i^t a^2(m) dm} \left( 1 - \int_i^t b(s) e^{j^2 \pi^2 \int_i^s a^2(r) dr} ds \right),$$

(10) has  $n$ -periodic solution

$$T_j(t) = T_j(0) \prod_{i=0}^{n-1} (M_j(i, i + 1)) M_j(n, t), \quad t \in [n, n + 1).$$

Since  $T_j(t)$  is a periodic function, we can conclude the following theorem.

**Theorem 4.1.** Let  $a(t)$  and  $b(t)$  be  $n$ -periodic continuous functions. Assume that there exists  $j \in \mathbb{N}$  such that

$$\prod_{i=0}^{n-1} M_j(i, i + 1) = 1.$$

Then, the zero solution of (6) is not asymptotically stable.

**Example 4.1.** Let  $a(t) = \sin 2\pi t$  and  $b(t) = \beta \cos 2\pi t$ . Consider the problem

$$\begin{aligned} u_t(x, t) &= a^2(t)u_{xx}(x, t) - b(t)u(x, [t]), \\ u(0, t) &= u(1, t) = 0, \\ u(x, 0) &= \sin(\pi x). \end{aligned}$$

The solution of this problem is as follows

$$u(x, t) = T_1(t) \sin \pi x,$$

where  $T_1(t)$  is a solution of

$$\begin{aligned} T_1'(t) &= -a^2(t)\pi^2 T_1(t) - b(t)T_1([t]), \\ T_1(0) &= 1. \end{aligned}$$

By Theorem 2.1, one has

$$T_1(t) = \prod_{i=0}^{n-1} (M_1(i, i + 1)) M_1(n, t), \quad t \in [n, n + 1),$$

where

$$M_1(i, t) = e^{-\pi^2(\frac{t-i}{2} - \frac{1}{8\pi}(\sin 4\pi t - \sin 4\pi i))} \left( 1 - \beta \int_i^t \cos 2\pi s e^{\pi^2(\frac{s-i}{2} - \frac{1}{8\pi}(\sin 4\pi s - \sin 4\pi i))} ds \right), \quad t > i.$$

Let  $\beta$  be a root of

$$M_1(0, 1)M_1(1, 2)M_1(2, 3) = 1.$$

Then, the function  $T_1(t)$  is a 3-periodic function defined as

$$T_1(t) = \begin{cases} M(0, t), & t \in [0, 1), \\ M(0, 1)M(1, t), & t \in [1, 2), \\ M(0, 1)M(1, 2)M(2, t), & t \in [2, 3). \end{cases}$$

Moreover, the solution  $u(x, t)$  is not asymptotically stable, i. e.

$$\lim_{t \rightarrow \infty} u(x, t) \neq 0, x \in [0, 1].$$

**Example 4.2.** Let  $a(t) = 1$  and  $b(t) = \beta \sin 2\pi t$ . Consider the problem

$$\begin{aligned} u_t(x, t) &= a^2(t)u_{xx}(x, t) - b(t)u(x, [t]), \\ u(0, t) &= u(1, t) = 0, \\ u(x, 0) &= \sum_{j=1}^5 \frac{1}{j} \sin(j\pi x). \end{aligned}$$

The solution of this problem is as follows

$$u(x, t) = \sum_{j=1}^5 T_j(t) \sin j\pi x,$$

where  $T_j(t)$  is a solution of

$$\begin{aligned} T_j'(t) &= -a^2(t)\pi^2 j^2 T_j(t) - b(t)T_j([t]), \\ T_j(0) &= \frac{1}{j} \end{aligned} \tag{11}$$

defined as

$$\begin{aligned} T_j(t) &= \frac{1}{j} \prod_{i=0}^{n-1} (M_j(i, i + 1)) M_j(n, t), \quad t \in [n, n + 1), \\ M_j(i, t) &= e^{-\pi^2 j^2 (t-i)} \left( 1 - \frac{\beta e^i}{\pi^2 j^2 (1 + 4\pi^2)} \left( 1 + e^{\pi^2 j^2 (t-i)} (\sin 2\pi t - \cos 2\pi t) \right) \right), \quad t > i. \end{aligned}$$

Let  $\beta$  be a root of

$$M_1(0, 1)M_1(1, 2) = 1.$$

Then,  $T_1(t)$  is a 2-periodic function defined as (See the Example 3.1 (a))

$$T_1(t) = \begin{cases} M_1(0, t), & t \in [0, 1), \\ M_1(0, 1)M_1(1, t), & t \in [1, 2). \end{cases}$$

## 5. Conclusion

In this note, we studied periodic solutions to the initial value problem (1, 2), where nonzero functions  $a(t)$ ,  $b(t)$  are assumed to be  $n$ -periodic and continuous on  $\mathbb{R}_+ = [0, \infty)$ .

The condition for possibility of the periodic solutions of the problem and explicit formula for the solutions are obtained. The positivity conditions for the periodic solutions is described, which claims non-oscillatory character for the solution (See [16]). Remark that the obtained results are true for the case when  $a(t)$ ,  $b(t)$  are one periodic functions, or satisfied the conditions  $a(t) = a(t + n)$ ,  $b(t) = b(t + n)$ . As an example, the example is constructed when  $a(t)$ ,  $b(t)$  are one-periodic, the equation have 2-periodic or 3-periodic solutions .

As an application of the obtained result, it is given a non-asymptotically stable condition for solution a certain class of partial differential equations with a piecewise constant argument, which claims the correctness of the conditions of asymptotically stable conditions for the solution given in [7].

## References

- [1] Cooke K.L., Wiener J. An equation alternately of retarded and advanced type. *Proc. Amer. Math. Soc.*, 1987, **99**, P. 726–732.
- [2] Cooke K.L., Wiener J. Retarded differential equations with piecewise constant delays. *J. Math. Anal. Appl.*, 1984, **99**, P. 265–297.
- [3] Hale J.K., Lunel V. *Introduction to Functional Differential Equations*. Springer, New York, 1993.
- [4] Hino Y., Naito T., Minh N., Shin V. *Almost Periodic Solutions of Differential Equations in Banach Spaces. Stability and Control: Theory, Method and Applications*, **15**, Taylor & Francis, London, 2002.
- [5] Busenberg S., Cooke K.L. Models of vertically transmitted diseases with sequentialcontinuous dynamics. *Nonlinear Phenomena in Mathematical Sciences*, V. Lakshmikantham, ed., Academic Press, New York, 1982, P. 179–187.
- [6] Cooke K.L., Wiener J. A survey of differential equations with piecewise continuous arguments. *Delay Differential Equations and Dynamical Systems*, 1991, **1475**, P. 1–15.
- [7] Wiener J. *Generalized Solutions of Functional Differential Equations*, World Scientific, Singapore, 1993.
- [8] Pinto M., Robledo G. Controllability and observability for a linear time varying system with piecewise constant delay. *Acta Appl. Math.*, 2014, P. 1–24.
- [9] Veloz T., Pinto M. Existence, computability and stability for solutions of the diffusion equation with general piecewise constant argument. *J. Math. Anal. Appl.*, 2015, **426** (1), P. 330–339.
- [10] Wiener J., Heller W. Oscillatory and periodic solutions to a diffusion equation of neutral type. *Int. J. Math. Math. Sci.*, 1999, **22** (2), P. 313–348.
- [11] Wiener J., Debnath L. Boundary value problems for the diffusion equation with piecewise continuous time delay. *Int. J. Math. and Math. Sci.*, 1997, **20** (1), P. 187–195.
- [12] Wiener J. Boundary-value problems for partial differential equations with piecewise constant delay. *Int. J. Math. and Math. Sci.*, 1991, **14**, P. 301–321.
- [13] Muminov M.I. On the method of finding periodic solutions of second-order neutral differential equations with piecewise constant arguments. *Advances in Difference Equations*, 2017, **2017**, 336.
- [14] Muminov M.I., Ali H.M. Existence conditions for periodic solutions of second-order neutral delay differential equations with piecewise constant arguments. *Open Mathematics*, 2020, **18** (1), P. 93–105.
- [15] Chiu K.S., Pinto M. Periodic solutions of differential equations with a general piecewise constant argument and applications. *E.J. Qualitative Theory of Diff. Equ.*, 2010, **46**, P. 1–19.
- [16] Aftabizadeh A.R., Wiener J., Jian-Ming Xu. Oscillatory and periodic solutions of delay differential equations with piecewise constant argument. *Proc. Amer. Math. Soc.*, 1987, **99**, P. 673–679.
- [17] Bula I., Radin M.A., Wilkins N. Neuron model with a period three internal decay rate. *Electronic J. of Qualitative Theory of Differential Equations*, 2017, **46**, P. 1–19.
- [18] Inese Bula, Radin M.A. Eventually periodic solutions of single neuron model. *Nonlinear Analysis: Modelling and Control*, 2020, **25** (6), P. 903–918.
- [19] Wheeler D., Schieve W. Stability and chaos in an inertial two-neuron system. *Phys. D: Nonlinear Phenom.*, 1997, **105**, P. 267–284.
- [20] Koch C. Cable theory in neurons with active linearized membrane. *Biol. Cybern.*, 1984, **50**, P. 15–33.
- [21] Babcock K., Westervelt R. Stability and dynamics of simple electronic neural networks with added inertia. *Phys. D: Nonlinear Phenom.*, 1986, **23**, P. 464–469.
- [22] Xu M., Du B. Periodic solution for neutral-type inertial neural networks with time-varying delays. *Adv. Difference Equ.*, 2020, **607**, P. 1–21.
- [23] Liu B., Huang L. Existence and exponential stability of periodic solutions for a class of Cohen–Grossberg neural networks with time-varying delays. *Chaos Solitons Fractals*, 2007, **32**, P. 617–627.
- [24] Du B. Anti-periodic solutions problem for inertial competitive neutral-type neural networks via Wirtinger inequality. *J. Inequal. Appl.*, 2019, **187**.

---

Submitted 28 September 2022

### Information about the authors:

**Mukhiddin I. Muminov** – Samarkand State University, 140104, University boulevard. 15, Samarkand, Uzbekistan;  
V. I. Romanovskiy Institute of Mathematics, Uzbekistan Academy of sciences, 100174, Tashkent, Uzbekistan;  
ORCID 0000-0003-0335-6558; mmuminov@mail.ru

**Tirkash A. Radjabov** – Samarkand State University, 140104, University boulevard. 15, Samarkand, Uzbekistan;  
radjabovtirkash@yandex.com

**Conflict of interest:** the authors declare no conflict of interest.

## Phase transitions for the “uncle–nephew” model

Nasir N. Ganikhodjaev<sup>1,a</sup>, Muzaffar M. Rahmatullaev<sup>1,2,b</sup>, Mahliyo R. Abdusalomova<sup>2,c</sup>

<sup>1</sup> Institute of Mathematics, Tashkent, Uzbekistan

<sup>2</sup> Namangan State University, Namangan, Uzbekistan

<sup>a</sup>nasirgani@yandex.com, <sup>b</sup>mrahmatullaev@rambler.ru, <sup>c</sup>mahliyo13abdusalomova@gmail.com

Corresponding author: N. N. Ganikhodjaev, gnasir@iiuum.edu.my

PACS 517, 98

**ABSTRACT** We investigate a problem of phase transition for all possible phases of “uncle–nephew” model on the semi-infinite Cayley tree of second order. It is proved that one can reach the phase transition for this model only in the class of ferromagnetic phase.

**KEYWORDS** Cayley tree, Ising model, phase transition, periodic Gibbs measures, family tree.

**FOR CITATION** Ganikhodjaev N.N., Rahmatullaev M.M., Abdusalomova M.R. Phase transitions for the “uncle–nephew” model. *Nanosystems: Phys. Chem. Math.*, 2022, **13** (5), 498–502.

### 1. Introduction

Lattice models with competing interactions on the Cayley tree have recently been considered extensively because of the appearance of non-trivial magnetic orderings (see [1–7]). The important point is that statistical mechanics on trees involve non-linear recursion equations which are naturally connected to the rich world of dynamical systems [1].

The Ising model with competing “uncle–nephew” interactions was introduced in [8] as a model on the Cayley tree with competing interactions up to the third nearest-neighbours with spins belonging to different branches of the tree when the Cayley tree is considered as family tree. In this paper, it has been proved that phase diagram of this model consists of four phases, namely, expected ferromagnetic, anti-ferromagnetic, and new paramagnetic and para-modulated phases. Later on in [9], the problem of phase transition in the class of ferromagnetic phases has been studied.

In this paper, we will discuss the problem of phase transition for the Ising model with competing “uncle–nephew” interactions in the classes of anti-ferromagnetic, paramagnetic and para-modulated phases.

### 2. Preliminary

Below, we consider a semi-infinite Cayley tree  $\Gamma_+^2 = (V, \Lambda)$  of the second order, i.e. an infinite graph without cycles with three edges issuing from each vertex except for  $x^0$  which has only two edges, where  $V$  is the set of its vertices and  $\Lambda$  is the set of edges.

Two vertices  $x, y \in V$  are called nearest-neighbours if there exists an edge  $l \in \Lambda$  connecting them, which is denoted by  $l = \langle x, y \rangle$ . The distance  $d(x, y)$ ,  $x, y \in V$  on the Cayley tree is the number of edges in the shortest path from  $x$  to  $y$ . For a fixed  $x^0 \in V$  we set

$$W_n = \{x \in V | d(x, x^0) = n\}, \quad V_n = \{x \in V | d(x, x^0) \leq n\},$$

and  $\Lambda_n$  denotes the set of edges in  $V_n$ . The fixed vertex  $x^0$  is called the 0-th level and the vertices in  $W_n$  are called the  $n$ -th level.

Two vertices  $x, y \in V$  are called *third-nearest-neighbors* if  $d(x, y) = 3$ . The third-nearest-neighbor vertices  $x$  and  $y$  are called *prolonged third-nearest-neighbors* and is denoted by  $\langle \tilde{x}, \tilde{y} \rangle$  if  $x \in W_n$  and  $y \in W_{n+3}$  for some  $n$ , i.e. they belong to the same branch of the tree.

The third-nearest-neighbor vertices  $x, y \in V$ , that are not prolonged, are called *two-level third-nearest-neighbours* and are denoted by  $\langle \tilde{x}, \tilde{y} \rangle$ . In this case vertices  $x$  and  $y$  belong to the different branches of the tree.

Considering a semi-infinite Cayley tree  $\Gamma_+^2$  of second order as a *genealogical* or *family* tree, we can reinterpret neighboring relations as a contiguous relations. If  $\langle x, y \rangle$  are nearest neighbors with  $x \in W_n$  and  $y \in W_{n+1}$  for some  $n$ , a vertex  $x$  is called the parent of vertex  $y$ , and  $y$  is called a child of  $x$ . If  $\langle \tilde{x}, \tilde{y} \rangle$  are prolonged third-nearest-neighbors, where  $x \in W_n$  and  $y \in W_{n+3}$  for some  $n$ , then a vertex  $x$  is called the great grandparent of vertex  $y$  and  $y$  is called a great grandchild of  $x$  respectively. If  $\langle \tilde{x}, \tilde{y} \rangle_l$  and  $\langle \tilde{x}, \tilde{y} \rangle_r$  are left and right two-level third-nearest-neighbors, then a vertex  $x$  is called the *uncle* of vertex  $y$  and  $y$  is called a *nephew* of  $x$ , respectively.

*The uncle–nephew Ising model.* A model with the following Hamiltonian

$$H(\sigma) = -J_1 \sum_{\langle x, y \rangle} \sigma(x)\sigma(y) - J_3 \sum_{\langle \tilde{x}, \tilde{y} \rangle} \sigma(x)\sigma(y) \quad (1)$$

is called the uncle–nephew Ising model (see [8]), where the sum in the first term ranges all nearest-neighbours, the second sum ranges all second-level third-nearest-neighbours. Here  $J_1, J_3 \in \mathbb{R}$  are coupling constants.

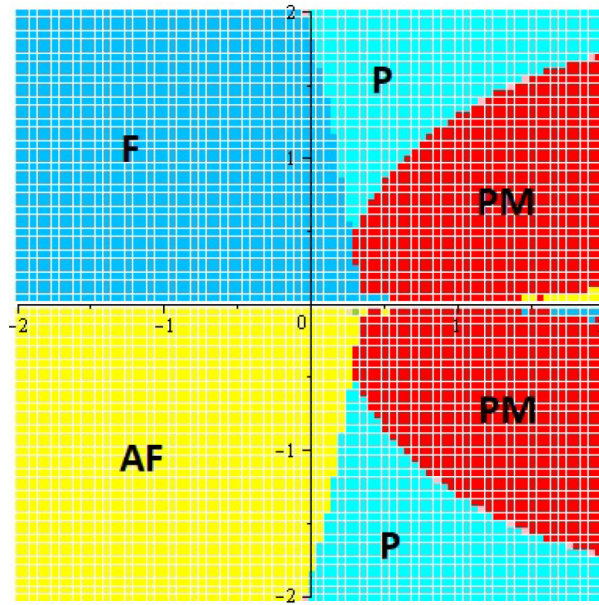


FIG. 1. Phase diagram of the uncle–nephew Ising model

Assume that  $a = \exp(2J_1/(k_B T))$ ,  $b = \exp(2J_3/(k_B T))$ , where  $k_B$  is the Boltzmann constant and  $T$  is the absolute temperature.

In [8], the following recurrent relations have been produced by renormalizing

$$\begin{aligned} x' &= \frac{1}{aD} [(1 + a^{-2}b^2 + 2bx)^2 - (1 - a^{-2}b^2)^2 y^2], \\ y' &= \frac{2}{D} (b^2 - a^{-2})(2bx + b^2 + a^{-2})y, \end{aligned} \tag{2}$$

where  $D = (2bx + b^2 + a^{-2})^2 + (b^2 - a^{-2})^2 y^2$ . This recursion relations provide us a numerically exact phase diagram in  $(\alpha, \gamma)$  space, where  $\alpha = (k_B T)/J_1$  is on  $y$ -axis and  $\gamma = J_3/J_1$  is on  $x$ -axis, with  $a = \exp(2\alpha^{-1})$  and  $b = \exp(2\alpha^{-1}\gamma)$ . To produce the phase diagram, one iterates the recurrence relations (2) starting with random initial conditions and looks after their behaviour after a large number of the iterations. In order to investigate the phase diagram, we have to look at local properties, namely, the local magnetization of the root  $x^0$ . Then, the average magnetization  $m^{(n)}$  for the  $n$ -th generation is given by

$$m^{(n)} = \frac{(a - 1)(a + 1)y^{(n)}}{a^2((1 + 2x^{(n)} + 1)}. \tag{3}$$

The resultant phase diagram on the plane  $(\gamma, \alpha)$  is shown in Fig. 1. The diagram consists of four phases, paramagnetic, ferromagnetic, para-modulated with period  $p = 2$  and anti-ferromagnetic. That is, for the dynamical system described by equation (2), some of the trajectories are converging, and other trajectories have a cycle of second order. It is evident that one can reach ferromagnetic phase if  $J_1 > 0, J_3 > 0$ , anti-ferromagnetic phase if  $J_1 < 0, J_3 < 0$ , and paramagnetic or para-modulated phases if  $J_1 J_3 < 0$ .

In [9], the problem of phase transition in the class of ferromagnetic phases has been solved, namely the following statement was proved.

**Theorem 1.** If  $1 < a^2 b^2 \leq 3$ , then there exists a unique translation-invariant Gibbs measure, and if  $a^2 b^2 > 3$  then there exist three translation-invariant Gibbs measures.

Below we consider the problem of phase transition for this model in the classes of anti-ferromagnetic phases, paramagnetic and para-modulated phases.

### 3. Functional equations

In [8], the following recurrent equation  $t' = f(t)$  has been obtained to investigate the problem of phase transition. Here

$$f(t) = \left( \frac{a^2 b^2 t + 1}{t + a^2 b^2} \right)^2, \tag{4}$$

Where  $a = \exp(2\beta J_1)$ ,  $b = \exp(2\beta J_3)$  and  $\beta = 1/k_B T$  is the inverse temperature. One can find all details in [9].

To investigate the problem of phase transition in the class of ferromagnetic phases, we have to describe the fixed points of the map  $t' = f(t)$  (see [9]). Thus, to investigate the same problem in the class of anti-ferromagnetic phases, one should investigate the recurrent equation  $t'' = f(f(t))$  that is, the following equation

$$t'' = \left( \frac{a^2b^2(a^2b^2t + 1)^2 + (t + a^2b^2)^2}{(a^2b^2t + 1)^2 + a^2b^2(t + a^2b^2)^2} \right)^2. \tag{5}$$

Then, to find the fixed points of (5), we consider the following algebraic equation

$$4a^4b^4t^5 - (a^8b^8 - a^4b^4 - 2a^6b^6 - 2a^2b^2 + 1)t^4 + (2a^6b^6 - 6a^4b^4 + 2a^2b^2)t^3 + (2a^6b^6 - 6a^4b^4 + 2a^2b^2)t^2 + (a^8b^8 - a^4b^4 - 2a^6b^6 - 2a^2b^2 + 1)t - a^4b^4 = 0.$$

After factorization, this equation is reduced to the following form:

$$(t - 1)[t^2 - (a^4b^4 - 2a^2b^2 - 1)t + 1][a^4b^4t^2 + (a^4b^4 + 2a^2b^2 - 1)t + a^4b^4] = 0. \tag{6}$$

One can see that the solutions of equation  $(t - 1)[t^2 - (a^4b^4 - 2a^2b^2 - 1)t + 1] = 0$  are the fixed points of the recursive equation

$$t' = \left( \frac{a^2b^2t + 1}{t + a^2b^2} \right)^2. \tag{7}$$

Since, the fixed points of (7) describe the translation-invariant (that is, ferromagnetic phases). Only solutions of the quadratic equation

$$a^4b^4t^2 + (a^4b^4 + 2a^2b^2 - 1)t + a^4b^4 = 0 \tag{8}$$

describe the anti-ferromagnetic phases.

The discriminant of this equation is equal to  $D = (a^4b^4 + 2a^2b^2 - 1)^2 - 4a^8b^8$ . If  $D > 0$  and  $a^4b^4 + 2a^2b^2 - 1 < 0$  then equation (8) has two positive solutions  $\tilde{t}_1$  and  $\tilde{t}_2$  such that  $\tilde{t}_2' = \tilde{t}_1$  and  $\tilde{t}_1' = \tilde{t}_2$ . The conditions  $D > 0$  and  $a^4b^4 + 2a^2b^2 - 1 < 0$  is equivalent to the  $a^2b^2 < \frac{1}{3}$ . Thus, we have proved the following theorem:

**Theorem 2.** If  $a^2b^2 < \frac{1}{3}$ , then there exist two anti-ferromagnetic phases, i.e. periodic phases with period 2.

#### 4. Paramagnetic phases

In [8], it was shown that we reach the paramagnetic phase if  $J_1J_3 < 0$  and it is described by the following recurrent equation

$$x' = \frac{1}{a} \left( \frac{1 + a^{-2}b^2 + 2bx}{2bx + a^{-2} + b^2} \right)^2. \tag{9}$$

To describe fixed points of (9), we have to solve the following equation

$$ax = \left( \frac{1 + a^{-2}b^2 + 2bx}{2bx + a^{-2} + b^2} \right)^2. \tag{10}$$

Let us assume that

$$f(x) = \left( \frac{1 + a^{-2}b^2 + 2bx}{2bx + a^{-2} + b^2} \right)^2. \tag{11}$$

Then

$$f'(x) = \frac{4b(a^{-2} - 1)(1 - b^2)(1 + a^{-2}b^2 + 2bx)}{[2bx + a^{-2} + b^2]^3}. \tag{12}$$

If  $J_1J_3 < 0$  then  $(a^{-2} - 1)(1 - b^2) < 0$ , thus,  $f'(x) < 0$ ,  $f(0) = \frac{1 + a^{-2}b^2}{a^{-2} + b^2} > 1$  and  $\lim_{x \rightarrow \infty} f(x) = 1$ . Therefore, equation (10) has single root. Thus, we have proved.

**Theorem 3.** On the set of paramagnetic phases, phase transition does not occur.

#### 5. Para-modulated phases

It was shown in [8] that one reaches the para-modulated phases if  $J_1J_3 < 0$ . As shown above, the paramagnetic phases are described by the following equation

$$x' = \frac{1}{a} \left( \frac{1 + a^{-2}b^2 + 2bx}{2bx + a^{-2} + b^2} \right)^2. \tag{13}$$

For brevity, let us introduce notations  $A = a^{-2}b + b^{-1}$  and  $B = a^{-2}b^{-1} + b$ . Then equation (13) can be rewritten as follows

$$x' = \frac{1}{a} \left( \frac{A + 2x}{2x + B} \right)^2. \tag{14}$$

Then, modulated and para-modulated phases are described by the following recurrent equation

$$x'' = \frac{1}{a} \left[ \frac{4(A+2)x^2 + 4A(B+2)x + AB^2 + 2A^2}{4(B+2)x^2 + 4(B^2+2A)x + B^3 + 2A^2} \right]^2. \quad (15)$$

Let us consider the fixed points

$$x = \frac{1}{a} \left[ \frac{4(A+2)x^2 + 4A(B+2)x + AB^2 + 2A^2}{4(B+2)x^2 + 4(B^2+2A)x + B^3 + 2A^2} \right]^2 \quad (16)$$

for paramagnetic and para-modulated phases and the fixed points

$$x = \frac{1}{a} \left( \frac{A+2x}{2x+B} \right)^2 \quad (17)$$

for paramagnetic phases. To find fixed points for para-modulated phases we rewrite equations (16) and (17) as polynomials of fifth and third degree, divide the first one by the second one and obtain the following quadratic equation.

$$4(B+2)^2x^2 - 16[A^2 + 3A - (2-a)B^3 - (5-4a)B^2 - 4B]x + (B+2A)^2 = 0. \quad (18)$$

This equation has two positive roots if

$$A^2 + 3A - (2-a)B^3 - (5-4a)B^2 - 4B > 0$$

and its discriminant  $D$  is positive. It is evident that  $D > 0$  if

$$A^2 - A - (2-a)B^3 - (6-4a)B^2 - 2AB - 6B > 0. \quad (19)$$

As shown in Fig. 1, one can reach a para-modulated phase if  $-J_3/J_1 \geq 1/3$  and  $T/J_1 < 2$ , that is  $a > e$  and  $b^3 < e^{-1}$ . Thus, one can rewrite this inequality as

$$A^2 - A + (a-2)B^3 + (4a-6)B^2 - 2AB - 6B > 0. \quad (20)$$

Substituting values of  $A$  and  $B$ , one comes to the following form of the inequality

$$\begin{aligned} & a^6(a-2)b^6 + a^2(4a^5 - 6a^4 - 2a^2 + 1)b^5 - a^4(6a^2 - 3a + 14)b^4 - 2a^2(a^4 + 5a^2 + 2)b^3 \\ & - a^2(a^4 - 8a^3 + 6a^2 + 6)b^2 + a^2(a^4 - 2a^2 + 4a - 6)b + a - 2 > 0. \end{aligned}$$

Correspondingly, the paramagnetic- para-modulated transition is given by the following condition

$$A^2 - A + (a-2)B^3 + (4a-6)B^2 - 2AB - 6B = 0. \quad (21)$$

Here  $a = \varphi(b)$  with  $a = \exp(J_1/T)$ ,  $b = \exp(J_3/T)$ . If  $A^2 - A + (a-2)B^3 + (4a-6)B^2 - 2AB - 6B > 0$  then equation (21) has two positive solutions  $\tilde{x}_1$  and  $\tilde{x}_2$  such that  $\tilde{x}_2' = \tilde{x}_1$  and  $\tilde{x}_1' = \tilde{x}_2$ . Thus, we have proved the following theorem:

**Theorem 4.** If  $A^2 - A + (a-2)B^3 + (4a-6)B^2 - 2AB - 6B > 0$  then there exist two para-modulated phases with period 2.

## 6. Conclusion

In this paper, we discussed the problem of phase transition for the Ising model with competing “uncle–nephew” interactions. In the previous paper [8], for  $J_1 > 0$ ,  $J_3 > 0$ , it was proved that there exists phase transition in the class of ferromagnetic phases.

In this paper, we proved that for  $J_1 < 0$ ,  $J_3 < 0$ , a phase transition occurs in the class of anti-ferromagnetic phases.

Also we investigated the problem of phase transition for remaining two classes of phases – paramagnetic and para-modulated phases. We proved that in the class of paramagnetic phase there is no phase transition. As for the class of para-modulated phases, it was shown that phase transition can occur. Thus, we investigated the problem of phase transition for all phase classes of the considered model.

## References

- [1] Vannimenus J. Modulated phase of an Ising system with competing interactions on a Cayley tree. *Z Phys B.*, 1981, **43**, P. 141–148.
- [2] Mariz A.M., Tsallis C., Albuquerque E.L. Phase diagram of the Ising model on a Cayley tree in the presence of competing interactions and magnetic field. *J Stat Phys.*, 1985, **40**, P. 577–592.
- [3] da Silva C.R., Coutinho C. Ising model on the Bethe lattice with competing interactions up to the third-nearest-neighbor generations. *Phys Rev B.*, 1986, **34**, P. 7975–7985.
- [4] Inavarisho S., Thompson C.J. Competing Ising interactions and chaotic glass-like behaviour on a Cayley tree. *Phys Lett A.*, 1983, **97**, P. 245–248.
- [5] Inawashiro S., Thompson C.J., Honda G. Ising model with competing interactions on a Cayley tree. *J Stat Phys.*, 1983, **33**, P. 419–436.
- [6] Yokio C.S.O., de Oliveira M.J., Salinas S.R. Strange attractor in the Ising model with competing interaction on the Cayley tree. *Phys Rev Lett.*, 1995, **54**, P. 163–166.
- [7] Thompson C.J. On mean field equations for spin glasses. *J Stat Phys.*, 1982, **27**, P. 457–472.
- [8] Ganikhodjaev N., Rodzhan M.H.M. Ising Model on the Cayley tree with competing interactions up to the third nearest-neighbors with spins belonging to different branches of the tree. *J Kor Phys Soc.*, 2015, **66**, P. 1200–1206.
- [9] Ganikhodjaev N.N., Ising model with competing *uncle–nephew* interactions. *Phase Transitions*, 2019, **92**(8), P. 730–736.

---

*Submitted 10 August 2022; revised 6 September 2022; accepted 7 September 2022*

*Information about the authors:*

*Nasir N. Ganikhodjaev* – Institute of Mathematics, 4B, St. University, 100174, Tashkent, Uzbekistan; gnasir@ium.edu.my

*Muzaffar M. Rahmatullaev* – Institute of Mathematics, 4B, St. University, 100174, Tashkent, Uzbekistan; Namangan State University, 316 Uychi street, Namangan, Uzbekistan; mrahmatullaev@rambler.ru

*Mahliyo R. Abdusalomova* – Namangan State University, 316 Uychi street, Namangan, Uzbekistan; mahliyo13abdusalomova@gmail.com

*Conflict of interest:* the authors declare no conflict of interest.

## Optical anisotropy in fullerene-containing polymer composites induced by magnetic field

Ivan V. Pleshakov<sup>1,a</sup>, Olga V. Proskurina<sup>1,2,b</sup>, Viktor I. Gerasimov<sup>3,c</sup>, Yuriy I. Kuz'min<sup>1,d</sup><sup>1</sup>Ioffe Institute, St. Petersburg, Russia<sup>2</sup>St. Petersburg State Institute of Technology (Technical University), St. Petersburg, Russia<sup>3</sup>Peter the Great St. Petersburg Polytechnic University, St. Petersburg, Russia<sup>a</sup>ivanple@yandex.ru, <sup>b</sup>proskurinaov@mail.ru, <sup>c</sup>viger53@rambler.ru, <sup>d</sup>iourk@yandex.ru

Corresponding author: Ivan V. Pleshakov, ivanple@yandex.ru

PACS 42.70.-a; 42.70.Jk; 78.40.Ri

**ABSTRACT** Using water-soluble hydrated fullerenes embedded in a polyvinyl alcohol matrix, samples were obtained that demonstrated the presence of optical anisotropy when they were formed in a magnetic field. Its existence was established in experiments on light scattering in films containing  $C_{60}(OH)_n$  and  $C_{70}(OH)_m$  molecules. The mechanism of the effect is presumably associated with the anisotropy of the shape of these molecules.

**KEYWORDS** carbon-containing composites, polymer matrices, fullerene, fullerenol, light scattering.

**ACKNOWLEDGEMENTS** The authors are grateful to A. V. Varlamov and D. M. Seliutin for their help in the experiments.

**FOR CITATION** Pleshakov I.V., Proskurina O.V., Gerasimov V.I., Kuz'min Yu.I. Optical anisotropy in fullerene-containing polymer composites induced by magnetic field. *Nanosystems: Phys. Chem. Math.*, 2022, **13** (5), 503–508.

### 1. Introduction

Composites, which are polymer matrices with embedded molecules or molecular complexes based on carbon, are currently being studied from various points of view. The interest in them is dictated by the desire to produce materials with special properties, for example, for improvement of mechanical characteristics, the need to obtain particular membranes and many other objectives [1–5]. One of the important trends in this field is fullerene-containing polymers and the possible creation of such optical media on their basis, the parameters of which could be controlled in one way or another, including control by the action of external fields.

In this paper, we consider the previously unexplored case of fullerene- and fullerenol-containing composites formed in the magnetic field  $H$ . As an experimental approach used to obtain information about this substance, the light scattering technique was applied.

### 2. Samples

The samples were made in the form of films of polyvinyl alcohol (PVA) with  $C_{60}(OH)_n$  or  $C_{70}(OH)_m$  molecules injected in it, solidified on glass substrates. Similar materials, but synthesized without the applying  $H$ , were studied by us earlier [6, 7]. In addition, films of epoxy resin with fullerene  $C_{60}$  were used as control samples.

Fullerene and its derivatives were obtained on the basis of principles outlined in [8]. Soot resulting from the erosion of graphite electrodes in an electric arc in a helium atmosphere was treated with xylene and separated in a chromatographic column. After multi-stage purification with a carbon sorbent, a product was formed, which was further hydrated using sodium hydroxide, and, as an interfacial catalyst, tetrabutylammonium hydroxide solution. At the final stage, drying was carried out in vacuum at 40 °C. According to the data of complex thermal and elemental analysis, the result was compounds that best correspond to the formulas  $C_{60}(OH)_{42} \cdot 4H_2O$  or  $C_{70}(OH)_{52}$  (hereinafter referred to as  $C_{60}HyFn$  and  $C_{70}HyFn$ , respectively).

In the manufacture of samples, the fact that PVA and fullerenols are water-soluble substances was used. To obtain composite films, their solutions were mixed in different proportions at a temperature of about 90 °C, subjected to ultrasonic treatment for 30 min, applied to a glass substrate and dried in a magnetic field, forming films with a thickness of 30 to 60  $\mu\text{m}$ . The concentrations of the starting compounds varied, but the best quality of the sample (acceptable transparency with a sufficiently high content of inclusions) was achieved by introducing 10 mg of fullerenol into a five percent solution of PVA (5 wt. % of dry material by weight of water), and the greatest effect associated with the magnetic field was observed at the maximum achievable value in the laboratory  $H = 15$  kOe. The results below relate to these values.

The preparation of control samples was performed differently, since fullerene  $C_{60}$  does not dissolve in water. Initially, powdered fullerene was added to the epoxy resin hardener (commercially available transparent product *Artline Crystal Epoxy*), and this mixture was subjected to ultrasonic stirring for 30 minutes. Then the resulting mass was combined with the resin in a ratio of 2:1 and sonified for another 10 minutes. The weights of the ingredients were selected so that the concentration of  $C_{60}$  in the liquid was 1 wt. %. Next, the liquid was deposited on glass and placed in the field  $H = 15$  kOe, in which it hardened to a solid state, while the thickness and visual optical characteristics of the film were approximately the same as in the case of PVA.

For comparison, samples were also made for all matrices and fillers at  $H = 0$ .

### 3. Measurements procedures and processing of data

The optical measurements performed in this work were experiments on static light scattering carried out according to the standard scheme. The setup included a semiconductor laser ( $\lambda = 650$  nm), the radiation of which was directed at the sample, and a block rotating around the sample on the limb, consisting of a photodetector and a polarizer located in front of it, which allowed one to separate either horizontally or vertically polarized components of the scattered light.

A horizontally polarized laser beam was formed by a diaphragm with a sufficiently large aperture (more than 1 mm) and was applied to the sample from the side of the substrate perpendicular to it. The degree of laser radiation linear polarization  $P_0$ , which is known to be determined by the expression

$$P_0 = \frac{I_1 - I_2}{I_1 + I_2},$$

where  $I_1$  is the intensity of the horizontally polarized light component, and  $I_2$  is the intensity of the orthogonal (i.e. vertically polarized) light component, was about 95 %.

The experiment is reduced to determining the dependence of the intensity of scattered radiation  $I_s$  recorded by the photodetector on the angle  $\theta$ , measured in the horizontal plane from the optical axis of the system to the direction of the scattered beam, that is, determining of the indicatrix  $I_s(\theta)$ . We also measured the degree of linear polarization of the scattered radiation given by the formula

$$P_s = \frac{I_{s1} - I_{s2}}{I_{s1} + I_{s2}},$$

where  $I_{s1}$  and  $I_{s2}$  are the intensities of horizontally and vertically polarized components of scattered light, respectively. Next, the relative value of  $P_s/P_0$  was determined – an important parameter for our study that characterizes the degree of impact of the substance under investigation to light.

All measurements were performed for two positions of the sample: when the mutual orientations of the field  $H$  in which it was prepared and the polarizations  $p$  of incident beam were parallel or perpendicular.

The scattering indicatrices  $I_s(\theta)$  were processed by fitting functions of the form  $f(\theta) = a \cdot \cos^2(\beta\theta)$ . This was necessary to estimate the value of  $I_s(0)$  (of course, measurements are impossible in the region close to  $\theta = 0$ ) and, thus, to determine the width of  $I_s(\theta)$  at half intensity  $\delta\theta_{0.5}$ . It should be noted that this approach is rather rough, but it introduces a simple unified criterion for all indicatrices (accurate analytical processing is extremely complicated by the fact that the phenomenon under study is a complex case of scattering on a system of non-spherical and differing in size objects with internal anisotropy). The lines shown in the figures below are drawn using this fit.

### 4. Experimental results

Figure 1 shows the  $I_s(\theta)$  indicatrices for two orientations of an epoxy resin-based sample obtained by recording scattered radiation with a polarization coinciding with the incident one (Fig. 1a) and perpendicular to it (Fig. 1b). It is noteworthy that these diagrams are rather narrow  $\delta\theta_{0.5} \cong 6^\circ$  and practically the same for the geometries of the experiment corresponding to different orientations of the magnetic field. In order to note the not quite exact correspondence of the chosen approximation to experimental data, an additional curve is shown in Fig. 1a, which is a fit of  $f(\theta)$  to points at  $|\theta| > 5^\circ$ . In Fig. 1b the calculated curve is a scaling transformation of the main diagram in Fig. 1a, that is, the ratio  $P_s/P_0$  within the main peak remains constant at all angles  $\theta$  and orientations of  $H$ .

Figure 2 demonstrates the  $I_{s1}(\theta)$  indicatrix (Fig. 2a) and the relative degree of linear polarization  $P_s/P_0$  (Fig. 2b), obtained for  $C_{60}$ HyFn film at different magnetic field orientations. The width  $\delta\theta_{0.5} \cong 5.8^\circ$  measured from  $I_{s1}(\theta)$  turned out to be approximately the same for every  $H$  direction (the dots that not described by the main peak function  $f(\theta)$  were not recorded here). However, in this case, the approximations of  $I_{s1}(\theta)$  and  $I_{s2}(\theta)$  differed not only by the scale factor, i.e., there was a pronounced angular dependence of the parameter  $P_s/P_0$ , which, moreover, was different for different orientations of the field. As an example, Fig. 2b shows the curves calculated from the above expressions using fitting functions  $I_s$ .

Another picture was observed for the  $C_{70}$ HyFn sample (Fig. 3). At different orientations of the field, the  $I_{s1}(\theta)$  indicatrices were noticeably different in width (Fig. 3a), and the difference in  $P_s(\theta)/P_0$  became very significant, reaching a value of about 10–15 %.

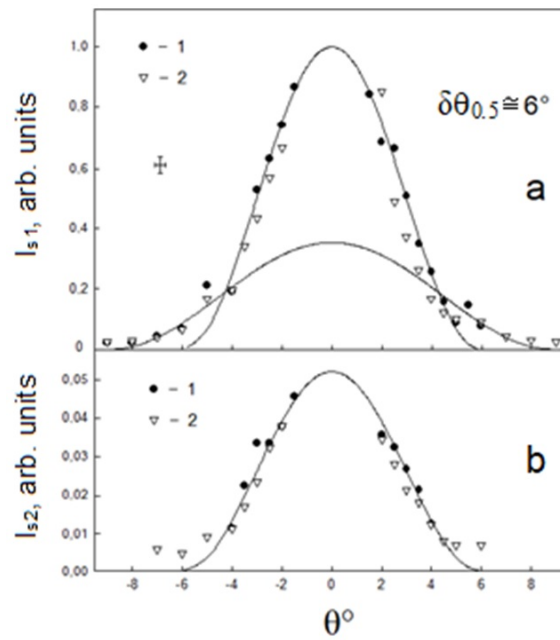


FIG. 1. Indicatrices of epoxy-based sample for registration of scattered light with polarization parallel (a) and orthogonal (b) to polarization  $p$  of incident beam. 1 – Perpendicular orientation of  $H$  to  $p$ , 2 – parallel orientation of  $H$  to  $p$

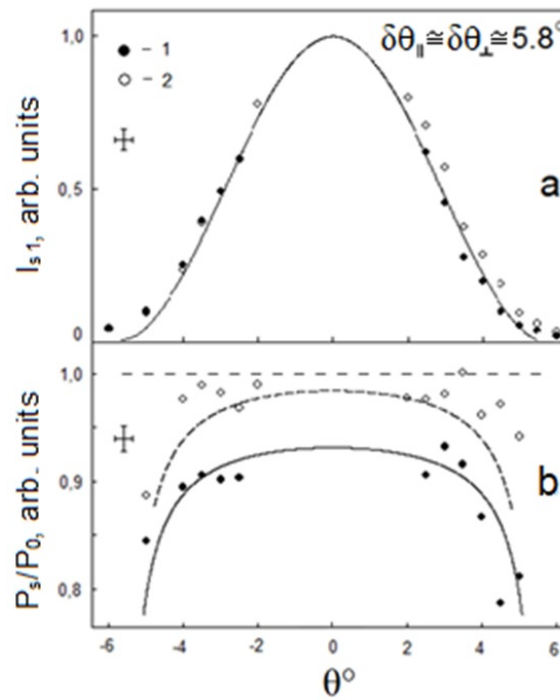


FIG. 2. Results of the experiment with the sample  $C_{60}HyFn$ : indicatrix  $I_{s1}(\theta)$  (a) and relative degree of linear polarization  $P_s/P_0$  (b). 1 – Perpendicular orientation of  $H$  to  $p$ , 2 – parallel orientation of  $H$  to  $p$

To display the effect of the magnetic field on the studied composites more clearly, the data obtained for  $C_{60}HyFn$  and  $C_{70}HyFn$  are presented together on a separate graph (Fig. 4), where the angular dependences of the relative degree of linear polarization are shown in the region  $-5^\circ < \theta < 0^\circ$ .

In control samples fabricated at  $H = 0$ , the effects described above were not observed.

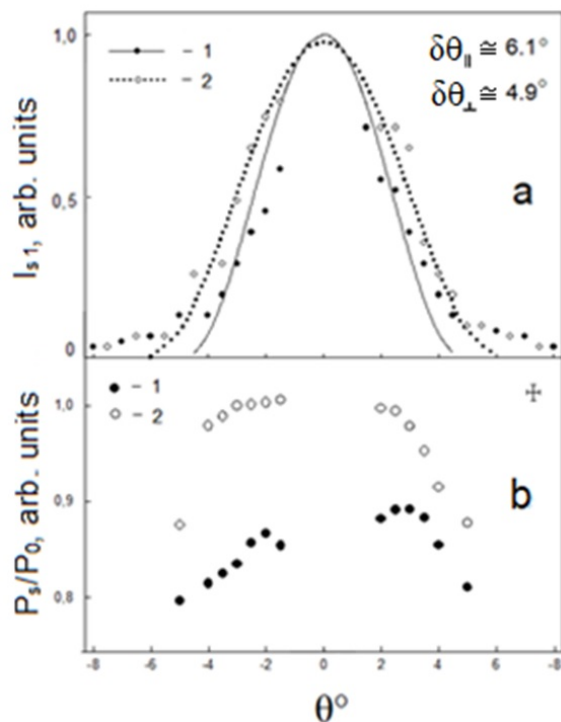


FIG. 3. Results of the experiment with the sample  $C_{70}HyFn$ : indicatrix  $I_{s1}(\theta)$  (a) and relative degree of linear polarization  $P_s/P_0$  (b). 1 – Perpendicular orientation of  $H$  to  $p$ , 2 – parallel orientation of  $H$  to  $p$

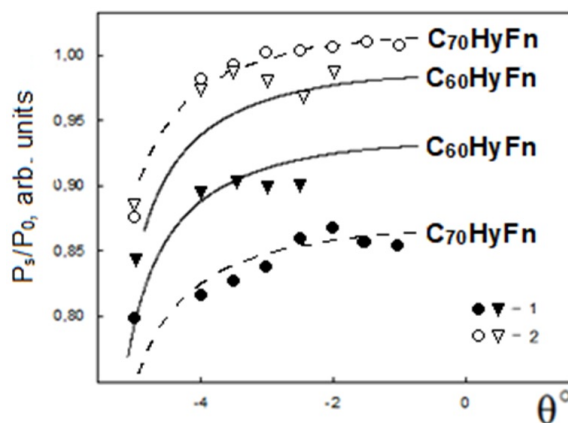


FIG. 4. Comparison of the dependences of relative linear polarization degree on the scattering angle in PVA films. 1 – Perpendicular orientation of  $H$  to  $p$ , 2 – parallel orientation of  $H$  to  $p$

## 5. Discussion

An obvious conclusion from the above data is that in systems containing  $C_{60}HyFn$  and  $C_{70}HyFn$  molecules, an external magnetic field induces optically detectable anisotropy. Comparison of the characteristics of the latter with the characteristics of the control sample shows that the shape of the molecules should play an essential role in this phenomenon. Assuming  $C_{60}$  to be a spherically symmetric object, it can be expected that no preferred direction under the action of  $H$  in a substance with “pure” fullerene can appear, which is confirmed by the measurement results of an epoxy-based composite (Fig. 1). At the same time, the width of the indicatrix (or, more precisely, the part of it that corresponds to the

most intense scattering) of the  $C_{60}$ -containing sample differs little from the value of the same parameter for  $C_{60}HyFn$  and  $C_{70}HyFn$ . This indicates that in all cases the scatterers are particles larger than individual molecules. The obtained values of the  $\delta\theta_{0.5}$  allow us, based on [9] and the references therein, to estimate qualitatively their average size  $d$  as units of microns ( $d \geq \lambda$ ), that is, to assume that we deal with a scattering close to the scattering of Mie (which is not quite strict, since the shape and structure of the scatterers, as mentioned above, differs from homogeneous sphere). An additional wide low-intensity line in Fig. 1a, corresponds, most likely, to the existence of a fine fraction of carbon inclusions in  $C_{60}$ -containing sample. The absence of angular dependence of  $P_s/P_0$  in the epoxy-based composite, while conserving the value of this parameter close to the same in incident beam, is a sign of the high symmetry of scatterers associated with  $C_{60}$  molecules.

In the  $C_{60}HyFn$ -containing sample, such a dependence exists (Fig. 1b), and, what is most important, it is different for different sample orientations, while the change in the width of the indicatrix is not observed also (Fig. 1a). It can be assumed that in this case, the optical anisotropy induced by the magnetic field mainly is owing to the internal anisotropy of the clusters formed by fullerene  $C_{60}HyFn$  molecules, which, in turn, is determined by a certain deviation of their shape from spherical. Of course, there is a question about how noticeable this effect is, since the carbon skeleton of this molecule continues to remain the same as that of fullerene  $C_{60}$ . However, according to the results of the simulation carried out in [10], the attachment of a certain amount of OH groups to the core of the  $C_{60}HyFn$  molecule can form structures with a fairly well-defined asymmetry.

Figure 3, referring to  $C_{70}HyFn$ , shows the most striking manifestation of field-induced anisotropy. Here, in addition to the very different for the two orientations of  $H$  angular dependences of the relative degree of linear polarization (Fig. 3b), a noticeable broadening of the scattering indicatrix appears (Fig. 3a), which probably reflects both the existence of internal anisotropy and the non-sphericity of the clusters formed by the molecules of this fullerene. The difference in the values of  $\delta\theta_{0.5}$  when light is scattered on extended objects of a different physical nature, but with the same experimental geometries as in present work was observed, for example, in [11]. Nucleation of structures elongated in the field, the constituents of which are the  $C_{70}HyFn$  molecules, is more obvious than in the case of  $C_{60}HyFn$ , since their carbon skeleton is already has an anisotropy of the shape, which persisting or increasing when the hydrate shell is formed. The significantly stronger influence of the magnetic field on such samples is illustrated by comparing the plots of  $P_s(\theta)/P_0$  of composites with  $C_{60}HyFn$  and  $C_{70}HyFn$  in a large scale (Fig. 4).

In the cases discussed above, and even if clustering does not occur at all, induced anisotropy required that non-magnetic molecules should line along the field. Of course, any molecules can be considered non-magnetic only in a certain approximation; it is more correct to take into account their diamagnetic properties, as is done, for example, when analyzing the behavior of liquid crystals. Therefore, as a simple explanation for the effects we observed, a mechanism similar to what occurs in these substances is proposed: non-spherical molecules, due to their anisotropy of dielectric susceptibility, rotate in the field, minimizing the corresponding energy and forming further larger objects (clusters). Being hypothetical, this model, of course, can be refined or modified, for instance, taking into account the complicated nature of the interaction of the hydrate shell of fullerene molecules with the matrix.

Note that the structure of clusters does not necessarily imply the presence of a large number of closely packed molecules in them. It is possible, for example, that variations in the density of the additive distribution in the matrix creates a scattering medium with a spatially varying refractive index, in which fullerene molecules are separated by PVA. A certain role in the formation of scattering objects can also be played by PVA crystallites [12], which are usually present in this polymer.

## 6. Conclusion

In the work, the light scattering method revealed the effect that a magnetic field can create optical anisotropy in a composite medium containing inclusions in the form of polyhydroxylated fullerenes molecules.

## References

- [1] Liming Dai, Albert W.H. Mau, Xiaoqing Zhang. Synthesis of fullerene- and fullerol-containing polymers. *J. Mater. Chem.*, 1998, **8**(2), P. 325–330.
- [2] Changchun Wang, Zhi-Xin Guo, Shoukuan Fu, Wei Wu, Daoben Zhu. Polymers containing fullerene or carbon nanotube structures. *Prog. Polym. Sci.*, 2004, **29**(11), P. 1079–1141.
- [3] Eletskii A.V., Knizhnik A.A., Potapkin B.V., Kenny J.M. Electrical characteristics of carbon nanotube doped composites. *Phys. Usp.*, 2015, **185**(3), P. 225–270.
- [4] Penkova A.V., Acquah S.F.A., Sokolova M.P., Dmitrenko M.E., Toikka A.M. Polyvinyl alcohol membranes modified by low-hydroxylated fullerene  $C_{60}(OH)_{12}$ . *J. Memb. Sci.*, 2015, **491**, P. 22–27.
- [5] Dmitrenko M., Liamin V., Kuzminova A., Mazur A., Lahderanta E., Ermakov S., Penkova A. Novel mixed matrix sodium alginate–fullerene membranes: development, characterization, and study in pervaporation dehydration of isopropanol. *Polymers*, **12**(4), P. 2020864.
- [6] Karpunin A.E., Gerasimov V.I., Mazur A.S., Pleshakov I.V., Fofanov Ya.A., Proskurina O.V. NMR investigation of composite material, formed by fullerene in polymer matrix of polyvinyl alcohol. *Proceeding of "International Conference on Electrical Engineering and Photonics (EExPolytech)"*. Saint Petersburg (Russia), 22–23 Oct. 2018, IEEE, 2018, P. 168.
- [7] Karpunin A.E., Pleshakov I.V., Proskurina O.V., Gerasimov V.I., Nechitailov A.A., Glebova N.V., Varlamov A.V., Parfenov M.V. Optical study of composite material with nanosized fullerene inclusions. *Journal of Physics: Conference Series*, 2019, **1236**, P. 012012.

- [8] Li J., Takeuchi A., Ozawa M., Li X., Saigo K., Kitazawa K. C<sub>60</sub> fullerol formation catalysed by quaternary ammonium hydroxides. *J. Chem. Soc. Chem. Commun.*, 1993, **23**, P. 1784–1785.
- [9] Bohren C.F., Huffman D.R. *Absorption and scattering of light by small particles*. John Wiley & Sons, Inc., NY, 1998, 544 p.
- [10] Keshri S., Tembe B.L. Thermodynamics of hydration of fullerols [C<sub>60</sub>(OH)<sub>n</sub>] and hydrogen bond dynamics in their hydration shells. *J. Chem. Phys.*, 2017, **146**(7), P. 074501.
- [11] Pleshakov I.V., Prokof'ev A.V., Bibik E.E., Kuz'min Yu.I. Investigation of structures formed by magnetic fluid nanoparticles in polymer matrices by static light scattering. *Nanosystems: Phys. Chem. Math.*, 2022, **13**(3), P. 285–289.
- [12] Thomas D., Cebe P. Self-nucleation and crystallization of polyvinyl alcohol. *J. Therm. Anal. Calorim.*, 2017, **127**, P. 885–894.

---

*Submitted 8 September 2022; revised 17 September 2022; accepted 18 September 2022*

*Information about the authors:*

*Ivan V. Pleshakov* – Ioffe Institute, 26 Politechnicheskaya str., St. Petersburg, 194021, Russia; ivanple@yandex.ru

*Olga V. Proskurina* – Ioffe Institute, 26 Politechnicheskaya str., St. Petersburg, 194021, Russia; St. Petersburg State Institute of Technology (Technical University), 26 Moskovsky ave., St. Petersburg, 190013, Russia; proskurinaov@mail.ru

*Viktor I. Gerasimov* – Peter the Great St. Petersburg Polytechnic University, 29 Polytechnicheskaya str., St. Petersburg, 195251, Russia; viger53@rambler.ru

*Yuriy I. Kuz'min* – Ioffe Institute, 26 Politechnicheskaya str., St. Petersburg, 194021, Russia; iourk@yandex.ru

*Conflict of interest:* the authors declare no conflict of interest.

## Pt(0) microscrolls obtained on nickel surface by galvanic replacement reaction in $H_2PtCl_6$ solution as the basis for creating new SERS substrates

Maria V. Kaneva<sup>a</sup>, Evgen V. Borisov<sup>b</sup>, Valeri P. Tolstoy<sup>c</sup>

Institute of Chemistry, Saint Petersburg State University, St. Petersburg, 198504, Russia

<sup>a</sup>skt94@bk.ru, <sup>b</sup>eugene.borisov@spbu.ru, <sup>c</sup>v.tolstoy@spbu.ru

Corresponding author: Valeri P. Tolstoy, v.tolstoy@spbu.ru

PACS 82.33.Pt, 82.45.Mp, 82.45.Yz

**ABSTRACT** The paper explores the morphology features of Pt(0) nanolayers obtained on the surface of chemically polished nickel as a result of the galvanic replacement reaction using  $H_2PtCl_6$  solution. In a series of samples synthesized at a treatment time of 1–60 minutes, it is shown that the nanolayers consist of Pt(0) nanocrystals 5–10 nm in size, which form a continuous porous layer with a thickness depending on the treatment time in solution. For example, it is about 80 nm and 120 nm for samples obtained after 3 minutes and 20 minutes, respectively. Moreover, on the outer side of the nanolayer with respect to the substrate, these nanocrystals form arrays of pointed agglomerates directed along the normal to the surface. After drying in air, the Pt(0) nanolayer cracks and partially folded microscrolls form on the nickel surface, the number of which is the largest for the samples obtained with a longer treatment time. The features of the practical application of these samples as SERS substrates are studied using the Raman spectra of Rodamin 6G as an example. It is shown that the amplification factor is about  $10^5$ – $10^6$  using 532 nm laser excitation.

**KEYWORDS** platinum, nanocrystals, microscrolls, galvanic replacement reaction, SERS.

**ACKNOWLEDGEMENTS** This work was supported by the RFBR grant (project # 20-33-90228/20-PhD-students). We are grateful to the “Centre for Optical and Laser Materials Research” and “Nanotechnology” Research Parks of Saint Petersburg State University, for their technical assistance with the synthesized samples investigation.

**FOR CITATION** Kaneva M.V., Borisov E.V., Tolstoy V.P. Pt(0) microscrolls obtained on nickel surface by galvanic replacement reaction in  $H_2PtCl_6$  solution as the basis for creating new SERS substrates. *Nanosystems: Phys. Chem. Math.*, 2022, **13** (5), 509–513.

### 1. Introduction

Application of Raman spectroscopy to the study of organic molecules and biological objects is one of the most widely discussed topics in optical spectroscopy. To confirm it, one can mention that more than 300 reviews were published on this topic in 2021 according to international databases, for example [1–3]. One of the central questions for choosing the conditions for obtaining such spectra is the creation of optimal, so-called SERS substrates, which the investigated substance is applied on and which provide high values of the effective signal amplification factor [4–8].

To date, many methods of creating such substrates have been tried and are being used. The use of precious metals with nano- and microtubular morphology for this purpose is one of the directions of further development of the topic. In particular, in article [9], microtubes of gold with a length of several microns and a diameter of 0.5 to 3.5  $\mu\text{m}$  with a wall thickness of several tens nm were obtained. The walls of these microtubes have a relatively large proportion of atoms on the surface and exhibit SERS signals nearly 20 times larger than those of the gold film. A similar SERS signal reinforcement effect was also found in the case of Au nanoparticles applied to the inner surface of microtubes with walls made of InGaAs/GaAs layers [10]. The original way of producing Au microtubes was proposed in the work [11]. For this purpose, nanoparticles Au were adsorbed on the surface of the *Trichoderma asperelum* and *Aspergillus sydowii* fungi and then the biological material was removed by solvent washing and heating in the air at 400°. The walls of the microtubes produced under these conditions were found to consist of nanoparticles Au with a size of about 20 nm and the microtubes were 2–4  $\mu\text{m}$  in diameter and several tens of  $\mu\text{m}$  in length. Moreover, the position of the maximum light absorption band Au lies in the range of 680 to almost 1000 nm and depends on the ratio of the diameter and length of the tube.

The last circumstance makes it possible to focus on specimens that provide maximum amplification of the useful signal in SERS. It should also be noted that the work [12] in which the authors studied the optical properties of microtubes with walls of Ag obtained by the method of template - synthesis using a solution of the mixture  $AgNO_3$  and Na-cit and porous membrane of polycarbonate. These microtubes had a diameter of about 3–4  $\mu\text{m}$ , a length of about 10  $\mu\text{m}$  and a wall thickness of several tens of nanometers. They have been found to exhibit SERS substrate properties in the production of Raman spectra of Rhodamine 6G molecules.

It is noteworthy to mention the work [13] devoted to fabrication of Ag-SiO<sub>x</sub> microtubules as robust SERS substrates based on roll-up nanotechnology. As an illustration, dramatic enhancement is achieved using Rhodamine 6G as a molecular probe, which indicates that a larger plasmonic density of states exist, leading to a greatly enhanced local electromagnetic field (EM) when the sample is irradiated with a laser beam. Optimized results are obtained by controlling the thickness of alumina coating onto Ag-SiO<sub>x</sub> microtubes using atomic layer deposition. Finite difference time-domain simulations further illustrate the excitation of localized surface plasmon modes by calculating the EM field properties on the surface of Ag-SiO<sub>x</sub> microtubes.

It should be noted that the potential of this approach has not yet been fully exploited, as other methods of producing nano- and microtubular structures, such as those published in papers [14–19], have not yet been tested.

The aim of this paper is to study the application characteristics of SERS substrates of Pt(0) microscrolls produced on the nickel surface as a result of galvanic replacement reaction (GRR) between its atoms and anions in H<sub>2</sub>PtCl<sub>6</sub> aqueous solution. For the first time in this way, such microscrolls were obtained in the work [20]. It was shown that they exhibit active electrocatalytic properties in the hydrogen evolution reaction during water electrolysis in an alkaline medium. We also note that earlier GRR have already been used to obtain SERS substrates, for example, in the synthesis of Au-Ag nanocomposites [21–23].

## 2. Experiment

Dihydrogen hexachloroplatinate (IV) hydrate (H<sub>2</sub>PtCl<sub>6</sub>·6H<sub>2</sub>O, JSC “Aurat”) and Ni foil with a size of 0.5 × 10 × 10.0 mm were used as precursor and a substrate, respectively, to synthesize the Pt(0) nanolayer by GRR. Ni plates were cleaned with acetone by ultrasonic treatment for 30 min and treated according to [24] in hydrochloric acid (HCl, 3 M). Then, the substrates were washed in deionized water and treated for 30 seconds in a solution of a mixture of CH<sub>3</sub>COOH, HNO<sub>3</sub> and HCl acids. At this stage, the chemical polishing of the surface took place and the samples acquired a mirror shine. Thereafter, Ni plates were immersed into a solution of H<sub>2</sub>PtCl<sub>6</sub> (C = 0.005 M) for 0.5–60 minutes. The GRR was carried out at room temperature and atmospheric pressure. As a result, the Pt(0) nanolayer is formed on the surface and rolls up into microscrolls during drying in air. SEM, TEM, STEM, EDX and HR-TEM methods were used to characterize the samples. SEM analysis was carried out with a Zeiss Merlin or a Zeiss EVO-40EP electron microscopes. TEM, STEM, and HR-TEM micrographs were obtained using a Zeiss Libra 200 microscope. EDX spectra were received with Oxford Instruments INCA 350 and INCAx-act spectrometers, which were equipped with a Zeiss EVO-40EP and Zeiss Libra 200 electron microscopes, respectively. The Raman spectra were recorded using a Bruker spectrometer (Senterra model) under excitation by a 532 nm laser and a power of 20 mW, the radiation focusing area on the sample had a diameter of about 1 mm without using a microscope objective. Alcoholic solutions of Rhodamine 6G of various concentrations were used as the research object which were applied to the surface.

## 3. Results and discussions

The study of the nickel surface by the SEM and STEM methods (Fig. 1) and by the EDX method (not shown in the figure) after its contact with an H<sub>2</sub>PtCl<sub>6</sub> solution made it possible to establish that, at a treatment time of more than 2–3 minutes, Pt(0) nanolayers with a morphology of partially formed microscrolls are observed. With an increase in treated time, the thickness of the walls of such microscrolls increases from 80 nm to about 120 nm for the samples obtained during treatment with a solution of 3 minutes and 20 minutes, respectively (Fig. 1d,e,f). An increase in the treatment time also leads to an increase in the number of such microscrolls per unit area of the substrate surface. It is also noteworthy that the Pt(0) layer is porous and consists of separate nanoparticles. These nanoparticles form agglomerates, which have the form of pointed vertices on the outer side of a layer with respect to the substrate, directed along the normal to the surface. Such peaks up to 100 nm in height can be clearly identified in the sample obtained during 10 min of treatment with an H<sub>2</sub>PtCl<sub>6</sub> solution (Fig. 1e). Increasing the treatment time to 20 minutes reduces the number of such vertices/ It is likely due to the fact that the new nanoparticles Pt(0) that are formed during the synthesis process are located between these vertices. It should also be noted that the thickness of the Pt(0) nanolayer is practically not increased by increasing the treatment time in the solution to 60 minutes, indicating that the nickel surface is blocked by the already formed Pt(0) nanolayer.

The study of Pt(0) nanolayer fragments by TEM and STEM methods made it possible to establish that the size of platinum nanocrystals is 5–10 nm, regardless of the treatment time. Each of these particles has a face-centered cubic crystal lattice characteristic of Pt(0). In this regard, we present in Fig. 2 the results of the STEM and HR-TEM study of only one sample obtained by treating Ni with a H<sub>2</sub>PtCl<sub>6</sub> solution for 3 minutes.

A series of experiments that were carried out with Ni foil samples and H<sub>2</sub>PtCl<sub>6</sub> solutions showed that the Pt(0) nanolayer with the microscroll morphology is relatively strongly retained on the Ni surface. In this regard, such Ni samples can be used as substrates for obtaining Raman spectra of organic compounds under conditions of signal amplification by the surface. To record such spectra, we used Ni foil substrates with Pt(0) nanolayers obtained on their surface by treatment under GRR conditions in an H<sub>2</sub>PtCl<sub>6</sub> solution for 3, 10, and 20 minutes. For comparison, similar spectra of this compound deposited on the single-crystal silicon surface were recorded using a similar technique. The obtained Raman spectra of such samples are shown in Fig. 3.

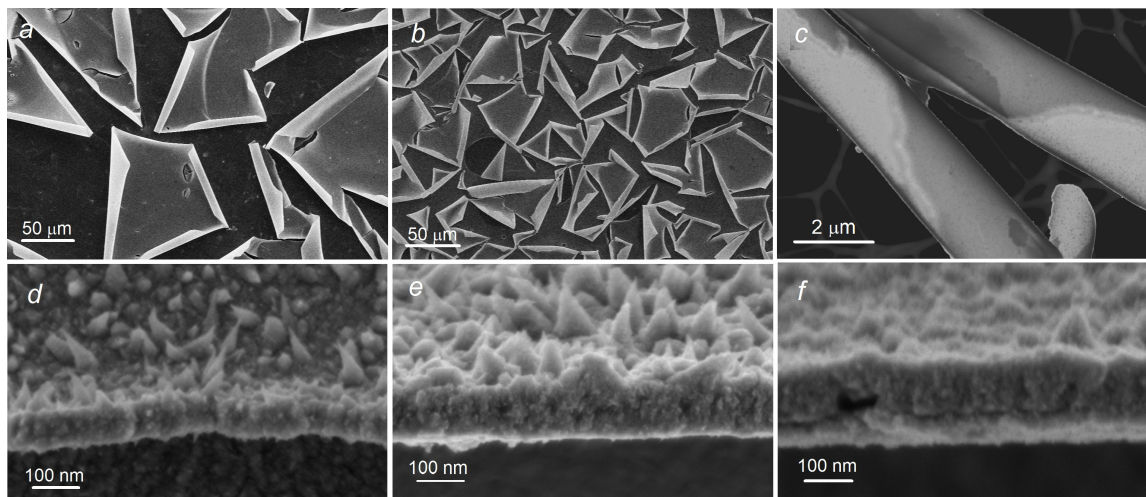


FIG. 1. SEM images of the Pt(0) nanolayers on the Ni surface obtained by treating it for 3 (a,d), 10 (e) and 20 (b,f) minutes with a  $\text{H}_2\text{PtCl}_6$  solution. (a,b) – general top views, (d,e,f) – side views of the Pt(0) nanolayers. (c) – STEM image of Pt microscrolls obtained after treatment with a solution for 3 minutes

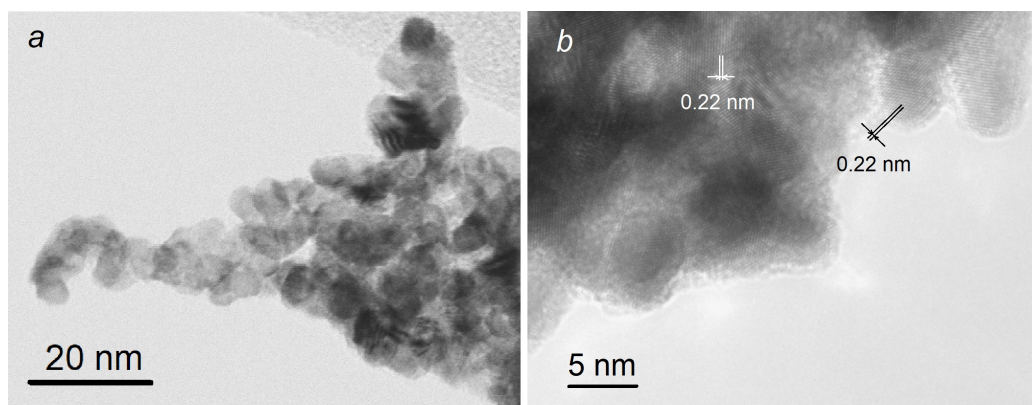


FIG. 2. STEM (a) and HR-TEM (b) images of Pt(0) nanocrystals, obtained after treatment Ni foil with a  $\text{H}_2\text{PtCl}_6$  solution for 10 minutes

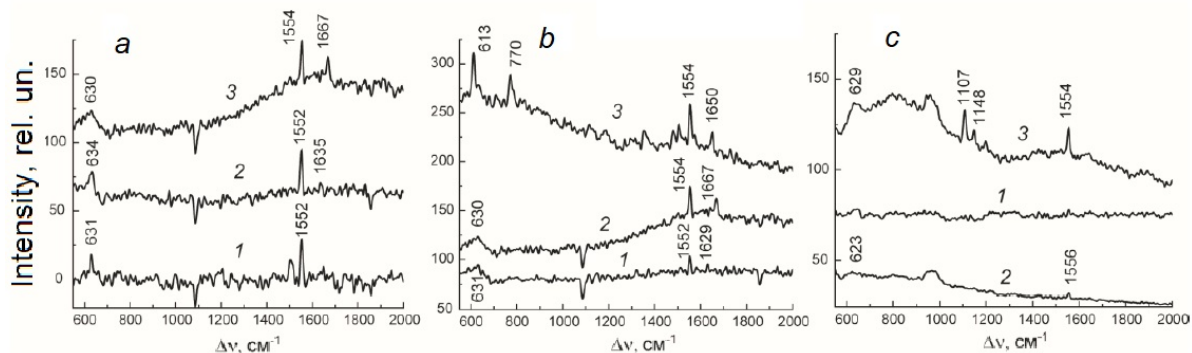


FIG. 3. Raman spectra Rhodamine 6G on the Pt microscrolls surface (a,b) and on single-crystal silicon surface (c) with different concentrations. a – the alcohol solution R6G was applied to the samples prepared under the GRR conditions of Ni treatment with a  $\text{H}_2\text{PtCl}_6$  solution for 3 (1), 10 (2) and 20 (3) minutes (the concentration of the Rhodamine 6G solution was  $10^{-6}\text{M}$ ); b – the concentration of Rhodamine 6G solution was  $10^{-7}$  (1),  $10^{-6}$  (2) and  $10^{-4}$  (3) M and it was applied to the sample prepared with a treatment time of Ni with a  $\text{H}_2\text{PtCl}_6$  solution equal to 20 minutes; c – substrate of the initial silicon (1) and after applying solutions with concentrations  $10^{-2}$  (2) and  $10^{-1}$  M (3)

Analyzing these spectra, first of all, we note that the most informative spectrum of Rhodamine 6G was obtained for the samples prepared by treating nickel in a  $\text{H}_2\text{PtCl}_6$  solution for 10 and 20 minutes (Fig. 3a(2,3)). In these spectra, in addition to peaks with maxima at 630–634 and 1552–1554  $\text{cm}^{-1}$ , one can distinguish peaks with maxima at 1635–1667  $\text{cm}^{-1}$ . Recall that the peaks in the region of 1500–1700  $\text{cm}^{-1}$  are due to stretching vibrations of C–C atoms in benzene rings, and in the region of 630  $\text{cm}^{-1}$ , they are due to vibrations of atoms of chains of C–C–C bonds [25]. Moreover, from the spectra shown in Fig. 3b, it is possible to detect these molecules already in a solution with a concentration of  $10^{-7}$  M. The intensity of the peaks in the Raman spectrum increases with increasing concentration up to  $10^{-4}$  M. In this regard, it can be argued that the detection limit of Rhodamine 6G when obtaining spectra by this method is the value of  $10^{-7}$  M. At the same time, if this solution is applied to the silicon surface, then the most intense peaks in its spectrum are observed only starting from a concentration of  $10^{-2}$ – $10^{-1}$  M.

Thus, the obtained results indicate that the amplification factor of the studied substrate, which consists of Pt(0) microscrolls on the nickel surface, is  $10^5$ – $10^6$  times. In our opinion, this result is achieved due to the special and unique morphology of the microscrolls layers, the walls of which, on the one hand, consist of nanocrystals with a high specific surface area, and, on the other hand, some of these nanocrystals form arrays of pointed agglomerates. It should also be noted that the walls of microscrolls form a kind of micromirrors for repeated reflection of laser radiation. In our opinion, this may lead to increase of the useful signal. It is also important to note that this effect of increasing the intensity of the bands in the spectrum was achieved using a 532 nm laser, i.e. far from the maximum of plasmon absorption by electrons of Pt(0) nanoparticles, which, as noted, for example, in [26], is at 250–450 nm. In this regard, the proposed substrates for the production of Raman spectra of organic molecules under SERS conditions certainly have great potential for further development. We believe that the creation of nano-composite series based on these samples with other metals, for example with Au and Rh, will make it possible to significantly increase the observed values of the efficiency signal amplification factor. The first experiments on the synthesis of Pt(0) nanocomposites with Rh(0) nanoparticles indicate the possibility of such synthesis.

#### 4. Conclusion

The treatment of chemically polished nickel in a  $\text{H}_2\text{PtCl}_6$  solution with a concentration of 0.005 M for 2 or more minutes leads to the formation of porous Pt(0) nanolayers with a thickness that depends on the treatment time. These nanolayers are formed by Pt(0) nanocrystals 5–10 nm in size, which, on the outer side with respect to the substrate, form arrays of pointed agglomerates directed along the normal to the surface. After drying in air, cracking of the Pt(0) nanolayers and the formation of partially rolled microscrolls on the nickel surface are observed. Their number is the largest for the samples obtained with a longer treatment time. The features of the practical application of these samples as SERS substrates are studied using the Raman spectra of Rodamin 6G as an example. It is shown that the amplification factor is about  $10^5$ – $10^6$  using 532 nm laser excitation.

#### References

- [1] Gong T., Das C.M., Yin M.-J., Lv T.-R., Singh N.M., Soehartono A.M., Singh G., An Q.-F., Yong K.-T. Development of SERS tags for human diseases screening and detection. *Coordination Chemistry Reviews*, 2022, **470**, P. 214711.
- [2] Yin Z., Li Y., Xu J., Qian Z.F., Xiong K. Recent advances of perovskite materials for surface enhanced Raman scattering and their applications. *Materials Today Physics*, 2022, **27**, P. 100815.
- [3] Liu C., Xu D., Dong X., Huang Q. A review: Research progress of SERS-based sensors for agricultural applications. *Trends in Food Science and Technology*, 2022, **128**, P. 90–101.
- [4] Povolotckaia A., Pankin D., Petrov Y., Vasileva A., Kolesnikov I., Sarau G., Christiansen S., Leuchs G., Manshina A. Plasmonic carbon nanohybrids from laser-induced deposition: controlled synthesis and SERS properties. *Journal of Materials Science*, 2019, **54**(11), P. 8177–8186.
- [5] Samodelova M.V., Kapitanova O.O., Evdokimov P.V., Eremina O.E., Goodilin E.A., Veselova I.A. Plasmonic features of free-standing chitosan nanocomposite film with silver and graphene oxide for SERS applications. *Nanotechnology*, 2022, **33**(33), P. 335501.
- [6] Eremina O.E., Sergeeva E.A., Ferree M.V., Shekhovtsova T.N., Goodilin E.A., Veselova I.A. Dual-purpose SERS sensor for selective determination of polycyclic aromatic compounds via electron donor-acceptor traps. *ACS Sensors*, 2021, **6**(3), P. 1057–1066.
- [7] Semenova A.A., Veselova I.A., Brazhe N.A., Shevelkov A.V., Goodilin E.A. Soft chemistry of pure silver as unique plasmonic metal of the Periodic Table of Elements. *Pure and Applied Chemistry*, 2020, **92**(7), P. 1007–1028.
- [8] Eremina O.E., Kapitanova O.O., Goodilin E.A., Veselova I.A. Silver-chitosan nanocomposite as a plasmonic platform for SERS sensing of polycyclic aromatic sulfur heterocycles in oil fuel. *Nanotechnology*, 2020, **31**(22), P. 225503.
- [9] Ye J., Jiang J., Zhao Y.S., Yao J. Nano- and microstructured gold tubes for surface-enhanced Raman scattering by vapor-induced strain of thin films. *Journal of Materials Chemistry A*, 2012, **22**, P. 19202.
- [10] Wang X., Wang Q., Chai Z., Mao G., Liu H., Ren X. Gold nanoparticle-induced diameter reduction and enhanced Raman shift in self-rolled-up InGaAs/GaAs microtubes. *Nanophotonics and Micro/Nano Optics III*, 2016, **10027**, P. 100270N.
- [11] Pal U., Castillo López D. N., Carcaño-Montiel M. G., López-Reyes L., Díaz-Núñez P., Peña-Rodríguez O. Nanoparticle-assembled gold microtubes built on fungi templates for SERS-based molecular sensing. *ACS Applied Nano Materials*, 2019, **2**(4), P. 2533–2541.
- [12] Perales-Rondon J.V., Colina A., González M.C., Escarpa A., Roughened silver microtubes for reproducible and quantitative SERS using a template-assisted electrosynthesis approach. *Applied Materials Today*, 2020, **20**, P. 100710.
- [13] Zhang Y., Han D., Du D. Rolled-up Ag-SiO<sub>x</sub> hyperbolic metamaterials for surface-enhanced Raman scattering. *Plasmonics*, 2015, **10**, P. 949–954.
- [14] Zhang Z., Tian Z., Mei Y., Di Z. Shaping and structuring 2D materials via kirigami and origami. *Materials Science and Engineering: R: Reports*, 2021, **145**, P. 100621.

- [15] Khalisov M.M., Lebedev V.A., Poluboyarinov A.S., Garshev A.V., Khrapova E.K., Krasilin A.A., Ankudinov A.V. Young's modulus of phyllosilicate nanoscrolls measured by the AFM and by the in-situ TEM indentation. *Nanosystems: physics, chemistry, mathematics*, 2021, **12**(1), P. 118–127.
- [16] Levin A., Khrapova E., Kozlov D., Krasilin A., Gusarov V. Structure refinement, microstrains and crystallite sizes of Mg-Ni-phyllosilicate nanoscroll powders. *Journal of Applied Crystallography*, 2022, **55**(3), P. 484–502.
- [17] Krasilin A.A., Gusarov V.V. Energy model of bilayer nanoplate scrolling: Formation of chrysotile nanoscroll. *Russian Journal of General Chemistry*, 2015, **85**, P. 2238–2241.
- [18] Tolstoy V.P., Gulina L.B. New way of As<sub>2</sub>S<sub>3</sub> microtubules preparation by roll up thin films synthesized at the air-solution interface. *Journal of Nano- and Electronic Physics*, 2013, **5**(1), P. 01003.
- [19] Gulina L.B., Tolstoy V.P., Solovov A.A., Gurenko V.E., Huang G., Mei Y. Gas-solution interface technique as a simple method to produce inorganic microtubes with scroll morphology. *Progress in Natural Science: Materials International*, 2020, **30**(3), P. 279–288.
- [20] Kaneva M.V., Tolstoy V.P. The “rolling up” effect of platinum layer obtained on nickel surface by interaction with solution of H<sub>2</sub>PtCl<sub>6</sub> and its electrocatalytic properties in hydrogen evolution reaction during water electrolysis in alkaline medium. *Nanosystems: Physics, Chemistry, Mathematics*, 2021, **12**(5), P. 630–633.
- [21] Yang C.-P., Fang S.-U., Tsai H.-Y., Chen J.-W., Liu Y.-C. Newly prepared surface-enhanced Raman scattering-active substrates for sensing pesticides. *Journal of Electroanalytical Chemistry*, 2020, **861**, P. 113965.
- [22] Navarro-Segura M.E., Rivera-Rangel R.D., Arizmendi-Morquecho A., López I., Alvarez-Quintana J., Sanchez-Dominguez M. Ultra-high Sensitivity Surface-Enhanced Raman Spectroscopy (SERS) Substrates Based on Au Nanostructured Hollow Octahedra. *Applied Materials Today*, 2022, **29**, P. 101598.
- [23] Jiang Z., Li C., Liu Y., Jing Q., Liang A. A sensitive Galvanic replacement reaction-SERS method for Au(III) with Victoria blue B molecular probes in silver nanosol substrate. *Sensors and Actuators, B: Chemical*, 2017, **251**, P. 404–409.
- [24] Kaneva M.V., Reveguk A.A., Tolstoy V.P. SILD-preparation of nanostructured Ru<sub>x</sub><sup>0</sup>-RuO<sub>2</sub>-nH<sub>2</sub>O thin films: Effect of deposition cycles on electrocatalytic properties. *Ceramics International*, 2022, **48**(8), P. 11672–11677.
- [25] Kirubha E., Palanisamy P.K. Green synthesis, characterization of Au–Ag core–shell nanoparticles using gripe water and their applications in nonlinear optics and surface enhanced Raman studies. *Advances in Natural Sciences: Nanoscience and Nanotechnology*, 2014, **5**, P. 045006.
- [26] Bigall N.C., Härtling T., Klose M., Simon P., Eng L.M., Eychemüller A. Monodisperse platinum nanospheres with adjustable diameters from 10 to 100 nm: synthesis and distinct optical properties. *Nano Letters*, 2008, **8**, P. 4588–4592.

---

Submitted 9 September 2022; accepted 12 September 2022

*Information about the authors:*

*Maria V. Kaneva* – Institute of Chemistry, Saint Petersburg State University, 26 University Prosp, St. Peterhof, Saint Petersburg, 198504, Russia; skt94@bk.ru

*Evgen V. Borisov* – Institute of Chemistry, Saint Petersburg State University, 26 University Prosp, St. Peterhof, Saint Petersburg, 198504, Russia; eugene.borisov@spbu.ru

*Valeri P. Tolstoy* – Institute of Chemistry, Saint Petersburg State University, 26 University Prosp, St. Peterhof, Saint Petersburg, 198504, Russia; v.tolstoy@spbu.ru

*Conflict of interest:* the authors declare no conflict of interest.

## Formation, structure, composition in the dispersed state, and behavior of nanoparticles heated in the $\text{Mg}(\text{OH})_2\text{--Ni}(\text{OH})_2$ system

Maria E. Kotova<sup>1,2,a</sup>, Tatiana P. Maslennikova<sup>1,2,b</sup>, Valery L. Ugolkov<sup>1,c</sup>, Victor V. Gusarov<sup>1,2,d</sup>

<sup>1</sup>I. V. Grebenshchikov Institute of Silicate Chemistry of the Russian Academy of Sciences, St. Petersburg, Russia

<sup>2</sup>V. I. Ulyanov St. Petersburg State Electrotechnical University “LETI”, St. Petersburg, Russia

<sup>a</sup>kotovamaria715@gmail.com, <sup>b</sup>maslennikova.tp@iscras.ru,

<sup>c</sup>ugolkov.52@gmail.com, <sup>d</sup>victor.v.gusarov@gmail.com

Corresponding author: Maria E. Kotova, kotovamaria715@gmail.com

**ABSTRACT** The effect of nickel content in  $\text{Mg}_{1-x}\text{Ni}_x(\text{OH})_2$  nanoparticles produced by reverse co-precipitation on their structural characteristics, morphology and size parameters of crystallites and particles has been studied. The plate-shaped nanoparticles were shown to be predominantly single crystals. It has been determined that when the nickel content  $x$  in the hydroxide solid solution is not less than 0.4, the particle size sharply decreases and the number of stacking faults increases. The dependence of the dehydration temperature of  $\text{Mg}_{1-x}\text{Ni}_x(\text{OH})_2$  nanoparticles on the nickel content has been revealed.

**KEYWORDS** magnesium hydroxide, nickel hydroxide, layered double hydroxide, nanoparticles.

**ACKNOWLEDGEMENTS** TEM was done by D. A. Kirilenko (Ioffe Institute) using the equipment of the Federal Collective Use Center “Materials Science and Diagnostics in Advanced Technologies” supported by the Ministry of Education and Science of Russia (Project Unique ID RFMEFI62117X0018).

**FUNDING OF THE WORK** The work was carried out in the framework of the State Assignment to the Institute of Silicate Chemistry of RAS with support from the Ministry of Education and Science of Russia (Topic No 0081-2022-0008).

**FOR CITATION** Kotova M.E., Maslennikova T.P., Ugolkov V.L., Gusarov V.V. Formation, structure, composition in the dispersed state, and behavior of nanoparticles heated in the  $\text{Mg}(\text{OH})_2\text{--Ni}(\text{OH})_2$  system. *Nanosystems: Phys. Chem. Math.*, 2022, **13** (5), 514–524.

### 1. Introduction

The brucite-structured magnesium hydroxide ( $\text{Mg}(\text{OH})_2$ ) is used in many areas of industry: in the production of refractory materials and rubbers, in the manufacture of plastics, ceramics and glass [1]. It is used as a flocculant for waste water purification from organic compounds, and for neutralizing waste acids in technical processes [2]. It was shown in [3,4] that the natural mineral brucite (consisting mainly of  $\text{Mg}(\text{OH})_2$ ) and the synthetic brucite-structured magnesium hydroxide with partial isomorphic substitution exhibit sorption properties with respect to heavy metal ions [5]. Magnesium hydroxide is also used as a filler in pharmaceutical preparations, and as an antacid to neutralize the acidic environment of the stomach [6].

Nanocrystalline  $\text{Mg}(\text{OH})_2$  is usually synthesized either under hydrothermal conditions or by chemical precipitation at atmospheric pressure [7, 8]. As a rule, the properties of magnesium hydroxide nanocrystals strongly depend on the method and conditions of preparation and, as a consequence, on the shape and size of crystallites and particles, and the degree of their agglomeration [9]. In [10–12], plate-shaped  $\text{Mg}(\text{OH})_2$  particles were obtained under a broad variation of synthesis conditions. Magnesium hydroxide nanoparticles, which are thin hexagonal plates, were used in [12, 13] for synthesizing  $\text{Mg}_3\text{Si}_2\text{O}_5(\text{OH})_4$  chrysotile-structured nanoscrolls under hydrothermal conditions.

Nickel hydroxide ( $\text{Ni}(\text{OH})_2$ ) is of interest due to its use in alkaline rechargeable batteries, which have found wide application in power tools, portable electronics, and electric vehicles [14].  $\text{Ni}(\text{OH})_2$  nanoparticles were used as a filler in nanocomposites based on cellulose acetate and polyvinyl alcohol to increase their fire resistance. Nickel hydroxide films can be used in photocatalytic flow reactors [15]. Like magnesium hydroxide, nickel hydroxide was used as one of reagents in the synthesis of layered hydrosilicate nanoscrolls [16].

A large number of works are devoted to the synthesis and study of  $\text{Ni}(\text{OH})_2$  with different morphology, since the electrochemical, electrocatalytic, photocatalytic and other properties of nickel hydroxide and possible areas of its application, including its use as precursor in the synthesis of complex compounds, largely depend on the structure, morphology and size of its particles [17–22].

TABLE 1. Structural parameters of polymorphic modifications of magnesium and nickel hydroxides

Designation	Structure type, space group	Unit cell parameters, Å		Unit cell volume, Å <sup>3</sup>	Density, g/cm <sup>3</sup>	Refs.
		<i>a</i>	<i>c</i>			
Mg(OH) <sub>2</sub>	Brucite-structured, P3 m1 space group	3.148	4.779	41.1	2.36	[25]
α-Ni(OH) <sub>2</sub> · <i>m</i> H <sub>2</sub> O	Theophrastrite-structured (brucite group), P3 m1 space group	3.08	8.0–23.6	65.7–193.9	—	[26–28]
β-Ni(OH) <sub>2</sub>	Theophrastrite-structured (brucite group), P3 m1 space group	3.129	4.611	39.09	4.1	[29]

Two structural modifications of Ni(OH)<sub>2</sub> are known, that is α-Ni(OH)<sub>2</sub> and β-Ni(OH)<sub>2</sub> (Table 1). Single-crystal β-Ni(OH)<sub>2</sub> nanosheets are widely used due to their high stacking density and stability in alkaline media, in contrast to α-Ni(OH)<sub>2</sub>. The α-Ni(OH)<sub>2</sub>-based phase differs from β-Ni(OH)<sub>2</sub> by the presence of water molecules and of acid residue anions in the interplanar space [23]. The unit cell parameter *c* of α-Ni(OH)<sub>2</sub> varies over a very wide range depending on the location and number of water molecules between nickel hydroxide layers [24].

It was asserted in [30] that α-Ni(OH)<sub>2</sub> always forms first during the deposition, but this product chemically ages quickly at high temperatures, loses interlayer water and transforms into β-Ni(OH)<sub>2</sub>. To obtain a pure β-Ni(OH)<sub>2</sub> phase, it is usually necessary to increase the temperature to values close to or above the boiling point of water [28]. The β-Ni(OH)<sub>2</sub> phase is also synthesized under hydrothermal conditions [31]. In [28], β-Ni(OH)<sub>2</sub> was obtained at 170 °C and atmospheric pressure using a very concentrated aqueous solution of NaOH (63–75 wt %).

In addition to the main two phases of nickel hydroxide, there exist several types of structural disorders that were previously attributed to independent phases, and such designations as β<sub>(bc)</sub>-, α\*- and α<sub>am</sub>-Ni(OH)<sub>2</sub> appeared in the literature [17, 32, 33]. Structural defects include a varying number of water molecules in the interlayer spaces of nickel hydroxide, the inclusion of foreign ions in the nickel hydroxide-based phase, and other crystalline defects. Structural disorder can largely affect properties of a substance, including their electrochemical activity. However, it is difficult to determine precisely the relationship between structural disorder and material properties. The data presented in [34] prove that the change in the electrochemical activity of α-Ni(OH)<sub>2</sub> and β-Ni(OH)<sub>2</sub> samples is associated not with the presence of intermediate phases, but with a different type of structural disorder. Raman and IR spectroscopy have shown that the presence of additional O–H modes in the Raman and IR spectra is associated with stacking faults and directly affects the broadening of X-ray diffraction peaks along the *c*-axis [34], while other factors associated with the inclusion of foreign ions, hydration and the decrease in the crystallite size are reflected in the entire diffraction pattern and lead to the broadening of all peaks. Stacking faults are explained by a strong ionic bond between Ni<sup>2+</sup>, O<sup>2-</sup> and H<sup>+</sup> ions inside each layer of nickel hydroxide, while the interaction between adjacent layers is weak. This can cause a shift and a change in relative position of the layers. Rotational displacement in the form of pivot relative to the *c*-axis, shear displacement of crystallographic planes perpendicular to the *c*-axis, and also shear displacement together with rotation are possible. Errors in stacking of layers associated with the listed displacements of layers relative to the *c*-axis cause selective broadening of peaks in X-ray diffraction patterns [35, 36]. The use of computer simulation in [37, 38] has shown the relationship between the width and intensity of peaks in β-Ni(OH)<sub>2</sub> diffraction patterns and the frequency of stacking faults. It is practically impossible to predict and model the orientation of α-Ni(OH)<sub>2</sub> layers, since the layers are arranged almost randomly [26].

As mentioned earlier, the composition and structure of synthesized hydroxides are affected to a significant extent by the methods and conditions for producing them. During the joint precipitation of salts containing, in particular, Mg<sup>2+</sup> and Ni<sup>2+</sup> cations, there can be formed layered double hydroxides with the Mg<sub>1-x</sub>Ni<sub>x</sub>(OH)<sub>2</sub> · *m*H<sub>2</sub>O variable composition, which contain *m* water molecules in the interlayer space of one formula unit of the compound. Depending on the co-precipitation conditions and the Mg:Ni ratio, hydroxides with different structures can potentially be formed. When the composition and structure of hydroxides change, their physical and chemical properties also change. In this regard, it is important to have information about the effect of synthesis conditions on the structure, crystallite size parameters, morphology, and particle sizes of magnesium-nickel hydroxides.

## 2. Experiment

Hydroxides with the  $\text{Mg}_{1-x}\text{Ni}_x(\text{OH})_2$  composition were obtained by reverse co-precipitation. Magnesium chloride hexahydrate ( $\text{MgCl}_2 \cdot 6\text{H}_2\text{O}$  (pur.)) was dissolved in distilled water together with nickel chloride hexahydrate ( $\text{NiCl}_2 \cdot 6\text{H}_2\text{O}$  (pur.)). A solution of metal salts was added dropwise to the precipitant, an aqueous solution of sodium hydroxide ( $\text{NaOH}$  (pur.)), with constant stirring with a magnetic stirrer. The reactions were carried out in 5 wt. % excess of sodium hydroxide relative to the reaction stoichiometry to ensure complete precipitation of hydroxides. The reacting mixtures were stirred for one hour. The precipitate was separated by decantation from the mother liquor containing sodium and chlorine ions. Hydroxides precipitates were rinsed with distilled water until a negative reaction to  $\text{Cl}^-$  ions was obtained. After that, the hydroxides were dried at 100 °C. Subsequently, the elemental, phase, and dispersion compositions were determined for each sample series.

The elemental composition of the samples was determined by the energy dispersive X-ray spectroscopy using an EDX attachment to a TESCAN VEGA 3 SBH scanning electron microscope (SEM).

The phase composition of hydroxide samples was determined from the XRD data obtained using a Rigaku SmartLab 3 diffractometer (Cu  $K_\alpha$ , Ni filter). Peaks in the diffraction pattern were identified using the PDWin4.0 software package with a powder diffraction database based on the PDF2 file. The crystallite size was calculated from the broadening of XRD lines using the Scherrer formula.

To determine the particle size of the obtained hydroxides, an electron microscopic study was carried out using a JEM-2100F transmission electron microscope (TEM).

The specific surface area of the samples was determined with a Sorbi-M sorbtometer using the low-temperature nitrogen adsorption method. The Sorbi-M meter allows the determination of the specific surface area of dispersed materials using the four-point BET method.

Spectra for each of the studied samples were obtained in the 450–4000  $\text{cm}^{-1}$  range by IR spectroscopy using an IR-Fourier spectrometer FSM-1201.

The total water content in the samples  $\text{Mg}_{1-x}\text{Ni}_x(\text{OH})_2 \cdot m\text{H}_2\text{O}$  was determined from thermal analysis data. Water adsorbed on the particles surface was removed at a temperature not exceeding 200 °C and sample heating rate of 20 °C/min. This water was excluded from the total water content. Thus, only interlayer water and water in the form of hydroxyl groups were recorded in the samples. Thermal decomposition of hydroxides was studied by means of complex thermal analysis on a NETZSCH STA 429 CD analyzer coupled with a QMS 403 C quadrupole mass spectrometer. Thermogravimetric analysis and differential thermal analysis were carried out in the 40–1000 °C range at 6 °C/min heating rate in an air flow of 40  $\text{cm}^3/\text{min}$ . The analyzed hydroxide sample weight was 22 to 23 mg.

## 3. Results and discussion

### 3.1. Elemental analysis

An analysis of the samples elemental composition showed the absence of sodium and chlorine impurities, as well as of other elements that are not listed in the chemical formula of  $\text{Mg}_{1-x}\text{Ni}_x(\text{OH})_2$  hydroxides. The elemental analysis of the composition performed by the energy dispersive X-ray spectroscopy showed a slight excess of the nickel content in the samples compared to their nominal composition (Table 2). It should be noted that further on, all the composition dependences employed the experimentally obtained data on the composition of samples, and the designation of samples themselves was based on their nominal composition.

### 3.2. X-ray diffractometry (X-ray analysis)

X-ray diffraction data show that all samples with the  $\text{Mg}_{1-x}\text{Ni}_x(\text{OH})_2$  composition are single-phase ones (Fig. 1) and can be considered as constituting a continuous series of solid solutions. With an increasing Ni content in the samples, all peaks broaden, which may evidence a decrease in the crystallite size (Fig. 1, Fig. 2, Table 3). The peaks associated with the crystallographic  $c$ -axis have the most significant broadening (Fig. 1). This may be due not only to a decrease in the crystallite size along the  $c$ -axis in comparison with the sizes along other directions, but also to the appearance of layer stacking faults in the  $\text{Mg}_{1-x}\text{Ni}_x(\text{OH})_2$  structure with an increase in the content of  $\text{Ni}^{2+}$  ions caused by the localization of water in the interlayer space, the possibility of which was pointed out in [34]. For example, the peaks of reflections 100 and 110 are noticeably narrower than those of the reflection 001, which, in accordance with the conclusions from [26, 34], indicates a greater structural ordering of the nickel hydroxide layers in crystallographic planes perpendicular to the  $c$ -axis than those along the  $c$ -axis.

The Rietveld method was applied to the XRD data to calculate parameters of the hydroxide unit cell, which belongs to the hexagonal crystal system, P3 m1 space group (Table 2).

Figure 2 presents dependences of  $a$  and  $c$  parameters on the nickel content in  $\text{Mg}_{1-x}\text{Ni}_x(\text{OH})_2$ , which show that while the  $a$  parameter is well described by the Vegard's law ( $a = 3.1432 - 0.0189x$  ( $R^2 = 0.9887$ )), there is a positive deviation for the  $c(x)$  dependence from the Vegard's law ( $c = 4.7723 - 0.0314x - 0.1159x^2$  ( $R^2 = 0.9756$ )). The deviation of the  $c$  parameter from the Vegard's law is apparently associated with the appearance of stacking faults in the

TABLE 2. Data on the studied  $Mg_{1-x}Ni_x(OH)_2$  hydroxide samples

Sample*	Sample nominal composition	Hydroxide EDX-derived formula**	Unit cell parameters			X-ray density $\rho$ , g/cm <sup>3</sup>
			$a$ , Å	$c$ , Å	$V$ , Å <sup>3</sup>	
0.0	Mg(OH) <sub>2</sub>	Mg(OH) <sub>2</sub>	3.14 ± 0.22	4.77 ± 0.19	40.85	2.37
0.1	Mg <sub>0.9</sub> Ni <sub>0.1</sub> (OH) <sub>2</sub>	Mg <sub>0.84</sub> Ni <sub>0.16</sub> (OH) <sub>2</sub>	3.14 ± 0.16	4.77 ± 0.14	40.74	2.60
0.2	Mg <sub>0.8</sub> Ni <sub>0.2</sub> (OH) <sub>2</sub>	Mg <sub>0.69</sub> Ni <sub>0.31</sub> (OH) <sub>2</sub>	3.14 ± 0.06	4.75 ± 0.24	40.45	2.83
0.3	Mg <sub>0.7</sub> Ni <sub>0.3</sub> (OH) <sub>2</sub>	Mg <sub>0.59</sub> Ni <sub>0.41</sub> (OH) <sub>2</sub>	3.14 ± 0.09	4.73 ± 0.19	40.27	2.99
0.4	Mg <sub>0.6</sub> Ni <sub>0.4</sub> (OH) <sub>2</sub>	Mg <sub>0.48</sub> Ni <sub>0.52</sub> (OH) <sub>2</sub>	3.13 ± 0.19	4.73 ± 0.10	40.20	3.15
0.5	Mg <sub>0.5</sub> Ni <sub>0.5</sub> (OH) <sub>2</sub>	Mg <sub>0.39</sub> Ni <sub>0.61</sub> (OH) <sub>2</sub>	3.13 ± 0.13	4.71 ± 0.09	39.96	3.30
0.6	Mg <sub>0.4</sub> Ni <sub>0.6</sub> (OH) <sub>2</sub>	Mg <sub>0.29</sub> Ni <sub>0.71</sub> (OH) <sub>2</sub>	3.13 ± 0.22	4.70 ± 0.14	39.86	3.45
0.7	Mg <sub>0.3</sub> Ni <sub>0.7</sub> (OH) <sub>2</sub>	Mg <sub>0.20</sub> Ni <sub>0.80</sub> (OH) <sub>2</sub>	3.13 ± 0.22	4.67 ± 0.14	39.54	3.61
0.8	Mg <sub>0.2</sub> Ni <sub>0.8</sub> (OH) <sub>2</sub>	Mg <sub>0.13</sub> Ni <sub>0.87</sub> (OH) <sub>2</sub>	3.13 ± 0.13	4.67 ± 0.14	39.57	3.70
0.9	Mg <sub>0.1</sub> Ni <sub>0.9</sub> (OH) <sub>2</sub>	Mg <sub>0.06</sub> Ni <sub>0.94</sub> (OH) <sub>2</sub>	3.13 ± 0.13	4.64 ± 0.19	39.27	3.83
1.0	Ni(OH) <sub>2</sub>	Ni(OH) <sub>2</sub>	3.12 ± 0.06	4.62 ± 0.14	39.01	3.95

\*from here on, the samples are designated in accordance with the nominal mole fraction of nickel hydroxide in the formula unit;

\*\*elemental composition determination error does not exceed 2.5 percent %

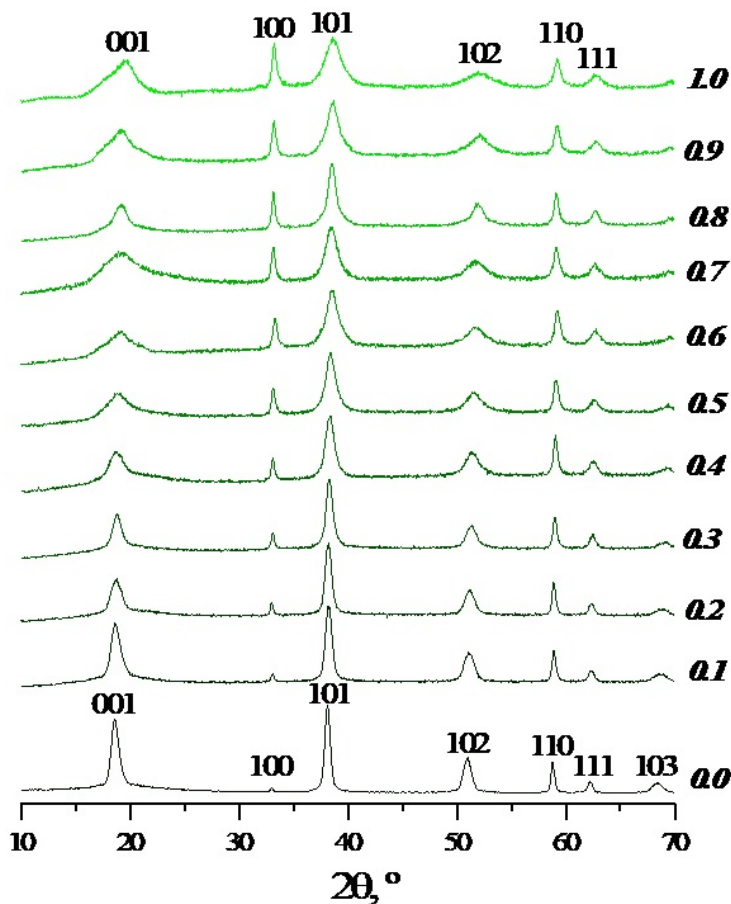


FIG. 1. XRD patterns of  $Mg_{1-x}Ni_x(OH)_2$  samples, (according to JCPDC card Nos. 44-1482 (brucite –  $Mg(OH)_2$ ), 14-117(theophrastite –  $Ni(OH)_2$ ))

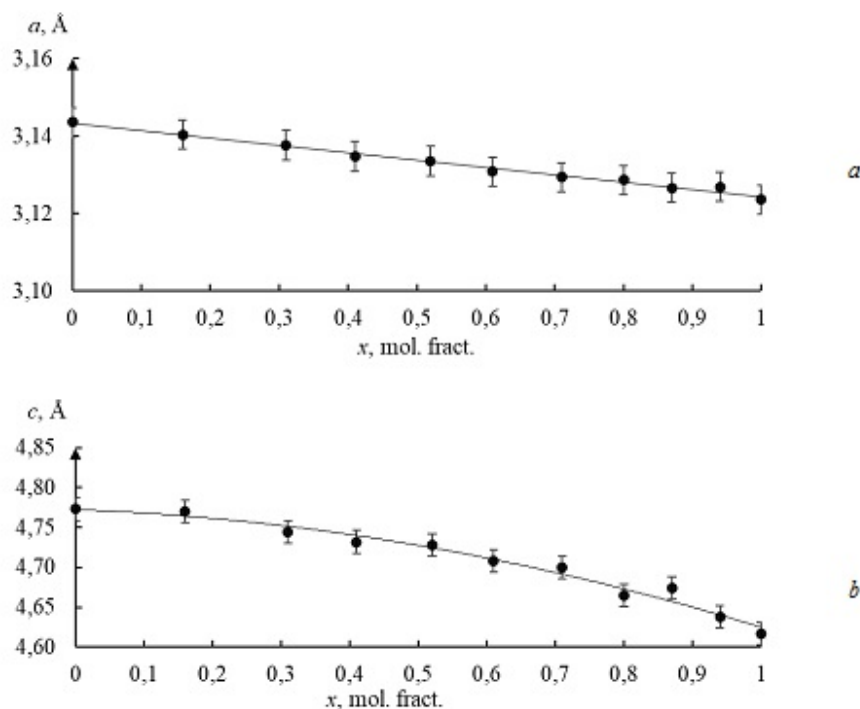


FIG. 2. Dependence of unit cell parameters on the nickel content in  $\text{Mg}_{1-x}\text{Ni}_x(\text{OH})_2$ : a)  $a(x)$  parameter, b)  $c(x)$  parameter

brucite-like structure and an increase in the amount of water in the interlayer spaces along with an increase in the nickel hydroxide content in the  $\text{Mg}_{1-x}\text{Ni}_x(\text{OH})_2$  solid solution, which can be assumed on the basis of the data from [26, 34].

The average thickness ( $h_{cr}$ ) and width ( $D_{cr}$ ) of crystallites were calculated from X-ray reflections 001 and 110 (Table 3). The crystallite thickness was not calculated for samples with a nominal value of  $x \geq 0.4$  due to the impossibility of separating the contributions of the reflection 001 to the broadening, which are associated with the size of crystallites along the  $c$ -axis and stacking faults.

An analysis of the crystallite size data shows that the crystallite thickness ( $h_{cr}$ ) for all the considered samples is about 8 nm on an average, and the width ( $D_{cr}$ ) is about 53 nm.

### 3.3. Electron microscopic examination

An analysis of the particle morphology of the samples has shown that they are thin plates several nm thick (Fig. 3). In plan view, lamellar nanoparticles have a rounded or hexagonal shape. It should be noted that it can be concluded from the analysis of TEM data that lamellar magnesium hydroxide nanoparticles aggregate in the form of stacks of plates in some cases (for example, such formation is noted in Fig. 3a). Such aggregation was not observed in TEM images of nickel-containing hydroxides. The size parameters of the particles presented as histograms indicate that the particle thickness varies mainly in the region of units of nm (Fig. 1e,f,g,h and Fig. 2d,e,f), and their width varies in the region of tens of nm (Fig. 1a,b,c,d and Fig. 2a,b,c). The histograms of particles distribution in terms of their thickness and width were described assuming that the lognormal distribution law is satisfied.

It follows from the data given in Table 3 that a clearly noticeable decrease in the thickness of particles is observed with an increase in the content of nickel hydroxide in samples with the  $\text{Mg}_{1-x}\text{Ni}_x(\text{OH})_2$  composition starting from samples with a nominal value of  $x$  greater than 0.5 (Table 3). The particle thickness correlates with the crystallite size along the  $c$ -axis. The particle width within the error also corresponds to the crystallite sizes (Table 3). The closeness of crystallites and particles size parameters allows making a conclusion that the particles are, apparently, mainly single-crystal.

The nanoparticles specific surface area  $S_{calc}$  ( $\text{m}^2/\text{g}$ ) calculated assuming that the particles are flat disks with thickness  $h$  and diameter  $D$  (Table 3, Fig. 1, Fig. 2), and their density  $\rho(x)$  taken from Table 2, are given in Table 4.

### 3.4. Samples specific surface area determined from the low-temperature nitrogen adsorption data

Table 4 contains the values of the specific surface area  $S_{exp}$  ( $\text{m}^2/\text{g}$ ) of  $\text{Mg}_{1-x}\text{Ni}_x(\text{OH})_2$  solid solution samples preheated at 200 °C for 30 minutes to remove the adsorbed water.

The systematically lower values of the experimentally determined samples specific surface area compared to the values calculated on the basis of the nanoparticles size and density data ( $S_{calc}$  in Table 4), can apparently be explained by the formation of nanoparticle agglomerates (see, e.g., Fig. 3a is the selected area), which covers part of the particle surface

TABLE 3. Dimensional parameters of crystallites and particles of  $Mg_{1-x}Ni_x(OH)_2$  samples

Sample	Crystallite average sizes, nm		Weighted average of plate dimensions **, nm	
	$h_{cr}$	$D_{cr}$	thickness, $h$	width, $D$
0.0	11	52	$7.0 \pm 1.0$	$55 \pm 9$
0.1	8	56	–	–
0.2	7	55	$7.7 \pm 1.6$	$61 \pm 15$
0.3	8	56	–	–
0.4	–	54	–	–
0.5	–	55	$4.2 \pm 1.3$	$47 \pm 24$
0.6	–	54	$4.3 \pm 1.1$	$49 \pm 16$
0.7	–	52	$4.0 \pm 1.1$	$46 \pm 16$
0.8	–	53	–	–
0.9	–	51	$4.9 \pm 1.2$	$45 \pm 13$
1.0	–	47	$4.7 \pm 1.0$	$49 \pm 16$

\*weighted averages are given with standard deviations data. Calculated using particle size distribution histograms

TABLE 4. Samples specific surface area

Sample	Composition	$S_{exp}$ (m <sup>2</sup> /g)	$S_{calc}$ (m <sup>2</sup> /g)
0.0	Mg(OH) <sub>2</sub>	$78 \pm 8$	151
0.1	Mg <sub>0.84</sub> Ni <sub>0.16</sub> (OH) <sub>2</sub>	$89 \pm 9$	–
0.2	Mg <sub>0.69</sub> Ni <sub>0.31</sub> (OH) <sub>2</sub>	$111 \pm 14$	115
0.3	Mg <sub>0.59</sub> Ni <sub>0.41</sub> (OH) <sub>2</sub>	$134 \pm 16$	–
0.4	Mg <sub>0.48</sub> Ni <sub>0.52</sub> (OH) <sub>2</sub>	$132 \pm 15$	–
0.5	Mg <sub>0.39</sub> Ni <sub>0.61</sub> (OH) <sub>2</sub>	$129 \pm 13$	170
0.6	Mg <sub>0.29</sub> Ni <sub>0.71</sub> (OH) <sub>2</sub>	$131 \pm 13$	159
0.7	Mg <sub>0.2</sub> Ni <sub>0.8</sub> (OH) <sub>2</sub>	$117 \pm 9$	161
0.8	Mg <sub>0.13</sub> Ni <sub>0.87</sub> (OH) <sub>2</sub>	$103.6 \pm 12$	–
0.9	Mg <sub>0.06</sub> Ni <sub>0.94</sub> (OH) <sub>2</sub>	$99 \pm 11$	130
1.0	Ni(OH) <sub>2</sub>	$124 \pm 13$	128

for nitrogen adsorption. Despite some differences in the values of the samples specific surface area obtained by different methods, there remains a general trend, which reflects a decrease in the particle size with an increase in the nickel content.

### 3.5. IR spectroscopy

The IR spectra of samples with the  $Mg_{1-x}Ni_x(OH)_2$  composition were found to contain bands characteristic of brucite. The difference in the IR spectra of samples with the  $Mg_{1-x}Ni_x(OH)_2$  composition in the 300 to 700 cm<sup>-1</sup> range is described in [39]. At  $\nu \sim 1030$  cm<sup>-1</sup>, the band corresponds to the E<sub>u</sub> mode (Fig. 3). The broad peak in the 1400–1450 cm<sup>-1</sup> range observed for all samples belongs to the combination of the E<sub>g</sub> and A<sub>2u</sub> modes [34]. A low intensity peak at  $\sim 1630 - 1645$  cm<sup>-1</sup> observed for all samples originates due to the O–H vibration mode of a free water molecule, which is adsorbed on the material. For samples with x greater than 0.4, there appears a  $\sim 1700$  cm<sup>-1</sup> band, which, apparently, can be related to vibrations of water molecules intercalated between hydroxide layers.

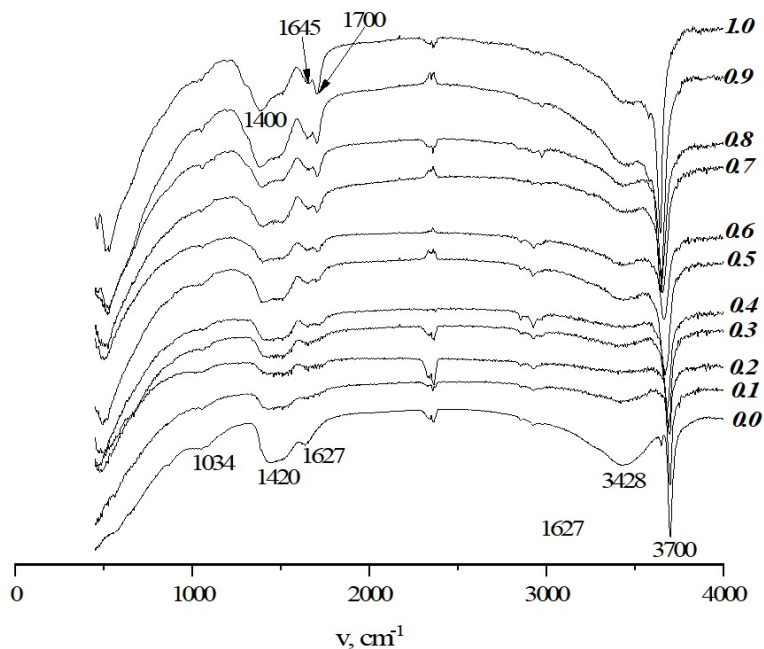


FIG. 3. IR spectra of  $\text{Mg}_{1-x}\text{Ni}_x(\text{OH})_2$  solid solution samples

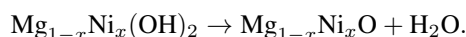
The intensity of the absorption band in the range of stretching vibrations (at  $3428\text{ cm}^{-1}$  for the sample 0.0) decreases along with the increasing amount of nickel in hydroxides. A sharp intense peak, related to the stretching vibrations of the OH group, is visible in all samples (at  $3700\text{ cm}^{-1}$  for the sample 0.0) and gradually shifts with the increasing nickel hydroxide content in the sample ( $3637\text{ cm}^{-1}$  for 1.0) (Fig. 3). This may be due to the fact that hydroxide samples contain  $\text{Mg}^{2+}$  and  $\text{Ni}^{2+}$  ions, which differ in electronegativity (for magnesium, the electronegativity is 1.28, and 1.98 for nickel, [40]), which changes the OH bond polarization [39].

### 3.6. Thermal analysis

DSC and TGA curves were plotted from the TGA data for hydroxide samples. Since the shape of the curves for all samples is similar, the results will be presented below in graphical form only for the several samples: 0.0, 0.3, 0.5, 1.0 (Fig. 4).

An analysis of the simultaneous thermal analysis data shows that an increase in temperature is accompanied by mass loss and endothermic effects in all samples. Depending on the increase in the amount of nickel in the samples, the most pronounced endothermic effect (DSC curve maximum) shifts to the region of lower temperatures (Table 5 shows the temperatures at the beginning of the effect ( $T_s$ ), its maximum ( $T_{max}$ ), and the total weight loss of the samples ( $\Delta m$ ).

The XRD data show that after heat treatment of samples under conditions of simultaneous thermal analysis up to  $1000\text{ }^\circ\text{C}$ , all samples are represented by nanocrystalline rock salt-structured particles with the  $\text{Mg}_{1-x}\text{Ni}_x\text{O}$  composition and crystallite sizes varying in the  $\sim 15\text{--}40\text{ nm}$  range (Fig. 6, Table 6). Thus, the endothermic effect can be associated with the dehydration reaction:



The rest of the water released from the samples was apparently adsorbed on the surface of the particles or was in the interlayer spaces. The dependence of the proportion of such water,  $n(\text{Mg}_{1-x}\text{Ni}_x(\text{OH})_2 + n\text{H}_2\text{O})$ , on the samples composition is shown in Fig. 5. The obtained data do not allow the identification of any trend in the  $n(x)$  dependence. This is apparently due to the high sensitivity of the water content on the surface and in the interlayer spaces of hydroxides to external conditions.

A comparison of the sizes of crystallites and particles of magnesium and nickel hydroxide solid solutions with the sizes of  $\text{Mg}_{1-x}\text{Ni}_x\text{O}$  crystallites formed by heat treatment with a linear increase in temperature up to  $1000\text{ }^\circ\text{C}$  shows not only a change in shape from lamellar to that close to isometric, but also a noticeable increase in the volume of oxide crystallites compared to the original hydroxides. This situation is completely different from the case of short-term heat treatment at  $1000\text{ }^\circ\text{C}$  of  $\text{Mg}(\text{OH})_2$  nanoplates described in [9], in which MgO nanoparticles were forming with crystallite sizes comparable with the thickness of  $\text{Mg}(\text{OH})_2$  nanoparticles. Apparently, the considered conditions ensure the intergrowth of  $\text{Mg}_{1-x}\text{Ni}_x\text{O}$  crystallites that formed during the dehydration of the corresponding hydroxides. Moreover, agglomerates of polycrystalline plates (which formed during the hydroxides dehydration) rather than individual plates [9] have most likely served as the initial material for the formation of oxide nanocrystals. This conclusion is supported by the fact that the volume of  $\text{Mg}_{1-x}\text{Ni}_x\text{O}$  crystallites is comparable with the volume that oxide particles may

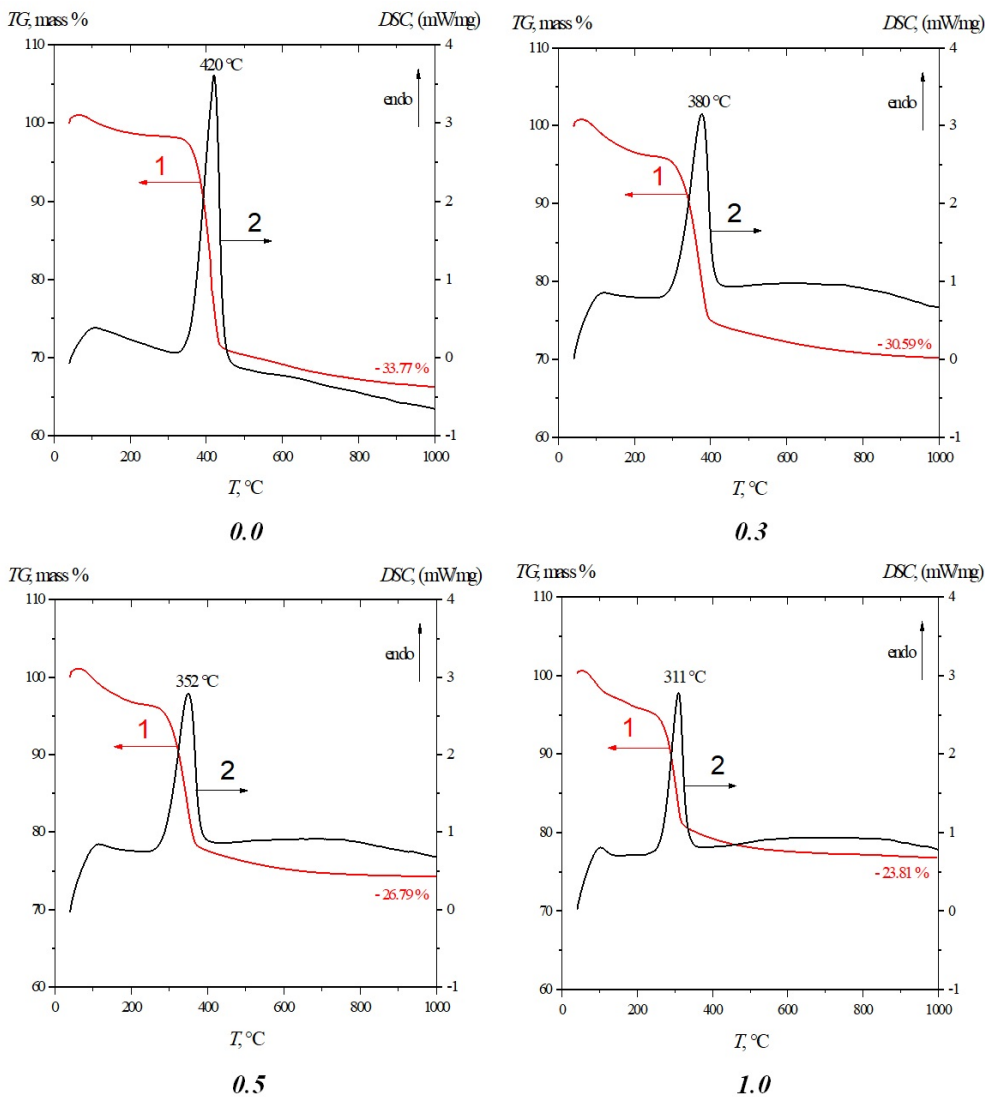


FIG. 4. TGA (1) and DSC (2) curves for the samples: 0.0, 0.3, 0.5, 1.0  
 TABLE 5. Results of simultaneous thermal analysis of hydroxide samples

Sample	$T_s$ , $^{\circ}\text{C}$	$T_{max}$ , $^{\circ}\text{C}$	$\Delta m$ , wt. %
0.0	324	420	33.77
0.1	290	413	29.83
0.2	245	390	28.55
0.3	228	380	30.59
0.4	245	365	30.68
0.5	227	352	26.79
0.6	230	343	26.94
0.7	228	330	27.61
0.8	212	317	26.62
0.9	229	316	21.89
1.0	221	311	23.81

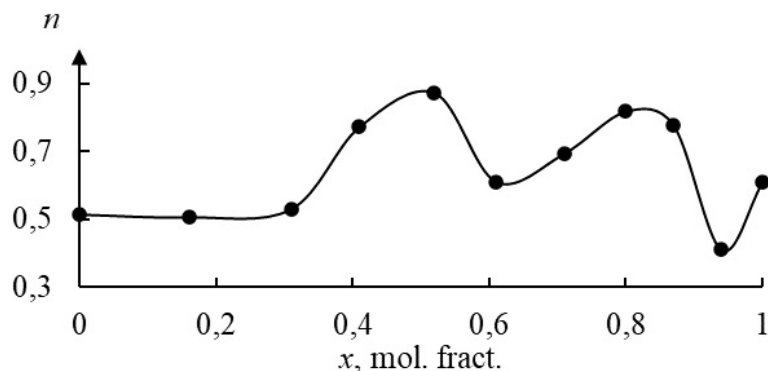


FIG. 5. Dependence of the number of water molecules on the amount of nickel in samples of  $Mg_{1-x}Ni_x(OH)_2$ -based solid solutions

have if they were formed from agglomerated hydroxide nanoplates (Fig. 3a – selected fragment) with a specific surface area  $S_{exp}$  (Table 4).

In this case, the formation of such oxide crystallites most probably follows the mechanism of coherent-accommodative intergrowth of small oxide clusters [41, 42].

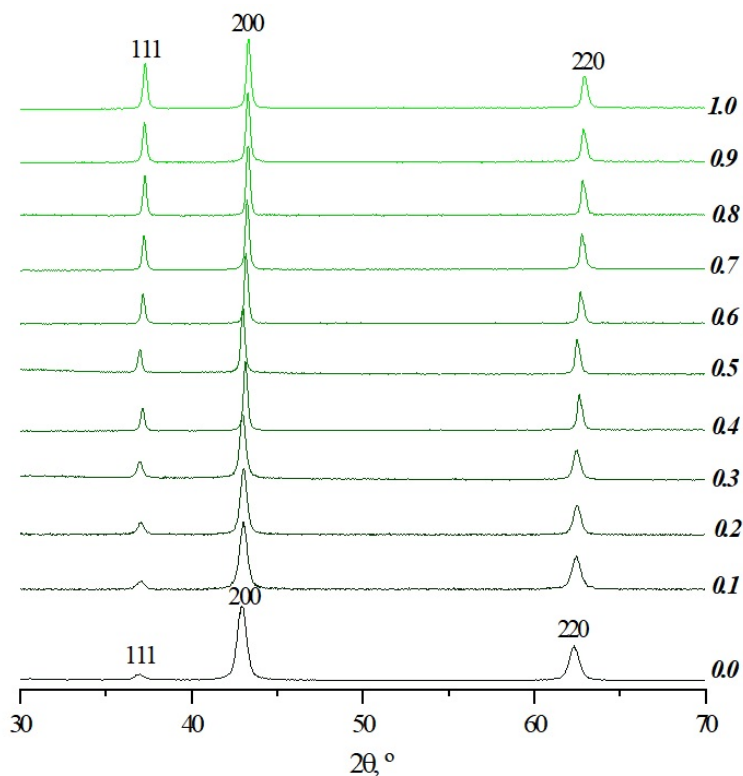


FIG. 6. XRD patterns of the initial samples 0.0 – 1.0 heated up to 1000 °C (according to JCPDC card Nos. 45-946 (periclase – MgO), 47-1049 (bunsenite – NiO))

#### 4. Conclusion

The performed study has shown that the formation of nanoparticles of  $Mg_{1-x}Ni_x(OH)_2$  hydroxides in the range of  $x$  not less than 0.4 goes with the formation of nanocrystals with a high proportion of stacking faults, which manifests itself, in particular, in the nature of the change in the broadening of XRD pattern lines with an increase in the nickel content in the solid solution. It has been revealed that the hydroxide nanoplates agglomeration affects the size of  $Mg_{1-x}Ni_xO$  crystallites that form during their dehydration. The effect of nickel content in the magnesium-nickel hydroxide on the size, morphology, and dehydration temperature of  $Mg_{1-x}Ni_x(OH)_2$  nanoparticles has been determined.

TABLE 6. Dimensional parameters of sample crystallites heated up to 1000 °C

Sample	Crystallite average sizes, nm	
	$D_{cr}$ (reflection 111)	$D_{cr}$ (reflection 001)
0.0	23	15
0.1	21	19
0.2	23	20
0.3	26	23
0.4	36	34
0.5	39	33
0.6	38	35
0.7	38	41
0.8	41	38
0.9	39	38
1.0	38	31

## References

- [1] Koverzanova E.V., Usachev S.V., Shilkina N.G., Lomakin S.M., Gumargalieva K.Z., Zaikov G.E. Specific features of thermal degradation of polypropylene in the presence of magnesium hydroxide. *Russian Journal of Applied Chemistry*, 2004, **77**(3), P. 445–448. <https://doi.org/10.1023/B:RJAC.0000031288.62488.04>
- [2] Saoud Kh.M., Saeed Sh., Al-Soubaihi R.M., Bertino M.F. Microwave assisted preparation of magnesium hydroxide nano-sheets. *American Journal of Nanomaterials*, 2014, **2**(2), P. 21–25.
- [3] Korolev V.A., Samarin E.N., Panfilov V.A., Romanova I.V. Sorption properties of brucite and brucite-based clay mixtures. *Ecology and Industry of Russia*, 2016, **20**(1), P. 18–24. (In Russ.)
- [4] Marchenko L.A., Marchenko L.A. Influence in common-besieged hydroxides on sorption ions of heavy metals. *Russian Journal of Sorption and chromatography processes*, 2009, **9**(6), P. 868–876.
- [5] Chanda D.K., Mukherjee D., Das P.S., Ghosh C. Toxic heavy metal ion adsorption kinetics of Mg(OH)<sub>2</sub> nanostructures with superb efficacies. *Materials Research Express*, 2018, **5**(7), P. 1–23.
- [6] Kang J., Schwendeman S.P. Comparison of the effects of Mg(OH)<sub>2</sub> and sucrose on the stability of bovine serum albumin encapsulated in injectable poly(D,L-lactide-co-glycolide) implants. *Biomaterials*, 2002, **23**, P. 239.
- [7] Henrist C., Mathieu J.-P., et al. Morphological study of magnesium hydroxide nanoparticles precipitated in dilute aqueous solution. *J. Cryst. Growth*, 2003, **249**, P. 321.
- [8] Matsukevich I.V., Ruchets A.N., Krutko N.P., et al. Synthesis and adsorption properties of nanostructured powders Mg(OH)<sub>2</sub> and MgO. *Proceedings of the National Academy of Sciences of Belarus, Chemical series*, 2017, **53**(4), P. 38–44.
- [9] Maslennikova T.P., Kotova M.E., Lomakin M.S., et al. Role of mixing reagent solutions in the formation of morphological features of nanocrystalline particles of magnesium hydroxide and oxide. *Russ. J. Inorg. Chem.*, 2022, **67**, P. 810–819.
- [10] Chen Y., Zhou T., Fang H., et al. A novel preparation of nano-sized hexagonal Mg(OH)<sub>2</sub>. *Procedia Engineering*, 2015, **102**, P. 388–394.
- [11] Kovalenko V.L., Kotok V.A., Malyshev V.V. Electrochemical obtaining of nickel hydroxide from nickel plating waste water for application in the alkali secondary cells. *Theoretical and applied ecology*, 2019, **2**, P. 108–112.
- [12] Maslennikova T.P., Gatina E.N., Kotova M.E., Ugol'kov V.L., Abiev R.Sh., Gusarov V.V. Formation of chrysotile-structured hydrous magnesium silicate nanoscrolls from nanocrystalline magnesium hydroxide and their thermally stimulated transformation. *Inorganic Materials*, 2022, In press. (In Russ.)
- [13] Bloise A., Barrese E., Apollaro C. Hydrothermal alteration of Ti-doped forsterite to chrysotile and characterization of the resulting chrysotile fibers. *Neues Jahrbuch für Mineralogie*, 2009, **185**, P. 297–304.
- [14] Yousefi S.R., Ghanbari D., Salavati-Niasari M. Hydrothermal synthesis of nickel hydroxide nanostructures and flame retardant poly vinyl alcohol and cellulose acetate nanocomposites. *Journal of Nanostructures*, 2016, **6**(1), P. 80–85.
- [15] E.V. Polyakov, R.R. Tsukanov, L.Yu. Buldakova, Yu.V. Kuznetsova, I.V. Volkov, V.P. Zhukov, M.A. Maksimova, A.V. Dmitriev, I.V. Baklanova, O.A. Lipina, A.P. Tyutyunnik Chemical bath precipitation and properties of  $\beta$ -Ni(OH)<sub>2</sub> films prepared in aqueous ammoniac solutions. *Russ. J. Inorg. Chem.*, 2022, **67**(6), P. 912–920.
- [16] Korytkova E.N., Pivovarova L.N., Drozdova I.A., Gusarov V.V. Synthesis of nanotubular nickel hydrosilicates and nickel-magnesium hydrosilicates under hydrothermal conditions. *Glass Physics and Chemistry*, 2005, **31**(6), P. 797–802.
- [17] Oliva P., Leonardi J., Laurent J.F., Delmas C., Braconnier J.J., Figlarz M., Fievet F., de Guibert A. Review of the structure and the electrochemistry of nickel hydroxides and oxy-hydroxides. *J. Power Sources.*, 1982, **8**, P. 229–255.
- [18] Yan Z., Yu X., Zhang Y., Jia H., Sun Z., Du P. Enhanced visible light-driven hydrogen production from water by a noble-metal-free system containing organic dye-sensitized titanium dioxide loaded with nickel hydroxide as the cocatalyst. *Applied Catalysis B: Environmental*, 2014, **160–161**, P. 173–178.
- [19] Vidotti M., Torresi R., De Torresi S.I.C. Nickel hydroxide modified electrodes: a review study concerning its structural and electrochemical properties aiming the application in electrocatalysis, electrochromism and secondary batteries. *Quim. Nova*, 2010, **33**, P. 2176–2186.

- [20] Aghazadeh M., Ghaemi M., Sabour B., Dalvand S. Electrochemical preparation of  $\alpha$ -Ni(OH)<sub>2</sub> ultrafine nanoparticles for high-performance supercapacitors. *J. Solid State Electrochem.*, 2014, **18**, P. 1569–1584.
- [21] Gao M., Sheng W., Zhuang Z., Fang Q., Gu S., Jiang J., Yan Y. Efficient water oxidation using nanostructured  $\alpha$ -nickel-hydroxide as an electrocatalyst. *J. Am. Chem. Soc.*, 2014, **136**, P. 7077–7084.
- [22] Cheng H., Su A.D., Li S., Nguyen S.T., Lu L., Lim C.Y.H., Duong H.M. Facile synthesis and advanced performance of Ni(OH)<sub>2</sub>/CNTs nanoflake composites on supercapacitor applications. *Chem. Phys. Lett.*, 2014, **601**, P. 168–173.
- [23] Bode H., Dehmelt K., Witte J. Zur Kenntnis der Nickelhydroxidelektrode—I. Über das Nickel (II)-Hydroxidhydrat. *Electrochim. Acta*, 1966, **11**, P. 1079–1087.
- [24] McEwen R.S. Crystallographic studies on nickel hydroxide and the higher nickel oxides. *J. Phys. Chem.*, 1971, **75**, P. 1782–1789.
- [25] Desgranges L., Calvarin G., Chevrier G. Interlayer interactions in Mg(OH)<sub>2</sub>: A Neutron Diffraction Study of Mg(OH)<sub>2</sub>. *Acta Cryst.*, 1996, **B52**, P. 82–86.
- [26] Hall D.S., Lockwood D.J., Bock C., MacDougall B.R. Nickel hydroxides and related materials: a review of their structures, synthesis and properties. *Proceedings of the Royal Society A: Mathematical, Physical and Engineering Sciences*, 2014, **471** (2174), P. 20140792–20140792.
- [27] Rall J.D., Seehra M.S., Shah N., Huffman G.P. Comparison of the nature of magnetism in  $\alpha$ -Ni(OH)<sub>2</sub> and  $\beta$ -Ni(OH)<sub>2</sub>. *J. Appl. Phys.*, 2010, **107**(9), 09B511.
- [28] Wallner H., Gatterer K. Growth of Pure Ni(OH)<sub>2</sub> Single Crystals from Solution – Control of the Crystal Size. *Anorg. Allg. Chem.*, 2002, **628**, P. 2818–2820.
- [29] Casas-Cabanas M., Palacín M.R., Rodríguez-Carvajal J. Microstructural analysis of nickel hydroxide: Anisotropic size versus stacking faults. *Powder Diffraction*, 2005, **20**(4), P. 334–344.
- [30] Wehrens-Dijksma M., Notten P.H.L. Electrochemical quartz microbalance characterization of Ni(OH)<sub>2</sub>-based thin film electrodes. *Electrochimica Acta*, 2006, **51**(18), P. 3609–3621.
- [31] Ramesh T.N., Kamath P.V. Synthesis of nickel hydroxide: Effect of precipitation conditions on phase selectivity and structural disorder. *J. Power Sources*, 2006, **156**, P. 655–661.
- [32] Rajamathi M., Kamath P.V., Seshadri P. Polymorphism in nickel hydroxide: role of interstratification. *J. Mater. Chem.*, 2000, **10**, P. 503–506.
- [33] Faure C., Delmas C., Fouassier M. J. Characterization of a turbostratic  $\alpha$ -nickel hydroxide quantitatively obtained from a NiSO<sub>4</sub> solution. *Power Sources*, 1991, **35**(3), P. 279–290.
- [34] Hall D.S., Lockwood D.J., Poirier S., Bock C., MacDougall B.R. Raman and Infrared spectroscopy of  $\alpha$  and  $\beta$  phases of thin nickel hydroxide films electrochemically formed on nickel. *J. Phys. Chem. A*, 2012, **116**(25), P. 6771–6784.
- [35] Delmas C., Tessier C. Stacking faults in the structure of nickel hydroxide: a rationale of its high electrochemical activity. *J. Mater. Chem.*, 1997, **7**, P. 1439–1443.
- [36] Tessier C., Haumesser P.H., Bernard P., Delmas C. The structure of Ni(OH)<sub>2</sub>: from the ideal material to the electrochemically active one. *J. Electrochem. Soc.*, 1999, **146**, P. 2059–2067.
- [37] Ramesh T.N., Jayashree R.S., Kamath P.V. Disorder in layered hydroxides: DIFFaX simulation of the X-Ray powder diffraction patterns of nickel hydroxide. *Clays Clay Miner.*, 2003, **51**, P. 570–576.
- [38] Ramesh T.N., Kamath P.V. The effect of stacking faults on the electrochemical performance of nickel hydroxide electrodes. *Mater. Res. Bull.*, 2008, **43**, P. 2827–2832.
- [39] de Oliveira E.F., Hase Y. Infrared study of magnesium–nickel hydroxide solid solutions. *Vib. Spectros.*, 2003, **31**, P. 19–24.
- [40] Batsanov S.S. Structural chemistry. *Facts and dependencies*. M.: Dialog-MGU, 2000, 292 p. (In Russ.)
- [41] Almjasheva O.V., Gusarov V.V. Metastable clusters and aggregative nucleation mechanism. *Nanosystems: Physics, Chemistry, Mathematics*, 2014, **5**(3), P. 405–417.
- [42] Gusarov V.V., Almjasheva O.V. The role of non-autonomous state of matter in the formation of structure and properties of nanomaterials. Chapter 13 in the book *Nanomaterials: properties and promising applications*. Ed. A.B. Yaroslvtsev, Scientific World Publishing House, Moscow, 2014, P. 378–403.

---

*Submitted 18 August 2022; revised 6 October 2022; accepted 11 October 2022*

*Information about the authors:*

*Maria E. Kotova* – I. V. Grebenshchikov Institute of Silicate Chemistry of the Russian Academy of Sciences, 2 Makarova Emb., St. Petersburg 199034, Russia; V. I. Ulyanov St. Petersburg State Electrotechnical University “LETI”, 5 Professora Popova Str., St. Petersburg 197022, Russia; kotovamaria715@gmail.com

*Tatiana P. Maslennikova* – I. V. Grebenshchikov Institute of Silicate Chemistry of the Russian Academy of Sciences, 2 Makarova Emb., St. Petersburg 199034, Russia; V. I. Ulyanov St. Petersburg State Electrotechnical University “LETI”, 5 Professora Popova Str., St. Petersburg 197022, Russia; maslennikova.tp@iscras.ru

*Valery L. Ugolkov* – I. V. Grebenshchikov Institute of Silicate Chemistry of the Russian Academy of Sciences, 2 Makarova Emb., St. Petersburg 199034, Russia; ugovkov.52@gmail.com

*Victor V. Gusarov* – I. V. Grebenshchikov Institute of Silicate Chemistry of the Russian Academy of Sciences, 2 Makarova Emb., St. Petersburg 199034, Russia; V. I. Ulyanov St. Petersburg State Electrotechnical University “LETI”, 5 Professora Popova Str., St. Petersburg 197022, Russia; victor.v.gusarov@gmail.com

*Conflict of interest:* the authors declare no conflict of interest.

## Synthesis 2D nanocrystals of Co-doped manganese oxide as cathode materials of zinc-ion hybrid supercapacitor

Artem A. Lobinsky<sup>a</sup>, Maxim I. Tenevich<sup>b</sup>

Ioffe Institute, Saint Petersburg, 194021, Russia

<sup>a</sup>lobinski.a@mail.ru, <sup>b</sup>mtenevich@gmail.com

Corresponding author: Artem A. Lobinsky, lobinski.a@mail.ru

PACS 81.07.Bc

**ABSTRACT** In the present work, we propose a novel promising route for synthesis of Co-doped manganese oxide nanostructure via successive ionic layer deposition method as cathode material of zinc-ion hybrid supercapacitor. The synthesized nanolayers were analyzed by SEM, EDX and XRD. It was shown that the synthesized nanolayers were formed from ultrathin (6–8 nm) two-dimensional nanocrystals containing birnessite MnO<sub>2</sub> and hausmannite Mn<sub>3</sub>O<sub>4</sub> crystal phases and having the morphology of “nanosheets”. Electrode based on nickel foam and Co-doped manganese oxide nanolayers exhibited a high specific capacity (514.5 F/g at 0.1 A/g) and excellent cycling stability (99 % capacity retention after 1000 charge-discharge cycles). Obtained results demonstrate that the 2D Co-doped manganese oxide is a promising material for effective zinc-ion hybrid supercapacitor.

**KEYWORDS** nanocrystals, manganese oxides, electrode materials, cathodes, zn-ion hybrid supercapacitor.

**ACKNOWLEDGEMENTS** This research was financial supported by RSF grant, project number 22-23-20138.

**FOR CITATION** Lobinsky A.A., Tenevich M.I. Synthesis 2D nanocrystals of Co-doped manganese oxide as cathode materials of zinc-ion hybrid supercapacitor. *Nanosystems: Phys. Chem. Math.*, 2022, **13** (5), 525–529.

### 1. Introduction

Rechargeable zinc-ion batteries are one of the most promising candidates for replacing lithium-ion batteries which meet the future requirements for promising electrical energy storage devices due to the greater availability of zinc-containing raw materials, low cost and high theoretical specific capacity (820 mAh/g) [1, 2]. Zinc-ion hybrid supercapacitors are of particular interest, because they combine the advantages of zinc-ion batteries (high energy density) and supercapacitors (power density and long cycling life) [3–5]. Recently, some progress has been achieved in improving the electrochemical characteristics of electrode materials for such devices, but there are still problems associated with the lack of suitable cathode materials that can withstand multiple intercalation/deintercalation of zinc-ions [6]. To meet these requirements, layered and tunnel structured compounds with redox components are often chosen [7]. The set of materials that meet the presented requirements includes analogues of Prussian blue, manganese and cobalt oxides, vanadium oxides, as well as organic compounds [8]. Among these materials, manganese oxides are of the greatest interest from the point of view of their further commercialization, since they have a high specific capacity and a wide working potential window, while they can be synthesized from relatively inexpensive and affordable precursors [9–11]. Recently published works [12, 13] have shown the high efficiency of using manganese oxides as cathode materials for zinc-ion hybrid supercapacitors, which have shown high energy density and ultra-long cycling life. However, these cathode materials have low electronic conductivity, which does not allow them to achieve the theoretical values of the specific capacitance.

One of the solutions to this problem is to obtain oxide materials with a two-dimensional structure. The key characteristic of 2D materials is ultrathickness (about few nanometers) so charge carriers can travel extremely short distances from the volume to the surface, while significantly improving electronic conductivity [14, 15]. The main problem in the creation of cathode materials for zinc-ion hybrid supercapacitors at the moment is the complexity of obtaining, by existing synthesis methods, ultrathin oxide nanocrystals with a graphene-like morphology of “nanosheets”, which would significantly reduce the degradation of the electroactive material and improve electronic conductivity.

The successive ionic layer deposition method (SILD) has a number of unique features and advantages for obtaining nanoscale capacity electrode materials. In particular, it allows the formation of nanolayers on the surface of substrates with a developed morphology and a large specific surface area, as well as the possibility of controlling a variety of synthesis parameters (concentration and ratio of reagents, pH value, processing time, number of deposition cycles, etc.) [16, 17]. In addition, due to the ability to regulate the flow of ionic reactions at the substrate-solution interface, it is possible to set the preferred crystallographic orientation and grain structure, thus controlling the growth of crystals. Previously, oxides and hydroxides of transition metals with various morphologies were successfully synthesized by this method [18–20]. The obtained nanomaterials showed excellent capacitive and electrocatalytic characteristics.

In this research, we propose a novel facile route synthesis of ultrathin two-dimensional nanocrystals of Co-doped manganese oxide via successive ionic layer deposition method from aqueous solutions of manganese and cobalt salts. We investigate its application as effective electrode materials for zinc-ion hybrid supercapacitor.

## 2. Experiment

### 2.1. Fabrication of the Co-doped manganese oxide via successive ionic layer deposition technique

Beforehand, nickel foam (NF) was cleaned in acetone, ethanol and distilled water sonication of 15 min to remove the impurities, then treated with 6 M HCl solution for 15 min to remove the oxidation layer and dried on air at 80°C for 30 min. The Co-doped manganese nanolayers were fabricated by SILD technique used for obtaining Co-doped manganese oxide nanolayers. Aqueous solutions of mixed analytical grade salts  $\text{MnSO}_4$  ( $C = 0.01$  M) and  $\text{CoSO}_4$  ( $C = 0.005$  M) were used as a precursor for synthesis and aqueous solution of  $\text{KMnO}_4$  ( $C = 0.01$  M,  $\text{pH} = 11$ ) plays the role of oxidizer. The precleaned NF substrates were first dipped in the solutions of mixed salts  $\text{MnSO}_4$  and  $\text{CoSO}_4$  for 30 s and then were washed from excess reagent in distilled water for 15 s. On second step, substrates were dipped in solution of  $\text{KMnO}_4$  for 30 s and again were washed in water. After repeating 50 SILD cycles, insoluble film of synthesized product was formed on the surface. Finally, the as-prepared nanolayers were annealed at 300°C in argon atmosphere for 3 hours to obtain oxide thin films.

### 2.2. Characterization and electrochemical measurement

The morphology and nanostructure of synthesized nanocrystals were analyzed by SEM (Zeiss Merlin microscope and Tescan Vega 3 SBH microscope) and XRD (Rigaku Miniflex II X-ray diffractometer with  $\text{Cu K}\alpha$  radiation ( $\lambda = 0.154056$  nm)) technique. The chemical composition of the samples was characterized by EDX (Oxford INCA x-act X-ray). The electrochemical experiment was carried out using Elins P45-X potentiostat with two-electrode electrochemical cell. The working electrode was obtained in the form of Co-doped manganese oxide nanolayers modified nickel foam. Carbon rod serves as an anode and 1M  $\text{ZnSO}_4$  aqueous solution is the electrolyte. Electrochemical characterization was performed by cyclic voltammetry (CVA) and galvanostatic charge-discharge (GCD) and also electrochemical impedance spectroscopy (EIS) techniques. The specific capacitance  $C$  (F/g) can be calculated via eq. (1):

$$C = \frac{I dt}{dV m}, \quad (1)$$

where  $I$  (mA) is a galvanostatic current,  $dV$  (mV) is the potential window,  $dt$  (s) is the discharge time and  $m$  (g) is the mass of the active material in the film electrode. The mass of the electroactive material of the working electrode was measured using a microbalance.

## 3. Result and discussion

Figure 1(a,b,c) shows SEM images of Co-doped manganese oxide nanolayers synthesized as a result of 15, 25 and 50 treatment SILD cycles. As can be seen from the presented SEM images, in the process of increasing the number of treatment cycles, the surface of the foam nickel is gradually overgrown with a layer of the synthesized compound. The nanolayer is formed by spherical agglomerates. Moreover, as can be seen from the image with a large magnification, the agglomerates, in turn, consist of a set of ultrathin (6–8 nm) manganese oxide nanosheets (Fig. 1d). The EDX spectrum (Fig. 2) data demonstrate the presence of Mn, Co, O, Na, K and Ni (from substrate) atoms in synthesized nanolayers, the Co:Mn atomic ratio is 0.27:1.00 (Na and K amounts are less than 10 %).

According to XRD data analysis, the prepared sample is crystalline one. XRD pattern (Fig. 3) shows evidence of well crystallized sample containing crystalline phases of hausmannite ( $\text{Mn}_3\text{O}_4$ ,  $I_{41}/amd$ ) (AMCSD #0002024) and birnessite ( $\delta\text{-MnO}_2$ ) (AMCSD #0004947). The peaks of the metallic cobalt and cobalt oxide phase were not observed.

Analyzing the results obtained via SEM, EDX and XRD technique, we can assume that the obtained nanolayers are formed by Co-doped manganese oxide ultrathin nanocrystals with nanosheets morphology containing both crystalline phases of hausmannite ( $\text{Mn}_3\text{O}_4$ ) and birnessite ( $\delta\text{-MnO}_2$ ).

Electrochemical characteristics of synthesized nanolayers as cathode material for zinc-ion hybrid supercapacitors were carrying out by cyclic voltammetry (CVA) and galvanostatic charge-discharge (GCD) techniques. The cyclic voltammograms of the nickel foil electrode with Co-doped manganese oxide nanolayers were recorded in a potential window from 0.5 to 2 V vs.  $\text{Zn}/\text{Zn}^{2+}$  electrode in 1M  $\text{ZnSO}_4$  electrolyte at scanning rates of 10 mV/s (Fig. 4a). At a scan rate of 10 mV/s, two electrochemical processes take place in the layer, including the intercalation of zinc-ions at and their de-intercalation, indicating that Co-doped manganese oxide is the battery-type electrode material. It is noted that, after the first cycle, subsequent cycles are almost overlapped, demonstrating the excellent reversibility of the  $\text{Zn}^{2+}$  intercalation/deintercalation and dual-ion reaction process. Fig. 4b shows the galvanostatic charge/discharge curves of the Co-doped manganese oxide/NF electrode at different current density (0.1, 0.2, 0.5 and 1 A/g). The specific capacitance of Co-doped manganese oxide/NF electrode was calculated by eq. (1) is 514.5 F/g at a current density of 0.1 A/g.

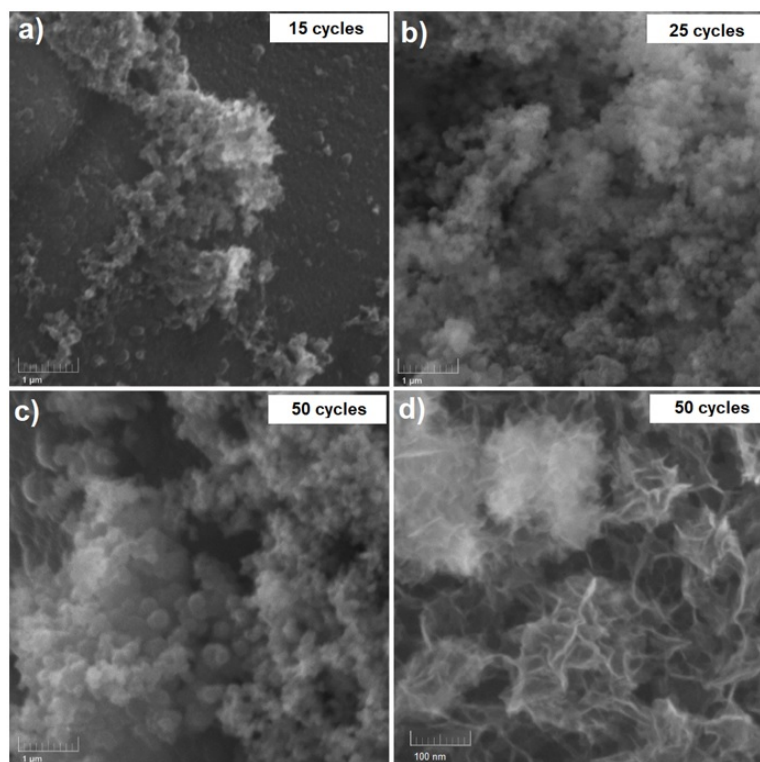


FIG. 1. SEM images of Co-doped manganese oxide nanolayers obtained after 15 (a); 25 (b); 50 (c) treatment SILD cycles and images of nanolayers after 50 (d) treatment cycles obtained at a higher magnification (d)

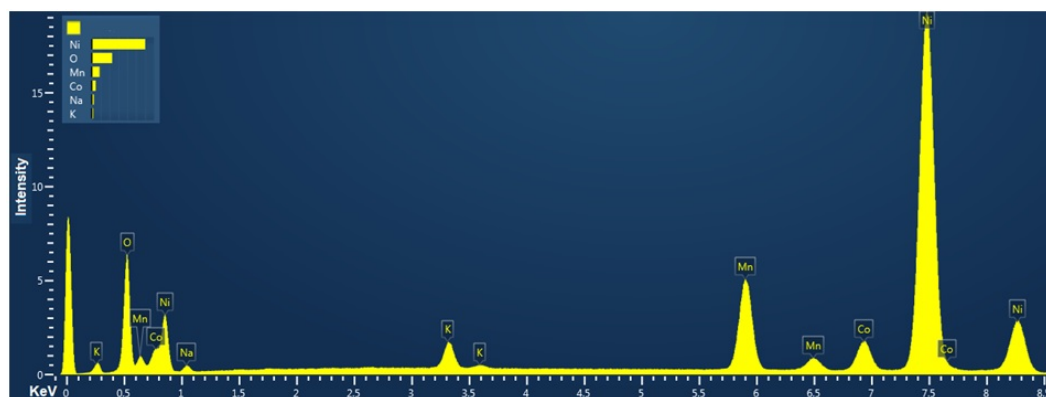


FIG. 2. EDX spectrum of Co-doped manganese oxide nanolayers

The EIS characterization of the electrode obtained at the frequency range from 100 kHz to 10 mHz (is not shown on figure). The Nyquist plot displays a linear part in the low-frequency region and an absence of semicircle in the high-frequency region which indicates very small transfer resistance and fast electrochemical reactions. The internal resistance was calculated from Nyquist plot and is equal to 1.9  $\Omega$ . Cycling performance is also important in the practical application of zinc-ion hybrid supercapacitor. It is important to note, that the electrode based on Co-doped manganese oxide exhibits a high cycling stability after 1000 cycles with high capacity retention of 99 %. Such high electrochemical performance, in our opinion, can be explained by a “synergy effect” of unique morphology ultrathickness nanocrystals and layered crystal structure of Co-doped manganese oxide, which enlarges the electroactive surface area of the electrode and the smaller size of nanocrystals brings about good intercalation/deintercalation of zinc-ions on the electrode surface on the frontier of the electrode/electrolyte and hence affects positively on the electrochemical stability.

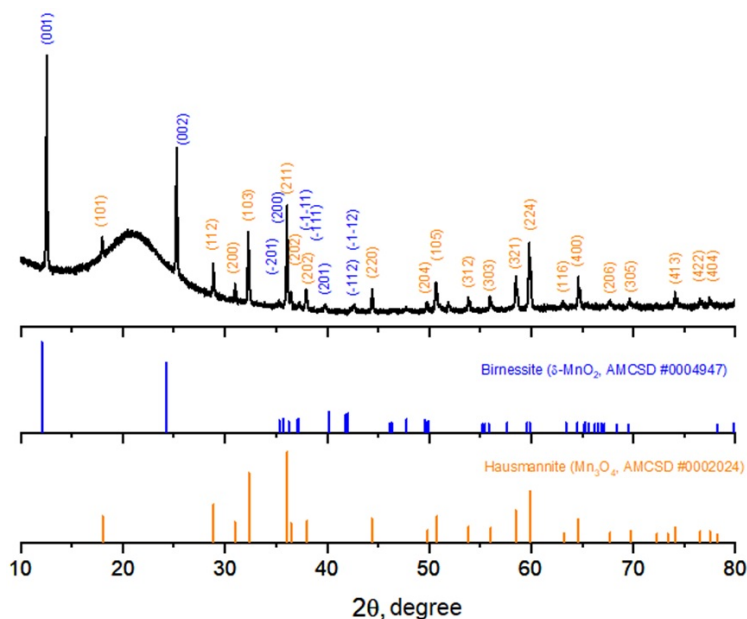


FIG. 3. XRD patterns of Co-doped manganese oxide nanolayers

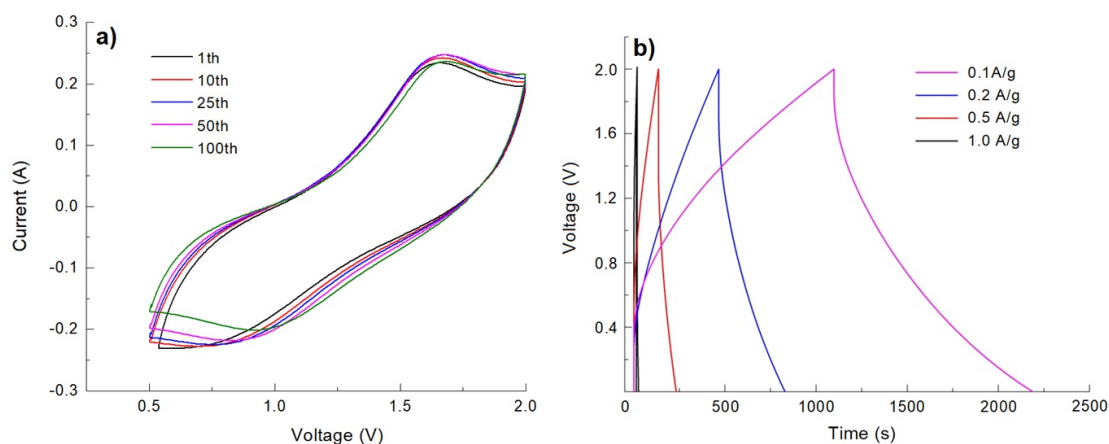


FIG. 4. CVA cycling stability after 100 cycles (at 10 mV/s) (a) and galvanostatic charge–discharge curves at different current density (b) of the electrode based on nickel foam and Co-doped manganese oxide nanolayers

#### 4. Conclusion

To conclude, we can remark that the possibility for direct synthesis of two-dimensional nanocrystals of Co-doped manganese oxide was shown for the first time. The obtained nanomaterial were formed from ultrathin (6–8 nm) two-dimensional nanocrystals of Co-doped manganese oxide with the “nanosheets” morphology which contains birnessite and hausmannite crystal phases. The electrochemical study of Co-doped manganese oxide nanolayers modified nickel foam electrodes, prepared as result 50 treatment SILD cycles, demonstrate that the specific capacitance is 514.5 F/g at a current density of 0.1 A/g. Repeated cycling for 1000 charge-discharge cycles demonstrates a relatively small 1 % capacitance fade.

#### References

- [1] Canepa P., Gautam G.S., Hannah D.C., Malik R., Liu M., Gallagher K.G., Persson K.A., Ceder G. Odyssey of multivalent cathode materials: Open questions and future challenges. *Chem. Rev.*, 2017, **117**, P. 4287–4341.
- [2] Zeng X.Q., Li M., Abd El-Hady D., Alshitari W., Al-Bogami A.S., Lu J., Amine K. Commercialization of lithium battery technologies for electric vehicles. *Adv. Energy Mater.*, 2019, **9**, P. 1900161.
- [3] Siliang Wang, Qiang Wang, Wei Zeng, Min Wang, Limin Ruan, Yanan Ma. New free-standing aqueous zinc-ion capacitor based on MnO<sub>2</sub>-CNTs cathode and MXene anode. *Nano-Micro Lett.*, 2019, 11:70.
- [4] Haiyan Wang, Wuquan Ye, Ying Yang, Yijun Zhong, Yong Hu. Zn-ion hybrid supercapacitors: Achievements, challenges and future perspectives. *Nano Energy*, 2021, **85**, P. 105942.

- [5] Jiaming Wang, Ying Huang, Xiaopeng Han, Zengyong Li, Shuai Zhang, Meng Zong. A flexible zinc-ion hybrid supercapacitor constructed by porous carbon with controllable structure. *Applied Surface Science*, 2022, **579**, P. 152247.
- [6] Changgang Li, Xudong Zhang, Wen He, Guogang Xu, Rong Sun. Cathode materials for rechargeable zinc-ion batteries: From synthesis to mechanism and applications. *Journal of Power Sources*, 2020, **449**, P. 227596.
- [7] Zhu K., Wu T., Sun S., Wen Y., Huang K. Electrode materials for practical rechargeable aqueous Zn-ion batteries: challenges and opportunities. *ChemElectroChem*, 2020, **7**, P. 2714–2734.
- [8] Yuan X., Ma F., Chen X., Sun R., Chen Y., Fu L., Zhu Y., Liu L., Yu F., Wang J. Aqueous zinc-sodium hybrid battery based on high crystallinity sodium-iron hexacyanoferrate. *Mater. Today Energy*, 2021, **20**, P. 100660.
- [9] Gao Y.N., Yang H.Y., Bai Y., Wu C. Mn-based oxides for aqueous rechargeable metal ion batteries. *J. Mater. Chem. A*, 2021, **9**, P. 11472–11500.
- [10] Wen Shi, Wee Siang, Vincent Lee, Junmin Xue. Recent development of Mn-based oxides as zinc-ion battery cathode. *ChemSusChem*, 2021, **14**, P. 1–26.
- [11] Xiong T., Zhang Y.X., Lee W.S.V., Xue J.M. Defect engineering in manganese-based oxides for aqueous rechargeable zinc-ion batteries: A review. *Adv. Energy Mater.*, 2020, **10**, P. 2001769.
- [12] Kaidi Li, Jialun Li, Liying Wang, Xuesong Li, Xijia Yang, Wei Lü. Flexible Zn-ion hybrid supercapacitor enabled by N-Doped MnO<sub>2</sub> cathode with high energy density and ultra-long cycle life. *Journal of Alloys and Compounds*, 2022, **928**, P. 167153.
- [13] Simin He, Zunli Mo, Chao Shuai, Wentong Liu, Ruimei Yue, Guigui Liu, Hebing Pei, Ying Chen, Nijuan Liu, Ruibin Guo. Pre-intercalation  $\delta$ -MnO<sub>2</sub> zinc-ion hybrid supercapacitor with high energy storage and ultra-long cycle life. *Applied Surface Science*, 2022, **577**, P. 151904.
- [14] Yingchang Yang, Xuejing Qiu, Wei Shi, Hongshuai Hou, Guoqiang Zou, Wei Huang, Ziyang Wang, Senling Leng, Yaozong Ran, Xiaobo Ji. Controllable fabrication of two-dimensional layered transition metal oxides through electrochemical exfoliation of non-van der Waals metals for rechargeable zinc-ion batteries. *Chemical Engineering Journal*, 2021, **408**, P. 127247.
- [15] Ning Zhang, Xuyong Chen, Meng Yu, Zhiqiang Niu, Fangyi Cheng, Jun Chen. Materials chemistry for rechargeable zinc-ion batteries. *Chem. Soc. Rev.*, 2020, **49**, P. 4203–4219.
- [16] Samantha Prabath Ratnayake, Jiawen Ren, Elena Colusso, Massimo Guglielmi, Alessandro Martucci, Enrico Della Gaspera. SILAR deposition of metal oxide nanostructured films. *Small*, 2021, P. 2101666.
- [17] Tolstoy V.P. Successive ionic layer deposition. The use in nanotechnology *Russ. Chem. Rev.*, 2006, **75**, P. 161.
- [18] Kodintsev I.A., Martinson K.D., Lobinsky A.A., Popkov V.I. Successive ionic layer deposition of co-doped Cu(OH)<sub>2</sub> nanorods as electrode material for electrocatalytic reforming of ethanol. *Nanosystems: Physics, Chemistry, Mathematics*, 2019, **10**(5), P. 573–578.
- [19] Kodintsev I.A., Martinson K.D., Lobinsky A.A., Popkov V.I. SILD synthesis of the efficient and stable electrocatalyst based on CoO-NiO solid solution toward hydrogen production. *Nanosystems: Physics, Chemistry, Mathematics*, 2019, **10**(6), P. 681–685.
- [20] Lobinsky A.A., Kaneva M.V. Synthesis Ni-doped CuO nanorods via successive ionic layer deposition method and their capacitive performance. *Nanosystems: Physics, Chemistry, Mathematics*, 2020, **11**(5), P. 608–614.

---

*Submitted 15 August 2022; revised 9 October 2022; accepted 11 October 2022*

*Information about the authors:*

Artem A. Lobinsky – Ioffe Institute, Saint Petersburg, 194021, Russia; lobinski.a@mail.ru

Maxim I. Tenevich – Ioffe Institute, Saint Petersburg, 194021, Russia; mtenevich@gmail.com

*Conflict of interest:* the authors declare no conflict of interest.

## Preparation and investigation of the screen-printed cobalt oxide (Co<sub>3</sub>O<sub>4</sub>) nanostructured thick film with annealing temperature

Ujwala M. Pagar<sup>1,a</sup>, Uglal P. Shinde<sup>2,b</sup>

<sup>1</sup>Department of Physics, H.P.T. Arts and R.Y.K. Science College, Nashik 422005, (M.S.) India

<sup>2</sup>Department of Physics, L.V.H. Arts, Science and Commerce College, Nashik 422005, (M.S.) India

<sup>a</sup>ujwalapagar7@gmail.com, <sup>b</sup>upshinde1965@gmail.com

Corresponding author: Ujwala M. Pagar, [ujwalapagar7@gmail.com](mailto:ujwalapagar7@gmail.com)

**ABSTRACT** In this study, spinel type cobalt oxide (Co<sub>3</sub>O<sub>4</sub>) thick films are deposited on glass substrate by screen printing technique. All characterization was carried out for unannealed, annealed at 250 – 400 °C. The X-ray Diffraction (XRD) analysis indicates that prepared films have polycrystalline nature with cubic structure having preferential orientation through (311) plane. Crystallite size is found to be 18.52 nm. The lattice parameter found to be 8.036 – 8.138 Å approaches to standard value ( $a = 8.08$  Å). Scanning Electron Microscopy (SEM) analysis of prepared films shows agglomeration of nanoparticles, occurrence of spherical-shaped grain aggregations. Spherical grain size increases from 47.66 to 77.33 nm with increase in annealing temperatures. A relation between structural and morphological properties is noted. The Energy Dispersive Analysis by X-Ray (EDAX) shows that all compositions have desired stoichiometric ratios. Besides electrical measurements, film D.C. resistance, resistivity was measured. It allows us to conclude that assured material has semiconducting nature. Specific surface area, Temperature Coefficient of Resistance (TCR), activation energy decreases with increase in annealing temperature were calculated. It was shown that structural, morphological and electrical properties of Co<sub>3</sub>O<sub>4</sub> films were improved by increasing annealing temperature.

**KEYWORDS** Co<sub>3</sub>O<sub>4</sub>, thick films, XRD, SEM-EDAX, resistivity, TCR, activation energy

**ACKNOWLEDGEMENTS** The authors wish to thank the Physics Research center M.S.G. College Malegaon camp Malegaon for giving instrument facilities to carry out this research work. Authors are also thankful to Savitribai Phule Pune University, Pune for providing EDAX and SEM characterization results.

**FOR CITATION** Pagar U.M., Shinde U.P. Preparation and investigation of the screen-printed cobalt oxide (Co<sub>3</sub>O<sub>4</sub>) nanostructured thick film with annealing temperature. *Nanosystems: Phys. Chem. Math.*, 2022, **13** (5), 530–538.

### 1. Introduction

Recently, transition metal oxides (TMOs) attracted great attention as an important and promising materials which have remarkable electronic, optical, magnetic, and catalytic properties. Cobalt oxides nanoparticles exhibit interesting properties and applications when compared with bulk. It is a p-type cubic spinel structure semiconducting material with two direct and indirect optical bandgaps (1.44 – 2.06) eV and (1.26 – 1.38) eV, respectively. Bulk cobalt oxide crystals appear in two stable crystallographic structures, the rock salt-type CoO and the normal-spinel-type Co<sub>3</sub>O<sub>4</sub>. One can mention applications in different areas such as smart windows, negative electrodes in Li-ion batteries and mirrors with variable reflectance. Basically, Co<sub>3</sub>O<sub>4</sub> is an electrochromic material and would be classified into two categories: cathodic like molybdenum oxide, tungsten oxide etc, and anodic coloured materials like ruthenium oxide, cobalt oxide, nickel oxide, etc. [1].

Among transition metal oxides, great attention has been focussed on spinel type trivalent cobalt tetra oxide is versatile metal oxides because of its two characteristics, namely, variable valence state and existence of oxygen vacancy defects. It exists in different forms such as CoO, Co<sub>2</sub>O<sub>3</sub>, CoO (OH), Co<sub>3</sub>O<sub>4</sub> and CoO. In these, Co<sub>3</sub>O<sub>4</sub> acquires the normal spinel structure: magnetic Co<sup>2+</sup> (3d<sup>7</sup>) cations are placed in tetrahedral sites and nonmagnetic Co<sup>3+</sup> (3d<sup>6</sup>) cations occupied octahedral ones. In bulk crystalline, Co<sub>3</sub>O<sub>4</sub> renders antiferromagnetic material while in nanostructures, it shows weak ferromagnetism with an energy band-gap of 1.4 – 1.8 eV [2]. On the other hand, semiconductor nanoparticles have attracted a great study of interest owing to their enhanced and exclusive properties when the surface to volume ratio increases. Due to its good chemical stability and high specific surface area, therefore it is used in field of gas sensors for detection purpose [3]. In most of the research work the Co<sub>3</sub>O<sub>4</sub> has been selected for investigation, because of its chemical stability, desired electrochemical property and high annealing temperature. Usually, SMO gas sensors worked at high temperature ( $\geq 150$  °C), and their response strongly depends on temperature. Also, kinetic reactions between semiconductors and gases are temperature dependent [4]. This Co<sub>3</sub>O<sub>4</sub> phase can be easily obtained in air atmosphere. Cobalt

oxide thin and thick films are prepared by different methods such as atomic layer deposition, sol-gel technique, chemical vapour deposition, RF magnetron sputtering, chemical bath deposition, screen printing technique, spray pyrolysis and nebulizer spray pyrolysis.

Among these techniques, screen printing technique has many advantages such as low cost, easy to handle, convenient for large area deposition, uniform film deposition and less deposition time. This technique has been employed by many researchers to fabricate thick films of tin oxide, cerium oxide, zinc oxide and indium oxide. [5, 6]. After preparation, films are ready for characterization by X-ray diffraction, scanning electron microscopy, energy dispersive X-ray analysis, electrical conductivity measurement etc. During synthesis of  $\text{Co}_3\text{O}_4$  nanostructures, many efforts have been taken by researchers with different morphologies such as hollow spheres, nano porous, nanospheres, nanotubes cubic single crystals, nano particles, nano rods, nano plates, nano wires, and nano cubes structures [7]. Improvement in the electrical conductivity, transmission stability and practical feasibility possible by different processes like doping, annealing and aging. Structural and morphological properties were improved by heat treatment. After annealing crystallinity, grain size of the film increased due to diminishing of oxygen vacancies and film surface area became smooth, reduces crystal defects [8]. Therefore, We say that annealing treatment can activate oxygen vacancies and also enhanced crystal quality of the nanostructure.

Film annealing up to  $200^\circ\text{C}$  results crystal having low-quality. Based on earlier studies it is interesting to study about  $\text{Co}_3\text{O}_4$ , and its associated various properties of prepared screen-printed  $\text{Co}_3\text{O}_4$  thick films and the effect of annealing temperature on it are important now a days.

Screen-printing technology has been demonstrated which is suitable for mass-production of thermoelectric modules with advantages [9]. Structural characterization, surface morphology and particle size of the samples were determined from XRD technique, scanning electron microscopy (SEM) instrument while the stoichiometric characteristic was proved from energy dispersive X-ray analysis [10].

In the present study, we have reported preparation of screen printed  $\text{Co}_3\text{O}_4$  thick films and investigates the effect of annealing temperature on structural, morphological and electrical characterization elaborated by a simplified screen-printing technique.

## 2. Materials method and measurements

The commercially available AR grade with 99.99 % purity cobalt oxide nano powder was used for preparation of thick films. Other than this, chemicals required for preparation of thick films are acetone, ethyl cellulose, B.C.A., etc purchased from Scientific Lab, Nashik. To verify structural properties and purity of samples, the X-ray diffraction (XRD) technique is used. The X-ray diffraction patterns of all the prepared samples are recorded for analysis purpose. They were plotted using Bruker D8 advance diffractometer, Germany with  $\text{CuK}\alpha$  ( $\lambda = 1.54$  angstrom) radiations operated at 40 KV and 40 mA in the scanning range of ( $2\theta$ ) between  $20^\circ$  and  $80^\circ$ . To observe chemical compositions and surface morphology, scanning electron microscopy named as SEM-JEOL JSM-6360A with OXFORD EDS attachment is used. For electrical characterization, simple half bridge method was used.

### 2.1. Preparation of thick films of cobalt oxide nanoparticles

The cobalt oxide based thick film sensor was constructed by standard screen-printing technique. The powder nanoparticle of  $\text{Co}_3\text{O}_4$  converted into paste form was used to prepare thick films by maintaining the inorganic ( $\text{Co}_3\text{O}_4$ ) to organic binder ratio as 70:30. The organic binder contains of 8 % ethyl cellulose (EC) which is in a powder form and 92 % butyl carbitol acetate (BCA) present in a liquid form. All these stoichiometric amounts of  $\text{Co}_3\text{O}_4$  and binders then mixed mechanochemically into mortar and pestle and crushed continuously for nearly 40 minutes. A solution of BCA which add on drop wise in order to get correct viscosity for screen printing. Prepared gel like paste can employed over glass substrate with dimensions  $1.5 \times 2$  cm. After completion of thick film coating, these films were air dried firstly for 30 minutes followed by IR drying for 30 minutes. Finally, the prepared binary oxide  $\text{Co}_3\text{O}_4$  film sensor was kept in muffle furnace for calcinations process at various temperatures 250, 300, 350,  $400^\circ\text{C}$  nearly 2 hours. After annealing films became black in colour and found to be uniform, pinholes free and strongly adherent to the glass substrates. Such annealed films are now ready for characterization.

### 2.2. Measurement of the film thickness

The thickness of the prepared films calculated by the using gravimetric (weight-difference) method assuming the samples were approximately uniform as compares to bulk form. Thickness measurement equation is given by

$$t = \Delta w / A \cdot \rho, \quad (1)$$

where  $\Delta w$  – actual weight of the prepared film,  $\rho = 6.11 \text{ gm/cm}^3$  – density of  $\text{Co}_3\text{O}_4$ ,  $A$  is the area of the film (length  $\times$  breadth).

Screen-printed thickness observed range varies from 33 to  $38 \mu\text{m}$ .

### 2.3. Characterisation of screen printed $\text{Co}_3\text{O}_4$ thick film sensor

The physical (structural), chemical properties and experimental performance of cobalt oxide NPs intensively depends on size, shape geometry, morphology etc. To characterise the prepared samples mainly X-ray diffraction technique (structural analysis), scanning electron microscopy with EDS (morphological and elemental analysis) and half bridge method (electrical analysis) were used. The success of the synthesised nanoparticles was easily confirmed by characterisation techniques.

## 3. Results and discussion

### 3.1. Structural characterisation: XRD analysis (Crystal structure determination)

The structural properties of thick film is the key to recognize its quality, the crystallinity and phases of transition metal oxides nanoparticles and composite nanoparticles were analysed by X-ray diffraction technique [11]. For recognition of the crystalline phase, JCPDS (Joint Committee on Powder Diffraction Standards) data and using Debye–Scherrer equation the crystallite size was calculated.

Figure 1(a–e) shows the XRD patterns of  $\text{Co}_3\text{O}_4$  thick films as deposited at room temperature (unannealed) and annealed at different temperatures namely 250, 300, 350, 400 °C. It indicates the purity of the product. From XRD study, diffraction peaks are located at  $2\theta$  of 31.0730, 36.7490, 38.470, 43.130, 44.710, 55.520, 59.250 and 65.160 indicating their polycrystalline nature corresponding to (220), (311), (222), (400), (422), (511), and (440) crystal planes, respectively. This demonstrated the formation of  $\text{Co}_3\text{O}_4$  with cubic crystal structure as per [JCPDS card no. 42-1467]. The peak intensity is strong, indicating high crystalline structure of the products [12]. The average crystallite size of the  $\text{Co}_3\text{O}_4$  thick films is estimated from the X-ray diffraction patterns using the Debye–Scherrer formula:

$$D = \frac{0.9\lambda}{\beta \cos \theta}, \quad (2)$$

where  $D$  is the crystallite size,  $\beta$  is the Full Width at Half Maxima (FWHM),  $\lambda$  is the wavelength of X-ray used and  $\theta$  is the diffraction angle.

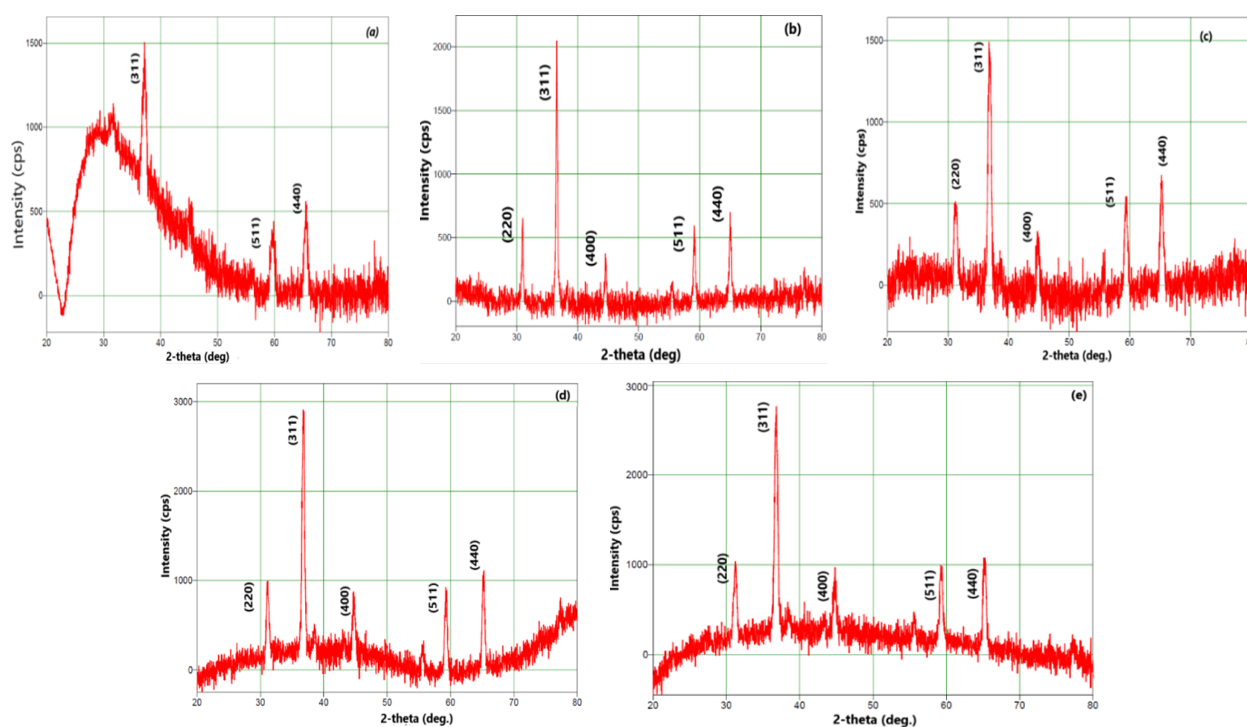


FIG. 1. XRD patterns of  $\text{Co}_3\text{O}_4$  thick films as deposited (unannealed) (a), annealed at 250 °C (b), 300 °C (c), 350 °C (d), 400 °C (e) respectively

The crystallite size of  $\text{Co}_3\text{O}_4$  calculated from the strongest peak, located at (311) plane at  $2\theta \approx 37^\circ$ , are estimated as 18.52 nm. The average crystallite size for pure cobalt oxide was found to be 18.20 nm [13, 14] and its distribution range lies from 18.52 to 36.38 nm depending on annealing temperature.

The obtained value of  $d_{hkl}$  (interplanar distances) values and the standard values confirm that the deposited and annealed films are nano crystallized in the spinel type cubic structure of  $\text{Co}_3\text{O}_4$ . The lattice parameter  $a$  of the unit cell is calculated from the peak positions using the formula of cubic system Formula. This value is found to be in the range

8.036–8.138 Å, which is close to standard value ( $a = 8.08$  Å) given by JCPDS 42-1467. When the annealing temperature increases, the intensity of the peak corresponding to the (311) plane is found to decrease due to the thermal strain. Sharp diffraction peaks are observed at 350 °C annealed temperature [15].

From XRD data, the crystalline parameters like lattice constant ( $a$ ), crystallite size ( $D$ ), dislocation density ( $\delta$ ), and micro strain ( $\epsilon$ ) were determined. The dislocation density is the length of dislocation lines per unit volume of the crystal. Greater  $D$  and smaller  $\delta$  values mean better crystallization of the films. The dislocation density and lattice strain were calculated from the diffraction pattern to obtain more information about structural properties. The observed changes of strain take places due to point defects and crystallite size. The lattice strain is calculated using Stokes–Wilson equation. To know more on the number of defects in the film, the dislocation density ( $\delta$ ) is calculated by using relation mentioned in Table 1. The induced strain causes reduction in crystallite size and increase in peak broadening. The average micro strain screen printed  $\text{Co}_3\text{O}_4$  thin film sensor is 0.27 %. Micro strain decreases from 0.00611 to 0.0009 due to good crystallinity.

TABLE 1. Shows dislocation density and micro strain for different annealing temperatures

Annealing temperature (°C)	Dislocation density $\delta = 1/D^2$ (lines/m <sup>2</sup> ) $10^{15}$	Micro strain $\epsilon = \beta \cos \theta/4$ , $10^{-3}$
Unannealed	13.18	6.11
250	0.75	0.952
300	5.10	2.475
350	2.92	1.870
400	3.695	2.1

The XRD spectrum is in full agreement with the standard spectrum of cubic crystalline  $\text{Co}_3\text{O}_4$ . JCPDS card no: (42–1467). The diffraction peaks revealed to the cubic nature of nanocrystalline  $\text{Co}_3\text{O}_4$ .

### 3.2. Morphological characterization

**3.2.1. SEM with EDS analysis (surface morphology).** The Scanning Electron Microscopy (SEM-JEOL JSM 6360 Model) images of prepared nanomaterial  $\text{Co}_3\text{O}_4$  thick film are displayed in Fig. 2. These 2D images with high magnification show surface texture, color and porosity  $\text{Co}_3\text{O}_4$  nanoparticles and indicate the formation of particles with different shapes and sizes. This porosity may be due to the evaporation of organic binder during the growing process and annealing treatment [16]. The surface characteristics of the prepared films investigated by scanning electron microscopy that shows heterogeneous, porous nanoparticles with varying dimensions. The observed particles are highly agglomerated and they are essentially cluster of nanoparticles. The surface morphology of screen printed  $\text{Co}_3\text{O}_4$  thick films shows that small sphere-shape particles are distributed. Some of them have heterogeneous surface, microspores and mesopores as seen from its surface micrographs [8]. It's greyish black in color, various sized nanoparticles image can be seen from SEM images as shown.

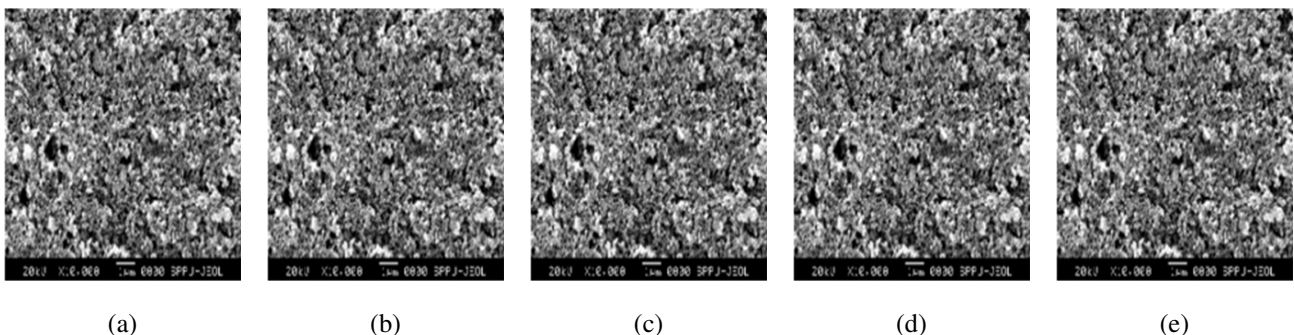


FIG. 2. SEM micrographs as deposited (unannealed) (a), annealed at 250 °C (b), 300 °C (c), 350 °C (d), 400 °C (e)  $\text{Co}_3\text{O}_4$  thick films respectively

Micrographs shows surface morphology of  $\text{Co}_3\text{O}_4$  thick films deposited on glass substrate annealed at unannealed, 250, 300, 350, 400 °C with higher resolution. It is observed that films show polycrystalline nature with no. of voids (pores) distributed on the surface of film. The particle size was obtained as the length of the segment joining the two ends of the particle and passing through its mass centre and the average particle size was measured using image software, increases

from 73 to 145 nm with increase in annealing temperatures. It is maximum when film is unannealed. The average particle size is 116.702 nm. Spherical grain size increases with respect to annealing temperature and its change from 47.66 to 77.33 nm and it has maximum when thick film is unannealed. Surface area decreases from 20.60 to 12.698 m<sup>2</sup>/gm with increase in annealing temperature and is a minimum for unannealed film as shown in Table 2. Surfaces of Co<sub>3</sub>O<sub>4</sub> thick films are cubical, spherical grains, so such a film can adsorb more atmospheric oxygen due to more exposed surface area of the film. Highly porous film shows high sensitivity.

TABLE 2. Mean particle size, grain diameter and surface area at various annealing temperatures

Annealing temperature (°C)	Mean particle size (nm)	Spherical grain diameter $d$ (nm)	Specific surface area $S_w = \frac{6}{\rho d}$ (m <sup>2</sup> /gm)
Unannealed	127.2	83.5	11.76
250	73.11	47.66	20.60
300	108.2	66.66	14.73
350	130	73.66	13.33
400	145	77.33	12.698

3.2.2. *EDS Analysis.* The elemental quantitative composition of grown Co<sub>3</sub>O<sub>4</sub> nanoparticles was determined using the spectra obtained by energy dispersive analysis of X-rays (EDAX). The weight percentage and atomic percentage of cobalt oxide nanoparticles are shown in Table 3. This declares proof that synthesized nanoparticles are non-stoichiometric. In cobalt oxide this nonstoichiometric is accompanied by change in colour with the stoichiometrically correct cobalt oxide being grey and non-stoichiometric being black. Fig. 3 shows elemental composition annealed Co<sub>3</sub>O<sub>4</sub> thick film sensors.

TABLE 3. Atomic % elemental composition of Pure Co<sub>3</sub>O<sub>4</sub> thick films as measured by EDS

Sample annealed temperature	Elements				Co/O Ratio
	Co		O		
	At. wt. %	At. Mass %	At. wt. %	At. Mass %	
Unannealed	53.90	24.09	46.10	75.91	1.17
250 °C	52.21	22.88	47.79	77.12	1.09
300 °C	53.76	23.99	46.24	76.01	1.16
350 °C	54.43	24.24	45.57	75.71	1.19
400 °C	54.17	24.29	45.83	75.51	1.18

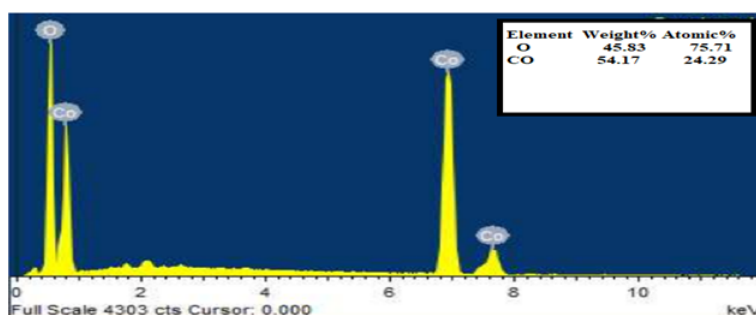


FIG. 3. EDAX results of Co<sub>3</sub>O<sub>4</sub> nanoparticle

3.2.3. *EDAX results of  $\text{Co}_3\text{O}_4$  nanoparticles.* The weight percentage of cobalt is increased with annealing temperature and mass percentage of oxygen decreases with increasing annealing temperature due to the release of excess oxygen. decreases which indicates the oxygen adequate nature of the films [17].

Table 3 shows quantitative elemental analysis of Cobalt oxide thick films. In figure, the major peaks of Co and O elements are observed. The observed compositional data from the EDX analysis responds positively with theoretically calculated values, representing a good elemental compositional homogeneity across the cobalt oxide nanoparticles. The EDX spectrum shows sharp peaks between 6.6 and 7.8 KeV for Co and between 0.4 and 0.6 KeV for O corresponding to crystalline  $\text{Co}_3\text{O}_4$  NPs. The EDAX results obtained for spinel type cobalt oxide thick are in good agreement with reported output. The straightforward stoichiometry of Co:O in case of Spinel type cobalt oxide was 3:4; is considerably more complicated CoO with rock salt structure. Due to high electron affinity of surface molecules, oxygen element gets attached to the molecules on the surface of the prepared thick films.

### 3.3. Crystallinity

It describes degree of structural order in a solid. Crystallinity index is denoted by  $I_{\text{cry}}$  can be calculated through comparison of crystallite size obtained from XRD and that obtained by SEM.

$$I_{\text{cry}} = \frac{D_p}{D}, \quad (3)$$

where,  $D_p = 116.70$  nm is the particle size from SEM and  $D = 18.20$  nm by using Debye–Sherrer formula.

When  $I_{\text{cry}}$  is close to 1, it is assumed that the crystallites represent monocrystalline units while larger value of  $I_{\text{cry}}$  means that the particles are of polycrystalline type.

From XRD and SEM,  $I_{\text{cry}} = 6.41$  for cobalt oxide thick film, it's much greater than 1 implies that the prepared thick films show polycrystalline type. Result shows particle has polycrystalline nature and good crystallinity.

### 3.4. Electrical characterization

The D.C. resistance of cobalt oxide prepared sample was measured by using half bridge method as a function of temperature in home built static gas measurement system. This system consists of glass chamber and heater of nichrome wire having Resistance-120 Ohm at room temperature. The heater was used to change the film sample temperature from room temperature 30 to 350 °C. In half bridge method the value of  $R_{\text{ref}} = 10$  M and 30 V<sub>DC</sub> power supply were used.

3.4.1. *Sample resistance.* The resistance of the thick film samples was determined using following equation

$$R_{\text{sample}} = R_{\text{ref}} \left\{ \frac{V_{\text{in}}}{V_{\text{out}}} - 1 \right\}. \quad (3)$$

Readings of temperature versus output voltage were taken by changing temperature 10 °C. The D.C. resistance of the films was measured by half bridge method in air atmosphere at 30 – 350 °C. The resistance of cobalt oxide thick films found to be decreases with increase in temperature. This gives the confirmation of semiconducting behaviour of  $\text{Co}_3\text{O}_4$  material by obeying  $R = R_0 \exp(-\Delta E/kT)$  in the 30 – 350 °C temperature range. Fig. 4 shows the change in resistance of pure  $\text{Co}_3\text{O}_4$  thick films with respect to change in temperature (K).

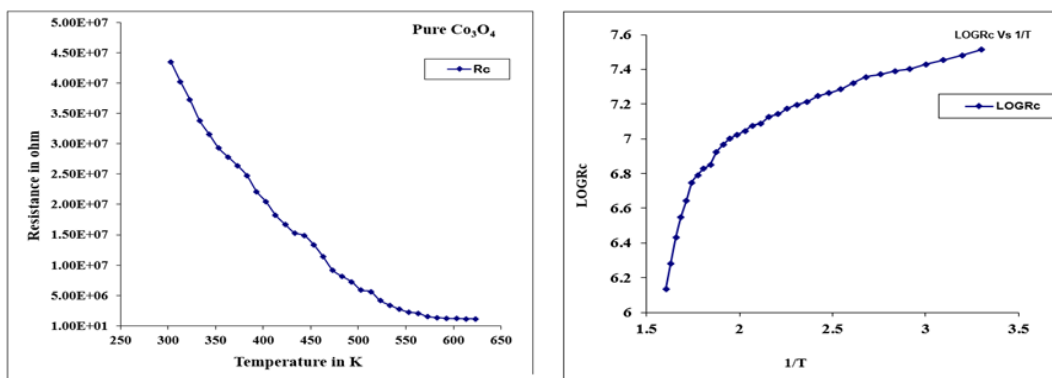


FIG. 4. Plot of resistance against temperature (a) and log  $R$  against inverse temperature (b) for  $\text{Co}_3\text{O}_4$  thick films

3.4.2. *Resistivity of Co<sub>3</sub>O<sub>4</sub> thick films.* The resistivity of prepared thick films was calculated as function of temperature within temperature range. The exponential nature of graph shows the resistance decreases steadily to lowest saturation level with respect to increase in temperature. The resistivity of thick films at constant temperature is calculated using equation

$$\rho = \frac{Rbt}{l}, \quad (4)$$

where,  $\rho$  is the resistivity of the film,  $R$  is the resistance at room temperature,  $b = 1.25$  cm is the breadth of film,  $t$  – thickness of the film,  $l = 2.5$  cm is the length of the film.

To calculate resistivity of unannealed thick film,  $R = 4.791 \times 10^7 \Omega$ ,  $t = 38 \mu\text{m}$  were taken. The value of resistivity  $\rho$  is  $910.38 \Omega\text{m}$  and has maximum with the corresponding conductivity  $1.098 \times 10^{-3} \Omega^{-1}\text{m}^{-1}$  and has a minimum. The resistivity of pure Co<sub>3</sub>O<sub>4</sub> thick films decreases with increase in annealing temperature. It represents the development of a semiconducting nature in the film. The conductivity is inverse of resistivity and is computed from the relation  $\sigma = 1/\rho$ , where  $\sigma$  is the conductivity. The electrical resistivity and conductivity values are found out at various annealing temperatures and are mentioned in table. From electrical properties, we observed that the electrical conductivity of pure Co<sub>3</sub>O<sub>4</sub> thick films increases with increase in annealing temperature, films deposited onto nonconductive substrate (250 – 400 °C) as mentioned in Table 4. In fact, annealing treatment provides sufficient thermal energy to the crystal which facilitates the electron delocalization through the elimination of a large number of defects [16].

TABLE 4. Electrical parameters of Co<sub>3</sub>O<sub>4</sub> thick film sensor annealed at different temperatures

Annealing temperature °C	Resistivity Ωm	Electrical conductivity $10^{-3} \Omega^{-1}\text{m}^{-1}$	T.C.R. per kelvin	Activation energy $\times 10^{-4}$ eV	
				At low temp.	At high temp.
250	782.57	1.28	-0.0036	0.78	2.71
300	634.42	1.58	-0.0044	0.35	6.43
350	570.74	1.75	-0.0048	0.32	9.59
400	365.55	2.74	-0.0059	0.29	12.44

3.4.3. *Temperature Coefficient of Resistance (TCR) of Co<sub>3</sub>O<sub>4</sub> thick film.* The temperature coefficient of resistance (TCR) of pure Co<sub>3</sub>O<sub>4</sub> thick films is calculated by using equation (6). Temperature coefficient of resistance is found negative to pure Co<sub>3</sub>O<sub>4</sub> thick film samples. The negative sign indicates the semiconductor behaviour of the prepared pure Co<sub>3</sub>O<sub>4</sub> thick films. Low resistivity of cobalt oxide thick film samples corresponds to a high TCR value or vice versa. TCR of pure Co<sub>3</sub>O<sub>4</sub> unannealed thick film is found  $-0.0115/k$ . The observed value of TCR decreases as annealing temperature increased.

To obtain the value of T.C.R. using graph following equation is used

$$\text{TCR}(\alpha) = \frac{1}{R_0} \frac{\Delta R}{\Delta T} = \frac{\text{Slope}}{R_0}, \quad (5)$$

per degree Kelvin.

3.4.4. *Activation energy of Co<sub>3</sub>O<sub>4</sub> thick films.* The activation energies at the low temperatures and the high temperatures of prepared spinel type Co<sub>3</sub>O<sub>4</sub> thick films were calculated using Arrhenius plot. Fig. 4(b) shows graph of  $\log R$  in ohm versus reciprocal of temperature ( $1/T$ ) in Kelvin for Co<sub>3</sub>O<sub>4</sub> thick films. The Arrhenius plot has two distinct regions of temperature namely low and high temperature region. The annealing temperature of films is an important quantity to decide the transition temperature from low region to high region. The observed values of activation energy for Co<sub>3</sub>O<sub>4</sub> unannealed thick film found to be  $1.89 \times 10^{-4}$  and  $5.62 \times 10^{-4}$  eV at low and at high temperature, respectively. The energy of activation within the low temperature region is low as compared to energy within the high temperature region because material passes from one conduction mechanism to a different. This region are regions of temperature conduction, during this region energy of activation decreases because a tiny low thermal energy quite sufficient for the activation of charge carriers to require part within the conduction process. Hence increase in conductivity within the lower temperature region may be attributed to the increase of charge mobility. It shows more thermal durability with increase in annealing temperature.

The activation energies are calculated by using the Arrhenius relation

$$R = R_0 e^{-\Delta E/k_B T}, \quad (6)$$

where,  $R_0$  is the pre-exponential factor,  $\Delta E$  is the activation energy,  $k_B$  is the Boltzmann constant and  $T$  is the absolute temperature.

The activation energy  $\Delta E$  for Co<sub>3</sub>O<sub>4</sub> films is calculated from the slope of the plot the  $\log R$  vs  $(1/T)$  and is given by  $\Delta E = 2.303k_B \times \text{slope of the graph}$ . At low and high temperatures, its values in electron volt are mentioned in table [14].

It shows that the electrical behaviour of the NPs was studied by measuring the dc conductivity as a function of temperature  $T$ , this results reveals that the materials are characterized by semiconductor behaviour i.e. by increasing the temperature, more and more charge carriers can overcome the energy barrier and participate in the electrical conduction is assigned to elevated temperatures provide enough energy for charge carriers to hop among sites or even from defects involving singly charged oxygen ions [17]. These oxygen defects would add additional charge carriers to increase conductivity.

#### 4. Conclusion

Cubic structured Co<sub>3</sub>O<sub>4</sub> thick films with different thickness have been successfully deposited on glass substrate by the simple, cost-effective screen-printing technique. The structural, morphological and electrical properties have been systematically investigated for Co<sub>3</sub>O<sub>4</sub> thick films with annealing temperature. The films were deposited at room temperature (unannealed) and annealed in the temperature range 250 to 400 °C. The XRD analysis reveals that Co<sub>3</sub>O<sub>4</sub> thick film shows a polycrystalline nature and cubic structure having a preferential orientation along the (311) plane. The high degree agglomeration of spherical shaped grains was observed. Increase in the thickness of the Co<sub>3</sub>O<sub>4</sub> films increased the crystallinity as well as morphological properties. The crystallite size calculated using Debye–Scherrer equation for strongest peak, locating at (311) plane at  $2\theta = 36.75^\circ$ , are estimated 18.52 nm. From SEM, observed that Co<sub>3</sub>O<sub>4</sub> nano particles are highly agglomerated and are spherical shaped with average particle size is 116.7 nm. Spherical grain size increases with respect to annealing temperature and its maximum 83.5 nm when thick film is unannealed. Surface area decreases from 20.60 to 12.698 m<sup>2</sup>/gm with increase in annealing temperature from 250 – 400 °C and is a minimum for unannealed film. The result shows grain size increases and specific surface area decreases as annealing temperature increased. Highly porous film shows high sensitivity. EDAX pattern shows that presence of chemical element as well as purity of Co<sub>3</sub>O<sub>4</sub> NPs. The EDAX results obtained for spinel type cobalt oxide thick are in good agreement with reported output. The dislocation density, lattice strain was calculated to obtain information about structural properties. The observed changes takes place due to point defects and crystallite size. The higher peak intensities are due to better crystallinity. From electrical characterization, resistivity decreases from 910.58 to 365.55  $\Omega\text{m}$  with increase in annealing temperature. It means that cobalt oxide thick films shows semiconductor behavior. The value of electrical conductivity and activation energy at high temperature increases  $1.09 \times 10^{-3}$  to  $2.74 \times 10^{-3} \Omega^{-1}\text{m}^{-1}$  and  $5.62 \times 10^{-4}$  to  $12.44 \times 10^{-4}$  eV as annealing temperature increased respectively. A study of these nanoparticles' temperature-dependent dc conductivity illustrated exponential behaviour confirming their semiconductive nature. Also, activation energy is affected by the sensor operating temperature. Additionally, the voids were filled up with the O<sub>2</sub> after annealing which enhanced the probability of main band transitions. From these results, we conclude that the annealing temperature strongly affects the structural, morphological and electrical properties of cobalt oxide thick films. However further investigation and optimization still need to be done for doped cobalt oxide thick films.

#### References

- [1] El Bachiri A., Soussi L., et al. Electrochromic and photoluminescence properties of cobalt oxide thin films prepared by spray pyrolysis. *Spectroscopy Letters*, 2019, **52** (1), P. 66–73.
- [2] Shinde M., Qureshi N., et al. Synthesis of Cobalt Oxide Nanostructures by Microwave Assisted Solvothermal Technique Using Binary Solvent System. *Physical Chemistry Communications*, 2015, **2** (1) P. 1–9.
- [3] Dhas C.R., Venkatesh R., et al. Visible light driven photocatalytic degradation of Rhodamine B and Direct Red using cobalt oxide nanoparticles. *Ceramics International*, 2015, **41** (8), P. 9301–9313.
- [4] Bilge S., Roussin L. F. Svitlana N. Review: Influences of Semiconductor Metal Oxide Properties on Gas Sensing Characteristics. *Frontiers in Sensors*, 2021, **2**, 657931.
- [5] Manickam M., Ponnuswamy V., et al. Influence of Substrate Temperature on the Properties of Cobalt Oxide Thin Films Prepared by Nebulizer Spray Pyrolysis (NSP) Technique. *Silicon*, 2016, **8**, P. 351–360.
- [6] Sethupathi N., Thirunavukkarasu P., et al. Deposition and optoelectronic properties of ITO (In<sub>2</sub>O<sub>3</sub>: Sn) thin films by Jet nebulizer spray (JNS) pyrolysis technique. *M. J. Mater. Sci.: Mater. Electron.*, 2012, **23** (1), P. 1087–1093.
- [7] Gustavo A.S., Camila M.B.S., et al. Sol-gel synthesis of silica-cobalt composites by employing Co<sub>3</sub>O<sub>4</sub> colloidal dispersions. *Colloids and Surfaces A: Physicochem. Eng. Aspects*, 2012, **395**, P. 217–224.
- [8] Azhar I.H., Sahar I.M. Preparation and characterization of Cu: Co<sub>3</sub>O<sub>4</sub>/Si heterojunction prepared by spray pyrolysis. *Energy Procedia*, 2017, **119**, P. 961–971.
- [9] Ngo V.N., Alfred J.S., Nini P., Linderoth S. Microstructure and thermoelectric properties of screen-printed thick-films of misfit-layered cobalt oxides with Ag addition. *J. of Electronic Materials*, 2012, **41** (6), P. 1–10.
- [10] Sook K.C., Zulkarnain Z., et al. Surface Morphology and Crystallinity of Metal Oxides in Nickel-Cobalt Binary System. *Sains Malaysiana*, 2012, **41** (4), P. 465–470.
- [11] Elsiddig M.S., Hasabo M.A., Ramadan M., Haythem S. Optical and Electrical Properties of Synthesized Cobalt Oxide (Co<sub>3</sub>O<sub>4</sub>) Nanoparticles Using Thermal Decomposition Method. *Int. J. of Software & Hardware Research in Engineering*, 2017, **5** (6), P. 49–54.
- [12] Yuxiao G., Yan W., et al. Carbon Nitride Decorated Ball-Flower like Co<sub>3</sub>O<sub>4</sub> Hybrid Composite: Hydrothermal Synthesis and Ethanol Gas Sensing Application. *Nanomaterials*, 2018, **132** (8), P. 1–11.
- [13] Noor M.K., Hanaa K.E., Nuha A.S.R. Electrochemical synthesis, characterization and evaluation of antioxidant activity of Co<sub>3</sub>O<sub>4</sub> nanoparticles and Co<sub>3</sub>O<sub>4</sub>/TiO<sub>2</sub> nanocomposite. *Eurasian J. of Biosciences*, 2020, **14**, P. 3595–3600.

- [14] Koli P.B., Kapadnis K.H., Deshpande U.G., Patil M.R. Fabrication and characterization of pure and modified  $\text{Co}_3\text{O}_4$  Nano catalyst and their application for photocatalytic degradation of eosine blue dye: a comparative study. *J. of Nanostructure in Chemistry*, 2018, **8**, P. 453–463.
- [15] Louardi A., Rmili A., et al. Effect of annealing treatment on  $\text{Co}_3\text{O}_4$  thin films properties prepared by spray pyrolysis. *J. of materials and Environmental Sciences*, 2017, **8** (2), P. 485–493.
- [16] Azhar I.H., Sahar I.M. Structural and Optical Properties of Copper- Doped Cobalt Oxide Thin Films Prepared by Spray Pyrolysis. *Int. J. of Engineering Sciences & Research Technology*, 2017, **6** (3), P. 527–534.
- [17] Ibrahim E.M.M., Ahmed M.A.D., Elshafaie A., Ahmed A.M. Electrical, thermoelectrical and magnetic properties of approximately 20-nm Ni-Co-O nanoparticles and investigation of their conduction phenomena. *Materials Chemistry and Physics*, 2017, **192**, P. 41–47.

---

*Submitted 14 August 2022; revised 14 September 2022; accepted 19 September 2022*

*Information about the authors:*

*Ujwala M. Pagar* – Department of Physics, H.P.T. Arts and R.Y.K. Science College, Nashik 422005, (M.S.) India; [ujwala-pagar7@gmail.com](mailto:ujwala-pagar7@gmail.com)

*Uglal P. Shinde* – Department of Physics, L.V.H. Arts, Science and Commerce College, Nashik 422005, (M.S.) India; [upshinde1965@gmail.com](mailto:upshinde1965@gmail.com)

*Conflict of interest:* the authors declare no conflict of interest.

## Transformation of siderite in the zone of hypergenesis

Pavel P. Fedorov<sup>a</sup>, Ivan A. Novikov<sup>b</sup>, Valery V. Voronov<sup>c</sup>, Lubov V. Badyanova<sup>d</sup>, Sergey V. Kuznetsov<sup>e</sup>, Elena V. Chernova<sup>f</sup>

Prokhorov General Physics Institute of the Russian Academy of Sciences, Moscow, 119991, Russia

<sup>a</sup>ppfedorov@yandex.ru, <sup>b</sup>ivan.a.novikov@gmail.com, <sup>c</sup>voronov@lst.gpi.ru, <sup>d</sup>badyanova.lubov@gmail.com, <sup>e</sup>kouznetzovsv@gmail.com, <sup>f</sup>e-chernova@yandex.ru

Corresponding author: Pavel P. Fedorov, ppfedorov@yandex.ru

**ABSTRACT** The structure of siderite aggregates and its weathering products from the Ruza deposit, Moscow Region, has been studied by X-ray phase analysis and electron microscopy. The initial siderite is a dense FeCO<sub>3</sub> aggregate of micron-sized grains. The nodules are covered with an ocher weathered crust, the color intensity of which varies from light yellow to brown-black. A successive replacement of siderite by FeOOH goethite and lepidocrocite was revealed. It is accompanied by a sharp decrease in volume (~ 30 %) and the formation of a microporous structure.

**KEYWORDS** carbonates, siderite, weathering, oxidation, nanomineralogy

**ACKNOWLEDGEMENTS** The equipment of the Collective Use Centers of the GPI RAS and IGEM RAS was used in this work.

**FOR CITATION** Fedorov P.P., Novikov I.A., Voronov V.V., Badyanova L.V., Kuznetsov S.V., Chernova E.V. Transformation of siderite in the zone of hypergenesis. *Nanosystems: Phys. Chem. Math.*, 2022, **13** (5), 539–545.

### 1. Introduction

Siderite (a ferrous II carbonate FeCO<sub>3</sub>) is a widespread mineral [1–4]. It is isostructural to calcite, crystallizes in hexagonal crystal system, SSG *R-3m*. In spite of its widespread occurrence, siderite is of limited use as a crude for ferrous metallurgy. The products of natural alteration of siderite in the hypergenesis zone, known as *iron hat*, or limonite, has a greater practical importance. The common popular name “bog ore” is very unfortunate, because the genesis of these formations, as a rule, has nothing to do with swamps. Many siderite deposits are of industrial importance, in particular, the Bakal deposit (the South Urals, the Chelyabinsk region) [5–10]. But the direct use of siderite ore from this and similar deposits is impossible. The preparation of raw materials for the subsequent steelmaking includes the obligatory energy-consuming process of annealing in an oxidizing flame, which only partially repeats the weathering process.

The purpose of this work is a study of the siderite transformation mechanism in zone of hypergenesis, i.e. in the process of weathering.

### 2. Experimental section

#### 2.1. Materials

Among many samples of siderite of sedimentary origin, we chose one with a small amount of chemical and mechanical impurities. The sample was taken from a small deposit of siderite, which is exposed near Ruza (Moscow Region) [11]. A distinctive feature of this deposit is low content of magnesium in siderite. According to rough estimates, about 30 000 tons of ore were excavated and used for metallurgical production in the Middle Ages. Partially limonitized siderite forms lenses in the upper part of the Carboniferous limestones. Siderite forms solid masses of a grayish-greenish color and is covered with yellow-brown crusts of iron hydroxides (Fig. 1). We will call the totality of iron hydroxides, mechanical impurities and associated minerals “limonite”, despite the fact that this is not a strict mineralogical term. Associated minerals are calcite CaCO<sub>3</sub>, nickel-bearing rancieite (Ca, Mn<sup>2+</sup>, Ni<sup>2+</sup>)<sub>0.2</sub>(Mn<sup>4+</sup>, Mn<sup>3+</sup>)O<sub>2</sub> · 0.6H<sub>2</sub>O, and natrojarosite NaFe<sub>3</sub><sup>3+</sup>(SO<sub>4</sub>)<sub>2</sub>(OH)<sub>6</sub>.



FIG. 1. General view of the sample: central zone – siderite (\*), outer zones - cocentric aggregate of limonite (natural oxidation products)

## 2.2. Characterization

X-ray diffraction analysis (XRD) of the samples was carried out on a BRUKER D8 ADVANCE diffractometer with  $\text{CuK}\alpha_1$  radiation. The lattice parameters and sizes of domains of coherent scattering ( $D$ ) were calculated using the TOPAS software Version 4.2.0.2 ( $R_{wp} < 5$ ).

The determination of the concentration of major oxides and some trace elements in natural samples was performed by X-ray fluorescence analysis (XRF) on a sequential vacuum spectrometer (with wavelength dispersion), AxiosmAX model by PANalytical (Netherlands) ([www.panalytical.com](http://www.panalytical.com)). The spectrometer is equipped with 4 kW X-ray tube with Rh anode. Maximum tube voltage 60 kV, maximum anode current 160 mA.

The preparations were made from sample powder by melting with a mixture of lithium borates at a temperature of 1150 °C to analyze of rock-forming oxides. From the resulting borate melt, glassy disks were formed, which were analyzed in the spectrometer. To determine trace elements, sulfur and chlorine, preparations were made from sample powder by cold pressing with plastic filler under a pressure of 30 tons into tablets with diameter of 32 mm, which were analyzed in the spectrometer.

The weight loss on calcination (WL) was measured from samples dried at 110 °C according to the NSAM VIMS 118-X method at a temperature of 1000 °C.

For visualization, we used a scanning electron microscope EVO LS10 (Zeiss, Germany) with  $\text{LaB}_6$  cathode. The observations were performed with accelerating voltage of 21 kV with backscattered (reflected) electron detector (BSE). Microstructure of specimen was visualized in the low vacuum mode (EP, 70 Pa) with the working distance of 6.5 – 4.5 mm.

Thermogravimetry analysis was made with a Q-1500 D derivatograph in platinum crucibles at the sample weight of 300 mg and the rate of heating under air of 10 °C/min.

## 3. Results and discussion

According to chemical analysis, the original siderite and its oxidation products have a similar set of main impurities (Table 1). For the main components, a significant decrease in the content of calcium and an increase in the content of iron and silicon in natural limonite can be noted in relation to the original substrate. The behavior of impurities is different. The magnesium content decreases when the transition of siderite to limonite takes place, while sodium and sulfur content increases. Phosphorus and manganese remain unchanged. The evolution of the chemical composition during the natural oxidation of siderite looks logical. Since the active agent during weathering is water, the depletion of the initial substrate in alkaline earth elements is natural. The increase in the content of sodium and sulfur in the oxidation products is probably due to the admixture of natrojarosite. The formation of natrojarosite at this deposit occurred during the later modifications of the mineral substance is not associated with the weathering process and is not considered in this study.

The results of the X-ray study are shown in Fig. 2, electron microscopy data are shown in Fig. 3. As it is seen from the SEM data, the original mineral consists of  $\text{FeCO}_3$  grains 5 – 10  $\mu\text{m}$  in size. The size of the regions of coherent reflection scattering with the Miller index (104) was  $D = 26$  nm.

According to XRD data, white edging at the boundary of the weathering zone contains, along with the main mass of siderite, an initial amount of goethite. The yellow (light ochre) zone contains mostly goethite with some siderite. The dark brown zone is mainly composed of goethite. There is also a small amount of lepidocrocite (Fig. 2). The size of the coherent scattering regions for the goethite phase in reflection (110) was  $D = 14 - 18$  nm.

TABLE 1. Chemical composition of siderite and limonite

	WL 1000 °C (%)	WL	(wt %)											
			Na <sub>2</sub> O	MgO	Al <sub>2</sub> O <sub>3</sub>	SiO <sub>2</sub>	K <sub>2</sub> O	CaO	TiO <sub>2</sub>	MnO	FeO (total)	P <sub>2</sub> O <sub>5</sub>	Cl	SO <sub>3</sub> (total)
Siderite	31.61	(CO <sub>2</sub> )	0.05	0.67	1.22	2.96	0.09	2.83	0.02	0.58	59.46	0.138	0.01	0.03
SD	0.36		0.01	0.09	0.13	0.20	0.02	0.19	0.01	0.08	0.48	0.029	0.01	0.01
Limonite	14.36	(H <sub>2</sub> O)	0.33	0.34	1.41	4.85	0.07	0.76	<0.01	0.67	76.61	0.163	0.05	0.11
SD	0.31		0.05	0.05	0.16	0.33	0.02	0.09	—	0.09	0.54	0.034	0.02	0.01

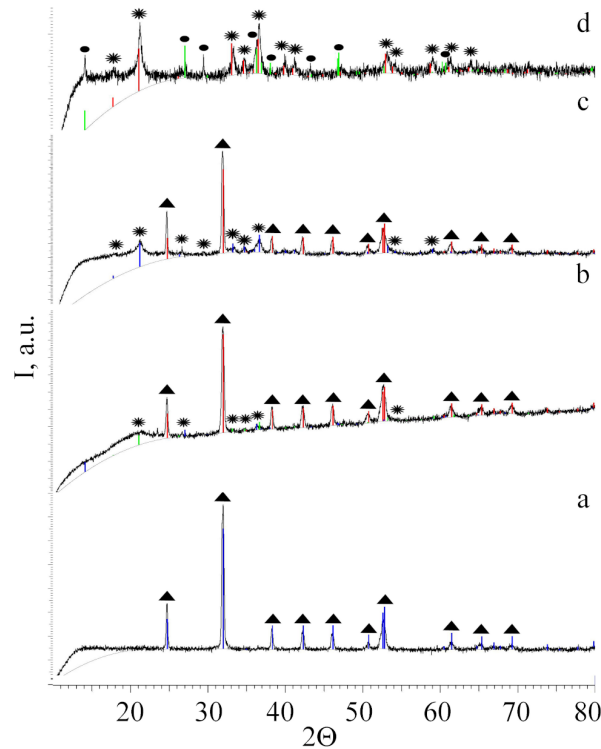


FIG. 2. X-ray diffraction patterns of siderite and weathering crust samples: a – central part ( $D_{\text{siderite}} = 26$  nm), b – bleaching zone ( $D_{\text{siderite}} = 23$  nm), c – light ocher zone ( $D_{\text{siderite}} = 28$  nm,  $D_{\text{hetite}} = 14$  nm), d – dark brown zone ( $D_{\text{hetite}} = 18$  nm). Triangles – siderite  $\text{FeCO}_3$ , asterisks – goethite  $\text{FeOOH}$ , dots – lepidocrocite  $\text{FeOOH}$

Based on the initial and final products, the weathering reaction can be written as follows:



Goethite and lepidocrocite have the same chemical composition:  $\text{FeOOH}$ . Thus, in accordance with equation (1), weathering of siderite is not a pure oxidation process: in addition to oxygen, which provides an increase in the valence of iron from +2 to +3, the reaction also requires the participation of water. At the first stage of the reaction, water and oxygen, apparently, penetrate into the siderite mass along the grain boundaries.

It should be noted that reaction (1) is accompanied by a very sharp decrease in volume. Molar volume of goethite is as follows  $V = 138.60 \text{ \AA}^3$  (JCPDS card #29-713),  $Z = 4$ ,  $V/Z = 34.65 \text{ \AA}^3$ , for siderite:  $V = 293.53 \text{ \AA}^3$  (JCPDS card #73-6522),  $Z = 6$ ,  $V/Z = 48.86 \text{ \AA}^3$ .

Thus, the shrinkage is 29 %. Note that in the remarkable work of Zemyatchensky [12], performed in the pre-X-ray period, the shrinkage value of 31 % was calculated based on the experimental values of the density of minerals. Reaction (1), once started, leads to the appearance of shrinkage cavities and microcracks, which facilitates the delivery of oxygen and the removal of the reaction product  $\text{CO}_2$  from the front of the chemical reaction and ensures its further flow.

Electron microscopy reveals the details of this process (Fig. 3). In the process of weathering, the contours of the initial grains, originally formed by siderite, practically do not change, which can be seen from a comparison of

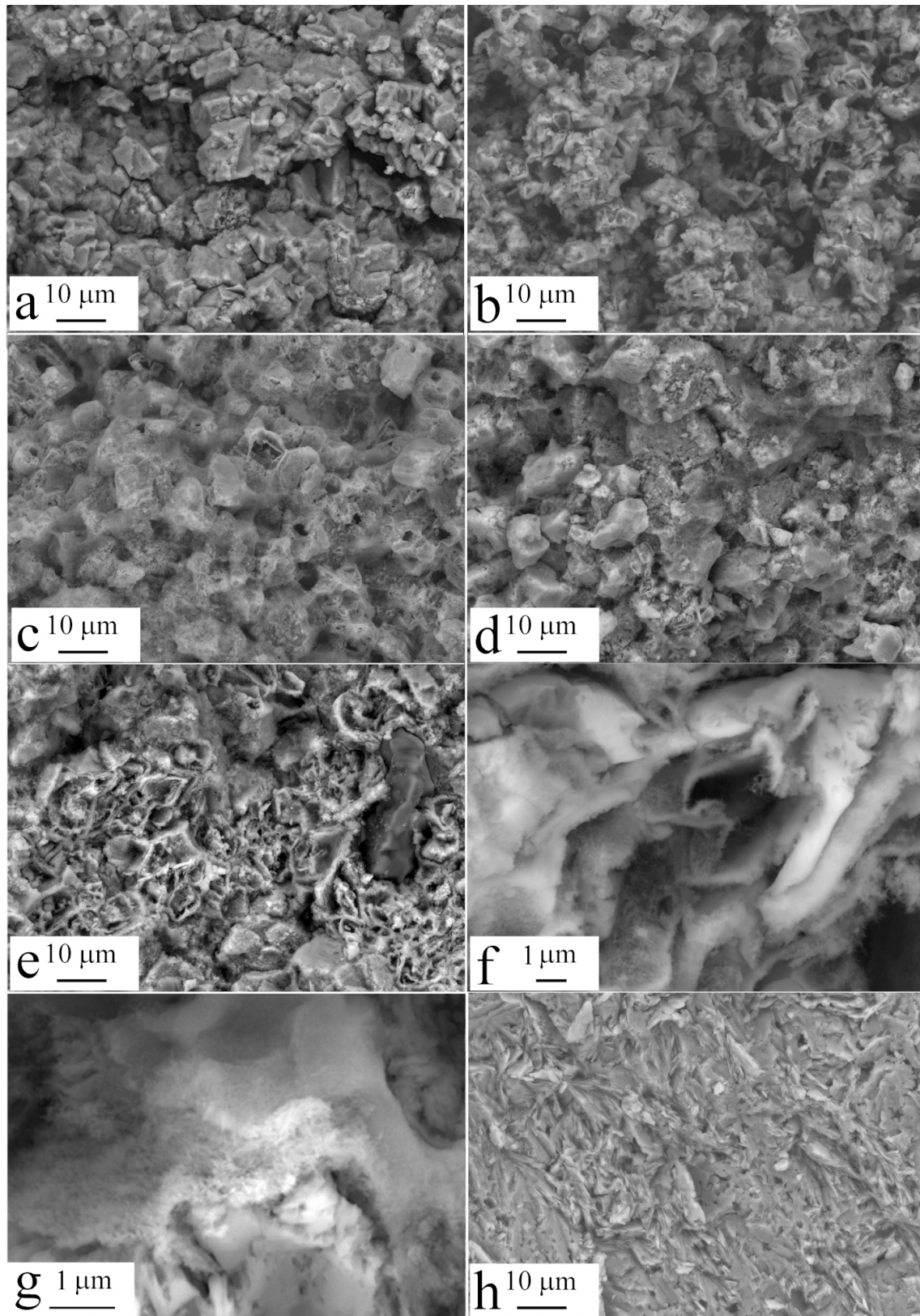


FIG. 3. Micrographs of siderite samples and weathering products. a – original siderite, b – bleaching zone, c – light ocher zone, d, e, f, g – brown zone, h – dark brown zone (goethite-lepidocrocite aggregate)

Figs. 3(a–d). However, this is only a visual resemblance. Siderite grains are replaced by a porous (spongy) aggregate of iron hydroxides.

Details of the formation of porous aggregate can be seen at the microscale (Figs. 3(e–g)). The resulting goethite particles shrink into two-dimensional films. At the beginning of the process, these films follow the contour of the original siderite grain. Further corrosion of siderite occurs with a decrease in the size of its single crystals and with their partial fragmentation *in situ* along cleavage planes (Fig. 3(f)). Periodically formed two-dimensional films of goethite repeat the shape of the surface of continuously decreasing siderite crystals and their fragments. The nature of the periodicity is not entirely clear. During the reaction, the surface of the initial grain recedes, but until a certain moment the cavity is filled with reaction products, and the resulting film of goethite nanocrystals adjoins siderite. Then the agglomerate of the reaction products and the original crystal are separated. For some time, the two-dimensional film continues to accept the reaction products and thicken without contact with the receding surface of the siderite crystal. The gap between them increases to 0.1 – 0.4 mm, which is probably the threshold value that partially determines the nature of the periodicity of the process at the nanoscale. Upon reaching this value, a new reaction layer is nucleated directly on the surface of the reduced siderite microcrystal, and the process is repeated.

At the microscale, this process leads to formation of a box-like (shell-shaped) structure with microcavities, open for access and removal of reagents (Figs. 3(f,g)). The proportion of free volume in these grains is about 30 % according to calculations.

According to XRD data, the size of the coherent scattering regions *D* of siderite practically does not change (Fig. 2).

Thus, reaction (1) describes a system with positive feedback. Such systems are characterized by nonlinear dynamics, which leads to periodic reaction.

The same periodicity is observed at the macroscale. The structure of the aggregate shows alternation of yellow and brown concentric zones in the crust around the core of initial siderite, similar to Liesegang rings [13, 14] (Fig. 1). The yellow and brown zones correspond to different degrees of goethite filling of the cavities in the spongy aggregate. Within the brown zones, the primary microscopic picture of the porous siderite oxidation product changes due to the filling of microscopic cavities with newly formed goethite and recrystallization (Fig. 3(h)). Despite this, the general appearance of the concentric-zonal aggregate fully confirms the deficient nature of the reaction in terms of volume. Cavities can be seen between the zones, and contraction cracks across the layers. The completed weathering process leads to the formation of hollow geodes, which are often found in the deposit.

As we have shown, at the micro level, the newly formed goethite aggregate repeats the contours of siderite grains, and at the macro level, the limonite zones repeat the primary contours of the siderite ore block. This situation can be described in terms of pseudomorphosis [15, 16], but not in terms of topotaxy [17, 18]: topotaxy in the narrow sense of the word implies an oriented growth of solid reaction products on the initial substrate.

There is a noticeable analogy of the discussed reaction with the process of interaction of calcium carbonate with a solution of potassium fluoride, in which the volume of fluorite nanoparticles formed is about 2/3 of the initial volume of calcium carbonate micrograins [19, 20].

It is the microporosity of the weathering products of siderite that ensures their successful use in ferrous metallurgy as iron ore [12]. Although it is energetically much more profitable to restore metallic iron from compounds in the +2 oxidation state than +3, kinetic difficulties make it impossible to use FeCO<sub>3</sub> in this capacity, because the density of siderite aggregates blocks the penetration of the reducing agent – carbon monoxide – into the volume. Weathering products differ radically from the original material in this respect.

The process of change in the hypergenesis zone differs significantly from the process of artificial oxidation of siderite ores, carried out in the preparation of the charge for the blast-furnace and converter processes [8–10].

The results of DTA heating a siderite sample under air are shown in Fig. 4. Weight loss starts at 385 °C and ends at 539 °C. The process has a two-stage character. According to XRD data (Fig. 5), the final product is hematite Fe<sub>2</sub>O<sub>3</sub> with a small admixture of magnetite Fe<sub>3</sub>O<sub>4</sub>. The sequence of oxidation can be described by the following reactions:



#### 4. Conclusion

Transformation of siderite in the zone of hypergenesis (weathering reaction) is not oxidation in its pure form, because it includes the mandatory participation of water. The transformation of minerals in this case does not occur through dissolution followed by precipitation [5]. We also did not record the formation of an amorphous phase in the weathering crust [3]. The process occurs with the preservation of the shape and volume of the original siderite grains. However, due to a sharp decrease in volume during the transformation of siderite into goethite, a microporous structure is formed. The weathering process of siderite belongs to the field of nanomineralogy.

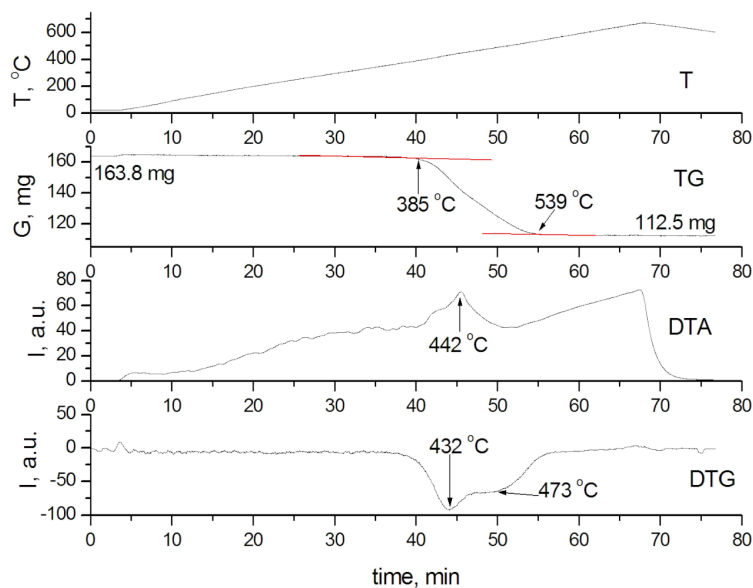


FIG. 4. Derivatogram of a siderite sample

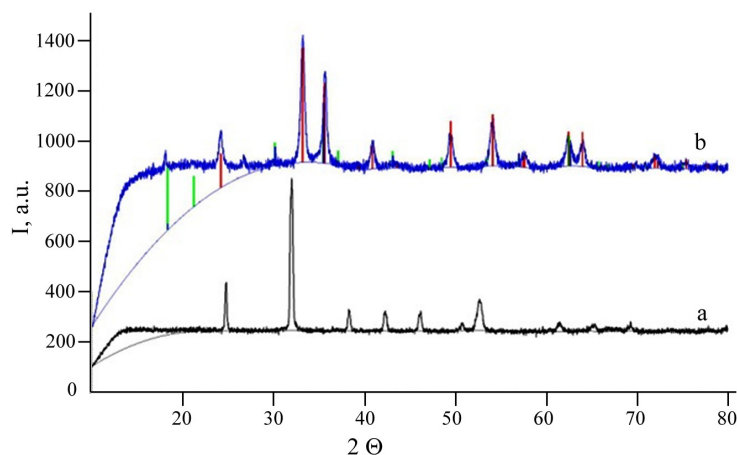


FIG. 5. XRD of the original sample (a) and the sample after thermogravimetry (b)

## References

- [1] Godovikov A.A. *Mineralogy*. M.: Nedra, 1983 (in Russian).
- [2] Kholodov V.N., Butuzova G.Yu. Problems of Siderite Formation and Iron Ore Epochs: Communication 2. General Issues of the Precambrian and Phanerozoic Ore Accumulation. *Lithology and Mineral Resources*, 2004, **39** (6), P. 489–508.
- [3] Kholodov V.N., Butuzova G.Yu. Siderite Formation and Evolution of Sedimentary Iron Ore Deposition in the Earth's History. *Geology of Ore Deposits*, 2008, **50** (4), P. 299–319.
- [4] Liao Shipan, Liang Tongrong, Zeng Mingguo. Geochemical Characteristics of Gossans Related to Siderite Deposits in Carbonate Strata, Western Guizhou. *Geochemistry*, 1983, **2** (4), P. 279–292.
- [5] Yanitskii Ya.L., Sergeev O.P. *Bakal iron ore deposits and their genesis*. M.: USSR Acad. Sci., 1962 (in Russian).
- [6] Timeskov V.A. *Mineralogy of carbonate ores and host carbonate rocks of the Bakal iron ore deposit in the South Urals*. Kazan': Kazan' University, 1963 (in Russian).
- [7] Ellmies R., Voigtländer G., et al. Origin of giant stratabound deposits of magnesite and siderite in Riphean carbonate rocks of the Bashkir mega-anticline, western Urals. *Geologische Rundschau*, 1999, **87** (4), P. 589–602.
- [8] Klochkovskii S.P., Smirnov A.N., Savchenko I.A. Development of physical and chemical bases for the integrated use of high-magnesian siderites. *Vestnik G.I. Nosov MGTU*, 2015, **1**, P. 26–31 (in Russian).
- [9] Matyukhin V.I., Melamud S.G., et al. The investigation of firing of siderite small fractions in a rotary furnace. *Izvestiya. Ferrous Metallurgy*, 2015, **58** (9), P. 652–657 (in Russian).
- [10] Sheshukov O.Yu., Mikheenkova M.A., et al. Changes in phase composition of siderites of the bakal deposit at heating. *Izvestiya. Ferrous Metallurgy*, 2018, **61** (11), P. 891–897 (in Russian).
- [11] URL: <https://webmineral.ru/minerals/image.php?id=5030>
- [12] Zemyatshenskii P. Iron ores of the central part of European Russia. *Proceedings of the Society of Naturalists*, St.-Petersburg, 1889, **20**.
- [13] Shemyakin F.M., Mikhalev P.F. *Physico-chemical periodic processes*. L.: USSR Acad. Sci., 1938. (in Russian)
- [14] Summ B.D., Ivanova N.I. The use of objects and methods of colloid chemistry in nanochemistry. *Russian Chemical Rev.*, 2000, **69**, P. 911.

- [15] Glover E.D., Sippel R.F. Experimental pseudomorphs: replacement of calcite by fluorite. *American Mineralogist*, 1962, **47**, P. 1156–1165.
- [16] Glikin A.E. *Polymineal metasomatic crystallogenesis*. St.-Petersburg: Neva, 2004 (in Russian).
- [17] Shannon R., Rossi R. Definition of Topotaxy. *Nature*, 1964, **202**, P. 1000–1001.
- [18] Oleinikov N.N. Effect of topochemical memory: nature and role in the synthesis of solid-phase substances and materials. *Rus. Chim. J.*, 1995, **39**, P. 85–93.
- [19] Fedorov P.P., Luginina A.A., Alexandrov A.A., Chernova E.V. Transformation of calcite CaCO<sub>3</sub> to fluorite CaF<sub>2</sub> by action of KF solution. *J. Fluorine Chemistry*, 2021. **251**, 109898.
- [20] Fedorov P.P., Luginina A.A., et al. Interaction of calcium and strontium carbonates with KF solution. *Russ. J. Inorg. Chem.*, 2022, **8**.

---

*Submitted 3 July 2022; revised 15 September 2022; accepted 19 September 2022*

*Information about the authors:*

*Pavel P. Fedorov* – Prokhorov General Physics Institute of the Russian Academy of Sciences, Moscow, 119991, Russia; ORCID 0000-0002-2918-3926; ppfedorov@yandex.ru

*Ivan A. Novikov* – Prokhorov General Physics Institute of the Russian Academy of Sciences, Moscow, 119991, Russia; ORCID 0000-0003-4898-4662; ivan.a.novikov@gmail.com

*Valery V. Voronov* – Prokhorov General Physics Institute of the Russian Academy of Sciences, Moscow, 119991, Russia; ORCID 0000-0001-5029-8560; voronov@lst.gpi.ru

*Lubov V. Badyanova* – Prokhorov General Physics Institute of the Russian Academy of Sciences, Moscow, 119991, Russia; badyanova.lubov@gmail.com

*Sergey V. Kuznetsov* – Prokhorov General Physics Institute of the Russian Academy of Sciences, Moscow, 119991, Russia; ORCID 0000-0002-7669-1106; kouznetzovsv@gmail.com

*Elena V. Chernova* – Prokhorov General Physics Institute of the Russian Academy of Sciences, Moscow, 119991, Russia; ORCID 0000-0001-7401-5019; e-chernova@yandex.ru

*Conflict of interest:* the authors declare no conflict of interest.

## Synthesis and optical properties of MnSe nanostructures: A review

Runjun Sarma<sup>1,a</sup>, Munmi Sarma<sup>2</sup>, Manash Jyoti Kashyap<sup>3,b</sup><sup>1</sup>Mehr Chand Mahajan DAV College for Women, Sector 36, Chandigarh, India<sup>2</sup>Sensors & Biosensors group, Autonomous University of Barcelona, Spain<sup>3</sup>Polymer Technology Consultant, Chandigarh, India<sup>a</sup>runjun2018chd@gmail.com, <sup>b</sup>manashjk@gmail.com

Corresponding author: Runjun Sarma, runjun2018chd@gmail.com

**ABSTRACT** Manganese selenide is an important diluted magnetic semiconductor (DMS) material having both optical and magnetic properties especially in the nanometer scale. Because of the phenomena of polymorphism exhibited by MnSe, it can be an interesting material for controlled polymorphism synthesis by using different synthesis procedures. In this review article, we discuss various synthesis procedures (wet chemical and deposition methods) of different MnSe nanostructures and their optical properties. The dependence of various optical properties (UV-Vis spectroscopy, photoluminescence spectroscopy and time resolved photoluminescence spectroscopy) of the MnSe nanostructures on the methods of synthesis is discussed in this article. We are specially focused on the reaction parameters of synthesis process that influence on the optical properties of the MnSe nanostructures. Moreover, the Stokes shift is calculated for the MnSe nanostructures synthesized by different procedures. Large Stokes shifts observed for MnSe nanostructures create a promising potentials in various applications including multiplex assay, bio-imaging, bio-sensing etc.

**KEYWORDS** diluted magnetic semiconductor, chalcogenides, stokes shift, wet chemical methods, deposition methods

**FOR CITATION** Sarma R., Sarma M., Kashyap M.J. Synthesis and optical properties of MnSe nanostructures: A review. *Nanosystems: Phys. Chem. Math.*, 2022, **13** (5), 546–564.

### 1. Introduction

Diluted magnetic semiconductors (DMS) known as semi-magnetic semiconductors are a new class of materials which is prepared by doping a host material commonly chosen from amongst II–VI, III–VI, IV–VI group semiconductor materials with a small concentration (< 10 %) of magnetic ions of transition metals [1–4]. Substitutional magnetic atoms such as Mn, Co, Fe, etc., make up a part of the lattices of the host material. The combinations of magnetic and non-magnetic materials lead to the co-existence of both magnetic and semiconducting properties in the alloyed DMS. The most extensively studied and most thoroughly described materials of this type are the  $A_{1-x}^{II}Mn_xB^{VI}$  alloys in which a fraction of the cation sites of the host semiconductor are replaced by manganese ions [2, 5, 6]. In manganese doped II-VI semiconductors, as the valency (+2) of Mn atoms is the same as that of cations of the host material,  $Mn^{2+}$  ions can be easily incorporated in the cationic sites. DMS of  $A_{1-x}^{II}Mn_xB^{VI}$  type are of interest for several distinct reasons. Their ternary nature opens up the possibility of “tuning” the lattice constant and band parameters by varying the concentration of Mn atoms. Furthermore, the presence of localized magnetic ions in these semiconductor alloys leads to an exchange interaction between the *sp* band electrons of the host semiconductor and the *d* orbital electrons associated with  $Mn^{2+}$  ion. This results in extremely large Zeeman splitting (order of tens of meV) of electronic band structures providing diverse magneto-optical effects [7, 8]. There are various applications in which the DMS are widely used, such as in the production of LEDs [9], spin transistors [10] capacitors [11], biological imaging [12], etc.

Manganese selenide belongs to the group of chalcogenides and are essentially binary-semiconductor systems denoted by  $Zn_{1-x}Mn_xSe$  where *x* equals 1 and, correspondingly, is a member of the family of these magnetic semiconductors signified by the absence of zinc ( $Zn_{1-1}$ ). Manganese selenide can be found in nature as three polymorphs: i) two cubic modified  $\alpha$ -MnSe, existing as a rock salt structure (RS) and  $\beta$ -MnSe existing as zinc blende (ZB) [13], and ii) hexagonally modified wurtzite structure (WZ), existing as  $\gamma$ -MnSe [14, 15]. In  $\alpha$ -MnSe, selenium ( $Se^{2-}$ ) anions are expanded in FCC lattice arrangements while  $Mn^{2+}$  ions occupy the octahedral sites. In  $\beta$ -MnSe, though the  $Se^{2-}$  anions are expanded in FCC lattice arrangements, the  $Mn^{2+}$  ions are located in half of the tetrahedral sites.  $\gamma$ -MnSe crystal structures comprises HCP lattice of  $Se^{2-}$  ions with half of the tetrahedral sites occupied by the  $Mn^{2+}$  ions. Fig. 1 shows schematic diagram of a crystal of three polymorphs of MnSe.

The polymorphic forms of MnSe differ in their stability of existence. While the octahedrally coordinated rock salt structure of cubic modified  $\alpha$ -MnSe is naturally stable, the  $\beta$ -MnSe existing as ZB and  $\gamma$ -MnSe existing as WZ are found to be metastable [15, 16]. Moreover, these polymorphic forms can be differentiated by their distinct magnetic

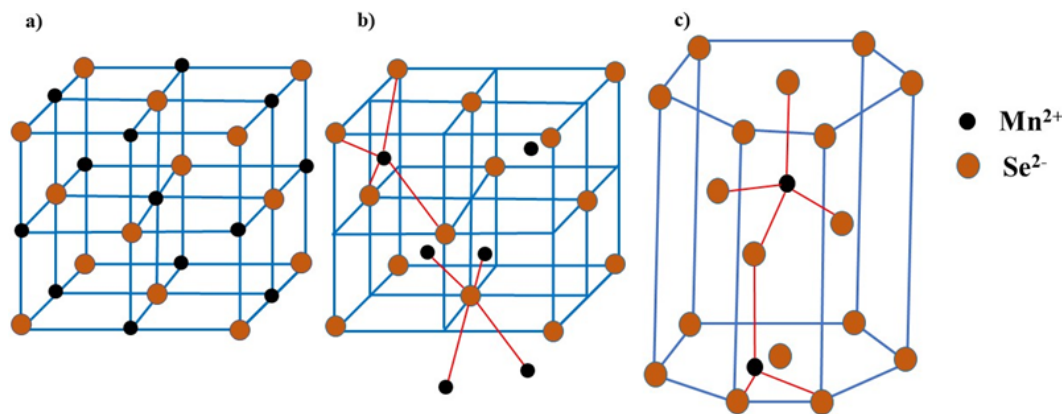


FIG. 1. Schematic diagram (not to scale) of cubic modified a)  $\alpha$ -MnSe; b)  $\beta$ -MnSe and hexagonally modified; c)  $\gamma$ -MnSe crystal structure

behavior. While  $\alpha$ -MnSe is antiferromagnetic [17] in nature,  $\beta$ -MnSe and  $\gamma$ -MnSe primarily exhibit ferromagnetic characteristics [18]. The  $\gamma$ -MnSe structures in spite of their instability are of significant interest due to their structural compatibility with semiconductor systems belonging to the II–VI groups that exhibit elevated fluorescent and photostable properties [19]. The fluorescent behavior [20,21], and magnetic response [22] characteristics of MnSe nanostructures can be collaboratively utilized in new applications requiring coordination of bright-fluorescent imaging in the presence of an externally applied magnetic field.

Amongst highly fluorescent semiconductor systems, Cd-based chalcogenide ones i.e., CdSe [23], CdTe [24], CdS [25], and CdSe/ZnS core-shell QDs [26] have attracted the maximum attention in biophysical research; particularly as tagging, labeling, and imaging agents. This takes place because of their unique properties such as large band gap tunability, bright emission response, high photostability, high quantum yield, narrow emission as well as wide absorption bands etc. [27,28]. Nevertheless, biocompatible nature of these QDs in cellular environments and under UV illumination remains questionable owing to the high toxicity level of free Cd, thereby limiting applications in nano-biotechnology and bioengineering fields are possible [29,30]. Since energy of the UV radiation is close to the chemical bond energy, there is a possibility of a process similar to photolytic dissolution releasing toxic heavy metal ions of  $\text{Cd}^{2+}$ . Replacing Cd by Mn (for instance, choosing MnS and MnSe instead of CdS and CdSe) would help one in reducing the toxicity level by avoiding the photobleaching of  $\text{Mn}^{2+}$  [31–34]. Knowing that,  $\text{Mn}^{2+}$  precursor is a hard Lewis acid [32,35] while  $\text{Cd}^{2+}$  precursor is a relatively softer one, the former is less reactive to the surrounding thus experiencing much lowered photobleaching as compared to the latter [32].

In this review article, we are focused on synthesis procedures of different MnSe nanostructures and their optical properties. Several bottom-up approaches ranging from wet chemical methods to vapor deposition methods used for the synthesis of MnSe nanostructures are summarized here. Moreover, variation of optical properties due to the methods of synthesis are discussed in the article. While discussing this behavior, various reaction parameters affecting their optical properties are also included.

## 2. Various synthesis procedures of MnSe nanostructures

Till now, a large number of synthesis methods have been developed for the preparation of MnSe nanostructures. The choice of an appropriate method of synthesis of nanostructures depends mainly on the targeted application and the technology involved. Various synthesis routes have their limitations but the choice of the most convenient method for preparation of nanostructures is influenced by the advantages or otherwise, encountered on account of different reaction conditions and the precursor or starting materials used. MnSe nanostructures can be synthesized by using various wet chemical and deposition methods. We discuss below different methods that are used for synthesizing MnSe nanostructures as reported by various research groups.

### 2.1. Wet chemical methods

Wet chemical methods are commonly used synthesis procedures where liquid dispersing media is used at one of the stages of the synthesis process. Hydrothermal, solvothermal and hot injection methods are various wet chemical methods that have been used for the synthesis of differently shaped crystalline MnSe nanostructures.

**2.1.1. Hydrothermal method.** Hydrothermal method is one of the simplest, environmentally friendly, cost-effective techniques for synthesis of various nanostructures. In spite of the low cost and simplicity, this process has various other advantages including i) highly controlled production of the nanostructures in terms of morphology, composition, structure etc., ii) fast reaction kinetics, iii) phase purity, iv) high crystallinity, v) narrow particle-size distributions etc. Water is used

as the main reaction medium in the hydrothermal synthesis process. The precursors and the other reacting materials to be used for a particular synthesis process are dissolved in water in a sealed autoclave vessel coated with Teflon layer. The reacting materials inside the autoclave are kept at a moderate temperature (usually higher than the boiling point of solvent, i.e.,  $> 100\text{ }^{\circ}\text{C}$ ) for a period of time (depending on the morphology and size) at a very high pressure. Fig. 2(a) depicts the schematic diagram of hydrothermal synthesis process.

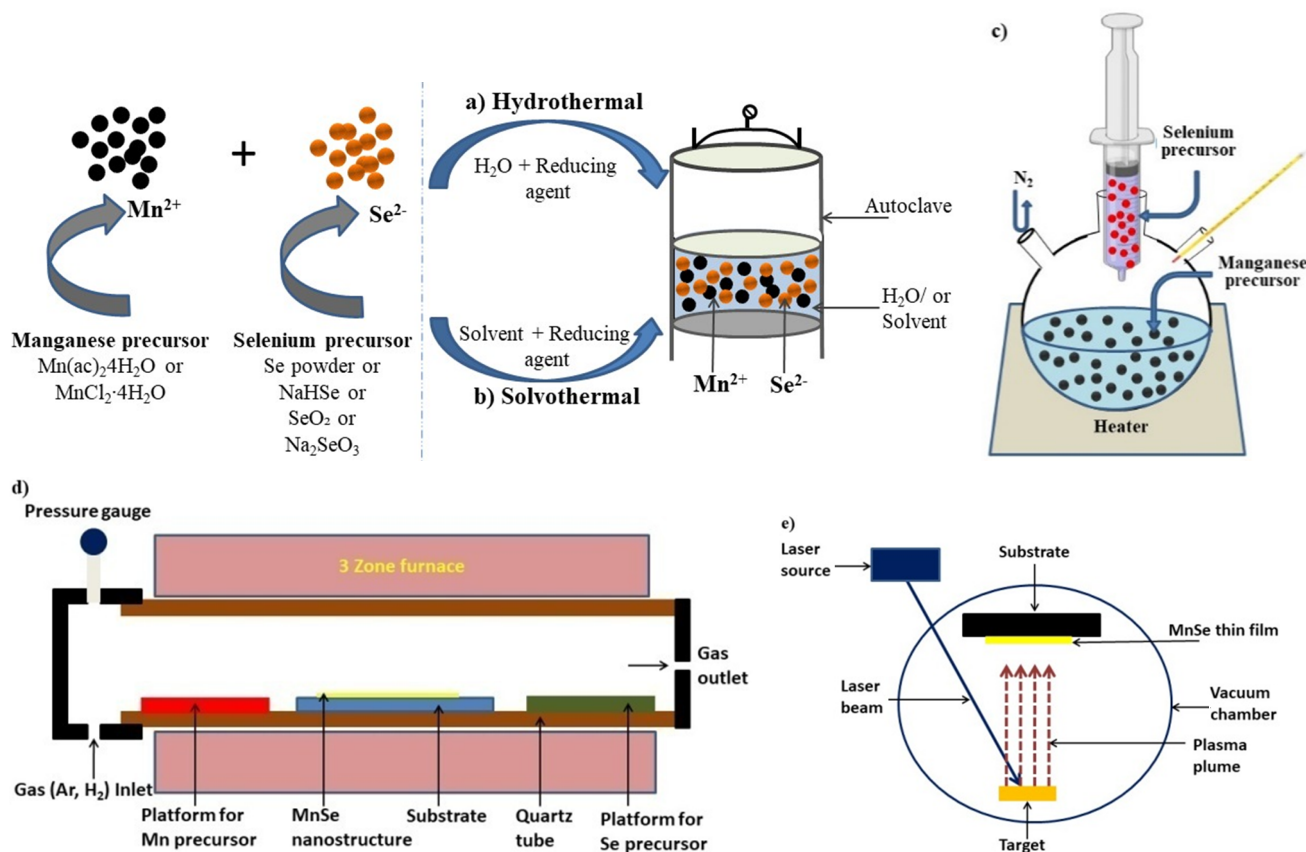


FIG. 2. Schematic diagram of various synthesis methods: a) hydrothermal; b) solvothermal; c) hot injection; d) chemical vapor deposition; e) pulsed laser deposition discussed in the article for the synthesis of MnSe nanostructures

The first hydrothermal synthesis of  $\alpha$ -MnSe in the form of nanorods was believed to be carried out via the reaction of aqueous alkaline Se powder (selenium precursor) with manganese acetate tetrahydrate ( $\text{Mn}(\text{CH}_3\text{COO})_2 \cdot 4\text{H}_2\text{O}$ ) (manganese precursor) in the presence of the reducing agent hydrazine hydrate. The reaction was carried out in the reaction temperature range of  $100 - 180\text{ }^{\circ}\text{C}$  for 12 h in a stainless-steel autoclave coated with Teflon layer. The research group used the hydrothermal synthesis procedure to study the effect of precursor concentration, time and temperature on the formation of MnSe. The pure phase of MnSe was found to be synthesized at a temperature of  $180\text{ }^{\circ}\text{C}$  and reaction time 6 h. Below  $180\text{ }^{\circ}\text{C}$  a combined phase of  $\text{MnSe}_2$  and MnSe was obtained. Morphologically different MnSe structures were obtained by varying the  $\text{Se}^{2-}$  ion concentration (in the reaction mixture) and controlling the reaction temperature [36]. In the presence of alkaline solution such as NaOH, commercially available Se powder dissolves to form  $\text{Se}^{2-}$  and  $\text{SeO}_3^{2-}$  ions in the reaction mixture on account of the formation and subsequent dissociation of  $\text{Na}_2\text{Se}$  and  $\text{Na}_2\text{SeO}_3$ . At low temperatures,  $\text{SeO}_3^{2-}$  reduces to elemental Se which is highly reactive as compared to the commercially available Se powder. Finally, this results in the production of  $\text{Se}^{2-}$  via deprotonation in alkaline condition. At high temperature ( $\sim 180\text{ }^{\circ}\text{C}$ ), largely available  $\text{Se}^{2-}$  concentrations, hinders the Se formation from  $\text{SeO}_3^{2-}$  which is responsible for forming of cubic sized nanocrystals. This results in higher driving force for the formation of rod structured nano MnSe compared to cubic structured. Whereas at the low temperature ( $\sim 100\text{ }^{\circ}\text{C}$ ), favorable condition (ideal  $\text{Se}^{2-}$  concentrations and Se formation) for the production of cubic shaped nano MnSe can be obtained [36].

A simpler hydrothermal method (a modification of the traditional hydrothermal method) can be used to synthesize monodisperse  $\alpha$ -MnSe rod like nanoparticles having average base diameter of 100 nm and tip diameter of 20 nm. In this method, sodium borohydride with reduced elemental selenium reacts with manganese precursor to produce MnSe nanorods by stirring at a low temperature of  $40\text{ }^{\circ}\text{C}$  for 60 minutes instead of using high temperature of  $180\text{ }^{\circ}\text{C}$  for 12 h at high pressure typical in hydrothermal synthesis methods [37].

Water solubility, biological stability, biocompatibility in MnSe QDs can be achieved by the use of coating (capping) agents/ligand molecules/surfactants in the hydrothermal synthesis method. However, depending on the chemistry and structure of these surface functionalized materials, the average size of the MnSe QDs significantly varies. Water solubility of MnSe nanoparticles have been achieved by using agents like Thioglycolic acid (TGA) and Sodium dodecyl sulfate (SDS) in the synthesis process. Amphiphilic ligands use their non polar part as a binding intermediate with the nanoparticle and the polar or hydrophilic groups on the other end ensures the water solubility of the same. The use of TGA molecules have led to the formation of spherically shaped, wurtzite (WZ) phase MnSe QDs of average size 5 nm. Substitution of TGA molecules with SDS surfactant in the synthesis of MnSe led to larger sized ( $\sim 14$  nm) QDs. The apparent difference in the sizes of the QDs produced by TGA and SDS routes in the hydrothermal method can be attributed to the short chained and long chain characteristics of TGA and SDS respectively [38]. Similarly,  $\alpha$ -MnSe QDs with sizes in the range of 5 to 11 nm can be obtained by using different capping agents such as cetyltrimethyl ammonium bromide (CTAB), TGA and dextran around the QDs while keeping other reaction parameters constant [39].

The size of the hydrothermally synthesized MnSe nanostructures was found to be pH dependent. With change of pH effective net charge on the surface of the nanostructure in the suspension changes which results in the formation of nanostructures of different size. Hexagonally shaped  $\alpha$ -MnSe nanodisc was synthesized by using the hydrothermal method with an increase in size from nanoscale to microscale by variation of pH value from 6 to 10 [40]. In contrast, spherical shaped MnSe QDs experienced decrease in hydrodynamic size (overall size of the particles covered by water molecules) from 46.5 to 20.3 nm with increasing pH of reacting medium from 2.5 to 9 [41].

The hydrothermal method was used to synthesize  $\alpha$ -MnSe nanoparticles of size in the range of 20 to 30 nm that was used to form a pseudocapacitive electrode material for supercapacitor [42]. Similarly, hydrothermally synthesized MnSe multilayered structures were formed by small quantities of microplates surrounded by many numbers of nanoplates were used to improve the performance of electrochemical energy storage devices [43]. Table 1 summarizes the data of MnSe nanostructures synthesized by hydrothermal method.

**2.1.2. Solvothermal method.** Solvothermal method is similar to the hydrothermal method used for the synthesis of various nanostructures. The mediums that can be used in solvothermal synthesis processes can be organic or inorganic solvents with high boiling point; but not water. The use of solvents offers high diffusivity, increased mobility of the dissolved ions thus allowing better mixing of the reagents. Moreover, the density, viscosity, and the molecular structure of solvents may strongly influence the properties of the final product. Similar to the hydrothermal method, chemical reactions in the solvothermal method are conducted in sealed autoclaves by heating both precursor and the solvent at high pressure and temperatures [44]. In this method, the autoclave is maintained at a temperature higher than the boiling temperature of the solvent. In spite of having other advantages as similar to hydrothermal method, another important advantage of the solvothermal method is that any material can be dissolved in the solvent by increasing the temperature and pressure to the critical points of the solvent. Fig. 2(b) depicts the schematic diagram of solvothermal synthesis process.

Solvothermal method was used for the synthesis of highly crystalline  $\alpha$ -MnSe nanostructures in nitrogen containing solvent ethylenediamine (en) by using  $\text{MnCl}_2 \cdot 4\text{H}_2\text{O}$  and selenium (Se) powder as Mn and Se precursors respectively at a temperature of 190 °C. The synthesized structures were of flaky morphology with irregular drapes of dimension 5 – 30 nm in width and 100 – 500 nm in length. However, the exact mechanism leading to the formation of these morphological nanostructures was not clearly understood [45].

Solvothermal process was used to synthesize MnSe nanostructures of various shapes, sizes and crystallographic phases by controlling various reaction parameters (Fig. 3). The effects of such parameters in controlling such behavior of the MnSe nanostructures are discussed below.

#### **i) The effect of route adopted for dispersion of the reactants into the solvent**

Nanospheres with diameter of  $\sim 200$  nm were synthesized via vigorous pre-stirring of the mixture of Se precursor (Se powder), Mn precursor ( $\text{MnCl}_2 \cdot 4\text{H}_2\text{O}$ ), reducing agent ( $\text{KBH}_4$ ) and the solvent (ethanol amine, EA) used in the solvothermal method. The nanospheres were then converted to nanorods (diameter of 50 – 60 nm and lengths of 1 – 3  $\mu\text{m}$ ) and nanowires (diameter 5 – 10 nm) with additional ultrasonic pretreatment of the reaction mixture mentioned above, for 20 min before autoclaving.

The route adopted for dispersion of the reactants into the EA solvent was found to directly influence the shape of the resulting MnSe entities formed. Direct addition of the Mn and Se precursors without stirring or ultrasonication resulted in the formation of  $\alpha$ -MnSe nanospheres. Vigorous stirring of the reaction mixture before the start of the solvothermal process was inferred to have accelerated the speed of reaction of the Mn and Se precursors as also the nucleation process, thus resulting in the MnSe microspheres. Partial substitution of the stirring process by ultrasonication of the reaction mixture resulted in MnSe nanorods. It was concluded that the ultrasonication process was promoting the preferential complexation of  $\text{Mn}^{2+}$  ions with ethanol amine solvent; and the resultant isotropic nature of the reaction mixture led to the formation of MnSe nanorods [46].

#### **ii) The effect of mixtures of various of solvents used**

The solvothermal process carried out in a three-neck flask heated at  $\sim 235$  °C for 4 hours under the flow of Ar gas in a Schlenk line resulted in the formation of WZ MnSe nanostructures. The solvent used in this process was a mixture

TABLE 1. Summarized data of MnSe nanostructures synthesized by hydrothermal method\*

Year Ref.	Mn precursor/ Se precursor	Crystallographic phase	MnSe product	Temperature (°C)	Average size (nm)	Method used for determining the size
2004, [36]	Mn(CH <sub>3</sub> COO) <sub>2</sub> · 4H <sub>2</sub> O/Se powder	$\alpha$ -MnSe	Nanorod	180	200	Transmission electron microscopy (TEM)
			Nanocube	100	80	TEM
2013, [37]	MnCl <sub>2</sub> · 4H <sub>2</sub> O/Se powder	$\alpha$ -MnSe	Rod like particles	60	100 (Base diameter), (25 Tip diameter)	TEM
2017, [20, 38]	MnCl <sub>2</sub> · 4H <sub>2</sub> O/ SeO <sub>2</sub>	$\gamma$ -MnSe	Spherical QDs	180	5 & 14	High resolution transmission electron microscopy (HRTEM)
2019, [39]	MnCl <sub>2</sub> · 4H <sub>2</sub> O/ SeO <sub>2</sub>	$\alpha$ -MnSe	Spherical QDs	180	5 to 11	HRTEM
2016, [40]	Mn(CH <sub>3</sub> COO) <sub>2</sub> · 4H <sub>2</sub> O/ NaHSe	$\alpha$ -MnSe	Nanodisc	180	80 to 1500	TEM
2019, [41]	MnCl <sub>2</sub> · 4H <sub>2</sub> O/ SeO <sub>2</sub>	$\alpha$ -MnSe	Spherical QDs	180	20.3 to 46.5(with pH variation)/5 nm	Dynamic light scattering/TEM
2018, [42]	Mn(CH <sub>3</sub> COO) <sub>2</sub> · 4H <sub>2</sub> O/ Na <sub>2</sub> SeO <sub>3</sub>	$\alpha$ -MnSe	Nanoparticles	180	20 to 30	High-definition field emission scanning electron microscopy (FESEM)
2020, [43]	MnCl <sub>2</sub> · 4H <sub>2</sub> O/SeO <sub>2</sub>	$\alpha$ -MnSe	Multilayer structure with a small quantity of microplates surrounded by lots of nanoplates	180	—	

\*Additional details on the product obtained by using hydrothermal method along with other properties have been discussed in Table 3

of oleic acid (OA, 15 mL), and tetraethylene glycol (TEG, 15 mL). Maintaining the OA:TEG ratio at 50:50 resulted in the formation of pure WZ phase MnSe nanoparticles 25 – 75 nm in size but irregular in shape. However, RS type MnSe nanostructures can also be predominantly formed in addition to a relatively smaller quantity of the WZ type MnSe if other types of solvents were used in the synthesis process [5].

### iii) The effect of heating rate

One of the prime objectives of any nanomaterial synthesis process is to be able to achieve control over the size distribution and morphology of the resulting product. The solvothermal synthesis process used to produce MnSe offers control over the morphology of the nanostructures through variation in the heating rates of the reaction mixture. The formation of MnSe nanocrystals can be divided into: i) the nucleation phase and ii) the growth phase. Different heating rates ranging from low (2 °C min<sup>-1</sup>) to medium (15 °C min<sup>-1</sup>) to rapid (25 °C min<sup>-1</sup>) was employed during the study [19]. Heating rate was found to have influenced on the formation of different types of nucleation seeds in all the three cases. At the low heat rate, the nucleation seeds were of ZB type over which the WZ type tetrapod structure proliferated. The thermodynamically controlled condition provided by the low heating rate favored the formation of anisotropic tetrapod (WZ phase) growth along the c-axis leading to the highest aspect ratio (4.5 ± 0.6) amongst the MnSe crystal structures formed by employing all three heat rates. Low heating rates, however, is characterized by lower purity of the resulting

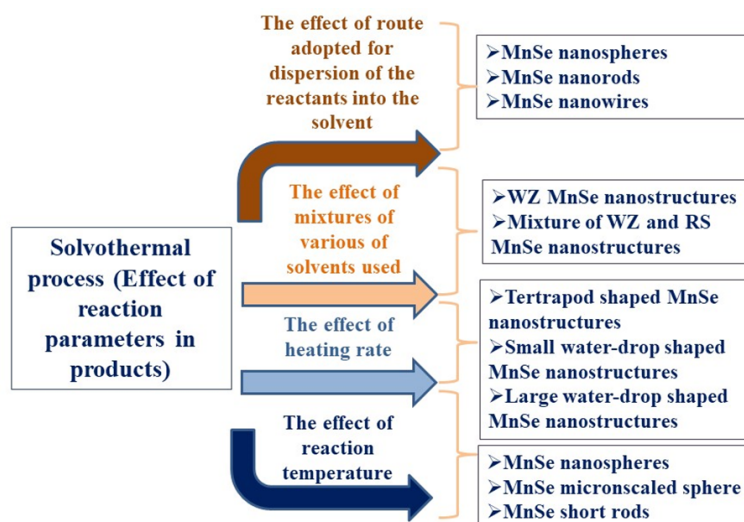


FIG. 3. Diagrammatic representation of effect of reaction parameters on the structure and morphology of the MnSe nanostructures synthesized by solvothermal method

MnSe nanostructures due to presence of both the WZ and ZB structures. Medium heating rates ( $15\text{ }^{\circ}\text{C min}^{-1}$ ) favored the formation of WZ nucleating seeds in addition to minute quantities of ZB phase. The final nanostructure formed consisted of small water-drop shaped MnSe formed by reaction of the MnSe-tetrapod shaped nanocrystals. The water-drop shaped nanocrystals were found to be of uniform size and lower aspect ratios ( $1.9 \pm 0.2$ ) as compared to the product formed via low heating rates ( $2\text{ }^{\circ}\text{C min}^{-1}$ ). Rapid heating rates ( $25\text{ }^{\circ}\text{C min}^{-1}$ ) favored the formation of WZ nucleation over that of the ZB nucleation seeds. The c-axis directional crystal growth was found to be favored for the WZ phase leading to anisotropic growth structures predominantly water-drop shaped but also rod shaped, nanotadpole structures etc. and resulted in the lowest aspect ratios ( $1.2 \pm 0.1$ ) of the MnSe amongst the nanostructures produced via all the three heating rate variations in the solvothermal synthesis [19]. The reaction temperature also plays a vital role on the morphology of the product. The nanospheres which were formed at  $180\text{ }^{\circ}\text{C}$  temperature, transformed into micron-scaled spheres and short rods on maintaining the reaction temperature between  $100$  to  $120\text{ }^{\circ}\text{C}$  [46]. Table 2 summarizes the data on synthesis of MnSe nanostructures by solvothermal method.

**2.1.3. Hot injection method.** The hot injection method is used as the most common synthesis method for obtaining highly monodisperse isotropic nanoparticles with narrow particle-size distribution. This method is based on rapid injection of cold precursor into a mixture of organic solvents heated at high temperatures. Here rapid injection of the precursors facilitates a high degree of supersaturation leading to instantaneous nucleation growth of the nanoparticles from the reaction mixture [47]. Nucleation of the nanostructures leads to homogeneity in diffusion-controlled growth across the reaction mixture thus favoring a size-focusing phenomenon due to delayed growth of larger sized nanoparticles as compared to the smaller ones. With time, Ostwald ripening occurs where smaller sized particles start dissolving in the solution with the simultaneous emergence of larger sized nanoparticles. The emergence of larger sized nanoparticles from the solution on account of Ostwald ripening favors a thermodynamically stable nanostructure due to the higher volume to surface ratio and thus unavailability of greater number of reactive sites on the nanoparticle surface [48]. Thus, the hot injection method separates out the nucleation and growth process efficiently to provide a highly monodisperse size-controlled nanoparticle. The requirement of inert atmospheric and high temperature environment inside the reaction chamber makes the hot injection method challenging for the synthesis of nanoparticles [49–51].

Hot injection method can be used to synthesize  $\alpha$ -MnSe nanostructures of different shapes, predominantly cubic and spherical. Using this method, monodisperse  $\alpha$ -MnSe nanocubes of morphological purity yield of 100 % were synthesized with average side length of 100 nm. A precise control over the size and morphology of the nanostructures were obtained, resulting in the production of  $\alpha$ -MnSe spherical nanoparticles (average size 25 nm as obtained from high resolution transmission electron microscopy (HRTEM)) and  $\alpha$ -MnSe nanocubes of uniform side length (50 nm). The variations of the characteristics of the MnSe nanostructures were studied by changing the reaction parameters such as precursor concentration, surfactant composition, the reaction temperature and the reaction time. The formation of aggregated  $\alpha$ -MnSe nanocubes at an extended reaction time of 18 hr was concluded as due to the occurrence of “Ostwald Ripening” process [52].

Cubic phase, highly crystalline, monodisperse MnSe nanospheres in the size range of 7 – 16 nm were synthesized by using the hot injection method. Manganese (II) acetate tetrahydrate ( $\text{CH}_3\text{COO}$ )<sub>2</sub>Mn·4H<sub>2</sub>O and Se powder were used as the Mn and Se precursors respectively and oleic acid was used as the capping agent for the production of various sized hydrophobic nanospheres. The size and polydispersity of the nanospheres were controlled by controlling the reaction

TABLE 2. Summarized data on synthesis of MnSe nanostructures by solvothermal method\*\*

Year Ref.	Mn precursor/ Se precursor	Solvent	Crystallographic phase	MnSe product	Temperature (°C)	Average size (nm)	Method used for determining the size
2002, [45]	MnCl <sub>2</sub> ·4H <sub>2</sub> O/Se powder	Ethylene-diamine	α-MnSe	Flaky morphology with irregular drapes	190	5 to 30 (width), 100 to 500 (length)	TEM
2006, [46]	MnCl <sub>2</sub> ·4H <sub>2</sub> O/Se powder	Ethanol amine	α-MnSe	Nanospheres	180	200 (diameter)	FESEM & TEM
				Nanorods		50 to 60 (diameter), 1 to 3 μm (length)	
				Nanowires		5 to 10 (diameter)	
2010, [5]	Anhydrous MnCl <sub>2</sub> /Se powder	Mixture of oleic acid & tetraethylene glycol	γ-MnSe	Irregular shaped nanoparticle	235	25 to 75	HRTEM
2012, [19]	Anhydrous MnCl <sub>2</sub> /Se powder	Mixture of oleic acid & tetraethylene glycol	Mixture of γ-MnSe & β-MnSe	Tetrapod shaped	200–300	148 (arm length), 30 (arm diameter)	TEM
			Mixture of γ-MnSe & β-MnSe	Small water-droplet shape		75 (length), 40 (diameter)	
			γ-MnSe	Large water-droplet shape		265 (length), 210 (diameter)	

\*\*Additional details on the product obtained by using solvothermal method along with other properties have been discussed in Table 3

temperature (200 to 280 °C) of the hot solution of the Mn precursor. Injection of the Se precursor stock solution which was maintained at room temperature (~ 25 °C) into the Mn precursor solution (200 °C) led to the formation of nanoparticles of average size 7 nm. The size of the nanoparticles increased to 12 and 16 nm (as obtained from high HRTEM) on raising the reaction temperature up to 240 and 280 °C respectively [53]. Fig. 2(c) depicts the schematic diagram of hot injection synthesis process.

## 2.2. Deposition techniques

Deposition techniques are commonly used synthesis processes for various nanostructures, preferably in the form of thin film that is created and deposited onto a substrate material. Various deposition methods that are used for the synthesis of MnSe nanostructures are chemical vapor deposition, pulsed laser deposition method etc.

**2.2.1. Chemical vapor deposition (CVD).** Chemical vapor deposition (CVD) is a well-known thin film coating process where thermally induced chemical reactions take place between the precursors/reagents supplied in vapor/gaseous form and the surface of a solid substrate. Highly controlled 2D nanomaterials with high crystal quality, purity and good structural regularity can be synthesized by CVD as compared to the other conventional synthesis procedures [54]. Flow rate, deposition temperature, pressure and reactor geometry are the key parameters that controls the deposition of the film.

Chemical vapor deposition method was used [55] to synthesize one dimensional MnSe nanostructures by using a temperature-controlled regime of reaction site on the Si substrate coated with Au nanoparticles. In this synthesis, MnCl<sub>2</sub> and CoSe powders were used as precursors for manganese and selenium respectively. While the temperature range of the precursor's sources were maintained between 1000 – 1100 °C, that of the Si substrate surface-coated with Au nanoparticles on which the actual reaction takes place leading to the formation of various nanostructures, was maintained between 900 – 800 °C. The vapour-liquid-solid phase transition mechanism was inferred to have been followed leading to the formation of the various manganese selenide/silicon-oxide composite nanostructures with the MnSe nanostructures which mostly form one-dimensional crystalline structures. Various morphologies formed were reaction temperature and/or MnSe

and  $\text{SiO}_x$  growth rate dependent. The gold nanoparticles deposited on the Si substrate catalysed the reaction of the Mn and Se vapor mixture. MnSe was synthesized within the gold nanoparticles which were saturated with the vapor of the individual elements. Similarly, the gold nanoparticles also catalysed the formation of  $\text{SiO}_x$  from Si vapor and oxygen that diffuses into the nanoparticle along with the Mn and Se vapors. Depending on the temperature/growth rates, different geometries of crystalline MnSe and amorphous  $\text{SiO}_x$  structures are formed. Apart from MnSe and  $\text{SiO}_x$  structures,  $\text{MnO}_x$  domains have also been characterized in some of the nanostructures formed. Various types of MnSe or MnSe/ $\text{SiO}_x$  nanocomposite structures formed in the CVD technique can be broadly classified into: i) nanowires (MnSe); ii) nanocomposites (MnSe/ $\text{SiO}_x$ ): core-shell nanocables as well as branched nanocables and pea-pod structures; iii) nano-cube/chain network structures (MnSe only). Fig. 4 summarizes various MnSe and MnSe/ $\text{SiO}_x$  nanocomposite structures formed. Fig. 2(d) depicts the schematic diagram of chemical vapor deposition method.

In another work, polycrystalline manganese selenide thin films of both rocksalt and zinc blende structures were prepared by organometallic chemical vapor deposition (OMCVD) by taking methyl pentacarbonyl manganese (MPCMn) as manganese precursor and diethyl selenium (DES) as selenium precursor. This study shows that MPCMn is not a suitable precursor for OMVPE processes that require high cracking temperatures. MPCMn produces manganese oxide (MnO) at temperature greater than 450 °C [56]. Moreover, the incorporation of elemental carbon or oxygen in the thin film with the use of carbonyl compound was another drawback obtained of the study.

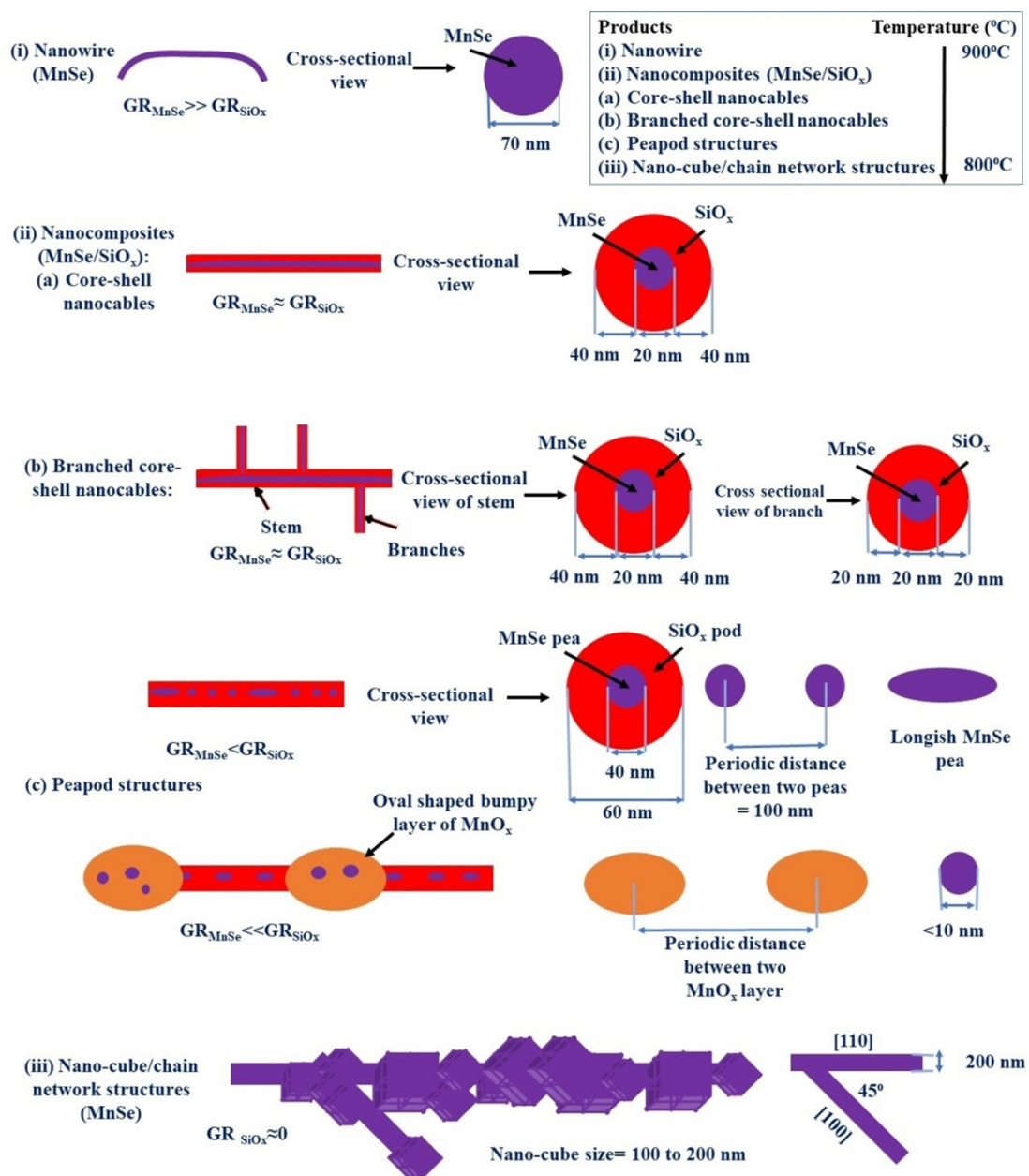


FIG. 4. Schematic diagram (not to scale) of various MnSe nanostructures produced by using CVD method [55]

Ultrathin two-dimensional zinc blende phase manganese selenide (2D  $\beta$ -MnSe) nanosheets were also prepared by the CVD process. The MnSe flakes that were forming the nanosheets were prepared on a mica substrate by using Se powder as the Se precursor and  $\text{MnCl}_2$  as the Mn precursor and keeping them in a quartz boat (Se) and an alumina boat (Mn) respectively. Both the boats were placed in two different zones of a heating furnace equipped with a quartz tube. Pre-treatment of the quartz tube was done by purging it with Ar gas for 5 min at 300 standard cubic centimetres per minute (sccm). The precursor sources of Mn and Se were heated up to 300 and 680 °C respectively for 20 min in presence of Ar gas (100 sccm) mixed with  $\text{H}_2$  gas (10 – 40 sccm) during the growth. After heating the precursors of Mn and Se to the required temperatures (300 and 680 °C) the furnace was kept idle for 10 min to finish the growth of  $\beta$ -MnSe flakes followed by rapid cooling to room temperature. During the growth process, the Ar- $\text{H}_2$  gas mixture helped in controlling precursor vapor transportation and, hence, the morphology and size of MnSe flakes. While the average thickness of the  $\beta$ -MnSe flake can be tailored to 3.5 nm, the lateral size of the flake can be measured in multiples of 12  $\mu\text{m}$ . Stoichiometric calculations of the  $\beta$ -MnSe flake revealed the presence of Mn and Se elements in equal proportions. The growth of  $\beta$ -MnSe flakes were reported to be significantly affected by the flow rate of  $\text{H}_2$ . When the flow rate of  $\text{H}_2$  increases from 10 to 35 sccm, the flakes' shapes evolve gradually from simple triangular shape to windmill, dendrite, and eventually more morphologically complex snowflakes shapes with increasing fractal dimensions from 1.02 to 1.4. As inferred, evolution of this  $\beta$ -MnSe flakes from simple to complex structures are dominated by diffusion-controlled kinetics. With lower flow rate of  $\text{H}_2$  simple triangular shaped MnSe flakes were formed due to the adequate diffusion of Mn and Se atoms of MnSe in the mica substrate. However, higher flow rate of  $\text{H}_2$  leads to increase of the diffusion rate of Mn and Se providing sufficient precursor to create more complicated structure. In addition, during the formation of complex structure in rich  $\text{H}_2$  environment, Mn terminated edge growth becomes more energetically favorable [57].

**2.2.2. Pulsed laser deposition.** A pulsed laser deposition (PLD) method is a physical vapor deposition (PVD) method which is carried out in a vacuum environment to produce multilayer films composed of two or more materials [58, 59]. In this process, with high laser energy density, laser pulses are focused on the targeted pellets which were then vaporized and the resulting ablation plume containing the atoms and the energetic ions of the vaporized material was deposited as a thin film on the substrate material. The high ablation rate of pulsed laser deposition ensures multicomponent thin film formation with desired stoichiometry ratio [60].

By forming pellets of 1.3 cm diameter from a mixture of Mn and Se powder (Mn to Se ratio of 1:1.5), and considering these pellets as ablated targets, PLD was used to form cubic structured MnSe thin films of 200 nm thickness (as determined by using scanning electron microscope (SEM)) in 30 minutes. The laser beam of wavelength 355 nm with laser energy intensity 2  $\text{J}/\text{cm}^2$  was created by the third harmonic frequency of a Q-switched Nd:yttrium aluminum garnet (YAG) laser. The laser pulses were used in a repetition rate of 10 Hz and the width was of 10 ns for this process. Moreover, the experiment was carried out by keeping the targeted pellets in a chamber of base pressure of  $10^{-2}$  Pa and 5 Pa during the deposition process. The substrate material used for the deposition of MnSe thin film was stainless steel maintained at a temperature of 200 °C and kept at a distance of 4 cm from the target [61]. Fig. 2(e) depicts the schematic diagram of pulsed laser deposition method.

### 3. Optical properties of MnSe nanocrystals

UV-visible (UV-Vis) spectroscopy and photoluminescence spectroscopy (PL) are the two main spectroscopic techniques that are used to evaluate the optical properties of nanoparticles.

UV-V is spectroscopy is a technique to study the electronic transition of materials which manifest across the near IR, visible and the UV region of the electromagnetic spectrum. It is a powerful technique to study the interband electronic transition in semiconductors. By using the first absorption peak of absorption spectra of nanoparticles, the band gap ( $E_g$ ) of the corresponding nanoparticles can be obtained by using the following standard equation:

$$E_g = \frac{1240}{\lambda} \quad (\text{eV}), \quad (1)$$

where  $\lambda$  is the wavelength (in nm) corresponding to the first absorption peak.

Photoluminescence is the emission of light after the absorbing a photon. The physical processes involved in photoluminescence are more complicated than those in absorption because it also involves the emission relaxation mechanism in the material. For direct band gap semiconductor materials, the bottom of the conduction band (conduction band edge,  $E_c$ ) and the top of the valence band (valence band edge,  $E_v$ ) occur at the same wave vector  $k$  (with  $k = 0$ ) providing change of momentum  $\Delta k = 0$ . In this case, during photon emission, accompanied by band-to-band transition, an electron recombines with a hole [62].

For indirect band gap semiconductor materials, the bottom of the conduction band does not occur at the momentum  $k = 0$ , i.e. it is shifted with respect to the top of the valence band. Therefore, any transition process from the bottom of the conduction band to the top of the valence band does not conserve momentum. As the photon is very light particle having no rest mass it cannot carry large momentum. Therefore, a particle such as phonon (quantized lattice vibration) is required that carries the momentum to conserve in the transition process. Thus, in indirect band gap semiconductor for conservation of the momentum in the transition process a phonon must be involved when the photon is emitted [63].

This makes it a second-order process, with a relatively low transition probability. Fig. 5 depicts the schematic diagram of direct and indirect band gap semiconductors.

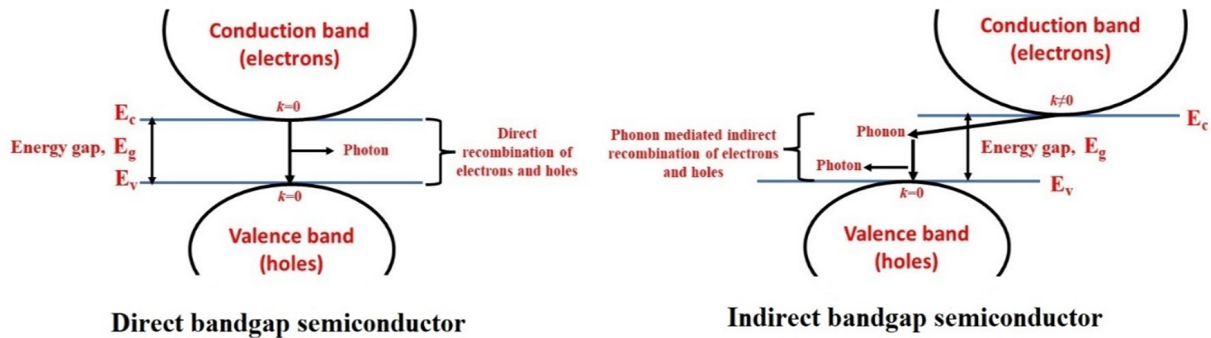


FIG. 5. Schematic diagram of direct and indirect band gap semiconductors

There are various parameters such as size [64], shape, surface capping agents, precursor concentration, reaction time, reaction temperature, the dispersing medium etc. which the optical properties of the nanostructures is relied on [65]. Recent years, one observes focusing of the study on optical properties of MnSe nanostructures caused by increasing area of optical and optoelectronic applications. However, very few reports have been published on the optical properties of MnSe nanostructures.

We discuss below the absorption and photoluminescence (PL) properties of MnSe nanostructures synthesized using different processes.

### 3.1. UV-Vis response of MnSe nanostructures synthesized by hydrothermal method

Hydrothermally synthesized cubic structured MnSe nanorods were characterized by two absorption peaks at  $\sim 372$  and  $\sim 437$  nm. The peak at 372 nm is blue-shifted from the bulk cubic MnSe (468 nm), signifying strong quantum confinement effects resulting in the MnSe nanorods (372 nm). The corresponding band gap for the MnSe nanorod was found to be 3.33 eV which is blue shifted by an amount of  $\sim 0.83$  eV from the bulk MnSe band gap ( $E_g$ ) of 2.5 eV [37].

Hydrothermal synthesis method was used to synthesize MnSe nanoparticles having different crystallographic phase and with different UV-Vis spectroscopic behavior by changing the Mn and Se precursor ratio ( $\text{Mn}^{2+}:\text{Se}^{2-}$ ). WZ phase MnSe QDs were prepared by keeping the following ratio:  $\text{Mn}^{2+}:\text{Se}^{2-}=2:1$ , which exhibited absorption feature at  $\sim 303$  nm ( $E_g = 4.09$  eV) with a blue shifted energy of ( $\Delta E \sim 0.59$  eV) from the bulk value of the WZ type MnSe ( $E_g = 3.5$  eV). With increasing this precursor concentration ratios up to 3:1 and 4:1, the absorption peak maxima were red shifted to  $\lambda = 408$  nm ( $E_g = 3.03$  eV) from  $\sim 303$  nm that was observed for 2:1 with an adequate blue shifting of ( $\Delta E \sim 0.5$  eV) with respect to the bulk RS type structure ( $E_g = 2.5$  eV). It was suggested that incorporation of excess amount of  $\text{Mn}^{2+}$  concentration in MnSe QDs prepared by taking precursor ratio 3:1 and 4:1 there was a probability of partial phase transformation of the WZ phase to an RS one [20]. By varying the type of capping material like TGA and SDS molecules, WZ MnSe nanoparticles were seen to exhibit significant variation in absorption behavior. The absorption peak which was observed at 303 nm ( $E_g = 4.09$  eV) for TGA capped MnSe QDs significantly red shifted to 330 nm ( $E_g = 3.75$  eV) while capped by SDS keeping the precursor ratio same. Thus, in hydrothermal method the optical properties of the MnSe nanostructure can be significantly altered by the precursor concentration ratio and the type of capping material used [38]. Fig. 6(i) depicts the change of excitonic wavelength of first excitonic absorption peak of MnSe nanostructures with precursor concentration ratio and type of capping agent used in the hydrothermal method.

### 3.2. UV-Vis response of MnSe nanostructures synthesized by solvothermal method

Cubic MnSe nanospheres synthesized via solvothermal process exhibited two broad peaks at around 336 nm and 419 nm and a weak shoulder peak centered at about 594 nm [66]. The WZ MnSe nanostructures of various shapes and sizes, synthesized by this method exhibit dependence of absorption spectra behavior with heating rates used in the synthesis process [19]. First absorption peaks at 389 nm ( $E_g = 3.2$  eV) and 391 nm ( $E_g = 3.17$  eV) were observed for tetrapod shaped (size 30 nm) and small water-drop shaped (size 40 nm) MnSe nanostructures respectively for the heating rates of 2 and 15 °C. Red shifting of the absorption peak to 398 nm from 391 was clearly observed for the larger sized water-drop shaped (size 210 nm) MnSe nanoparticles synthesized by using heating rate of 25 °C. However, in case of all differently shaped nanoparticles the band gaps obtained were found slightly smaller than the bulk WZ type MnSe of 3.5 eV. Fig. 6(ii) shows the change of excitonic wavelength of the first absorption peak of MnSe nanostructures with heating rate used in the solvothermal method.

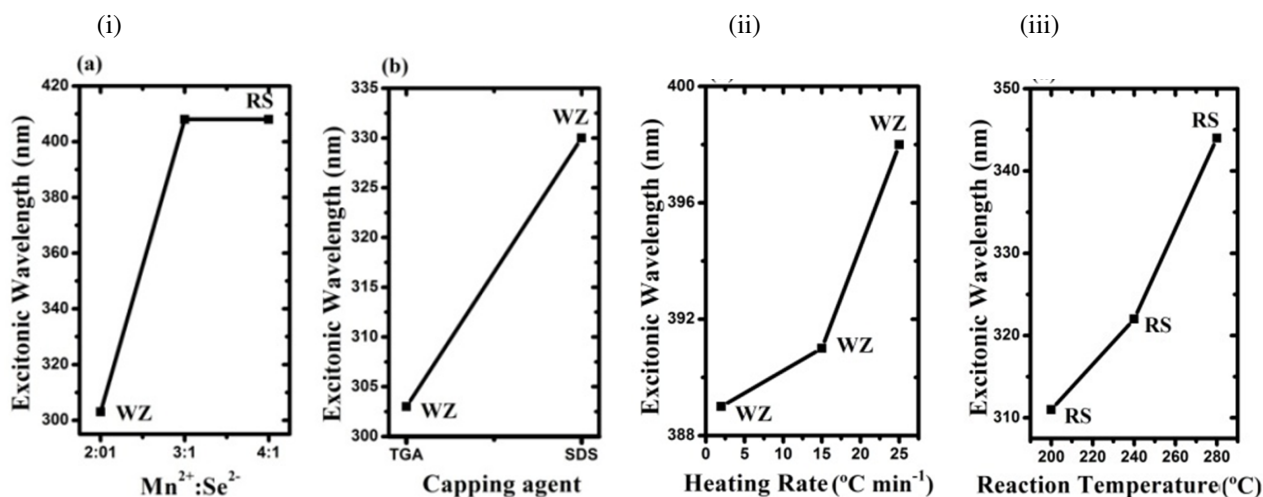


FIG. 6. i) Change of excitonic wavelength of MnSe nanostructures with a) precursor concentration ratio and b) type of coating (capping) agent used in hydrothermal method; ii) Change of excitonic wavelength of MnSe nanostructures with heating rate used in solvothermal method; iii) Change of excitonic wavelength of MnSe nanostructures with reaction temperature used in hot injection method

Size dispersion in the case of water-drop-shaped MnSe nanoparticles was attributed to the exhibition of broadening of the absorption peak width observed in this type of MnSe nanostructure [19]. The wurtzite shaped MnSe nanoparticles produced by solvothermal method was the first reported with a band gap in the range of 3.5 – 3.8 eV [5].

### 3.3. UV-Vis response of MnSe nanostructures synthesized by hot injection method

Similar to the effect of heating rates on the absorption peaks of nanostructures as synthesized by the solvothermal process, reaction temperature can also influence the quantum confinement of MnSe nanostructures as obtained by the hot injection method. Absorption peaks of cubic MnSe spherical nanoparticles red shifted from 311 to 322 nm and from 322 to 344 nm on increasing the reaction temperature from 200 to 240  $^{\circ}C$  and from 240 to 280  $^{\circ}C$ ; respectively thus indicating an increase in size of the nanoparticles. The nanoparticles having the largest size (16 nm) blue shifted by an amount of 1.11 eV from cubic bulk MnSe indicating effective quantum confinement of charge carriers [53]. Fig. 6(iii) depicts the change of excitonic wavelength of MnSe nanostructures with reaction temperature used, in hot injection method.

### 3.4. Comparison of UV-Vis response of MnSe nanostructures synthesized by different method

It can be observed that in both cubic and wurtzite MnSe nanostructures synthesized by different methods, the blue shifting from the corresponding bulk MnSe band gaps are very small. For WZ MnSe nanostructures the highest blue shifted energy was observed to be 0.59 eV from the bulk WZ MnSe band gap (3.5 eV). The corresponding energy is maximum of 1.48 eV for cubic MnSe nanostructures that is shifted from cubic MnSe band gap (2.5 eV). The observed lower value of blue shifted energy may be due to the highly localized nature of 3d electronic bands of Mn atoms in the nanostructures [67]. While comparing the first absorption peak of cubic MnSe nanostructures synthesized by different methods, the position of this peak is observed to be significantly different. For cubic MnSe nanorods synthesized by hydrothermal method this peak was found to be located at 372 nm while, for cubic nanoparticles synthesized by solvothermal and hot injection method the peaks were found to be located at 336 nm and 311 nm respectively. Thus, the blue shifted energy for the cubic MnSe nanostructure synthesized by hot injection method was observed to be the largest ( $\Delta E = 1.48$  eV). In case of WZ MnSe nanostructure, the first absorption peak for hydrothermally synthesized QDs was observed to be located at significantly lower wavelength (303 nm) as compared to the nanostructures synthesized by solvothermal method (389 nm). Fig. 7 show the variation of the first excitonic peak position of (a) cubic and (b) WZ MnSe nanostructures with the method of synthesis.

Moreover, the cubic structured MnSe nanorods synthesized by the hydrothermal method exhibited two absorption peaks (372 and 437 nm). One of the peaks was attributed to the electronic transition in the core state and the other one to the electronic transitions in the surface states. Similar to the hydrothermal method, solvothermally synthesized cubic MnSe nanoparticles also exhibited two absorption peaks (336 and 419 nm) and a shoulder peak (594 nm). The shoulder peak is dependent on the type of the solvent used in the nanoparticle synthesis process. However, the cubic structured MnSe nanoparticles synthesized by hot injection method showed only a single absorption peak in the UV Vis spectra. Thus, the absorption behavior can be significantly altered by changing the synthesis procedure used for the MnSe nanostructures in addition to the reaction parameters used in a specific process. Similar behavior has been also observed

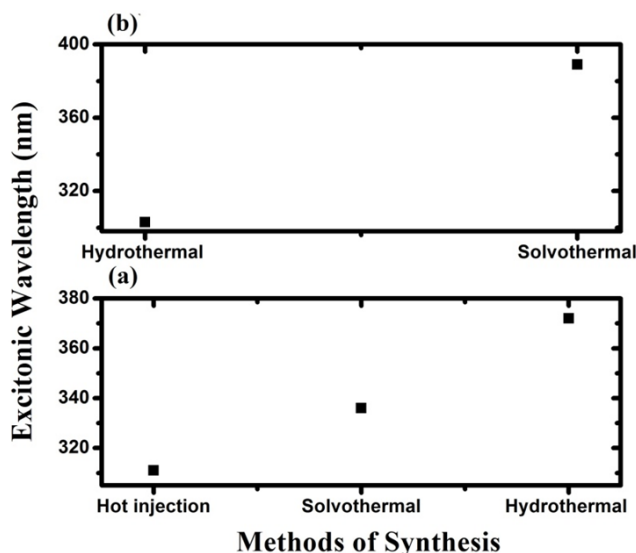


FIG. 7. Variation of the first excitonic peak position of (a) cubic and (b) WZ MnSe nanostructures with the method of synthesis ( $y$ -axis-excitonic wavelength,  $x$ -axis-methods of synthesis)

for other nanoparticles [68]. Table 3 depicts the summarized data obtained from UV-Vis spectroscopy study of MnSe nanostructures synthesized by various methods.

### 3.5. PL response of MnSe nanostructures synthesized by hydrothermal method

To get the photoluminescence spectra, the nanostructures were excited by a wavelength lower than the wavelength corresponding to the band gap. For a defect-free nanomaterial, the emission due to the corresponding excitation will lie at the band gap region only and is known as band edge emission. Whereas a nanomaterial having multiple defects (point defects, surface defects etc.) shows emissions in the direct band gap region as well as in other regions at higher wavelengths than the direct emission wavelength. These emissions corresponding to higher wavelength region are known as defect related emissions.

Important characteristics of nanostructures such as the suppression or improvement of the photoluminescence intensity, the ratio of band gap to defect related emission intensity ( $I_{BE}/I_{DE}$ ), quantum yield ( $\Phi_Q$ ) and stability are dependent on the reaction parameters and the nature of the surfactant capping material on the nanostructures.

Different PL behavior was observed for MnSe QDs prepared with different Mn and Se precursor concentration ratios ( $Mn^{2+}: Se^{2-}$ ). With increasing precursor ratio ( $Mn^{2+}: Se^{2-}$ ), red shifting of the emission spectra was observed for the QDs when excited with a constant excitation wavelength,  $\lambda_{ex} = 300$  nm. The emission maxima observed at  $\sim 400$  nm for MnSe QDs prepared with  $Mn^{2+}: Se^{2-} = 2:1$  was red shifted to  $\sim 535$  nm for the QDs synthesized with higher precursor ratios of 3:1 and 4:1. The corresponding band edge emission ( $\lambda_{BE}$ ) peaks were located at 400, 515 and 517 nm. The positions of the defect related emission ( $\lambda_{DE}$ ) peaks were 459, 554 and 566 nm.

By varying the type of the surfactant, the behavior of the PL spectra could be tuned significantly. The band edge emission ( $\lambda_{BE}$ ) and defect related emission ( $\lambda_{DE}$ ) peaks of TGA capped WZ MnSe QDs synthesized by hydrothermal method were found to be located at  $\sim 368$  and 400 nm respectively ( $\lambda_{ex} = 300$  nm). However, on changing the capping agent to SDS, the  $\lambda_{BE}$  was shifted to  $\sim 365$  nm and the  $\lambda_{DE}$  to  $\sim 405$  nm. The intensity ratio ( $I_{BE}/I_{DE}$ ) between band edge emission and defect related emission were found to be nearly  $\sim 0.4$  and  $\sim 0.78$  respectively for TGA and SDS capped MnSe QDs. The defect related emission in MnSe QDs was expected to arise from the defects present in the metastable WZ MnSe nanocrystal core [69].

The red shift of the emission peak with respect to the absorption peak of a nanoparticle is known as Stokes shift, which reveals the energy losses between absorption and emission [70]. This is one of the most important characteristics that influence on the optical properties of nanostructures. Stokes shift is commonly observed in semiconductor QDs and originates from surface states (vacancies and dangling bonds) and interstitial states (interstitial atoms and vacancies) acting as sites for the recombination of electron and hole [71]. Moreover, Stokes shifts of colloidal QDs are related to phonon interactions [72]. The authors of this review article have considered the shifting of the emission peak maxima from the absorption peak maxima of the QDs while calculating the Stokes shift. It was observed that the emission peak maxima at  $\sim 400$  nm ( $E_g = 3.1$  eV) for MnSe QDs synthesized with  $Mn^{2+}/Se^{2-}: 2:1$ , was significantly shifted by  $\sim 97$  nm ( $\Delta E_g = 910$  meV) from the excitonic absorption peak position of  $\sim 303$  nm ( $E_g = 4.09$  eV) as per calculations by the authors. The shifting has been calculated to be 127 nm ( $\Delta E_g = 730$  meV) for the QDs synthesized with  $Mn^{2+}/Se^{2-}$  ratio of 3:1 and 4:1. For different capping agents TGA and SDS the Stokes shifts are calculated to be 84 nm ( $\Delta E_g = 890$  meV) and 47 nm ( $\Delta E_g = 470$  meV), respectively. MnSe QDs exhibiting extremely large Stokes shifts (in the range of 470

TABLE 3. Summarized data on UV visible spectroscopic properties of MnSe nanostructures

Synthesis Method	Crystallographic phase	Shape	Parameter change	Size (diameter) (nm)	Excitonic Wave-length, $\lambda$ (nm) of the 1st absorption peak	$E_g$ (eV)	Blue shifted energy (eV) from RS bulk ( $E_g = 2.5$ eV)/WZ bulk (3.5 eV)	
Hydrothermal [36]	$\alpha$ -MnSe-	Nanorods	—	100	372	3.33	0.83 (from RS)	
Hydrothermal [20]	$\gamma$ -MnSe	Spherical	Change of $Mn^{2+}$ : $Se^{2-}$	2:01	7	303	4.09	0.59 (from WZ)
	$\alpha$ -MnSe	—		3:1	—	408	3.03	0.5 (from RS)
	$\alpha$ -MnSe	—		4:1	—	408	3.03	0.5 (from RS)
Hydrothermal [37]	$\gamma$ -MnSe	Spherical	Change of type of capping agent	TGA	5	303	4.09	0.59 (from WZ)
				SDS	14	330	3.75	0.25 (from WZ)
Solvothermal [65]	$\alpha$ -MnSe	Spherical	—	—	200	336	3.69	1.1 (from RS)
Solvothermal [19]	Mixture of $\gamma$ -MnSe & $\beta$ -MnSe	Tetrapod shaped	Change of heating rate	2 °C $min^{-1}$	30	389	3.2	—
	Mixture of $\gamma$ -MnSe & $\beta$ -MnSe	Small water-drop shaped		15 °C $min^{-1}$	40	391	3.17	—
	$\gamma$ -MnSe	Large water-drop shaped		25 °C $min^{-1}$	210	398	3.11	—
Solvothermal [5]	$\gamma$ -MnSe	Irregular	—	25–75	350	3.54	0.04 (from WZ)	
Hot injection [52]	$\alpha$ -MnSe	Spherical	Change of reaction temperature	200 °C	7	311	3.98	1.48 (from RS)
				240 °C	12	322	3.85	1.35 (from RS)
				280 °C	16	344	3.60	1.1 (from RS)

to 910 meV) are of interests for use as a down-conversion phosphor [73], and in high-quality (high sensitivity and high spatial resolution) bioimaging response [74, 75]. Large Stokes shift in nanomaterials leads to reducing of the probability of the self-absorption mechanism and, hence, the fluorescence quenching that arises from the overlapping of absorption and emission spectra [70, 76].

Typically, the fluorescence quantum yield ( $\Phi_Q$ ) gives the efficiency of any process exhibiting fluorescence phenomenon. It is defined as the ratio of the number of photons emitted to the number of photons absorbed. In general,

$$\Phi_Q = \frac{N_e}{N_a}, \quad (2)$$

where  $N_e$  is the number of emitted photons,  $N_a$  is the number of absorbed photons.

The quantum yield ( $\Phi_Q$ ) of the QDs can be predicted more accurately using the following relation [77]:

$$\Phi_Q \cdot 100 = Q_{ref} \left( \frac{n}{n_{ref}} \right)^2 \frac{I_Q A_{ref}}{I_{ref} A_Q}. \quad (3)$$

The  $Q_{\text{ref}}$  represents the quantum yield of a reference specimen;  $I_Q$  and  $I_{\text{ref}}$  are the integrated emission intensities of QDs and reference respectively;  $A_Q$  and  $A_{\text{ref}}$  are the absorption intensities of QDs and reference respectively;  $n$  (sample) and  $n_{\text{ref}}$  (reference) are the refractive indices of the solvents of sample and reference respectively. By taking Rhodamine 6G<sup>®</sup> as the reference, MnSe QDs coated with TGA showed significantly larger values ( $\sim 3$  fold) of  $\Phi_Q$  (75 %) as compared to the SDS coated ones (24 %) [38].

The dynamics of different emission behaviors exhibited by the QDs capped by various functionalizing materials can be studied by time resolved photoluminescence (TRPL) spectroscopy. TRPL can also resolve the spectral and decay kinetic properties of nanostructures [78].

The study of TRPL spectra of TGA and SDS capped MnSe QDs revealed that in the both cases the capped MnSe QDs exhibited bi-exponential decay behavior accompanied by fast ( $\tau_1$ ) and slow ( $\tau_2$ ) decay parameters. The presence of both fast and slow time components in TRPL spectra indicates that two distinct emitting states having different lifetimes are involved in the visible photoluminescence process of the QDs [79]. Parameter  $\tau_1$  corresponds to direct exciton recombination emission whereas  $\tau_2$  corresponds to surface trapped emission associated with the carriers trapped at the surface sites for the respective nanostructure. The values of  $\tau_1$  and  $\tau_2$  for MnSe-TGA QDs were found to be  $\sim 0.65$  and  $\sim 3.05$  ns, respectively, and for MnSe-SDSQDs the corresponding values were  $\tau_1 \sim 1.04$  ns, and  $\tau_2 \sim 5.11$  ns.

The average life time of the QDs were calculated by using the following expression: [80, 81],

$$\tau_{\text{average}} = \frac{A_1\tau_1^2 + A_2\tau_2^2}{A_1\tau_1 + A_2\tau_2^3},$$

where  $A_1$  and  $A_2$  are the pre-exponential factors for the fast and slow processes respectively.

The average life time values were found to be  $\sim 0.87$  and  $\sim 1.20$  ns for MnSe-TGA and MnSe-SDS QDs respectively. Alkyl chains of SDS molecules which were six times longer as compared to TGA molecules were believed to be responsible for surface passivation while offering QD emission for longer time duration as compared to the TGA counterpart [38, 82–84].

Cubic structured MnSe QDs synthesized by the hydrothermal method, exhibited emission response with the emission peak at  $\sim 430$  nm ( $\lambda_{\text{ex}} = 300$  nm). When capped with different surfactants such as CTAB, TGA and dextran, the emission peaks were slightly blue shifted to 428 nm. In the both cases (coated and uncoated QDs), the emission response was very symmetric with FWHM (full width at half maximum) of 11 nm [39]. Lower FWHM of the QDs signifies higher probability of uniform emission energies and uniform physical properties such as size, strain and composition etc. throughout the sample [85]. The relaxation time study of the uncoated and surfactant coated QDs showed significant variation of the relaxation time ( $\tau_2$ ) related to surface trapped emissions but almost a constant value of relaxation time ( $\tau_1$ ) related to band edge emission. The maximum  $\tau_2$  was observed for dextran coated MnSe QDs ( $\tau_2 = 5.5$  ns), whereas on capping by TGA the QDs exhibited significantly lower  $\tau_2$  ( $\tau_2 = 2.7$  ns) as compared to the dextran capped one (by a factor of 2.03). Hence, capping of QDs using surfactants such as short chain type (TGA) and long chain polysaccharide types dextran leads to different types of surface behaviour of the QDs (different values of  $\tau_2$ ) [38, 39, 86]. Larger hydrophilic cross-sectional area formed by the dextran molecules around the QDs, helps in filling vacancies and surface defects enhancing surface passivation.

### 3.6. PL response of MnSe nanostructures synthesized by solvothermal method

Similar to the hydrothermally synthesized MnSe QDs,  $\alpha$ -MnSe nanospheres synthesized by solvothermal method exhibited two emission peaks due to near band edge and defect related emissions ( $\lambda_{\text{ex}} = 365$  nm). The intensity of the defect related emission peak observed at  $\sim 437$  nm is comparatively higher (by factor of 1.1) than that of the band edge emission peak located at  $\sim 416$  nm [87]. If we calculate the corresponding Stokes shift for these  $\alpha$ -MnSe nanospheres it is observed that the emission peak maxima positioned at  $\sim 416$  nm ( $E_g = 2.98$  eV) is significantly shifted by 710 meV ( $\sim 80$  nm) from the excitonic absorption peak position at  $\sim 336$  nm ( $E_g = 3.69$  eV).

MnSe nanoparticles of wurtzite phase ( $\gamma$ -MnSe) having different shapes exhibit smaller Stokes shift as compared to that of cubic phase ( $\alpha$ -MnSe) nanospheres. These nanostructures having tetrapod shapes show a Stokes shift of 11 nm from the absorption maxima at 389 nm to the emission maxima at 400 nm. Similar amount of Stokes shift (11 nm) is observed for small water-droplet nanospheres (absorption maxima 391 nm, emission maxima 402 nm). However, for the large water-droplet shaped nanostructures, the Stokes shift steeply decreases to 7 nm (absorption maxima 398 nm, emission maxima 405 nm) [19]. Thus, different shapes and hence different aspect ratios (length/diameter) have a direct influence on the Stokes shift for nanostructures. The Stokes shift of the anisotropic nanostructures does not change while the aspect ratio changes from  $4.5 \pm 0.6$  (tetrapod shaped) to  $1.9 \pm 0.2$  (small water-droplet shaped). But surprisingly with a sudden decrease of the aspect ratio from  $1.9 \pm 0.2$  (small water-droplet shaped) to  $1.2 \pm 0.1$  (large water-droplet shaped), the Stokes shift reduces to 7 nm. Therefore, it can be observed that the nanostructures with less aspect ratio showed lower Stokes shift as compared to that of nanostructures with higher aspect ratio. Different aspect ratios of the MnSe nanostructures resulted in energy fluctuations and thus providing variations in the calculated Stokes shift. The dependence of Stokes shift on the aspect ratio as observed for MnSe nanostructures were also reported for other nanostructures including CdSe/ZnS Core/Shell Nanorods [88, 89]. This type of size dependent Stokes shift has been

observed for other nanoparticles including CdSe Quantum dots [19, 90, 91]. Fig. 8(a) depicts the variation of Stokes shift with aspect ratio of cubic phase MnSe nanostructures synthesized by solvothermal method.

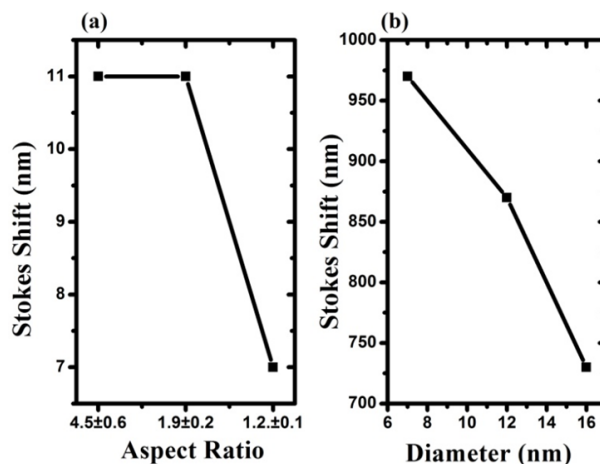


FIG. 8. Variation of Stokes shift with (a) aspect ratio of  $\alpha$ -MnSe nanostructures synthesized by solvothermal method and (b) diameter of  $\gamma$ -MnSe nanostructures synthesized by hot injection method

### 3.7. PL response of MnSe nanostructures synthesized by hot injection method

Two emission peaks corresponding to band edge emission and defect related emission can be observed in MnSe nanostructures synthesized by hot injection method. The both peaks are significantly red shifted with an increase in size (diameter) of the nanoparticles. The position of band edge emission peak ( $\lambda_{BE}$ ) was observed to have shift from 407 to 418 nm with the increase in size of the nanoparticles from 7 to 12 nm. The  $\lambda_{BE}$  for 16 nm sized nanoparticle was found to be located at 427 nm. The defect related emission peaks are positioned at 442, 474 and 495 nm for 7, 12 and 16 nm MnSe nanoparticles, respectively. Variation of emission peaks with the size of nanoparticles signifies effective quantum confinement behavior. The change of emission response with size in MnSe nanoparticles makes it a promising material that can be used in light emitting devices in the ultraviolet region. Similar size dependent PL emission response was observed for MnS nanocube structures and other various nanostructures including CdSe QDs [92]. The intensity of defect related emission peaks showed a dominant response over the intensity of band edge related emission peaks with increase in size of the nanoparticles. It was concluded that surface passivation in nanoparticles of different sizes could influence on the intensity of band edge and defect related emission peaks.

Cubic phase MnSe nanoparticles synthesized by hot injection method exhibited size-dependent Stokes shift values of 970 and 730 meV for nanoparticles of sizes 7 and 16 nm, respectively. Fig. 8(b) depicts the variation of Stokes shift with diameter of WZ MnSe nanoparticles synthesized by hot injection method.

### 3.8. PL response of MnSe nanostructures synthesized by CVD method

MnSe nanowires synthesized by chemical vapor deposition method exhibited temperature dependent PL spectra with two broad emissions peaks around 413 and 435 nm ( $\lambda_{ex} = 325$  nm) and were assumed to be from the band edge emission spectra. It was observed that below  $-173$  °C the nanowires show another emission peak at 751 nm originating from spin forbidden transition. The appearance of this peak signifies the presence of octahedrally coordinated  $Mn^{2+}$  sites of the  $\alpha$ -MnSe nanostructures. It is observed that the intensities of the band edge emission peaks significantly decrease with the increase in temperature from  $-266$  to  $27$  °C. TRPL spectra of the nanostructures revealed single exponential decay behavior with average decay time of  $\tau_{av} = 18$   $\mu$ s for the  $Mn^{2+}$  transition. The average decay time values were found to remain constant as the temperature was increased from  $-266$  to  $-173$  °C [93].

### 3.9. Comparison of PL response of MnSe nanostructures synthesized by different methods

The PL spectrum of the MnSe nanostructures prepared using various synthesis techniques, comprised of mainly two emission peaks: band edge and defect related emission. Moreover, the Stokes shift calculated for MnSe nanostructures is very large in magnitude and is dependent on size, crystalline phase and the method of synthesis of the nanostructures. The Stokes shift obtained for MnSe nanostructures was compared for nanostructures synthesized by various synthesis procedures. Cubic phase MnSe nanoparticles exhibited the largest Stokes shift of 970 meV (101 nm) when synthesized by the hot injection method. On the other hand, MnSe nanoparticles of the same crystalline phase exhibited the lowest Stokes shift of 710 meV (80 nm) when synthesized using solvothermal method. Wurtzite phase MnSe nanoparticles exhibited the largest Stokes shift of 910 meV (97 nm) when synthesised by the hydrothermal method. On the other hand, MnSe nanoparticles of the same crystalline phase exhibited the lowest Stokes shift of 50 meV (7 nm) when synthesized

using solvothermal method. Table 4 depicts the calculated Stokes shift values of various MnSe nanostructures prepared by different synthesis procedures.

TABLE 4. Stokes shift calculated for MnSe nanostructures synthesized by various methods

Synthesis method	Crystal-line phase of MnSe	Shape	Parameter changed	Size (diameter) in nm	Excitonic wavelength $\lambda$ in nm ( $E_g$ in eV)	Emission maxima wavelength $\lambda$ in nm ( $E_g$ in eV)	Stokes shift nm ( $\Delta E_g$ in meV)	
Hydrothermal [20]	$\gamma$ -MnSe	Spherical	Change of $Mn^{2+}$ ; $Se^{2-}$	2:01	7	303(4.09)	400 (3.1)	97 (910)
	$\alpha$ -MnSe	—		3:1	—	408 (3.03)	535 (2.31)	127 (730)
	$\alpha$ -MnSe	—		4:1	—	408 (3.03)	535 (2.31)	127 (730)
Hydrothermal [38]	$\gamma$ -MnSe	Spherical	Type of capping agent	TGA	5	303 (4.09)	387 (3.2)	84 (890)
				SDS	14	330 (3.75)	377 (3.28)	47 (470)
Solvothermal [19]	Mixture of $\gamma$ -MnSe & $\beta$ -MnSe	Tetrapod shape	Change of heating rate	2 °C $min^{-1}$	30	389 (3.2)	400 (3.1)	11 (100)
	Mixture of $\gamma$ -MnSe & $\beta$ -MnSe	Small water-droplet shape		15 °C $min^{-1}$	40	391 (3.17)	402 (3.08)	11 (90)
	$\gamma$ -MnSe	Large water-droplet shape		25 °C $min^{-1}$	210	398 (3.11)	405 (3.06)	7 (50)
	$\alpha$ -MnSe	Spherical	—		200	336 (3.69)	416 (2.98)	80 (710)
Hot injection [52]	$\alpha$ -MnSe	Spherical	Change of reaction temperature	200 °C	7	311 (3.98)	411 (3.01)	101 (970)
				240 °C	12	324 (3.82)	419 (2.95)	95 (870)
				280 °C	16	344 (3.60)	432 (2.87)	88 (730)

#### 4. Conclusion

We presented a review of various wet-chemical and deposition methods that are used to synthesize  $\alpha$ -,  $\beta$ - and  $\gamma$ -MnSe nanostructures. Various reaction parameters influencing on the controlled growth as well the growth mechanism of the MnSe nanostructures is also discussed. The optical properties of the MnSe nanostructures were observed to be dependent on the method of synthesis procedure. UV-Vis spectroscopy studies showed that the blue shifting of absorption peaks of the MnSe nanostructures from the corresponding bulk MnSe band gaps were very small. However, the absorption peak maxima positions as well as the number of absorption peaks were dependent on the synthesis procedure used. Moreover, Stokes shift calculated from the absorption peak and emission peak maxima for the MnSe nanostructures are very large. A very high signal to noise ratio can be achieved when a nanostructure or any fluorescent dye exhibiting Stokes shift typically greater than 80 nm are used in biological imaging applications [94–97]. Time resolved photoluminescence spectroscopy (TRPL) indicates that the MnSe nanostructures synthesized by wet chemical methods exhibit bi-exponential decay characteristics with fast ( $\tau_1$ ) and slow ( $\tau_2$ ) relaxation time components. The both parameters depend significantly on the type of the capping material used in the MnSe nanostructure. Whereas nanostructures synthesized by using chemical vapor deposition exhibit single exponential decay in TRPL. This review article is expected to act as a reference to researchers in the controlled synthesis of MnSe nanostructures that exhibit special optical properties. Keeping in mind unlimited potential of nanostructure advantages, future research on MnSe looks promising in electrical and magnetic applications, biological labeling and in drug delivery applications.

## References

- [1] Furdyna J.K. Diluted magnetic semiconductors. *J. of Applied Physics*, 1988, **64** (4), R29–R64.
- [2] Furdyna J.K. Diluted magnetic semiconductors: An interface of semiconductor physics and magnetism. *J. of Applied Physics*, 1982, **53** (11), P. 7637–7643.
- [3] Dietl T. Diluted magnetic semiconductors. In *Handbook on semiconductors*, T.S. Moss ed., 1994, **3b**, Elsevier, Amsterdam Publishing, P. 1254–1329.
- [4] Alsaad A. Structural and magnetic properties of Mn-based diluted magnetic semiconductors and alloys. *Physics Research International*, 2009, **2009**, P. 1–4.
- [5] Sines I.T., et al. Colloidal synthesis of non equilibrium wurtzite type MnSe. *Angewandte Chemie International Edition*, 2010, **49** (27), P. 4638–4640.
- [6] Wu M., et al. Hydrothermal preparation of  $\alpha$ -MnSe and MnSe<sub>2</sub> nanorods. *J. of Crystal Growth*, 2004, **262** (1–4), P. 567–571.
- [7] Bououdina M., Song Y., Azzaza S. Nano-structured diluted magnetic Semiconductors. In *Reference module in materials science and materials engineering*, 2016, Elsevier, Amsterdam Publishing, P. 1–7.
- [8] Kacman P. Spin interactions in diluted magnetic semiconductors and magnetic semiconductor structures. *Semiconductor Science and Technology*, 2001, **16** (4), R25–R39.
- [9] Wang C., Yang F., Gao Y. The highly-efficient light-emitting diodes based on transition metal dichalcogenides: from architecture to performance. *Nanoscale Advances*, 2020, **2** (10), P. 4323–4340.
- [10] Rai D.P., et al. Spin-induced transition metal (TM) doped SnO<sub>2</sub> a dilute magnetic semiconductor (DMS): A first principles study. *J. of Physics and Chemistry of Solids*, 2018, **120**, P. 104–108.
- [11] Brozek C.K., et al. Soluble supercapacitors: large and reversible charge storage in colloidal Iron-doped ZnO nanocrystals. *Nano Letters*, 2018, **18** (5), P. 3297–3302.
- [12] Balti I., et al. Nanocrystals of Zn(Fe)O-based diluted magnetic semi-conductor as potential luminescent and magnetic bimodal bioimaging probes. *RSC Advances*, 2014, **4** (102), P. 58145–58150.
- [13] Decker D.L., Wild R. Optical properties of  $\alpha$ -MnSe. *Physical Review B*, 1971, **4** (10), 3425.
- [14] Bouroushian M. *Electrochemistry of metal chalcogenides*, 2010, Springer, Berlin, Heidelberg Publishing, 358 pp.
- [15] Murray R.M., Forbes B.C., Heyding R.D. The preparation and paramagnetic susceptibility of  $\beta$ -MnSe. *Canadian J. of Chemistry*, 1972, **50** (24), P. 4059–4061.
- [16] Schlesinger M. The Mn–Se (manganese-selenium) system. *J. of phase equilibria*, 1998, **19** (6), P. 588–590.
- [17] Prasad M., et al. Electrical transport properties of manganese selenide. *Materials Chemistry and Physics*, 1991, **30** (1), P. 13–17.
- [18] O'Hara D.J., et al. Room temperature intrinsic ferromagnetism in epitaxial manganese selenide films in the monolayer limit. *Nano Letters*, 2018, **18** (5), P. 3125–3131.
- [19] Yang X., et al. Morphology-controlled synthesis of anisotropic wurtzite MnSe nanocrystals: optical and magnetic properties. *Cryst. Eng. Comm.*, 2012, **14** (20), P. 6916–6920.
- [20] Sarma R., et al. Physical and biophysical assessment of highly fluorescent, magnetic quantum dots of a wurtzite-phase manganese selenide system. *Nanotechnology*, 2014, **25** (27), 275101.
- [21] Song G., et al. Core-Shell MnSe@Bi<sub>2</sub>Se<sub>3</sub> fabricated via a cation exchange method as novel nanotheranostics for multimodal imaging and synergistic thermoradiotherapy. *Advanced Materials*, 2015, **27** (40), P. 6110–6117.
- [22] Chen S.-H., et al. Ultrasmall MnSe nanoparticles as t1-mri contrast agents for in vivo tumor imaging. *ACS Applied Materials & Interfaces*, 2022, **14** (9), P. 11167–11176.
- [23] Bharathi M V., et al. Green synthesis of highly luminescent biotin-conjugated CdSe quantum dots for bioimaging applications. *New J. of Chemistry*, 2020, **44** (39), P. 16891–16899.
- [24] Chakraborty S., et al. Multifunctional, high luminescent, biocompatible cdte quantum dot fluorophores for bioimaging applications. *International J. of Nanoscience*, 2011, **10**(04n05), P. 1191–1195.
- [25] Wang Z., et al. L-Aspartic acid capped CdS quantum dots as a high performance fluorescence assay for Silver ions (I) detection. *Nanomaterials*, 2019, **9** (8), 1165.
- [26] Kim J., et al. High-quantum yield alloy-typed core/shell CdSeZnS/ZnS quantum dots for bio-applications. *J. of Nanobiotechnology*, 2022, **20** (1), P.1–12.
- [27] Ji X., et al. Fluorescent quantum dots: Synthesis, biomedical optical imaging, and biosafety assessment. *Colloids and Surfaces B: Biointerfaces*, 2014, **124**, P. 132–139.
- [28] Chan W.C.W., et al. Luminescent quantum dots for multiplexed biological detection and imaging. *Current Opinion in Biotechnology*, 2002, **13** (1), P. 40–46.
- [29] Xing Y., Rao J. Quantum dot bioconjugates for in vitro diagnostics & in vivo imaging. *Cancer biomarkers: section A of Disease markers*, 2008, **4** (6), P. 307–319.
- [30] Derfus A.M., Chan W.C.W., Bhatia S.N. Probing the cytotoxicity of semiconductor quantum dots. *Nano letters*, 2003, **4** (1), P. 11–18.
- [31] Pradhan N., et al. Efficient, stable, small, and water-soluble doped ZnSe nanocrystal emitters as non-cadmium biomedical labels. *Nano letters*, 2007, **7** (2), P. 312–317.
- [32] Pradhan N., et al. An alternative of CdSe nanocrystal emitters: pure and tunable impurity emissions in ZnSe nanocrystals. *J. of the American Chemical Society*, 2005, **127** (50), P. 17586–17587.
- [33] Wang C., et al. Aqueous synthesis of mercaptopropionic acid capped Mn<sup>2+</sup>-doped ZnSe quantum dots. *J. of Materials Chemistry*, 2009, **19** (38), P. 7016–7022.
- [34] Zhu D., et al. Green synthesis and potential application of low-toxic Mn: ZnSe/ZnS core/shell luminescent nanocrystals. *Chem. Commun.*, 2010, **46** (29), P. 5226–5228.
- [35] Pearson R. Hard and soft acids and bases. *J. of the American Chemical Society*, 1963, **85** (22), P. 3533–3539.
- [36] Wu M., et al. Hydrothermal preparation of  $\alpha$ -MnSe and MnSe<sub>2</sub> nanorods. *J. of crystal growth*, 2004, **262** (1–4), P. 567–571.
- [37] Moloto N., et al. Synthesis and characterization of MnS and MnSe nanoparticles: Morphology, optical and magnetic properties. *Optical Materials*, 2013, **36** (1), P. 31–35.
- [38] Sarma R., Mohanta D. Anomalous carrier life-time relaxation mediated by head group interaction in surface anchored MnSe quantum dots conjugated with albumin proteins. *Materials Chemistry and Physics*, 2017, **187**, P. 46–53.
- [39] Deka A., Saha A., Mohanta D. Consequence of surfactant coating on the Raman active modes and highly symmetric blue-emission decay dynamics of cubic phase MnSe quantum dots. *Physica E: Low-dimensional Systems and Nanostructures*, 2019, **113**, P. 226–232.

- [40] Sun J., et al. Controlled synthesis of ferromagnetic MnSe particles. *Chinese Physics B*, 2016, **25** (10), P. 107405.
- [41] Deka A., Mohanta D. Noticeable size dispersity and optical stability of sodium dodecyl sulphate (SDS)-coated MnSe quantum dots in extreme natural environment. *Applied Physics A*, 2019, **125** (9), P. 1–10.
- [42] Sahoo S., et al. Hydrothermally prepared  $\alpha$ -MnSe nanoparticles as a new pseudocapacitive electrode material for supercapacitor. *Electrochimica Acta*, 2018, **268**, P. 403–410.
- [43] Tang H., et al. Hydrothermally synthesized MnSe as high cycle stability anode material for lithium-ion battery. *Ionics*, 2020, **26** (1), P. 43–49.
- [44] Kharisov B.I., Kharissova O.V., ed., *Handbook of greener synthesis of nanomaterials and compounds: volume 1: fundamental principles and methods*. 2021, Elsevier Publishing, 976 pp.
- [45] Qin T., et al.  $\alpha$ -MnSe crystallites through solvothermal reaction in ethylenediamine. *Inorganic Chemistry Communications*, 2002, **5** (5), P. 369–371.
- [46] Lei S., Tang K., Zheng H. Solvothermal synthesis of  $\alpha$ -MnSe uniform nanospheres and nanorods. *Materials Letters*, 2006, **60** (13), P. 1625–1628.
- [47] Luo Q. Nanoparticles inks. In *Solution processed metal oxide thin films for electronic applications*, Z. Cui, G. Korotcenkov, eds., 2020, Elsevier, New York Publishing, P. 63–82.
- [48] Thanh N.T., Maclean N., Mahiddine S. Mechanisms of nucleation and growth of nanoparticles in solution. *Chemical reviews*, 2014, **114** (15), P. 7610–7630.
- [49] Donegá de M., Liljeroth C.P., Vanmaekelbergh D. Physicochemical evaluation of the hot-injection method, a synthesis route for monodisperse nanocrystals. *Small*, 2005, **1** (12), P. 1152–1162.
- [50] Salaheldin A.M., et al. Automated synthesis of quantum dot nanocrystals by hot injection: mixing induced self-focusing. *Chemical Engineering J.*, 2017, **320**, P. 232–243.
- [51] LaMer V.K., Dinegar R.H. Theory, production and mechanism of formation of monodispersed hydrosols. *J. of The American Chemical Society*, 1950, **72** (11), P. 4847–4854.
- [52] Li N., et al. Synthesis of high-quality  $\alpha$ -mnsse nanostructures with superior lithium storage properties. *Inorganic Chemistry*, 2016, **55** (6), P. 2765–2770.
- [53] Das K., et al. Size-dependent magnetic properties of cubic-phase MnSe nanospheres emitting blue-violet fluorescence. *Materials Research Express*, 2018, **5** (5), 056106.
- [54] Martin P.M. Chemical vapor deposition. In *Handbook of deposition technologies for films and coatings: science, applications and technology*, 2009, William Andrew Publishing, P. 314–361.
- [55] Chun H., et al. Morphology-tuned growth of  $\alpha$ -mnsse one-dimensional nanostructures. *J. of Physical Chemistry C*, 2006, **111** (2), P. 519–525.
- [56] Tomasini P., et al. Methylpentacarbonylmanganese as organometallic precursor for the epitaxial growth of manganese selenide heterostructures. *J. of crystal growth*, 1998, **193** (4), P. 572–576.
- [57] Zou J., et al. Controlled growth of ultrathin ferromagnetic  $\beta$ -MnSe semiconductor. *Smart Mat.*, 2022, **3** (3), P. 482–490.
- [58] Balakrishnan G., et al. Growth of nanolaminate structure of tetragonal zirconia by pulsed laser deposition. *Nanoscale research letters*, 2013, **8** (1), P. 1–7.
- [59] Norton D.P. Pulsed laser deposition of complex materials: progress toward applications in pulsed laser deposition of thin films: applications-led growth of functional materials, R. Eason, ed., 2007, Wiley Publishing, P. 1–31.
- [60] Zhu X.N., et al. Piezoelectric and dielectric properties of multilayered BaTiO<sub>3</sub>/(Ba,Ca)TiO<sub>3</sub>/CaTiO<sub>3</sub> thin films. *ACS Applied Materials & Interfaces*, 2016, **8** (34), P. 22309–22315.
- [61] Xue M.-Z., Fu Z.-W. Manganese selenide thin films as anode material for lithium-ion batteries. *Solid State Ionics*, 2007, **178** (3), P. 273–279.
- [62] Perkowitz S. *Optical characterization of semiconductors: infrared, Raman, and photoluminescence spectroscopy*, 1993, Elsevier Publishing, 220 pp.
- [63] Stepniak G., Schüpbert M., Bunge C.-A. Polymer-optical fibres for data transmission. In *Polymer optical fibres*, C.-A. Bunge, T. Gries, M. Beckers, eds., 2017, Woodhead Publishing, P. 217–310.
- [64] Alivisatos A.P. Semiconductor clusters, nanocrystals, and quantum dots. *Science*, 1996, **271** (5251), P. 933–937.
- [65] Nair A.K., et al. Optical characterization of nanomaterials. In *Characterization of nanomaterials*, S.M. Bhagyaraj, et al. eds., 2018, Woodhead Publishing, P. 269–299.
- [66] Lei S., Tang K., Zheng H., Solvothermal synthesis of  $\alpha$ -MnSe uniform nanospheres and nanorods. *Materials Letters*, 2006, **60** (13–14), P. 1625–1628.
- [67] Heulings, et al. Mn-substituted inorganic/organic hybrid materials based on ZnSe: nanostructures that may lead to magnetic semiconductors with a strong quantum confinement effect. *Nano Letters*, 2001, **1** (10), P. 521–525.
- [68] Dwandaru W.S.B., Bilqis S.M., Wisnuwijaya R.I. Optical properties comparison of carbon nanodots synthesized from commercial granulated sugar using hydrothermal method and microwave. *Materials Research Express*, 2019, **6** (10), 105041.
- [69] Zhu K., et al. Manganese-doped MnSe/CdSe core/shell nanocrystals: Preparation, characterization, and study of growth mechanism. *J. of Materials Research*, 2011, **26** (18), P. 2400–2406.
- [70] Zhou R., et al. Nanocrystals for large Stokes shift-based optosensing. *Chinese Chemical Letters*, 2019, **30** (10), P. 1843–1848.
- [71] Bera D., et al. Quantum dots and their multimodal applications: a review. *Materials*, 2010, **3** (4), P. 2260–2345.
- [72] Kim S.H., et al. Influence of size and shape anisotropy on optical properties of CdSe quantum dots. *Nanomaterials*, 2020, **10** (8), 1589.
- [73] Kundu J., et al. Giant nanocrystal quantum dots: stable down-conversion phosphors that exploit a large stokes shift and efficient shell-to-core energy relaxation. *Nano Letters*, 2012, **12** (6), P. 3031–3037.
- [74] Galiyeva P., et al. Mn-doped quinary Ag–In–Ga–Zn–S quantum dots for dual-modal imaging. *ACS omega*, 2021, **6** (48), P. 33100–33110.
- [75] Zhou R., et al. Enriching Mn-doped znse quantum dots onto mesoporous silica nanoparticles for enhanced fluorescence/magnetic resonance imaging dual-modal bio-imaging. *ACS Applied Materials & Interfaces*, 2018, **10** (40), P. 34060–34067.
- [76] Ren T.-B., et al. A general method to increase stokes shift by introducing alternating vibronic structures. *J. of the American Chemical Society*, 2018, **140** (24), P. 7716–7722.
- [77] Deng Z., et al. Water-based route to ligand-selective synthesis of ZnSe and Cd-doped ZnSe quantum dots with tunable ultraviolet a to blue photoluminescence. *Langmuir*, 2009, **25** (1), P. 434–442.
- [78] Artesani A., et al. A photoluminescence study of the changes induced in the zinc white pigment by formation of zinc complexes. *Materials*, 2017, **10** (4), 340.
- [79] Hung C.-C., et al. Strong green photoluminescence from In<sub>x</sub>Ga<sub>1-x</sub>N/GaN nanorod arrays. *Optics express*, 2009, **17**, P. 17227–17233.
- [80] Sheats G.F., Forster L.S. Fluorescence lifetimes in hydrated bovine serum albumin powders. *Biochemical and Biophysical Research Communications*, 1983, **114** (3), P. 901–906.
- [81] Schlegel G., et al. Fluorescence decay time of single semiconductor nanocrystals. *Physical Review Letters*, 2002, **88** (13), 137401.

- [82] Telgmann T., Kaatz U. Monomer exchange and concentration fluctuations of micelles broad-band ultrasonic spectrometry of the system triethylene glycol monohexyl ether/water. *The J. of Physical Chemistry A*, 2000, **104** (6), P. 1085–1094.
- [83] Yang W., et al. Surface passivation extends single and biexciton lifetimes of InP quantum dots. *Chemical science*, 2020, **11** (22), P. 5779–5789.
- [84] Chatterjee A., Maity B., Seth D. Photophysics of 7-(diethylamino)coumarin-3-carboxylic acid in cationic micelles: effect of chain length and head group of the surfactants and urea. *RSC Adv.*, 2014, **4** (64), P. 34026–34036.
- [85] Saha J., et al. Enhancing the performance of heterogeneously coupled InAs Stranski-Krastanov on submonolayer quantum dot heterostructures. *Superlattices and Microstructures*, 2019, **135**, 106260.
- [86] Bautista M., et al. Surface characterisation of dextran-coated iron oxide nanoparticles prepared by laser pyrolysis and coprecipitation. *J. of Magnetism and Magnetic Materials*, 2005, **293**, P. 20–27.
- [87] Lei S., Tang K., Zheng H. Solvothermal synthesis of  $\alpha$ -MnSe uniform nanospheres and nanorods. *Materials Letters*, 2006, **60** (13–14), P. 1625–1628.
- [88] Li L.-S., et al. Semiconductor nanorod liquid crystals. *Nano Letters*, 2002, **2** (6), P. 557–560.
- [89] Mokari T., Banin U. Synthesis and properties of CdSe/ZnS core/shell nanorods. *Chemistry of Materials*, 2003, **15** (20), P. 3955–3960.
- [90] Brennan M.C., et al. Origin of the size-dependent Stokes shift in CsPbBr<sub>3</sub> perovskite nanocrystals. *J. of the American Chemical Society*, 2017, **139** (35), P. 12201–12208.
- [91] Placencia D., et al. Synthesis and optical properties of PbSe nanorods with controlled diameter and length. *The J. of Physical Chemistry Letters*, 2015, **6** (17), P. 3360–3364.
- [92] Qu L., Peng X. Control of photoluminescence properties of cdse nanocrystals in growth. *J. of the American Chemical Society*, 2002, **124** (9), P. 2049–2055.
- [93] Chun H.J., et al. Morphology-tuned growth of  $\alpha$ -MnSe one-dimensional nanostructures. *The J. of Physical Chemistry C*, 2007, **111** (2), P. 519–525.
- [94] Gao, Z., Hao Y., Zheng M.-L. A fluorescent dye with large Stokes shift and high stability: synthesis and application to live cell imaging. *RSC Adv.*, 2017, **7**, P. 7604–7609.
- [95] He X., et al. Fluorescence resonance energy transfer mediated large Stokes shifting near-infrared fluorescent silica nanoparticles for in vivo small-animal imaging. *Analytical Chemistry*, 2012, **84** (21), P. 9056–9064.
- [96] Zhang S., et al. One-step synthesis of yellow-emissive carbon dots with a large Stokes shift and their application in fluorimetric imaging of intracellular pH. *Spectrochimica Acta Part A: Molecular and Biomolecular Spectroscopy*, 2020, **227**, 117677.
- [97] Zhang J., et al. Highly stable near-infrared fluorescent organic nanoparticles with a large Stokes shift for noninvasive long-term cellular imaging. *ACS Applied Materials & Interfaces*, 2015, **7** (47), P. 26266–26274.

---

Submitted 10 June 2022; revised 25 August 2022; accepted 29 August 2022

*Information about the authors:*

*Runjun Sarma* – Mehr Chand Mahajan DAV College for Women, Sector 36, Chandigarh, India; ORCID 0000-0003-4000-7787; runjun2018chd@gmail.com

*Munmi Sarma* – Former Research Scholar, Sensors & Biosensors group, Autonomous University of Barcelona, Spain; munmisarma11@gmail.com

*Manash Jyoti Kashyap* – Polymer Technology Consultant, Chandigarh, India; manashjk@gmail.com

*Conflict of interest:* on behalf of all authors, the corresponding author states that there is no conflict of interest.

## Optimizing the carbonization temperature in the fabrication of waste cotton based activated carbon used as electrode material for supercapacitor

Nguyen K. Thach<sup>1,2,a</sup>, Ilya S. Krechetov<sup>1,b</sup>, Valentin V. Berestov<sup>1,c</sup>,  
Tatyana L. Lepkova<sup>1,d</sup>, Svetlana V. Stakhanova<sup>1,3,e</sup>

<sup>1</sup>National University of Science and Technology “MISIS”, Moscow, Russia

<sup>2</sup>Vietnam National University of Forestry, Hanoi, Vietnam

<sup>3</sup>Mendeleev University of Chemical Technology of Russia, Moscow, Russia

<sup>a</sup>[nguyenkienthach@gmail.com](mailto:nguyenkienthach@gmail.com), <sup>b</sup>[ilya.krechetov@misis.ru](mailto:ilya.krechetov@misis.ru), <sup>c</sup>[vberestov97@gmail.com](mailto:vberestov97@gmail.com),

<sup>d</sup>[lepkoval.tl@misis.ru](mailto:lepkoval.tl@misis.ru), <sup>e</sup>[stakhanova.s.v@muctr.ru](mailto:stakhanova.s.v@muctr.ru)

Corresponding author: N. K. Thach, [nguyenkienthach@gmail.com](mailto:nguyenkienthach@gmail.com)

**ABSTRACT** H<sub>3</sub>PO<sub>4</sub>-impregnated waste cotton was used as precursor to fabricate high porous activated carbon (AC) by the carbonization and activation processes with ultrahigh heating rate. The obtained activated carbon has unique physicochemical properties such as the structure mainly amorphous and ultrahigh specific surface area of 2769.7 m<sup>2</sup>/g for samples fabricated at carbonization temperature of 600 °C. The double-layer supercapacitors with activated carbon electrodes and electrolyte based on 1,1-dimethylpyrrolidinium tetrafluoroborate solution in acetonitrile of 1 M concentration were fabricated. The specific capacitance of electrode material fabricated from AC obtained at carbonization temperature of 600 °C reached 110.8 F/g at the current density of 50 mA/g and 85.1 F/g at 1000 mA/g. At 1000 mA/g, the degradation was less than 25% after 5000 charge/discharge cycles. The carbonization temperature of 600 °C is considered as optimum for fabricating activated carbon and the obtained activated carbon can be used for supercapacitor electrode materials.

**KEYWORDS** cotton, waste cotton, activated carbon, porous carbon, electrode material, supercapacitor, cellulose.

**FOR CITATION** Thach N.K., Krechetov I.S., Berestov V.V., Lepkova T.L., Stakhanova S.V. Optimizing the carbonization temperature in the fabrication of waste cotton based activated carbon used as electrode material for supercapacitor. *Nanosystems: Phys. Chem. Math.*, 2022, **13** (5), 565–573.

### 1. Introduction

Supercapacitors (SCs), also known as Electrochemical Capacitors, are devices that store electrical energy inside an electrical double layer (EDL) formed at the interface between the electrolyte solution and the solid-surface electrode with large surface area [1]. When compared to batteries, SCs have outstanding advantages such as high power density, large power conversion ratio, fast charge/discharge time, long life cycle, etc. While their disadvantage when compared in terms to batteries of the same mass and volume is their much lower energy density. Therefore, in commercial applications, SCs are often used in devices that support battery or fuel cell operation in the starting systems in which it is necessary to provide instantaneous electrical energy with high capacity for a short period of time such as automobiles, vehicles, trucks, buses, etc [2]. With the development of electronic technology in mobile devices, SCs are also used in intermittent energy recovery systems in automotive brake systems, solar cells, and small power electrical devices, etc.

The electrical energy capacity ( $E$ ) of an electrochemical double-layer supercapacitor (EDLS) is determined by  $E = \frac{1}{2}CV^2$ , where  $C$  is the capacitance of the capacitor and  $V$  is the operating voltage applied across the two electrodes. Consequently, operating voltage and capacitance are the two main factors affecting the energy storage capacity of EDLS. The operating voltage of SCs depend mainly on the electrolytes and solvents used. So, the electrolyte solutions need to have a large working potential window to maximize the electrical energy capacity. The aqueous electrolytes (acids, alkalis, inorganic salts) have a narrow potential window (0.8 – 1.2 V), making them unsuitable for commercial SCs. Moreover, during the capacitor's operation, the collectors are destroyed by the electrochemical corrosion that occurs on their surface, so the material used to make the current collectors must have high corrosion resistance such as stainless steel [3], silver, gold, etc. Therefore, it is expensive. However, the mobility and conductivity of ions in aqueous electrolytes are high and making them easy to use without strict storage conditions. In contrast to the aqueous electrolytes, organic electrolytes have large potential windows (2.5 – 3.5 V), and organic salts allow cheaper and less corrosive collector and enclosure materials. Recently, organic electrolyte solutions are increasingly used in commercial SCs.

Meanwhile, the capacitance of SCs depends on the surface area of the electrodes, the functional groups present on the surface, and the compatibility between the pore size distribution and the size of the electrolyte molecules. To increase the electrode surface area, materials with high porosity, specific surface area greater than  $1000 \text{ m}^2/\text{g}$ , have been commonly used in commercial SCs. With highly porous electrode materials, when the pore size is equivalent to the size of the electrolyte molecule, the interaction between the surface active sites and the electrolyte ions is quite weak and between the electrolyte–electrolytes dominate. Electrolyte–electrolyte interactions reduce the surface adsorption capacity for the electrolyte and thus lead to a decrease in the capacitance of the capacitor. If the pore size is too large compared to the electrolyte molecular size, the specific surface area of electrode is small, the density of surface active sites decreases, the electrolyte adsorption capacity decreases and leads to decrease capacitance of SCs.

In recent years, high porosity activated carbon from biomass has attracted much research attention of scientists, especially agricultural residues such as rice husk residue [4], sugarcane bagasse [5], cassava peel waste [6], cotton, cotton waste [7–10], etc. The activated carbon products meet the requirements for electrode materials such as large surface area, pore size that can be changed according to fabricating conditions and many surfaces functional groups. Moreover, these materials have many advantages such as low cost, availability, environment friendly and perfected electrode producing technology.

In our study, we focused on investigating the effect of carbonization temperature with ultrahigh heating rate on the properties of activated carbon obtained from  $\text{H}_3\text{PO}_4$ -impregnated waste cotton. First, the carbonization process conducted in argon atmosphere at various temperature from  $400 \text{ }^\circ\text{C}$  to  $800 \text{ }^\circ\text{C}$  with ultrahigh heating rate. Then, the physical activation process conducted in carbon dioxide atmosphere. By investigating the texture and electrochemical properties of obtained activated carbon, we propose the optimal carbonization temperature to produce activated carbon from waste cotton impregnated  $\text{H}_3\text{PO}_4$  used as electrode materials for supercapacitors.

## 2. Materials and methods

### 2.1. Preparation of activated carbon

*2.1.1. Impregnation of waste cotton.* Waste cotton was collected from Yartsevo Cotton Mill, LLC (Russia). 10 g of waste cotton was soaked in 300 g of 5 %  $\text{H}_3\text{PO}_4$  solution in a standard water bath. Then, the mixture was heated to a temperature range of  $80\text{--}85 \text{ }^\circ\text{C}$  and kept for 30 min. After the impregnation process, the cotton was squeezed out of water and dried at room temperature at least 24 h.

*2.1.2. Carbonization of waste cotton.* The carbonization was carried out in a horizontal furnace, the temperature and time controlled by Termodat controller. The carbonization temperatures were  $400 \text{ }^\circ\text{C}$ ,  $500 \text{ }^\circ\text{C}$ ,  $600 \text{ }^\circ\text{C}$ ,  $700 \text{ }^\circ\text{C}$  and  $800 \text{ }^\circ\text{C}$ . Initially, 4 g of shredded cotton was put into a quartz reactor chamber and supplied with a flow of Ar gas at a flow rate of 800 ml/min for 15 min to remove the air inside the reactor chamber. To achieve the ultrahigh heating rate for carbonization, the furnace was heated at a rate of  $10 \text{ }^\circ\text{C}/\text{min}$  until achieving the carbonization temperature. Then, the reactor chamber with cotton inside was put immediately into the furnace and maintained with a flow of Ar gas at a flow rate of 800 ml/min. The time of carbonization was 1 h. When the carbonization process finished, the reactor chamber was taken out, and cooled to the room temperature by the electric fan and the Ar flow at flow rate of 800 ml/min. The obtained products were weighed, and labeled with SP400, SP500, SP600, SP700, SP800 with carbonization temperatures of  $400 \text{ }^\circ\text{C}$ ,  $500 \text{ }^\circ\text{C}$ ,  $600 \text{ }^\circ\text{C}$ ,  $700 \text{ }^\circ\text{C}$  and  $800 \text{ }^\circ\text{C}$ , respectively.

*2.1.3. Activation.* All obtained products of carbonization are put into the reactor chamber. Ar gas with a flow rate of 800 ml/min was introduced into the reactor chamber for 15 minutes to remove air. The furnace first was heated to  $900 \text{ }^\circ\text{C}$  with the heating rate of  $10 \text{ }^\circ\text{C}/\text{min}$ . Then, the reactor chamber was put immediately into the furnace and maintained with a flow of Ar gas at a flow rate of 800 ml/min until reaches activation temperature of  $900 \text{ }^\circ\text{C}$ . Then, the Ar flow was interrupted, the  $\text{CO}_2$  flow was started and maintained at flow rate of 800 ml/min during the activation process. The activation time was 1 h. When activation process finished, the  $\text{CO}_2$  gas was interrupted, the Ar gas was started supplying at a flow rate of 800 ml/min. Then, the reactor chamber was taken out, and cooled to the room temperature by the electric fan and the Ar flow at flow rate of 800 ml/min. The activated carbon product was weighed and stored in a plastic bag to avoid dust and used for the next processes.

### 2.2. Physical characterization measurements of activated carbon

The surface morphology investigation of the activated carbon was performed on the focusing ion beam scanning electron microscope (SEM) TESCAN SOLARIS (Czech).

The investigation of specific surface area, pore volume, and pore size distribution was carried out by  $\text{N}_2$  adsorption-desorption isotherms at 77 K using a Gemini VII 2390 V1.02 (Micromeritics, USA).

The X-ray diffraction (XRD) spectra were conducted on an XPERT-PRO (Latvia).

TABLE 1. Minimum reactor chamber temperature, and heating rate of cotton carbonization

Samples	SP400	SP500	SP600	SP700	SP800
Minimum reactor chamber temperature, ( °C)	380 ± 10	471 ± 9	557 ± 13	638 ± 14	705 ± 7
Heating rate, ( °C/min)	321 ± 45	412 ± 44	466 ± 47	510 ± 62	577 ± 41

### 2.3. Preparation of supercapacitors and electrochemical measurements

Activated carbon was crushed with a mortar and mixed with polytetrafluoroethylene suspension F4D (Russia) as the binding material and carbon black (CABOT® VULCAN® XC72) as the electrically conductive component according to the mass ratio of 80:10:10, respectively. The mixture was placed in a glass flask containing 100 ml of 95 % alcohol (FEREIN, Russia) and stirred at room temperature for 30 minutes. The slurry was filtered through filter paper and rolled on a mechanical roller to form thin films with a thickness of 150  $\mu\text{m}$ . The thin films will then be cut into squares of different sizes for use as the capacitor's electrodes. The electrodes were dried at room temperature at least 24 h. Before use, the carbon electrodes were heated up to 120 °C for 2 h in the quartz tube with a flow rate of Ar of 100 ml/min and then weighed on a balance with an accuracy of 0.001 g.

The obtained carbon electrodes were pasted onto aluminum foils (OKURA-801, Japan) used as the collector of the supercapacitors by conductive adhesive (RIKON, Russia). The two complete electrodes are placed opposite each other and separated by a separator TF-40-30 (Japan). The electrode system was placed in an adhesive enclosure and kept under vacuum at 120 °C for 48 h. Next, the enclosure was filled with 1 ml of 1,1-dimethylpyrrolidinium tetrafluoroborate (DMP·BF<sub>4</sub>) solution of 1 M concentration in acetonitrile (AN) solvent and packed to form a complete capacitor.

The cycle voltammetry characteristics of the capacitors were measured using P20-X potentiostat (Elins, Russia).

The charge/discharge tests were performed by the method of galvanostatic charge-discharge using ASK2.5.10.8 HIT analyzer (Russia).

## 3. Results and discussion

### 3.1. Heating rate and carbon yield

Cotton is a highly porous natural material. When conducting pyrolysis of cotton in an inert gas environment, cotton begin to thermally decompose at 250 °C and the process is intense in the range of 310 – 350 °C [11]. The pyrolysis's products include CO, CO<sub>2</sub>, H<sub>2</sub>O, and cellulose derivatives in liquid and gaseous states. When the temperature reaches above 350 °C, the cellulose decrystallization occurs. Currently, most studies in the field of biomass materials are conducted with heating rates between 5 °C and 20 °C and the reactor chamber is placed inside the furnace from room temperature along with the heating process. Therefore, the time of the heating process is usually greater than 1 h, and part of the cotton will undergo slow thermal decomposition. The products of the decomposition process penetrate inside the cotton fiber structure to prevent evaporation, reduce the decomposition rate of cellulose, and reduce the porosity of the cotton, leading to a decrease in the porosity of the obtained carbon.

To avoid slow thermal decomposition of cotton, we reduced the heating time for cotton from room temperature to the cellulose decrystallization temperature region to about 1 minute by carbonization method as described above. After the reactor was placed in the furnace, the temperature of the system suddenly dropped to the minimum value. The system then was heated up again to the carbonization temperature by the heating controller. The minimum temperature of the furnace and the heating rate of each carbonization temperature are shown in Table 1. From the data of Table 1, the minimum temperature of the reactor chamber for all samples is greater than 350 °C, the region where the cellulose decrystallization occurs. Above the cellulose decrystallization temperature, the thermal decomposition of cellulose takes place intensely and produces many derivatives in the liquid, gas, and vapor states. At high temperature and high Ar flow rate of 800 ml/min, these derivatives partly evaporate quickly from the cotton fiber surface and partly penetrate the cellulose crystal, destroying the crystal structure causing micro-swelling within the microstructure of the cellulose crystal, and facilitating the porous structure development. As a result, there are many close or open cavities inside the cotton fiber.

The carbon and activated carbon yields obtained after carbonization and activation processes are shown in Fig. 1. The yield of carbon obtained after carbonization decreased from 39.5% to 23.8% when the carbonization temperature was increased from 400 to 800 °C. This is consistent with the studies of M. J. Antal, et al [12]. As the carbonation temperature increases, the heating rate also increases, the decomposition of cellulose becomes more intense, producing more volatile derivatives and thus reducing the amount of coal obtained [13]. In contrast, we found that the yield of activated carbon is low and does not vary much for the samples. We suggested that, at high gas flow rates, CO<sub>2</sub> did not have enough time to diffuse deep into the carbon black structure and so instead of opening and expanding the inner pore structure, CO<sub>2</sub> burned most of carbon during activation.

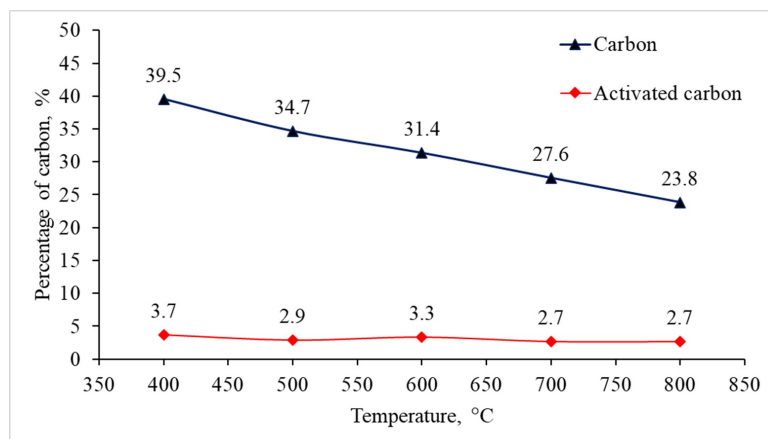


FIG. 1. Carbon yield after carbonization and activation of waste cotton at different carbonization temperatures

### 3.2. Physical properties

Figure 2 shows the X-ray diffraction (XRD) spectrum of the samples at different temperatures. The peak of graphite crystals (002) at  $2\theta \sim 25^\circ$  was low and no significant existence of graphite (001) at  $2\theta \sim 44^\circ$  was observed. This shows that the obtained activated carbon material has a structure mainly of amorphous carbon material.

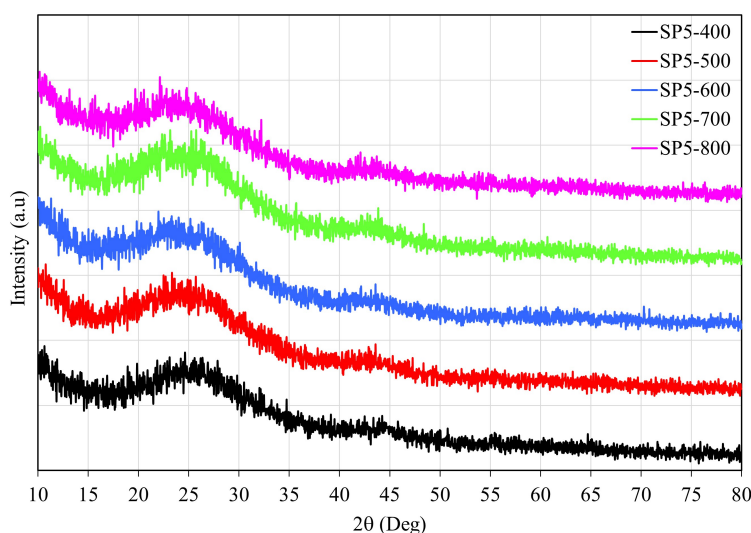


FIG. 2. X-ray diffraction spectrum of activated carbons prepared at different carbonization temperatures

Figure 3 shows the SEM image of the SP600 sample at different magnitudes. Fig. 3a shows that the activated carbon fiber surface is quite smooth, clear, and free of impurities adhering to the surface. Cotton fibers are characteristically flattened, twisted, and have an average diameter of less than  $10 \mu\text{m}$ . As in Fig. 3b, the surface structure of cotton fibers after activation retains the characteristic structure of cotton with many folds on the surface. At  $100 \text{ nm}$  magnitude (Fig. 3c), there are many small and uniform pore structures at the cotton fiber surface. This demonstrates that there has been a well-developed porous structure within the obtained activated carbon material. The size of the porous structures distributed in the region of micropores and mesopores.

The texture characteristics of activated carbon were identified by  $\text{N}_2$  adsorption-desorption measurement at  $77 \text{ K}$ . The Brunauer, Emmet, and Teller (BET) method and the Barrett, Joyner, and Halenda (BJH) method were used to determine the specific surface area and pore size distribution within the activated carbon. The  $\text{N}_2$  adsorption-desorption isotherms of the samples (Fig. 4) have the form corresponding to Type I(b) and Type II according to the IUPAC classification system [14, 15]. When the relative pressure  $p/p_0 < 0.99$ , the sorption isotherm has the form corresponding to Type I(b) with the pore structure distributed mainly in the micropores region and partly extended to the mesopores region with pore size less than  $2.5 \text{ nm}$ . These adsorption isotherms do not show the appearance of hysteresis loops for all samples. When the relative pressure  $p/p_0 = 1$ , there is an increasing without limit in the adsorption isotherms, corresponding to Type II with the appearance of macropores.

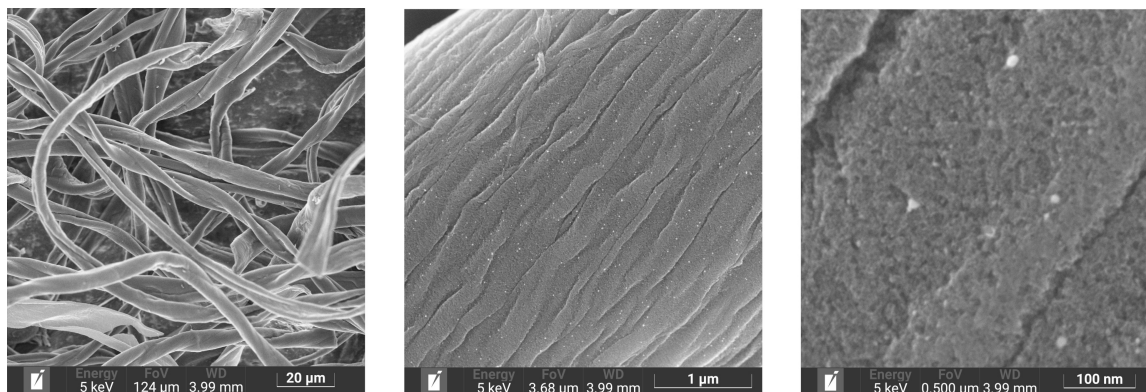


FIG. 3. SEM images of the sample SP600 at different magnitudes

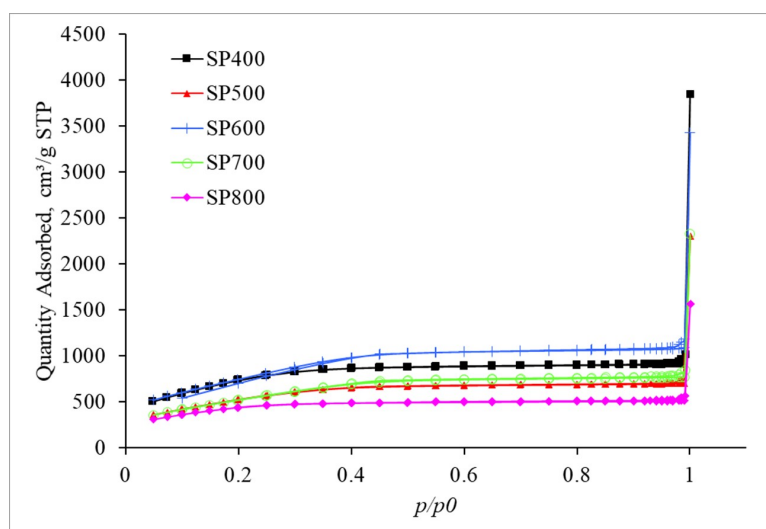


FIG. 4.  $N_2$  adsorption-desorption isotherms at 77 K of the samples prepared at different carbonization temperatures

Table 2 is the surface characteristic of activated carbon of all samples. The specific area ( $S_{BET}$ ) was calculated by BET method with relative pressure ( $p/p_0$ ) from 0.05 to 0.35. Total pore volume ( $V_{pore}$ ) and average pore size ( $d$ ) were calculated by BJH method. According to the data of Table 2, the specific surface area and total pore volume of the porous activated carbon samples reached the highest value for the sample SP600 with  $S_{BET} = 2769.7 \text{ m}^2/\text{g}$ ,  $V_{pore} = 2.09 \text{ cm}^3/\text{g}$  and the lowest value with sample SP800 with  $S_{BET} = 1433.4 \text{ m}^2/\text{g}$ ,  $V_{pore} = 0.74 \text{ cm}^3/\text{g}$ . When the carbonization temperature is less than  $600 \text{ }^\circ\text{C}$ , the specific surface area and total pore volume change randomly. Meanwhile, when the carbonization temperature is greater than  $600 \text{ }^\circ\text{C}$ , the specific surface area and total pore volume decrease as the carbonization temperature increases. This can be explained that at the carbonization temperature of  $400 \text{ }^\circ\text{C}$  and  $500 \text{ }^\circ\text{C}$ , the thermal decomposition of cellulose in cotton creates small-sized and partially sealed primary pores inside the cotton fiber structure. During activation,  $\text{CO}_2$  reacts with the carbon on the pore wall and partially opens these sealed hollow structures. Therefore, the specific surface area and total pore volume change unevenly with increasing temperature. But at the carbonization temperature of  $600 \text{ }^\circ\text{C}$ ,  $700 \text{ }^\circ\text{C}$ , and  $800 \text{ }^\circ\text{C}$ , the thermal decomposition takes place intensely and creates more open primary pore structures and larger sizes when increasing temperature. When activation takes place,  $\text{CO}_2$  removes carbon and further enlarges these pores and thereby reduces the specific surface area and total pores volume of the porous material. The BJH method is only applicable to determine the size of pores distributed in the mesopores and macropores regions. Therefore, the calculated average size of pores in Table 2 does not vary much for all samples and ranges from 2 – 3 nm.

Figure 5 shows the distribution of the pore sizes determined by the BJH method. It shows that all samples have a major peak in the micropores region and neighboring mesopores with size less than 2.5 nm and a minor peak in the macropores region with size larger than 50 nm. This is consistent with the characteristics of the nitrogen adsorption isotherms discussed above. Furthermore, as the carbonization temperature increases, there is an additional peak in the 4 – 5 nm region for SP700 and SP800 samples. This again demonstrates that as the carbonation temperature increases, the size of the primary pores inside the carbon black structure becomes larger, so there is a shift in pores size to a larger region.

TABLE 2. Surface characteristics of activated carbon of the SP400, P500, SP600, SP700, SP800 samples

Samples	$S_{BET}$ (m <sup>2</sup> /g)	$V_{pore}$ (cm <sup>3</sup> /g)	$d$ (Å)
SP400	2535.5	1.49	25.18
SP500	1883.7	1.47	27.67
SP600	2769.7	2.09	26.17
SP700	1931.0	1.53	27.90
SP800	1433.4	0.74	24.80

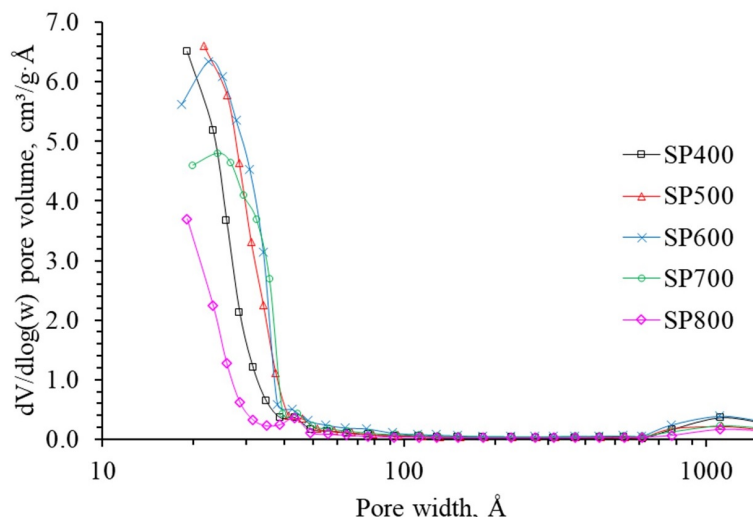


FIG. 5. The pore size distribution of the samples according to the BJH method

### 3.3. Electrochemical properties

Figure 6 shows the cyclic voltammogram (CV) curves with potential scan rates of 100 mV/s and the galvanostatic charge-discharge (GCD) curves at specific current density of 1000 mA/g for all samples. The change in shape of the CV curves is closely related to the equivalent series resistance (ESR) of the supercapacitor. The more like-rectangular the shape of the CV curves, the smaller the ESR and vice versa [16]. As shown in the Fig. 6a, the CV curves of the SP500, SP600, SP700 samples have the characteristic like-rectangular shape of an ideal capacitor and good reversibility but the samples SP400 and SP800 have not. This evidence shows that the electrochemical properties of the carbon electrode of the two samples SP400 and SP800 are worse than that of the other samples. Fig. 6b shows that the SP600 has the symmetric GCD curve, and the lowest voltage drop. The symmetry of the GCD curves reduces corresponding to the SP500, SP700 and finally SP400, and SP800. Again, the information from Fig. 6b shows that the SP600, and therefore the carbonization of the cotton at 600 °C, yielded activated carbon with the best electrochemical properties.

To assess the performance of fabricated capacitors, the specific capacitance of the capacitors was determined by the GCD method at specific density current from 50 mA/g to 5000 mA/g and presented at the diagram in Fig. 7. The SP600 capacitor achieved the highest specific capacitance from others with a value of 110.8 F/g at 50 mA/g and 85.1 F/g at 1000 mA/g. The value of the specific capacitance of the samples decreases as the specific current increases. However, Fig. 7 shows that there is a large difference between the change of the specific capacitance of the samples with increasing current density. Accordingly, the specific capacitance change of the SP600 capacitor is the smallest, followed by the SP700, SP500, and finally the SP400 and SP800 samples. The decrease in capacitance at high specific current densities is caused by the diffusion limitations of electrolyte ions inside the carbon electrodes [17].

One of the parameters affecting the performance of capacitors with organic electrolytes and organic solvents is their decomposition process when operating for a long time. The capacitors with AN solvent and ionic liquid electrolyte containing  $[BF_4]^-$  ion were studied in detail in our previous publish [18]. Accordingly, the carbon electrode fabrication process cannot completely remove the adsorbed water vapor inside the electrode material pores. The presence of water during the capacitor performance at high voltage causes water decomposition and leads to the decomposition of AN solvent and  $[BF_4]^-$  ions. The products of decomposition are usually a mixture of gases and precipitates. They diffuse into the porous structure, sealing the pores, thus preventing the adsorption of electrolyte solute molecules, reducing the

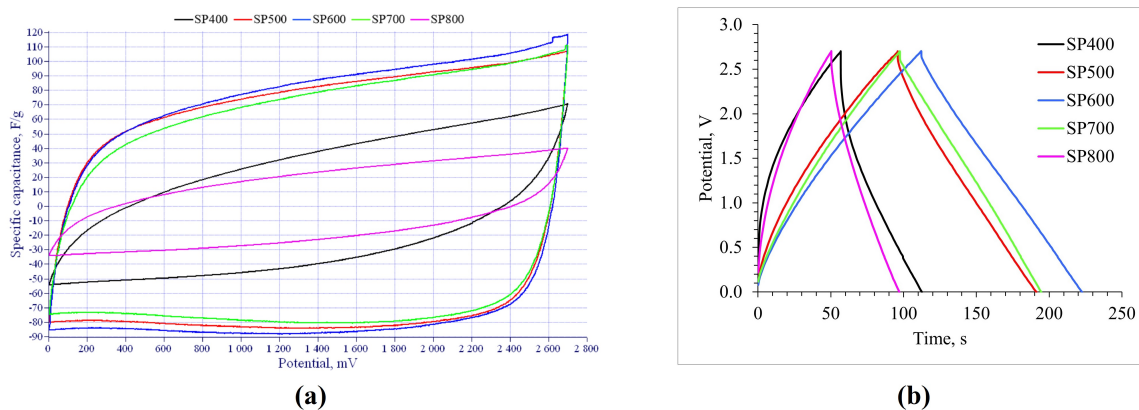


FIG. 6. (a) Cyclic voltammograms curves at potential scan rate of 100 mV/s and (b) galvanostatic charge-discharge curves at current density 1000 mA/g of the SCs with carbon electrodes fabricated at different carbonization temperatures

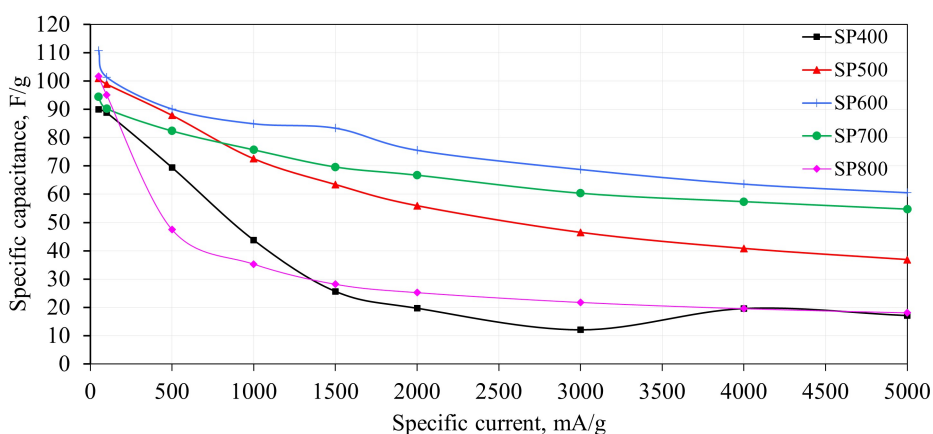


FIG. 7. Dependence of specific capacitance on the specific current densities of the capacitors

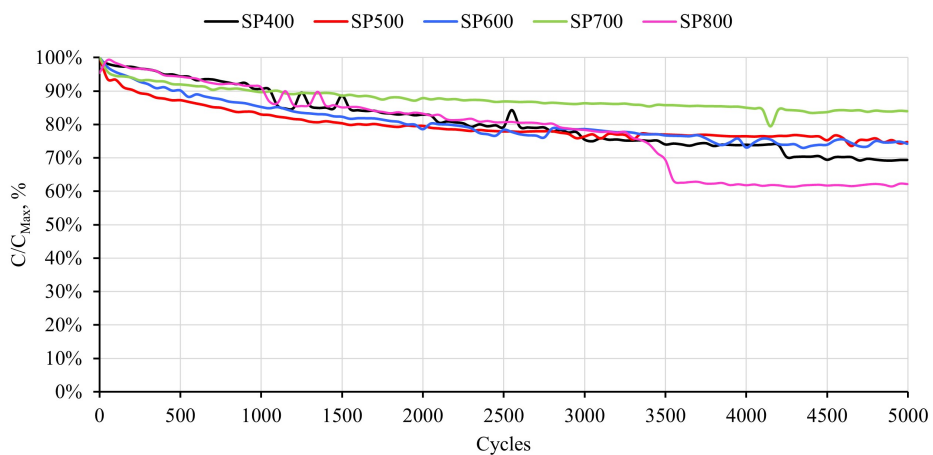


FIG. 8. Relative specific capacitance as a function of the charge-discharge cycles of the capacitors with 5000 cycles at a current density of 1000 mA/g

surface functional groups and specific surface area. The result is a decrease in the specific capacitance of the capacitor during operation.

The GCD method was used to investigate the life cycle of the capacitors. Fig. 8 shows the GCD curves of all capacitor samples with 5000 charge/discharge cycles at a specific current density of 1000 mA/g. The characteristic curve of the three samples SP500, SP600 and SP700 is quite smooth, and the relative specific capacitance decline is less than 25%, especially the SP700 sample, about 15%. This shows that the electrochemical properties of the carbon electrode as well as the electrode/collector junction of these capacitors are highly stable. On the opposite side, the relative specific capacitance curves of the SP400 and SP800 samples are unstable and have a sudden decline when the number of cycles reaches about 4200 and 3500 cycles, respectively. It shows that the electrochemical properties of the electrodes of the two samples are unstable.

#### 4. Conclusion

By the method of fast raising temperature of cotton carbonization above the cellulose decrystallization temperature in a short time with extra high heating rate, we have created activated carbon with unique physical and electrochemical properties. The ultrahigh specific surface area of ca. 2769.7 m<sup>2</sup>/g was obtained at carbonization temperature of 600 °C, with the pore size distribution mainly on the micropores region. There is a shift in pore size distribution from the micropores to the mesopores region with the increasing carbonization temperature. The capacitor with electrodes from activated carbon fabricated at the carbonation temperature of 600 °C exhibits better electrochemical properties and stable long-life cycles. Its specific capacitance values at current density 50 mA/g reached 110.8 F/g and the degradation of capacitance after 5000 cycles at 1000 mA/g less than 25 %. Therefore, the optimal temperature to obtain activated carbon with the best physicochemical properties for H<sub>3</sub>PO<sub>4</sub>-impregnated waste cotton is 600 °C and the obtained activated carbon can be fully satisfied used as electrode material for double layer supercapacitor.

#### References

- [1] Winter M., Brodd R.J. What are batteries, fuel cells, and supercapacitors? *Chemical Review*, 2004, **104**(10), P. 4245–4269.
- [2] Kö Tz R., Carlen M. Principles and Applications of Electrochemical Capacitors. *Electrochimica Acta*, 2000, **45**(15-16), P. 2483–2498.
- [3] Vijayakumar M., Santhosh R., Adduru J., Rao T.N., Karthik M. Activated carbon fibres as high performance supercapacitor electrodes with commercial level mass loading. *Carbon*, 2018, **140**, P. 465–476.
- [4] Luo Y., Li D., Chen Y., Sun X., Cao Q., Liu X. The performance of phosphoric acid in the preparation of activated carbon-containing phosphorus species from rice husk residue. *Journal of Materials Science*, 2019, **54**(6), P. 5008–5021.
- [5] Adib M.R.M., Suraya W.M.S.W., Rafidah H., Attahirah M.H.M.N., Hani M.S.N.Q., Adnan M.S. Effect of phosphoric acid concentration on the characteristics of sugarcane bagasse activated carbon. IOP Conf. Ser.: Mater. Sci. Eng. Langkawi, Malaysia, 27–29 October 2015, **136**(1), P. 012061.
- [6] Ismanto A.E., Wang S., Soetaredjo F.E., Ismadji S. Preparation of capacitor's electrode from cassava peel waste. *Bioresource Technology*, 2010, **101**(10), P. 3534–3540.
- [7] Sartova K., Omurzak E., Kambarova G., Dzhusmaev I., Borkoev B., Abdullaeva Z. Activated carbon, obtained from the cotton processing wastes. *Diamond and Related Materials*, 2019, **91**, P. 90–97.
- [8] Nahil M.A., Williams P.T. Pore characteristics of activated carbons from the phosphoric acid chemical activation of cotton stalks. *Biomass and Bioenergy*, 2012, **37**, P. 142–149.
- [9] Ma G., Guo D., Sun K., Peng H., Yang Q., Zhou X., Zhao X., Lei Z. Cotton-based porous activated carbon with a large specific surface area as an electrode material for high-performance supercapacitors. *RSC Advances*, 2015, **5**(79), P. 64704–64710.
- [10] Nahil M.A., Williams P.T. Characterisation of activated carbons with high surface area and variable porosity produced from agricultural cotton waste by chemical activation and co-activation. *Waste and Biomass Valorization*, 2012, **3**(2), P. 117–130.
- [11] Lewin M., Backer S., Hersh S.P., et al. *Cotton fiber chemistry and technology*. Phillip J. Wakelyn, Boca Raton, 2006, 176 p.
- [12] Antal M.J., Várhegyi G., Jakab E. Cellulose pyrolysis kinetics: Revisited. *Ind. Eng. Chem. Res.*, 1998, **37**(4), P. 1267–1275.
- [13] Brunner P.H., Roberts P.V. The significance of heating rate on char yield and char properties in the pyrolysis of cellulose. *Carbon*, 1980, **18**(3), P. 217–224.
- [14] Sing K.S.W., Everett D.H., Haul R.A.W., Moscou L., Pierotti R.A., Rouquérol J., Siemieniowska T. Reporting physisorption data for gas/solid systems-with special reference to the determination of surface area and porosity (Recommendations). *Pure and Applied Chemistry*, 1985, **57**(4), P. 603–619.
- [15] Thommes M., Kaneko K., Neimark A.V., Olivier J.P., Rodriguez-Reinoso F., Rouquerol J., Sing K.S.W. Physisorption of gases, with special reference to the evaluation of surface area and pore size distribution (IUPAC Technical Report). *Pure and Applied Chemistry*, 2015, **87**(9-10), P. 1051–1069.
- [16] Galimzyanov R.R., Stakhanova S.V., Krechetov I.S., Kalashnik A.T., Astakhov M.V., Lisitsin A.V., Rychagov A. Yu., Galimzyanov T.R., Tabarov F.S. Electrolyte mixture based on acetonitrile and ethyl acetate for a wide temperature range performance of the supercapacitors. *Journal of Power Sources*, 2021, **495**, P. 229442.
- [17] Tabarov F.S., Astakhov M.V., Kalashnik A.T., Klimont A.A., Krechetov I.S., Isaeva N.V. Micro-mesoporous carbon materials prepared from the hogweed (Heracleum) stalks as electrode materials for supercapacitors. *Russian Journal of Electrochemistry*, 2019, **55**(4), P. 265–271.
- [18] Kalashnik A.T., Galimzyanov R.R., Stakhanova S.V., et al. Degradation processes, leading to the generation of gas in a deep polarization of supercapacitors with organic electrolytes. *Rev. Adv. Mater. Sci.*, 2017, **50**, P. 62–68.

*Information about the authors:*

*Nguyen K. Thach*<sup>1,2,a</sup>, *Ilya S. Krechetov*<sup>1,b</sup>, *Valentin V. Berestov*<sup>1,c</sup>,

*Tatyana L. Lepkova*<sup>1,d</sup>, *Svetlana V. Stakhanova*. *K. Thach* – National University of Science and Technology “MISIS”, Leninskiy prospect 4, Moscow, 119049, Russia; College of electromechanical and civil engineering, Vietnam National University of Forestry, Hanoi, Vietnam; [nguyenkienthach@gmail.com](mailto:nguyenkienthach@gmail.com)

*Ilya S. Krechetov* – National University of Science and Technology “MISIS”, Leninskiy prospect 4, Moscow, 119049, Russia; [ilya.krechetov@misis.ru](mailto:ilya.krechetov@misis.ru)

*Valentin V. Berestov* – National University of Science and Technology “MISIS”, Leninskiy prospect 4, Moscow, 119049, Russia; [vberestov97@gmail.com](mailto:vberestov97@gmail.com)

*Tatyana L. Lepkova* – National University of Science and Technology “MISIS”, Leninskiy prospect 4, Moscow, 119049, Russia; [lepkova.tl@misis.ru](mailto:lepkova.tl@misis.ru)

*Svetlana V. Stakhanova* – National University of Science and Technology “MISIS”, Leninskiy prospect 4, Moscow, 119049, Russia; Mendeleev University of Chemical Technology of Russia, Miusskaya square 9, Moscow, 125047, Russia; [stakhanova.s.v@muctr.ru](mailto:stakhanova.s.v@muctr.ru)

*Conflict of interest:* the authors declare no conflict of interest.

## Growth of carbon nanotubes on a finely dispersed nickel metal and study its electrochemical application

Vilas Khairnar

B. K. Birla College (Autonomous), Kalyan, 421304 (M.S.), India

khairnar.vilas@gmail.com

**ABSTRACT** Growth of Carbon nanotubes (CNTs) were obtained by Chemical Vapour Deposition (CVD) technique. Castor oil was vapourised above its boiling point and pyrolysis of oil was carried out by passing vapours over finely dispersed nickel metal at 650 °C. After characterization study of carbon material, scanning electron microscope (SEM) image reveals that there is a growth of densely packed nanotubes with average diameter 30 – 40 nm. The XRD study of purified carbon nanotubes shows graphitic nature of carbon. Electrochemical application of CNTs obtained was studied in Supercapacitor. Cyclic Voltammetry (CV) was used to study the capacitive behaviour of carbon nanotubes in KOH electrolyte. A capacitance of 9.89 F/g (based on the weight of the carbon material) was obtained.

**KEYWORDS** Carbon nanotube, castor oil, pyrolysis, nickel metal, capacitance

**ACKNOWLEDGEMENTS** Dr. Vilas Khairnar expresses his sincere acknowledgment to the SAIF, IIT Bombay for sample characterizations. Author also like to thanks principal, B. K. Birla College (Autonomous) for providing the facilities. Colleagues and laboratory staff of Department of Chemistry also acknowledged for providing necessary support.

**FOR CITATION** Khairnar Vilas Growth of carbon nanotubes on a finely dispersed nickel metal and study its electrochemical application. *Nanosystems: Phys. Chem. Math.*, 2022, **13** (5), 574–577.

### 1. Introduction

Supercapacitors or electric double-layer capacitors (EDLCs), are the new generation of energy storage devices to store electrical charges and provide high power densities and long cyclic life compared to other storage devices (e.g., Li-ion, lead acid, and alkaline batteries). These capacitors are intermediate systems that mainly use high dielectric materials to store more energy in a shorter time. Owing to high charging–discharging rate, large power density, as well as excellent longevity, supercapacitors have been widely seen as some of the most prospective energy storage devices [1, 2].

Supercapacitor known as “electric double-layer capacitor” utilizes the phenomenon called electric double layer whereby electricity is stored at the interface of a solid electrode and a liquid electrolyte. Hence, due to the accessible electrode/electrolyte interface and a low electrical resistance of nanotubes, a high power is expected for devices built with electrodes from these materials [3, 4]. Various carbonaceous materials have been discussed as electrode materials in supercapacitor. CNT possess many unique properties such as high mechanical strength [5], capillary properties [6], remarkable electrical conductivity and, more importantly, high specific surface area [7] which makes it a promising material for supercapacitor applications.

It is widely accepted that CNMs of various different morphologies are synthesized from plants parts as well as plant derivatives by the process of Chemical Vapor Deposition (CVD) under pyrolytic conditions [8, 9]. Researchers have also successfully prepared carbon nanotubes (CNTs) from vegetable sources by a modified traditional process [10, 11].

Hydrocarbons which are derived from fossil fuels have been used as precursor for CNT [12]; but greater availability and low cost of natural precursor sources might be advantage. Sharon et al have obtained various forms of graphitic carbon by pyrolysis of camphor [13–15].

In this paper, we report on the preparation of CNT by low temperature (650 °C) CVD of Castor oil (derived from castor seed) over finely dispersed Ni metal as a catalyst. Our point of interest was to see whether abundant growth of CNT can be brought by using a finely dispersed Ni catalyst and to study its capacitive behaviour.

### 2. Experimental: synthesis of carbon material

Metals particles such as Ni, Co, Fe are known for their catalytic role in growth of CNTs [16]. Ni metal catalyst was prepared by thermal decomposition method. Mixture of Ni (NO<sub>3</sub>)<sub>2</sub> and urea (1:3 weight ratio) was prepared in aqueous medium [17]. The solution was then heated at around 500 °C at the flash point of urea. The decomposition of urea is highly exothermic and large amounts of ammonia and carbon dioxide are liberated and fine nickel oxide is obtained. The explosive gas blows off the material resulting into ultra-fine crystallite powder. The nickel oxide was reduced in H<sub>2</sub> at

600 °C for 2 hours yielding a very fine metal powder which was used as catalyst to grow CNT by CVD of castor oil. In CVD unit two furnaces with heating zones were used.

Initially H<sub>2</sub> gas was allowed to pass through quartz furnace to make oxygen free atmosphere. Carrier gas H<sub>2</sub> was allowed to flow into the quartz tube with a fixed flow rate (6 ml/min). After 15 min of flow, the furnace was switched on to reach the desired temperature 650 °C. When the desired temperature in the second zone was reached the oil was heated in the first zone to 400 °C so as to vaporize the oil. Temperature of the second zone of furnace was also maintained at this pyrolyzing temperature for 3 h to insure maximum deposition. At the end of the desired time, the furnace was switched off which allows one to cool for overnight at room temperature.

Carbon material formed inside the quartz boat was collected and purified by treating with 50 % HCl for 24 h, in order to separate the CNT from Ni catalyst [18]. After that CNT were filtered off and finally washed with distilled water to neutral pH and dried in an air at 400 °C to remove amorphous carbon. This Carbon material was characterized by SEM, XRD and Raman spectra.

This way of carbon nanotubes synthesizing on a finely dispersed nickel metal was studied from the point of view of its electrochemical applications. All electrochemical measurements were performed with a potentiostat. With the help of potentiostat, voltage was applied for measuring of the current-voltage characteristics of the carbon material.

A set of half-cell electrode assembly of configuration “Pt / carbon nanotubes / electrolyte/ Pt” was made and specific capacitance was measured by cyclic voltammetry with the scan rate 20 mV/s, in 30 % KOH electrolyte. Pt plate and saturated calomel electrode were used as the counter and reference electrode respectively.

### 3. Results and discussion

#### 3.1. SEM study

Microstructure and morphology of the carbon material was studied by SEM image (Fig. 1). SEM image shows that the CNT are densely packed. The average diameter of CNTs is in the range of 30 to 40 nm. It is well known that such high surface area material is very useful to assemble capacitor for better capacitance. Usually carbon nanotubes produced by CVD method are mixed with nanotubes of disordered structure and amorphous carbon [19].

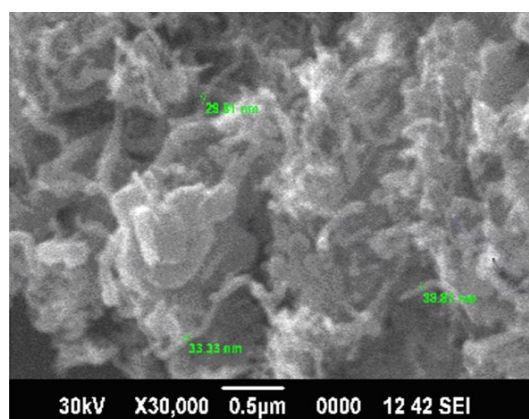


FIG. 1. SEM of CNT synthesized from Castor oil

#### 3.2. Spectroscopic studies

**3.2.1. Interpretation of XRD patterns.** XRD shows similar diffracted pattern peak (002) with graphite sheet, but not identical (Fig. 2) [20]. XRD (Fig. 2) spectrum suggests the presence of graphitic carbon which can be indicated by the sharp peak at  $2\theta = 26.45$  (002) [21] along with 44.40 (101) and 54.25 (004) values. Presence of broad peak attributed to partial crystalline nature of carbon.

**3.2.2. Raman spectroscopy.** The G-band and D-band which are characteristic for graphitic nature of carbon are prominent in Raman spectrum (Fig. 3). The G-band at  $1584\text{ cm}^{-1}$  originates from ordered graphitic nature of carbon while D-band at  $1354\text{ cm}^{-1}$  is due to disordered carbon. Raman spectrum showed well resolved D-band characteristic peak due to destabilization of graphitic plane [22]. These peaks are slightly shifted from its original position at  $1580\text{ cm}^{-1}$  of G-band and  $1340\text{ cm}^{-1}$  for D-band, respectively. The prominent G-band characteristic peak corresponds to tangential vibration in all  $\text{sp}^2$  carbon atoms in materials.

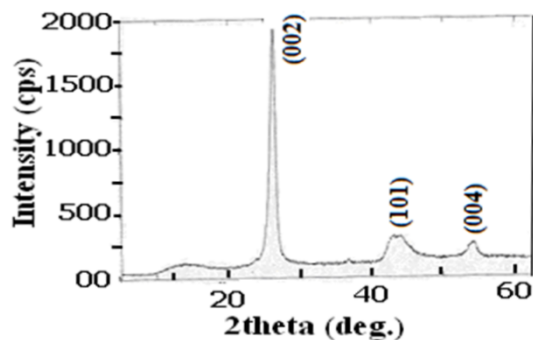


FIG. 2. XRD of CNT synthesized from Castor oil

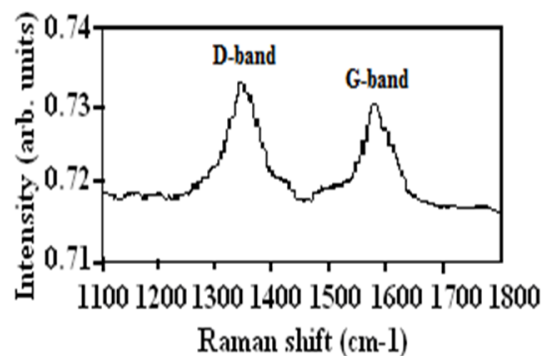


FIG. 3. Raman spectra of CNT synthesized from Castor oil

### 3.3. Electrochemical characterization

With the help of potentiostat instrument, electrochemical study of carbon nanotubes was carried out for three electrode system in 30 % KOH electrolyte. Cyclic voltammetry study of CNT material was carried out at 20 mV/S scan rates. Potential window, where no prominent oxidation-reduction peak observed (that is  $-0.4$  to  $+0.4$ ) was used for CV (Fig. 4); which indicates that the carbon material is stable in provided potential range. Capacitance was calculated from CVs at low scan rate, namely, 20 mV/s scan rate [23].

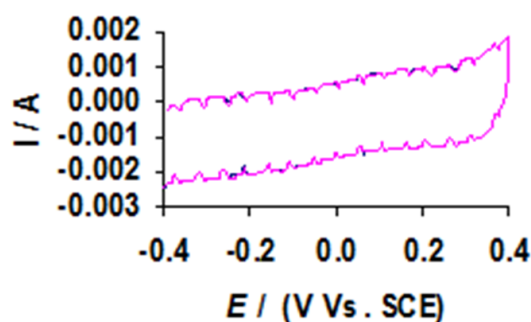


FIG. 4. CV of CNT in 30 % KOH; weight of electroactive material – 5 mg

From a potentiodynamic sweep, the capacitance ( $C$ ) was calculated by considering equation,  $C = \frac{dQ}{dE}$ , where  $\frac{dQ}{dE}$  is the rate of change of the surface charge density of the double layer with electrode potential.

Capacitance of the supercapacitor or electrochemical double layer capacitor was tested and specific capacitance of carbon nanotubes derived from castor oil was calculated on the basis of weight of the electroactive material taken (5 mg).

Hence, specific capacitance 9.89 F/g was reached for CNTs obtained from castor oil. Though CNT are known for their high surface area; its unorganized structure may lead to less accessibility to electrolyte solution. The surface area of those non-accessible pores will not contribute to the total double-layer capacitance of the material [24, 25].

## 4. Conclusion

Growth of carbon nanotubes on a finely dispersed nickel metal was very effective method. Highly dense carbon nanotubes (CNTs) were obtained by pyrolysis of castor oil vapours. Supercapacitor was assembled by using CNT electrode and electrochemical study was performed in 30 % KOH electrolyte and specific capacitance of 9.89 F/g was reached for this device.

## References

- [1] Simon P., Gogotsi Y. Materials for electrochemical capacitors. *Nat. Mater.*, 2008, **7**, P. 845–854.
- [2] Wang Y., Song Y., Xia Y. Electrochemical capacitors: Mechanism, materials, systems, characterization and applications. *Chem. Soc. Rev.*, 2016, **45**, P. 5925–5950.
- [3] An K.H., Kim W.S., et al. Supercapacitors using single-walled carbon nanotube electrodes. *Advance Materials*, 2000, **13** (7), P. 497–500.
- [4] Morinobu Endo, Takuya Hayashi, Yoong Ahm Kim, Hiroyuki Muramatsu. Development and application of carbon nanotubes. *Applied Physics*, 2006, **45**, P. 4883–4892.
- [5] Ali Eatemadi, Hadis Daraee, et al. Carbon nanotubes: properties, synthesis, purification, and medical applications. *Nanoscale Research Letters*, 2014, **9** (393).

- [6] Pederson M.R., Broughton J.Q. Nanocapillarity in fullerene tubules. *Phys. Rev. Lett.*, 1992, **69**, P. 2689–2692.
- [7] E. Frackowiak, K. Metenier, V. Bertagna, F. Beguin. Supercapacitor electrodes from multiwalled carbon nanotubes. *Appl. Phys. Lett.*, 2000, **77** (15), P. 2421–2423.
- [8] Kumar M., Ando Y. Chemical vapor deposition of carbon nanotubes: A review on growth mechanism and mass production. *J. of Nanoscience and Nanotechnology*, 2010, **10**, P. 3739–3758.
- [9] Koziol K., Boskovich B.O., Yahya N. Synthesis of carbon nanostructures by CVD method. In: *Carbon and Oxide Nanostructures. Advanced Structured Materials*, 2010, **5**, Springer, Berlin, Heidelberg, P. 23–49.
- [10] Jayaprakasan M.V., Viswanathan K., Pradyumnan P.P. Nanocarbon material from edible oils: Synthesis and characterization. *J. of Applied Physics*, 2013, **3** (6), P. 51–58.
- [11] Venkatanarayan P.S., Velmurugan R., Stanley A.J. Experimental characterisation of catalyst free carbon nanomaterials from mixed vegetable and animal base oils through modified traditional process. *J. of Nanomaterials*, 2011, **2011** (5), 959818.
- [12] Benito A.M., Maniette Y., Munoz E., Martinez M.T. Carbon nanotubes production by catalytic pyrolysis of benzene. *Carbon*, 1998, **36** (5), P. 681–683.
- [13] Sharon M., Mukhopadhyay K., et al. Spongy carbon nanobeads – a new material. *Carbon*, 1998, **36** (506), P. 507–511.
- [14] Sharon M., Mukhopadhyay K. Glassy carbon from camphor – A natural source. *Materials Chemistry and Physics*, 1996, **49** (2), P. 105–109.
- [15] Pradhan D., Sharon M., Kumar M., Ando Y. Nano-Octopus: A new form of branching carbon Nanofiber. *J. of Nanoscience and Nanotechnology*, **2003**, **3** (3), P. 215–217.
- [16] Flahaut E., Govindaraj A., et al. Synthesis of single-walled carbon nanotubes using binary (Fe, Co, Ni) alloy nanoparticles prepared in situ by the reduction of oxide solid solutions. *Chemical Physics Letters*, 1999, **300** (1–2), P. 236–242.
- [17] Chatterjee A.K., Sharon M., Ranganbanerjee, Neumann-Spallart M. CVD synthesis of carbon nanotubes using a finely dispersed cobalt catalyst and their use in double layer electrochemical capacitor. *Electrochimica Acta*, 2003, **48**, P. 3439–3446.
- [18] Djordjević V., Djustebek J., et al. Methods of purification and characterization of carbon nanotubes. *J. of Optoelectronics and Advanced Materials*, 2006, **8** (4), P.1631–1634.
- [19] Colomer J.-F., Stephan C., et al. Large-scale synthesis of single-wall carbon nanotubes by catalytic chemical vapor deposition (CCVD) method. *Chemical Physics Letters*, 2000, **317** (1–2), P. 83–89.
- [20] Belin T., Epron F. Characterization methods of carbon nanotubes: a review. *Mater. Sci. Eng. B*, 2005, **119**, P. 105–118.
- [21] Liu H.Y., Wang K.P., Teng H.S. A simplified preparation of mesoporous carbon and the examination of the carbon accessibility or electric double layer formation. *Carbon*, 2005, **43** (3), P. 559–566.
- [22] Sankaran M., Viswanathan B. Nitrogen containing carbon nanotubes as possible hydrogen storage medium. *Indian J. of Chemistry*, 2008, **47A**, P. 808–814.
- [23] Chen Quiao-Ling, Xue Kuan-Hong, et al. Fabrication and electrochemical properties of carbon nanotube array electrode for Supercapacitors. *Electrochimica Acta*, 2004, **49** (24), P. 4157–4160.
- [24] Deyang Qu, Hang Shi. Studies of activated carbons used in double-layer capacitors. *J. of Power Sources*, 1998, **74**, P. 99–107.
- [25] Heimböckel R., Hoffmann F., Fröba M. Insights into the influence of the pore size and surface area of activated carbons on the energy storage of electric double layer capacitors with a new potentially universally applicable capacitor model. *Phys. Chem. Chem. Phys.*, 2019, **6** (21), P. 3122–3133.

---

Submitted 30 January 2022; accepted 25 August 2022

#### Information about the authors:

Vilas Khairnar – B. K. Birla College (Autonomous), Kalyan, 421304 (M.S.), India; khairnar.vilas@gmail.com

## Investigation of boron-doped delta layers in CVD diamond grown on single-sector HPHT substrates

Mikhail A. Lobaev<sup>1,a</sup>, Anatoly L. Vikharev<sup>1,b</sup>, Aleksey M. Gorbachev<sup>1,c</sup>, Dmitry B. Radishev<sup>1,d</sup>, Ekaterina A. Arkhipova<sup>1,e</sup>, Mikhail N. Drozdov<sup>1,f</sup>, Vladimir A. Isaev<sup>1,g</sup>, Sergey A. Bogdanov<sup>1,h</sup>, Vladimir A. Kukushkin<sup>1,2,i</sup>

<sup>1</sup>Federal research center Institute of Applied Physics of the Russian Academy of Sciences, 603950 Nizhny Novgorod, Russia

<sup>2</sup>National Research Lobachevsky State University of Nizhny Novgorod, 603022 Nizhny Novgorod, Russia

<sup>a</sup>lobaev@ipfran.ru, <sup>b</sup>val@ipfran.ru, <sup>c</sup>gorb@ipfran.ru, <sup>d</sup>dibr@ipfran.ru, <sup>e</sup>suroveginaka@ipmras.ru,

<sup>f</sup>drm@ipmras.ru, <sup>g</sup>isaev@ipfran.ru, <sup>h</sup>bogser@ipfran.ru, <sup>i</sup>vakuk@ipfran.ru

Corresponding author: Anatoly L. Vikharev, val@ipfran.ru

PACS 81.05.ug, 73.63.-b

**ABSTRACT** This work is devoted to experimental study of boron doped delta layers in CVD diamond. Delta layers with a thickness of 0.8 – 2 nm were grown with a concentration of boron atoms of  $(1 - 1.7) \cdot 10^{21} \text{ cm}^{-3}$ , and localized inside undoped defect-free diamond. The layers thickness and boron concentration were measured by secondary ion mass spectrometry (SIMS). The surface density and the Hall mobility of holes, the layer resistance at room temperature, and temperature dependences of these parameters are presented. Performed electrical measurements showed that, despite the perfect (from the point of view of the possibility of quantum effects) profile of delta layers, no significant increase was observed in the hole mobility compared to uniform doping with the same concentration of boron atoms. An explanation is proposed for the results of electrical measurements based on calculations of the delta layer profile and the concentration of delocalized holes depending on the layer thickness. It is discussed which parameters of the boron doped delta layers are needed in order to obtain a significant increase of the hole mobility in heavily doped diamond.

**KEYWORDS** CVD diamond, boron delta-doping, electrical measurements, hole mobility

**ACKNOWLEDGEMENTS** The work was carried out within the frame of the Federal research center Institute of Applied Physics of the Russian Academy of Sciences project No. 0030-2021-0003. We express our sincere thanks to Dr. J. Butler for a fruitful discussion on delta doping of diamond during his collaboration with IAP RAS in the period of 2013 – 2018.

**FOR CITATION** Lobaev M.A., Vikharev A.L., Gorbachev A.M., Radishev D.B., Arkhipova E.A., Drozdov M.N., Isaev V.A., Bogdanov S.A., Kukushkin V.A. Investigation of boron-doped delta layers in CVD diamond grown on single-sector HPHT substrates. *Nanosystems: Phys. Chem. Math.*, 2022, **13** (5), 578–584.

### 1. Introduction

Semiconductor single-crystal diamond is produced by adding dopants (boron or phosphorus) during chemical vapor deposition (CVD synthesis) of a diamond layers on a diamond substrate, usually produced by high pressure and high temperature (HPHT) method. With its unique characteristics, such epitaxial layers are considered as promising material for electronic applications [1]. But until now, diamond electronics is still under development. The main difficulty in realizing the potential of CVD diamond is the problem of obtaining a high density of charge carriers with high mobility. Boron or phosphorus atoms create deep energy levels in semiconductor diamond, which leads to low activation of impurities in the diamond. To create an acceptable conductivity level, it is necessary to increase the doping level, but in the case of boron doping, this leads to a decrease in the hole mobility in diamond [2]. In order to increase the hole mobility, the delta doping approach was proposed [3]. Inside the undoped defect-free epitaxial layer, a doped delta layer with a thickness of 1 – 2 nm and a concentration of boron atoms of more than  $5 \cdot 10^{20} \text{ cm}^{-3}$  is formed. It is believed that in a heavily doped layer of nanometer thickness, all impurities are ionized, and most of the holes may be spread outside the delta layer, where they should have high mobility. The delocalization of free holes outside the delta layer occurs due to the effect of quantum penetration [4].

There were several attempts to create delta layers in CVD diamond [5–10]. In these studies, heavily doped delta layers of nanometer thickness were grown, but further electrical measurements did not show a high mobility of charge carriers [8, 9]. The results of these experiments [5–10] were summarized in Table 1 presented in the article [11]. The Table also lists the results obtained by that time on a CVD reactor [12] specially designed for delta doping. In the first

experiments on this reactor, several samples with delta layers of nanometer thickness were obtained, which demonstrated the Hall mobility of holes close to  $100 \text{ cm}^2/\text{V}\cdot\text{s}$  at room temperature [11]. Along with these measurements, one of the samples from this series was used for angle resolved photoemission spectroscopy (ARPES) measurements [13]. ARPES was used to compare the electronic structure of a 1.8 nm doped delta layer with a thick 3 mm boron doped diamond film [13]. The occupied electronic structure of the boron-doped layer was found to be similar to that of a uniformly doped film, with no additional features that could be attributed to the electron-occupied quantum well states and no modification of the pre-existing bands, except for a slight modification of the effective mass [13].

Thus, as was noted, the results of [8, 9] and [11, 13] diverge from each other and do not coincide with the results of modeling [8, 14] (predicting delocalization of holes). In experiments [8, 9], the measured Hall mobility of holes at room temperature was  $1 - 4.4 \text{ cm}^2/\text{V}\cdot\text{s}$ , which approximately coincides with the mobility in uniformly doped diamond with the same concentration of boron atoms of  $5 \cdot 10^{20} \text{ cm}^{-3}$ . In the experiment [11], the mobility reached approximately  $100 \text{ cm}^2/\text{V}\cdot\text{s}$ , which was close to the desired mobility values. With a clear discrepancy between the results, it was natural to want to repeat the data of [11]. We assumed that the reason for the discrepancy between the results could be the imperfection of the delta layers, i.e. insufficiently sharp and narrow dopant profiles were obtained. Therefore, a series of experiments was performed to find the delta doping regime, which ensures the growth of delta layers with a boron atom concentration of  $10^{21} \text{ cm}^{-3}$  and a thickness of 1 nm. The results of growing such doped samples were published in [15, 16].

This article presents the data of electrical measurements of a new series of samples with delta layers grown in the found regime [15, 16]. Different delta layers, both surficial and buried under the surface of the epitaxial layer, were grown. The parameters of the delta layers (thickness and boron concentration) for each sample were measured by the SIMS method. It should be noted that in previous works, either surface [5] or buried [8] layers were studied. In addition, in [8], not every sample, for which electrical measurements were carried out, was controlled by the SIMS method. Such control is important for samples, since the thickness of the delta layer and the concentration of boron in it can depend on the angle of misorientation of the surface with respect to the crystallographic direction (001) and on the level of background boron in the reactor. The performed electrical measurements showed that, despite the perfect (from the point of view of the possibility of quantum effects) profile of delta layers, there was no significant increase in the hole mobility compared to uniform doping with the same concentration of boron atoms. At the same time, according to calculations [8, 14], the quantum effect should manifest itself for such structures. Therefore, questions arise whether the theoretical calculations are predictive and which profile of the delta layer should be experimentally obtained to achieve the goal. In this article, we tried to answer these questions by analyzing our latest experimental data and the results of recent numerical calculation of delta layer profiles [17], taking into account a new effect that was not taken into account earlier [8, 14].

## 2. Experimental conditions

CVD diamond containing boron doped delta layers was grown in home-made CVD reactor, which was described in detail in [12]. The reactor consists of a cylindrical resonator with a quartz tube located on its axis. In the tube, the plasma was maintained above the substrate holder by microwave radiation from a magnetron at a frequency of 2.45 GHz. Inside the quartz tube, a laminar vortex-free gas flow was created with a flow rate of  $900 \text{ cm}^3/\text{min}$ , which made it possible to quickly switch the composition of the gas mixture. A buffer layer (undoped diamond) was first deposited on an HPHT substrate (produced by the high pressure and high temperature method) in  $\text{H}_2 + \text{CH}_4$  gas mixture ( $\text{CH}_4/\text{H}_2 = 0.2 \%$ ). Then, to grow the delta layer, this mixture was rapidly (with a characteristic time of 5 seconds) switched to a gas mixture containing boron  $\text{H}_2 + \text{CH}_4 + \text{B}_2\text{H}_6$  using a gas switch. Typical rates of diamond epitaxial growth were close to  $60 \text{ nm/h}$ . Next, the gas mixture was switched to  $\text{H}_2 + \text{CH}_4$  mixture with the addition of hydrogen sulfide, which was used as a chemical getter to reduce the level of residual contamination of the reactor with boron during the growth of the undoped layer [18]. As a result, the top layer of undoped diamond had a low concentration of boron, usually less than  $10^{17} \text{ cm}^{-3}$ .

The main conditions for the synthesis of epitaxial diamond were chosen based on the results of our previous experiments [15, 16]. In [15], the dependence of the boron concentration in the delta layer on the substrate temperature and the ratio of boron to carbon ( $B/C$ ) in the gas mixture were studied. Therefore, for the new series of experiments, the optimal ones were chosen: the deposition temperature of the delta layer and the  $B/C$  ratio equal to  $850 \text{ }^\circ\text{C}$  and 25000 ppm, respectively. In [16], the effect of the surface misorientation angle relative to the (001) crystallographic direction on the boron concentration in the delta layer was studied. At small misorientation angles, a large number of defects in the form of pyramidal hillocks were found on the surface of the epitaxial layers. At large misorientation angles, an increase in the diamond growth rate occurred, at which it was not possible to obtain a delta layer of small thickness. As a result, it was found that the optimal angle of surface misorientation should be about  $1^\circ$ . Therefore, in the experiments, type IIa diamond substrates with (100) orientation,  $3.0 \times 3.0 \times 0.5 \text{ mm}^3$  in size and with the same misorientation angles of about  $1^\circ$  were used.

In addition to control of the misorientation angle of the HPHT surface, the substrates were carefully selected according to another criterion. Using a scanning microwave microscope [19], the substrates were checked for the presence of growth and conduction sectors along the substrate surface. Studies have shown that a combination of dielectric and conductive regions was observed in some substrates [20]. Therefore, substrates with nonuniform surface conductivity

were replaced, and for a new series of experiments, single-sector and non-conductive HPHT substrates were selected. Note that prior to the beginning of the previous experiments [11], such a selection of substrates was not carried out. As before, all substrates were mechanically polished to a surface roughness ( $R_a$ ) of 0.1 nm, measured with a Zygo NewView 7300 white light interferometer over an area of  $0.22 \times 0.22 \text{ mm}^2$ . A layer of 4–5  $\mu\text{m}$  was uniformly etched from the substrates in ICP plasma (Oxford Instruments, Plasmalab 80) to remove defects introduced into the surface by mechanical polishing, without deterioration of the substrates roughness. As a result defect-free substrates with an atomically smooth surface were used to grow delta-doped CVD diamond.

The depth distribution of boron in the grown samples was measured by secondary ion mass spectroscopy (SIMS) on a time-of-flight SIMS setup (IONTOF TOF.SIMS-5). The depth of etch craters for calculating the depth of analysis from the etch time was determined using Talysurf CCI 2000 and Zygo NewView 7300 white light interference microscopes. Sputtering was performed with  $\text{Cs}^+$  ions with an energy of 1 keV at an angle of  $45^\circ$ . Probing was carried out with  $\text{Bi}^+$  ions with an energy of 25 keV. Quantitative calibration of the mass spectrometer was performed using a test HPHT substrate implanted with boron ions.

### 3. Experimental results

The performed series of experiments, in which the optimized delta doping regime was used, made it possible to obtain samples with a high concentration of boron atoms in a layer of nanometer thickness, Fig. 1. The samples had different delta layers: for sample SS4-2, the layer was located on the surface; for sample SS5-2, buried at a depth of 72 nm from the surface of the epitaxial layer; for samples SS9, SS10, and SS1-3, the layer was located at depth of 15, 12 and 13 nm, respectively. In addition, heavily doped surface layers 3 nm thick were grown on the last three samples to create ohmic contacts without additional thermal annealing for electrical measurements. The boron concentration profile in the epitaxial layer for these three samples was approximately the same, corresponding to the profile shown in Fig. 1(c) for sample SS9. Boron atoms concentration, delta layer thickness, and other characteristics are summarized for all samples in Table 1. To quantitatively describe the distribution of boron in delta-doped diamond, we considered the simplest approximation, which is a rectangular concentration distribution or “top-hat” distribution. According to SIMS measurements, the maximum concentration of boron in the delta layers was  $(0.99 - 1.68) \cdot 10^{21} \text{ cm}^{-3}$ . The profile width determined using the reconstruction procedure described in [15] was 0.85 – 2.01 nm. Taking into account the width of the profile and the maximum concentration of boron, the surface densities of  $N_{2D}$  boron atoms in the delta layers were calculated equal to  $(14.3 - 19.9) \cdot 10^{13} \text{ cm}^{-2}$ . These  $N_{2D}$  values, according to electrical measurements, were several times higher than the surface concentrations of charge carriers (holes).

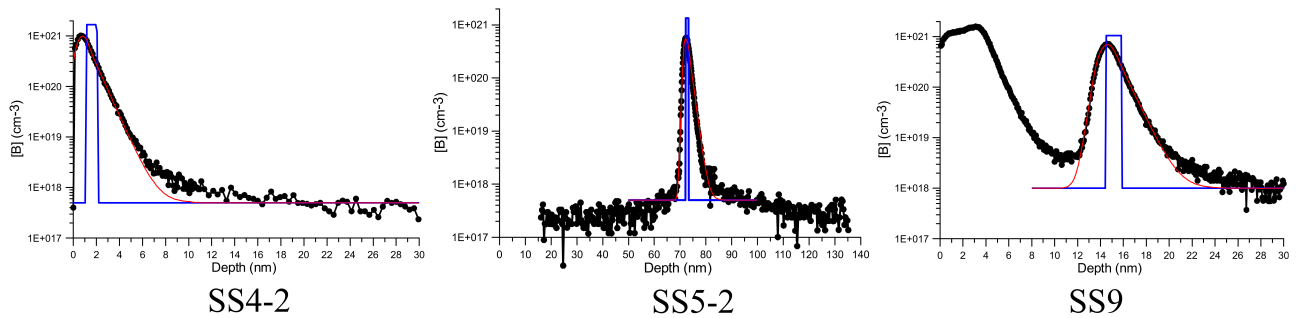


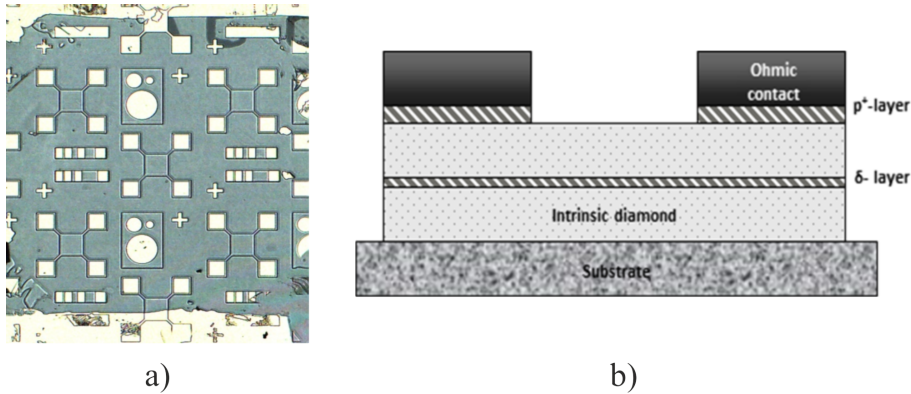
FIG. 1. Boron concentration profiles obtained from SIMS data (black dots), reconstructed boron profiles (blue line) and convolutions of the reconstructed profile and instrumental function of the SIMS instrument (red line) for samples SS4-2, SS5-2 and SS9

To carry out electrical measurements on samples with two layers (SS9, SS10 and SS1-3), measuring test cells were formed, including the process of etching mesa structures. The measurements were performed using Hall effect methods. Fig. 2 shows a photograph of a diamond surface ( $0.22 \times 0.22 \text{ mm}^2$  in size) with test cells formed for Hall measurements in Van der Pauw geometry, TLM lines and CV cells, as well as a scheme for the formation of a mesa structure and an ohmic contact to the delta layer using  $p^+$  layer on the surface. To create ohmic contacts, we chose the composition Ti/Mo/Au with a layer thickness of 20 nm for Ti, 30 nm for Mo, and 100 nm for Au. The creation of ohmic contacts to a heavily doped diamond layer was described in detail in [21]. The contact resistances were measured by the transmission line modeling (TLM) method using the Keithley SCS 4200 measuring system. The contacts turned out to be ohmic without additional thermal annealing and had a contact resistance of  $10^{-4} - 10^{-5} \text{ Ohm}\cdot\text{cm}^2$  [21]. The surface  $p^+$  layer between the contact pads was etched away; therefore, the current flow in the structure occurred only along the buried delta layer. The results of electrical measurements are also shown in Table 1.

Table 1 lists the surface densities  $N_{2D}$  of boron atoms in grown delta layers. In the case of complete ionization of boron atoms in the delta layer, the value of  $N_{2D}$  in the delta layers should coincide with the measured surface concentration

TABLE 1. Boron concentration, delta layer thickness, surface concentration and Hall mobility of holes at room temperature, layer resistance

Sample label	Boron concentration ( $10^{21} \text{ cm}^{-3}$ )	Delta layer thickness (nm)	$N_{2D}$ boron density ( $10^{13} \text{ cm}^{-2}$ )	$P_s$ ( $10^{13} \text{ cm}^{-2}$ ) sheet hole concentration at $T = 300 \text{ K}$	Mobility at $T = 300 \text{ K}$ ( $\text{cm}^2/\text{Vs}$ )	Resistivity at $T = 300 \text{ K}$ ( $\text{k}\Omega/\text{sq}$ )
SS4-2	1.68	0.85	14.3	0.23	24.4	112
SS5-2	1.33	1.08	14.4			
SS9	1.05	1.39	14.6	2	4	70.5
SS10	0.99	2.01	19.9	11	1.4	37.75
SS1-3	1.29	1.43	18.4	7.0	1.5	58

FIG. 2. Photograph of a diamond surface ( $0.22 \times 0.22 \text{ mm}^2$  in size) with test cells formed for Hall measurements in Van der Pauw geometry, TLM lines and CV cells (a), a scheme for the formation of a mesa structure and an ohmic contact to the delta layer using  $p^+$  layer on the surface (b)

of holes. As can be seen from Table 1, the difference is quite significant, from 2.6 times for sample SS1-3 up to 63 times for sample SS4-2. Such a difference can be caused either by incomplete ionization of boron in the delta layer (for example, due to the formation of boron dimers) or by the presence of a sufficiently large number of traps for free holes, which can arise due to the presence of defects in the epitaxial layer [22].

The thinnest of all delta layers (0.85 nm) was the layer located on the surface of sample SS4-2. The Hall mobility of holes at room temperature was the highest for this sample and was  $24.4 \text{ cm}^2/\text{V}\cdot\text{s}$ . It can be assumed that in this series of experiments, with a decrease of the layer thickness from 2.01 to 0.85 nm, a tendency was observed for an increase of the mobility of holes with a narrowing of the dopant profile.

For the SS10 sample, the temperature dependence of the surface concentration and the Hall mobility of holes was studied in the temperature range  $100 \text{ K} < T < 500 \text{ K}$ . Measurements were also performed using Hall effect methods on etched mesa structures, Fig. 3. It can be seen from the figure that the hole mobility in the delta layer of this sample varied from 1 to  $4 \text{ cm}^2/\text{V}\cdot\text{s}$  over the entire temperature range. The hole density also weakly depended on temperature and varied from  $6 \cdot 10^{13}$  to  $10^{14} \text{ cm}^{-3}$ . Such a weak temperature dependence of the density and the mobility of holes and the resistance of the layer indicate that in the delta layer under consideration, a transition from semiconductor to metallic conductivity (MIT transition) occurred.

The error in measuring the resistivity by the four-point probe method did not exceed 10%. With a sufficiently high mobility, above several tens of  $\text{cm}^2/\text{V}\cdot\text{s}$ , measurements of the mobility and concentration of charge carriers will have the same error. However, with a decrease of mobility, the measurement error of the Hall EMF increases sharply. With a mobility of  $\sim 1 \text{ cm}^2/\text{V}\cdot\text{s}$ , the error of determining the concentration and mobility may reach 100%. Apparently, this is the reason for the strong scatter of the experimental points for mobility and concentration in Figs. 3(b,c) as the temperature decreases below 200 K. An additional reason for such a scatter may be the occurrence of a nonlinear I-V characteristic of ohmic contacts in this temperature range. At  $T = 300 \text{ K}$ , the I-V characteristic is linear.

When growing epitaxial layers with doped delta layers, we studied the roughness of the diamond surface for each sample. For example, one can make an assumption about the delta layer surface by comparing the surface roughness of samples SS4 and SS5-2. Table 2 compares two values characterizing the surface roughness RMS (root mean square roughness) and Ra (mean deviation) for these samples before and after the CVD growth process.

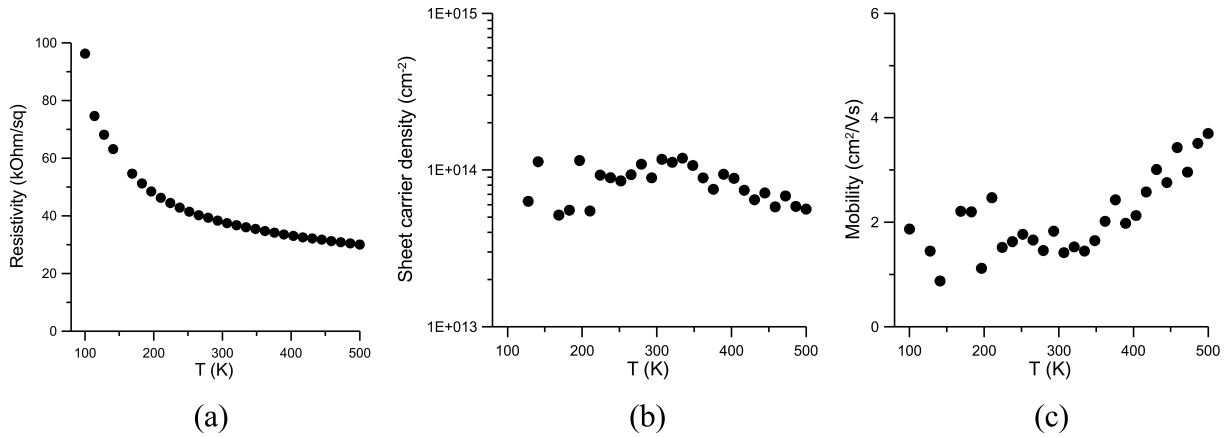


FIG. 3. Temperature dependence of surface resistance (a), Hall density of carriers (b), and Hall mobility (c) for the SS10 sample

TABLE 2. RMS and Ra surface roughness before and after CVD growth

	RMS for substrate, nm	RMS after CVD growth, nm	Ra for substrate, nm	Ra after CVD growth, nm	Etch pits/cm <sup>2</sup> × 10 <sup>4</sup>	Hillocks /cm <sup>2</sup> × 10 <sup>4</sup>	Σ def/cm <sup>2</sup> × 10 <sup>4</sup>
SS4-2	0.179	0.584	0.102	0.171	3.4	2.5	5.9
SS5-2	0.181	0.817	0.096	0.220	3.15	2.8	5.95

The surface analysis of the samples was carried out using a Zygo NewView 7300 white light interferometer. As can be seen from Table 2, the roughness of the epitaxial layer increased compared to the roughness of the substrate. The deterioration of the measured roughness after the CVD growth process is largely associated not with the deterioration of the roughness of the entire surface, but with the appearance of a small number of point relatively deep (high) defects: etch pits and pyramidal hillocks. This can be seen from the surface profile image shown in Fig. 4 (blue/red spots), and by the ratio of RMS/Ra values. Ra after growth, which is less sensitive to point defects, deteriorated by only 0.07 – 0.12 nm (1.7 – 2.3 times), while RMS deteriorated by 0.40 – 0.60 nm (3.3 – 4.5 times). The defect density for sample SS4-2 was  $5.9 \cdot 10^4$  def/cm<sup>2</sup>, and for sample SS5-2 it was  $5.95 \cdot 10^4$  def/cm<sup>2</sup>. Despite such a low density, apparently, surface defects of the SS4-2 sample influenced the results of electrical measurements (reduced the hole mobility).

#### 4. Discussion

In [11], higher values of the hole mobility in samples with delta layers were obtained than in the present work. However, according to our latest studies, the results of [11] can not be unambiguously interpreted as the mobility of delta layers. In [11], multisectoral diamond substrates were used, which could contain both dielectric and conductive regions, which was not analyzed in [11] when choosing substrates. Such an analysis became possible only due to the use of local microwave conductivity microscopy [20]. All the substrates used in this work underwent such an analysis and did not contain conductive inclusions.

In our experiments single-sector and non-conductive substrates were used; layers with a boron atom concentration of  $10^{21}$  cm<sup>-3</sup> and a thickness of 0.85 – 2.01 nm were grown on them. However, the hole mobility did not increase significantly compared to uniform doping, which would be a consequence of a noticeable delocalization of holes. An increase in the mobility of holes is achieved due to the quantum penetration of the wave functions of holes from the potential well formed by the doped layer into the surrounding undoped diamond. As a result, their scattering by ionized boron atoms located in the doped layer decreases, while the mobility increases. When choosing the doping regime (to obtain the required concentration of boron atoms in diamond and the thickness of the delta layers), we were guided by the results of earlier calculations [8, 14], which predict a noticeable delocalization of holes for the above layer parameters.

The results obtained in the new series of experiments can be explained using the results of recent calculations of the delta layer profiles [17]. These calculations took into account the increase in the energy of the upper boundary of the valence band, which was not previously taken into account in [8, 14], which arises in such layers due to the high concentration of ionized boron atoms and leads to a significant deepening of the potential wells for holes created by them. As a result, the penetration of the wave functions of the holes into the undoped material surrounding the delta layer turns out to be much weaker than was previously thought. Thus, calculations show that at a concentration of boron atoms in the delta layer of the order of  $10^{21}$  cm<sup>-3</sup> and its thickness of 2 nm, only 7 % (and not 50 % as stated in [14]) of holes

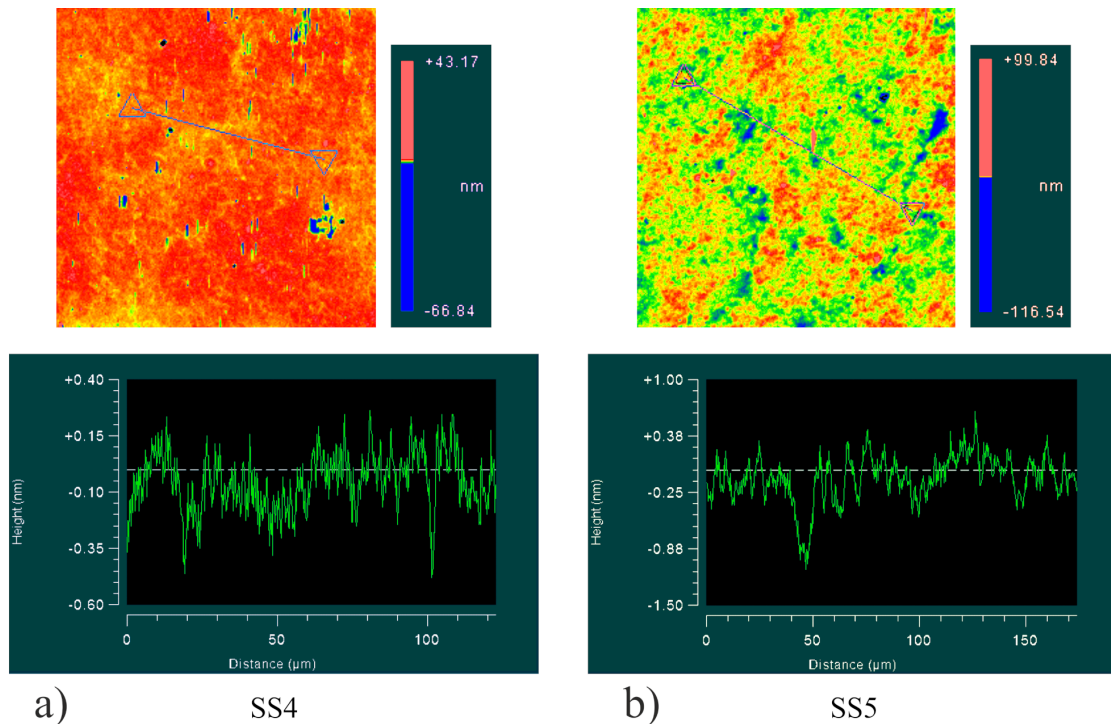


FIG. 4. Surface defects of the epitaxial layer of samples SS4-2 (a) and SS5-2 (b), investigated area  $0.22 \times 0.22 \text{ mm}^2$

are outside it, at 1 nm, 19 % (and not 70 % as in [14]) and at 0.5 nm – 47 % (and not 75 % as in [14]). Thus, an increase in the hole mobility in delta layers, as compared with homogeneous doping with the same concentration of boron atoms, can only be expected at delta layer thicknesses of the order of 0.5 nm or less.

In the presented results (Tables 1 and 2), the obtained hole mobility values, firstly, can be explained by the insufficiently small thickness of the delta layers and a small fraction of delocalized holes. Second, effects other than quantum penetration can manifest themselves, additionally affecting the resulting mobility and density of free holes in the structure. Such effects may include the scattering of holes on the surface roughness of the layer and the presence of defects (traps) in the delta layer. Based on the temperature dependence of the surface resistance, Hall density, and hole mobility, it can be assumed that an insulator–metal phase transition occurred and all boron atoms were ionized, but the density of free holes was significantly lower (Fig. 3). In our experiment, the measured density of defects was quite high (Table 2) and such a high density of defects (traps) can explain the experimental difference between the density of ionized boron atoms and the measured density of charge carriers.

We also note the results of the recent work of the authors [23], which presents data on the mobility of holes in delta-doped boron layers grown on multisectoral HPHT substrates. In deep delta layers, about 1.5 nm thick, a hole mobility of  $200 \text{ cm}^2/\text{V}\cdot\text{s}$  was observed, and in a layer on the surface, up to  $600 \text{ cm}^2/\text{V}\cdot\text{s}$ . However, the two-dimensional concentration of free carriers was only 0.1 % of the two-dimensional concentration of boron atoms, which indicated an extremely low concentration of delocalized holes. These results also confirm the main conclusion of this work about the need for thinner delta layers to create a conductive 2D channel.

Thus, to achieve high hole mobility in deep delta layers in CVD diamond, it is necessary to obtain both a thin (about 0.5 nm thick) delta layer with a high surface hole concentration of  $5 \cdot 10^{13} \text{ cm}^{-2}$ , and a sufficiently smooth layer surface with a minimum number of defects, providing a slight increase in roughness compared to the substrate surface, for which the RMS value is less than 0.2 nm. In such a structure, in our opinion, one can expect a significant increase of the mobility of charge carriers in semiconducting diamond. It seems to us that such layers can be obtained by improving of our doping regime.

## References

- [1] Sussman R.S. *CVD Diamond for Electronic Devices and Sensors*, Wiley, 2009.
- [2] Lagrange J.-P., Deneuve A., Gheeraert E. A large range of boron doping with low compensation ratio for homoepitaxial diamond films. *Carbon*, 1999, **37** (5), P. 807–810.
- [3] Kobayashi T., Ariki T., et al. Analytical studies on multiple delta doping in diamond thin films for efficient hole excitation and conductivity enhancement. *J. Appl. Phys.*, 1994, **76**, 1977.
- [4] Schubert E.F. *Delta-doping of semiconductors*, Cambridge University Press, UK, 1996.
- [5] Balmer R.S., Friel I., et al. Transport behavior of holes in boron delta-doped diamond structures. *J. Appl. Phys.*, 2013, **113**, 033702.

- [6] Scharpf J., Denisenko A., et al. Transport behaviour of boron delta-doped diamond. *Phys. Status Solidi A*, 2013, **210** (10), P. 2028–2034.
- [7] Mer-Calfati C., Tranchant N., et al. Sharp interfaces for diamond delta-doping and SIMS profile modelling. *Materials Letters*, 2014, **115**, P. 283–286.
- [8] Chicot G., Fiori A., et al. Electronic and physico-chemical properties of nanometric boron delta-doped diamond structures. *J. Appl. Phys.*, 2014, **116** (8), 083702.
- [9] Chicot G., Tran Thi T.N., et al. Hole transport in boron delta-doped diamond structures. *Appl. Phys. Lett.*, 2012, **101**, 162101.
- [10] Edgington R., Sato S., et al. Growth and electrical characterisation of  $\delta$ -doped boron layers on (111) diamond surfaces. *J. Appl. Phys.*, 2012, **111**, 033710.
- [11] Butler J.E., Vikharev A., et al. Nanometric diamond delta doping with boron. *Phys. Status Solidi RRL*, 2017, **11** (1), 1600329.
- [12] Vikharev A.L., Gorbachev A.M., et al. Novel microwave plasma-assisted CVD reactor for diamond delta doping. *Phys. Status Solidi RRL*, 2016, **10** (4), P. 324–327.
- [13] Pakpour-Tabrizi A.C., Schenk A.K., et al. The occupied electronic structure of ultrathin boron doped diamond. *Nanoscale Adv.*, 2020, **2**, P. 1358–1364.
- [14] Fiori A., Pernot J., Gheeraert E., Bustarret E. Simulations of carrier confinement in boron  $\delta$ -doped diamond devices. *Phys. Status Solidi A*, 2010, **207** (9), P. 2084–2087.
- [15] Lobaev M.A., Gorbachev A.M., et al. Investigation of boron incorporation in delta doped diamond layers by secondary ion mass spectrometry. *Thin Solid Films*, 2018, **653**, P. 215–222.
- [16] Lobaev M.A., Gorbachev A.M., et al. Misorientation Angle Dependence of Boron Incorporation Into CVD Diamond Delta Layers. *Phys. Status Solidi B*, 2019, 1800606.
- [17] Kukushkin V.A., Lobaev M.A., et al. Experimental and theoretical study of boron-doped delta layers of diamond deposited from the gas phase to ensure high hole mobility. *Proc. of the XXVI Int. Symposium “Nanophysics and Nanoelectronics”*, Nizhny Novgorod, 2022, **2**, P. 887–888.
- [18] Eaton S.C., Anderson A.B., et al. Co-doping of Diamond with Boron and Sulfur. *Electrochem. Solid-State Lett.*, 2002, **5**, G65.
- [19] Reznik A.N., Korolyov S.A. Monopole antenna in quantitative near-field microwave microscopy of planar structures. *J. Appl. Phys.*, 2016, **119**, 094504.
- [20] Reznik A.N., Korolev S.A., Drozdov M.N. Microwave microscopy of diamond semiconductor structures. *J. Appl. Phys.*, 2017, **121**, 264503.
- [21] Arkhipova E.A., Demidov E.V., et al. Ohmic contacts to CVD diamond with boron-doped delta layers. *Semiconductors*, 2019, **53** (10), P. 1348–1352.
- [22] Schreck M., Ščajev P., et al. Charge carrier trapping by dislocations in single crystal diamond. *J. Appl. Phys.*, 2020, **127**, 125102.
- [23] Arkhipova E.A., Drozdov M.N., et al. Electrophysical properties of delta-boron-doped diamond layers. *Proc. of the XXVI Int. Symposium “Nanophysics and Nanoelectronics”*, Nizhny Novgorod, 2022, **2**, P. 689–690.

---

Submitted 25 July 2022; revised 8 September 2022; accepted 15 September 2022

#### Information about the authors:

*Mikhail A. Lobaev* – Federal research center Institute of Applied Physics of the Russian Academy of Sciences, 603950 Nizhny Novgorod, Russia; ORCID 0000-0002-7261-6766; lobaev@ipfran.ru

*Anatoly L. Vikharev* – Federal research center Institute of Applied Physics of the Russian Academy of Sciences, 603950 Nizhny Novgorod, Russia; ORCID 0000-0001-6478-3911; val@ipfran.ru

*Aleksey M. Gorbachev* – Federal research center Institute of Applied Physics of the Russian Academy of Sciences, 603950 Nizhny Novgorod, Russia; ORCID 0000-0003-0712-2898; gorb@ipfran.ru

*Dmitry B. Radishev* – Federal research center Institute of Applied Physics of the Russian Academy of Sciences, 603950 Nizhny Novgorod, Russia; ORCID 0000-0002-8416-1738; dibr@ipfran.ru

*Ekaterina A. Arkhipova* – Federal research center Institute of Applied Physics of the Russian Academy of Sciences, 603950 Nizhny Novgorod, Russia; ORCID 0000-0002-0358-3438; suroveginaka@ipmras.ru

*Mikhail N. Drozdov* – Federal research center Institute of Applied Physics of the Russian Academy of Sciences, 603950 Nizhny Novgorod, Russia; ORCID 0000-0001-5577-2460; drm@ipmras.ru

*Vladimir A. Isaev* – Federal research center Institute of Applied Physics of the Russian Academy of Sciences, 603950 Nizhny Novgorod, Russia; ORCID 0000-0003-0873-6584; isaev@ipfran.ru

*Sergey A. Bogdanov* – Federal research center Institute of Applied Physics of the Russian Academy of Sciences, 603950 Nizhny Novgorod, Russia; ORCID 0000-0001-8087-7723; bogser@ipfran.ru

*Vladimir A. Kukushkin* – Federal research center Institute of Applied Physics of the Russian Academy of Sciences, 603950 Nizhny Novgorod, Russia; National Research Lobachevsky State University of Nizhny Novgorod, 603022 Nizhny Novgorod, Russia; ORCID 0000-0002-8528-3884; vakuk@ipfran.ru

*Conflict of interest:* the authors declare that they have no conflict of interest.



# NANOSYSTEMS:

**PHYSICS, CHEMISTRY, MATHEMATICS**

## INFORMATION FOR AUTHORS

The journal publishes research articles and reviews, and also short scientific papers (letters) which are unpublished and have not been accepted for publication in other magazines. Articles should be submitted in English. All articles are reviewed, then if necessary come back to the author to completion.

The journal is indexed in Web of Science Core Collection (Emerging Sources Citation Index), Chemical Abstract Service of the American Chemical Society, Zentralblatt MATH and in Russian Scientific Citation Index.

### Author should submit the following materials:

1. Article file in English, containing article title, the initials and the surname of the authors, Institute (University), postal address, the electronic address, the summary, keywords, MSC or PACS index, article text, the list of references.
2. Files with illustrations, files with tables.
3. The covering letter in English containing the article information (article name, MSC or PACS index, keywords, the summary, the literature) and about all authors (the surname, names, the full name of places of work, the mailing address with the postal code, contact phone number with a city code, the electronic address).
4. The expert judgement on possibility of publication of the article in open press (for authors from Russia).

Authors can submit a paper and the corresponding files to the following addresses: nanojournal.ifmo@gmail.com, popov1955@gmail.com.

### Text requirements

Articles should be prepared with using of text editors MS Word or LaTeX (preferable). It is necessary to submit source file (LaTeX) and a pdf copy. In the name of files the English alphabet is used. The recommended size of short communications (letters) is 4-6 pages, research articles– 6-15 pages, reviews – 30 pages.

#### Recommendations for text in MS Word:

Formulas should be written using Math Type. Figures and tables with captions should be inserted in the text. Additionally, authors present separate files for all figures and Word files of tables.

### Recommendations for text in LaTeX:

Please, use standard LaTeX without macros and additional style files. The list of references should be included in the main LaTeX file. Source LaTeX file of the paper with the corresponding pdf file and files of figures should be submitted.

References in the article text are given in square brackets. The list of references should be prepared in accordance with the following samples:

- [1] Surname N. *Book Title*. Nauka Publishing House, Saint Petersburg, 2000, 281 pp.
- [2] Surname N., Surname N. Paper title. *Journal Name*, 2010, 1 (5), P. 17-23.
- [3] Surname N., Surname N. Lecture title. In: Abstracts/Proceedings of the Conference, Place and Date, 2000, P. 17-23.
- [4] Surname N., Surname N. Paper title, 2000, URL: <http://books.ifmo.ru/ntv>.
- [5] Surname N., Surname N. Patent Name. Patent No. 11111, 2010, Bul. No. 33, 5 pp.
- [6] Surname N., Surname N. Thesis Title. Thesis for full doctor degree in math. and physics, Saint Petersburg, 2000, 105 pp.

### **Requirements to illustrations**

Illustrations should be submitted as separate black-and-white files. Formats of files – jpeg, eps, tiff.



# ***NANOSYSTEMS:***

***PHYSICS, CHEMISTRY, MATHEMATICS***

**Журнал зарегистрирован**

Федеральной службой по надзору в сфере связи, информационных технологий и массовых коммуникаций

(свидетельство ПИ № ФС 77 - 49048 от 22.03.2012 г.)

ISSN 2220-8054

**Учредитель:** федеральное государственное автономное образовательное учреждение высшего образования

«Национальный исследовательский университет ИТМО»

**Издатель:** федеральное государственное автономное образовательное учреждение высшего образования

«Национальный исследовательский университет ИТМО»

**Отпечатано** в Учреждении «Университетские телекоммуникации»

Адрес: 197101, Санкт-Петербург, Кронверкский пр., 49

**Подписка на журнал НФХМ**

На первое полугодие 2023 года подписка осуществляется через

ОАО «АРЗИ», подписной индекс Э57385